



UNIVERSITY OF
LIVERPOOL

**STRUCTURAL BEHAVIOUR OF VARIOUS
CORRUGATED SANDWICH STRUCTURES
SUBJECTED TO QUASI-STATIC AND
DYNAMIC LOADING**

Thesis submitted in accordance with the requirement of the
University of Liverpool for the degree of
Doctor of Philosophy

By
CDR. Tawan Boonkong
June 2017

PUBLICATIONS

- T. Boonkong, Y. Shen, Z. Guan, and W. Cantwell, The low velocity impact response of curvilinear-core sandwich structures, *International Journal of Impact Engineering*, vol. 93, 2016, pp. 28-38.
- T. Boonkong, Y.O. Shen, Z.W. Guan and W.J. Cantwell (2014), Numerical modelling of curvilinear corrugated-core sandwich structures subjected to low velocity impact loading, *Proceedings of the 5th International Conference on Computational Methods (ICCM2014)*, Cambridge, England, July 28, 2014 – July 30, 2014.
- R.A. Alia, Z.W. Guan, W.J. Cantwell and T. Boonkong, Modelling the macro-mechanical axial progressive damage of carbon/glass epoxy circular tubes, In: Presented at the 13th U.S. National Congress for Computational Mechanics, San Diego, 2015.
- T. Boonkong, Z.W. Guan, W.J. Cantwell and R.A. Alia, The mechanical behaviour of new hybrid sandwich structures based on corrugated-core and fibre metal laminates under low velocity impact loading, In: Presented at the 13th U.S. National Congress for Computational Mechanics, San Diego, 2015.

ABSTRACT

New designs of sandwich structures for modern high performance shipcraft have been proposed to be used in the Royal Thai Navy ships. Here, novel hybrid sandwich structures based on corrugated reinforced foam cores have been developed by combining various corrugated cores and Fibre Metal Laminates (FMLs) based on aluminium alloy and fibre reinforced composites, to maximise the functionality of the structures.

New manufacturing and fabrication techniques have been introduced to improve the integrity of the corrugated core and the skins by achieving a strong bond across the skin-core interface, as well as the fabrication efficiency. The aim of this research work is to investigate the mechanical properties and structural response of the various novel hybrid corrugated sandwich structures under three-point bending, quasi-static and dynamic compression, impact and blast loading. Firstly, tests are conducted to obtain mechanical properties of constituent materials. Then extensive experimental work is undertaken to determine the load-displacement relationships, the failure mechanisms and energy-absorbing characteristics of a large number of corrugated-cores with different cell wall thickness, core configurations and reinforcement, types of foam cores, foam core densities, unit cell sizes, core-layers, core materials and cores with vertical reinforcements. The results reveal relationships of the structural response and types of the failure mode occurred during the tests.

The finite element models have then be developed to simulate the response of the corrugated structures tested, which are validated against the corresponding experimental results in terms of deformation and failure modes. The agreement

between the numerical predictions and the experimental results is very good across the range of the structures and configurations investigated. Here, the fibre reinforced composites before the onset of damage is modelled as an orthotropic linear elastic material and the damage is modelled using Hashin's criteria. The aluminium alloys are simulated as an isotropic elastic material before the yield point, followed by strain hardening. The ultimate failure is modelled using the shear failure and ductile failure available in the commercial code Abaqus. Parametric studies are also carried out using the validated numerical models to investigate the structural responses of the corrugated curvilinear aluminium structures subjected to various loading and geometric and material conditions.

The dynamic characteristics of the composite sandwich structures through series of experimental tests and numerical predictions investigated in this project can be used in the design of lightweight composite structures for energy-absorbing applications in aerospace, marine and vehicle transportation industries.

ACKNOWLEDGEMENTS

First, I would like to sincere thanks and appreciation to my supervisors, Professor Zhongwei Guan and Professor Wesley Cantwell for supervising me as his PhD student. Besides the actual research, he also guides me to become a good and responsible academician. I really value his advice, support, encouragement, respect, comments and most importantly his patience throughout the years that I have been working with him. My special thanks to Dr Mohd Ruzaimi Mat Rejab for inspiring and guiding me to do on this project

My sincere gratitude to members of School of Engineering, including Mr Stephen Pennington, Mr Jijimon Mathew, Mr Dave Atkinson as well as my friends in Composite Research Group, including Dr Mohamad Zaki Hassan (UTM), Dr Rafidah Hasan (UTeM), Dr Siti Hajar Sheikh Md Fadzullah (UTeM), Dr Mohd Zuhri Mohamed Yusoff (UPM), Dr Alia Ruzanna Aziz (UniKL), Major Mohamed Al-Tenaiji (UAE Army), Dr Amit Haldar (IIT Guwahati), Adil Jamil, Kanna Subramaniyan, Moradi Alireza, Ali Al-Rifaie, Muhd Azimin. I enjoy being with them. My appreciation is also due to all the staffs and friends in the university that I have been associating directly or indirectly during my stay at Liverpool.

I am delighted to the love and support of my family, Thanya, my wife, and my parents over the past years for their love, support, understanding and patience throughout the ups and downs during this study. And finally, I would also like to thank the Royal Thai navy and the Government of Thailand for sponsoring this PhD study.

CONTENTS

PUBLICATIONS	ii
ABSTRACT	iii
ACKNOWLEDGEMENTS	v
CONTENTS	vi
LIST OF FIGURE.....	xii
LIST OF TABLE	xxxii
NOTATION	xxxiii
CHAPTER 1 INTRODUCTION	1
1.1 Overview of composite structures.....	2
1.2 Composite Materials	3
1.3 Composite Sandwich Structures	5
1.4 Applications of corrugated core sandwich structures	5
1.4.1 Packaging applications.....	5
1.4.2 Transportation applications.....	6
1.4.3 Aerospace applications.....	6
1.4.4 Marine applications	7
1.5 Motivation of the research work	8
1.6 Research aim and objectives	11
1.7 Significance of the study	12

1.8 Thesis outline	13
CHAPTER 2 LITERATURE REVIEW	14
2.1 Overview of composite sandwich structures	15
2.1.1 Sandwich types	15
2.2 Manufacturing techniques of making sandwich structures.....	16
2.3 Background and classification of Fibre metal laminates (FMLs).....	25
2.4 Corrugated-core Sandwich Structures.....	27
2.4.1 Curvilinear Corrugated-core	28
2.4.2 Straight Corrugated core	31
2.4.3 Hat-type Corrugated-core.....	32
2.4.4 Triangular Corrugated-core.....	34
2.5 Mechanical properties of corrugated-core sandwich structures.....	36
2.5.1 Mechanical response under quasi-static loading.....	36
2.5.2 Mechanical response under dynamic loading	41
2.6 Concept of energy absorption	50
2.6.1 Energy-absorbing capacities of core structures.....	53
2.7 Review of modelling of sandwich structures	54
2.7.1 Background of the finite element method.....	54
2.7.2 Modelling of Corrugated-core Sandwich Structures.....	55
2.8 Failure mechanisms of corrugated-core sandwich structures	61
2.8.1 Failure mechanisms from quasi-static loading.....	61

2.8.2 Failure mechanisms from dynamic loading	63
2.9 Summary of literature review.....	66
CHAPTER 3 EXPERIMENTAL PROCEDURE	67
3.1 Materials examined	68
3.1.1 Aluminium 2024-T3	68
3.1.2 Glass fibre reinforced plastic (GFRP).....	68
3.1.3 Core materials	69
3.1.4 Fibre metal laminates (FMLs).....	70
3.2 Manufacturing methods	70
3.2.1 Design of corrugated cores.....	71
3.2.2 Fabrication processes	73
3.3 Test specimens and configurations	77
3.3.1 The effect of the core thickness of plain GFRP corrugated sandwich structures	78
3.3.2 Different core configurations	79
3.3.3 Various core thickness of GFRP corrugated reinforced foam core	81
3.3.4 Different types of foam cores.....	82
3.3.5 Samples with different foam core densities and multi-layer.....	83
3.3.6 Samples with different unit cell sizes	85
3.3.7 Samples with different number of core layers	86
3.3.8 Sandwich structures based on FML cores.....	87

3.3.9 Cores with vertical reinforcements	88
3.4 Mechanical tests of the plain composite, metal and FMLs	90
3.4.1 Tensile tests on the aluminium alloy.....	90
3.4.2 Tensile tests on the composites	91
3.4.3 In-plane shear tests on composites	92
3.4.4 Compression tests on rigid foams	94
3.5 Quasi-static structural tests	95
3.5.1 Three-point bending tests	95
3.5.2 Static compression tests	95
3.6 Dynamic testing	98
3.6.1 Low velocity impact tests with a flat head impactor.....	98
3.6.2 Perforation tests.....	101
3.6.3 Blast tests	104
3.7 Failure mechanisms and damage observations	112
3.8 Summary	113
CHAPTER 4 RESULTS AND DISCUSSION	114
4.1 Mechanical properties of materials	115
4.1.1 Tensile tests of aluminium alloy	115
4.1.2 Tensile tests on the composites	119
4.1.3 In-plane shear tests on the composites	121
4.1.4 Compression tests on the rigid foam.....	123

4.2 Quasi-static test results of various corrugated sandwich beams	125
4.2.1 Three point bending tests to determine the structural stiffness.....	125
4.2.2 Static compression behaviour of hybrid corrugated sandwiches	142
4.3 Dynamic response	168
4.3.1 Compressive behaviour of hybrid sandwich structures subjected to impact loading.....	169
4.3.2 Perforation behaviour.....	176
4.3.3 Blast tests	187
4.4 Discussion.....	195
4.4.1 The effect of filling foam	195
4.4.2 The number of ply and specific energy absorption.....	196
4.4.3 Specific energy absorption of corrugated core sandwich structures	199
4.5 Summary	203
CHAPTER 5 FINITE ELEMENT MODELLING	204
5.1 The low velocity impact response of curvilinear-core sandwich structures ..	204
5.1.1 Introduction.....	204
5.1.2 Experimental Procedure	208
5.1.3 Finite element modelling	210
5.1.4 Experimental results and validation of the numerical model.....	215
5.1.5 Parametric studies	225
5.1.6 The main outcomes of the numerical modelling of aluminium curvilinear structures	232

5.2 Modelling of the response of hybrid sandwich structure based on GFRP corrugated core subjected to flexural loading	234
5.2.1 Modelling of the Composite material (GFRP).....	234
5.2.2 Geometrical model and contact conditions	236
5.2.3 Mesh Sensitivity Analysis.....	238
5.2.4 Results and Discussion.....	240
5.3 Modelling of corrugated sandwich panel subjected to compressive loading.	242
5.3.1 The modelling output	242
5.3.2 Results and Discussion.....	243
5.4 Summary	246
CHAPTER 6 CONCLUSIONS AND RECOMMENDATIONS	247
6.1 Conclusions	248
6.2 Recommendations for Future Work.....	251
REFERENCES.....	253

LIST OF FIGURE

Figure 1.1: Shows comparison of the mechanical performance between composites and traditional light metals in terms of specific modulus and strength[1].3	
Figure 1.2: Ship container made of corrugated sandwich structures and used for transportation industries.	6
Figure 1.3: LASCO metallic sandwich panel [6].....	7
Figure 1.4: Illustrates the battle ship experiences with a severe corrosion around the superstructures[7].	9
Figure 1.5: The image of the newest Visby class corvette that the whole superstructure was built by using composite material[8].	10
Figure 2.1: Cellular material classifications used for cores of sandwich structures [22].	16
Figure 2.2: Fabrication process of corrugated sandwich beams with unfilled and aluminium foam-filled cores [25].	18
Figure 2.3: Typical as-fabricated empty and aluminum foam-filled sandwich beams with corrugated cores. Long beam: (a) empty; and (b) filled. Short beam: (c) empty; and (d) filled [25].	18
Figure 2.4: Ceramic prism integration in hybrid core sandwich panels. (a) 136 mm × 127 mm × 25.4 mm thick, Coorstek grade AD-995 alumina tile showing prism cuts. (b) Application of adhesive to 136 mm × 22 mm × 19.3 mm ceramic prisms. (c) Insertion of prisms into the [26].	20

Figure 2.5: The manufacturing of triangular corrugated-core using hot press technique (a) Corrugated mould is made from steel and, (b) the profile angle of the mould [29].	22
Figure 2.6: (a) Unit cell geometry of the corrugated-core sandwich panel, (b) the triangular corrugated-core samples made of aluminium, GFRP, and CFRP from top to bottom.	23
Figure 2.7: (a) Expanded polyurethane foam (PU) used for filling in the corrugated-core, (b) sandwich structures using a foamless carbon fibre corrugated-core, semi-filled foam or fully-filled foam [28].	24
Figure 2.8: (a) dry corrugated-core assembly procedure, (b) the corrugated core test specimens with all leading dimensions and materials used for the various components labelled illustrating the 3D fibre lay-ups in the specimens and the geometry of the test coupon used to investigate material properties of the corrugated core strut material on the right [30].	25
Figure 2.9: A combination of corrugated-core and fibre metal laminates[28]	27
Figure 2.10: Traditional corrugated-core sandwich panels [34]	27
Figure 2.11: The corrugated-cardboard studied by [37]	29
Figure 2.12: Free-body diagram of the corrugated-core[20].	31
Figure 2.13: Shear modulus as function of the corrugation angle. (a) Monolithic core members and (b) sandwich core members [20].	32
Figure 2.14: Hat-type corrugated core sandwich panel [39].	33
Figure 2.15: Schematic of trapezoidal machined aluminium mould and prepreg laminates of glass fibre [47]	34

Figure 2.16: Sketches of (a) the first and (b) the second order corrugated cores sandwiched between two rigid face sheets [49].	35
Figure 2.17: Triangular corrugated-core sandwich structures made of (a) Aluminium 2024 O (b) GFRP (c) CFRP [28].	36
Figure 2.18: Deformation images of the $\rho = 0.05$ corrugated-core in out-of-plane compression [17].	39
Figure 2.19: A comparison of the experimental and predicted values of out-of-plane compressive strength of stainless steel corrugated-core panels [17].	39
Figure 2.20: Solution methods for different categories of impact [78].	43
Figure 2.21: The variation of the first damage threshold energy with impactor mass for the eight-ply (+/-45 °) laminate [75].	46
Figure 2.22: Low magnification optical micrographs of the cross-sections of (a) unidirectional FML and (b) woven FML-reinforced sandwich specimens after being subjected to impact energies at 120 J [69].	47
Figure 2.23: Perforation and specific perforation energies of the composite and FML skinned aluminium foam sandwich structures [69].	48
Figure 2.24: (a) Schematic of loading arrangement, (b) photograph of ballistic pendulum setup[104].	50
Figure 2.25: The transformaiton of energy[110].	52
Figure 2.26: Typical load-displacement regions of a specimen tested under quasi-static compression [114].	52
Figure 2.27: Photographs of the $\rho =0.05$ corrugated core showing the deformation mode during tests in out-of-plane compression and (b)measured	

responses and finite element predictions of the corrugated core specimens in out-of-plane compression of $\rho = 0.05$ (top), $\rho = 0.05$ (bottom) [17]. ... 57

Figure 2.28: (a) A comparison between the observed and FE predictions of the quasistatic deformation mode of the corrugated-core specimens and (b) FE predictions of the dynamic strength enhancement with and without material strain-rate sensitivity [56]. 58

Figure 2.29: The predicted impact damage of specimen C for the 10 J case: (a) the fiber tensile failure; (b) the fiber compressive failure; (c) the matrix tensile failure; (d) the matrix compressive failure; (e) the delamination failure; and (f) the corrugated core failure [132]..... 60

Figure 2.30: (a) Photographs of progressive damage development beside with (b) failure mode related to (c) load-displacement curve for a GFRP sandwich corrugated-core structure [28]..... 61

Figure 2.31: Post-damage photos of the AL corrugated-core sandwich structures [28] 62

Figure 2.32: Photographs of progressive damage development in the GFPUS sandwich structure during (a) initial compression, (b) the buckling process and (c) the final stages of testing..... 63

Figure 2.33: Photographs of progressive damage development showing the buckling failure from (a) initial compression, (b) buckling in the cell wall structure and (c) core crushing [28] 63

Figure 2.34: Deformation sequences in the filled (left) and unfilled (right) corrugated core specimens impacted at a velocity $v_0 = 150\text{ms}^{-1}$. Impact occurs on the top face of the specimens in the photographs [30]...... 64

Figure 2.35: Bottom layer delamination and fiber failures [87]	65
Figure 2.36: Some representative photographs of damaged samples taken with strong backlighting [87].	65
Figure 3.1: Cross-linked polymer foam specimens.....	69
Figure 3.2: A typical fibre metal laminates 3/2 [4].....	70
Figure 3.3: The triangular corrugated core moulds. (a) Drawing design with dimensions, (b) Assembly showing the core sample, (c) Images of the lower and upper moulds	72
Figure 3.4: Foam core elements cut into a prism shape.....	73
Figure 3.5: The prepared GFRP cut into a required dimension.....	73
Figure 3.6: The prism foam core elements are wrapped into GFRP woven along the 0/90° direction. (a) The first prism was wrapped, (b) become a panel. ..	74
Figure 3.7: Shows the sample panel placed between upper and lower platens of Meyer hot press machine and the thermocouple displaying the operating temperature on the screen.	75
Figure 3.8: The sample panels after cured from hot press process.....	76
Figure 3.9: Time and temperature of curing profile during hot press process.....	76
Figure 3.10: The samples ready for testing.....	77
Figure 3.11: Dimensions of a typical specimen (a)Front, (b) Top, (c) perspective. ..	78
Figure 3.12: Photograph of a plain GFRP triangular corrugated sandwich structure without an embedded foam.	79

Figure 3.13: Schematic in front view and photographs of the hybrid sandwich shows in different core configurations.	80
Figure 3.14 : The hybrid sandwich samples in different GFRP corrugated core thickness. (a) Schematic in side view, (b) GFRP core hickness values, (c)The samples in perspaective	81
Figure 3.15: Hhybrid sandwich samples with different types of foam cores. Foam cores using (a) PMI uesd in group PMI4P , (b) combination of PMI and C70.55 used in group PC54P, (c) combination of PMI and C70.200 used in group PC24P, (d) C70.55 used in group C554P, (e) C70.130 used in group C134P, (f) 70.C200 used in group C204P.	82
Figure 3.16: Photographs of the hybrid sandwich samples showing in different foam core densities. (a) Multi-layyers with homogeneous density, (b) Multi-layers with graded foam core craedted using foam types, C70.55, 130, 200, from the top surface to bottom.	84
Figure 3.17: Photograph of the hybrid sandwich samples showing the different sizes of the unit in mm.	85
Figure 3.18: Images of the hybrid sandwich samples in different layers. (a) 1 , (b) 2, (c) 3 layers.....	86
Figure 3.19: Photographs of the hybrid sandwich samples using FMLs as core or skins. (a) Group FA10Sx, (b) Group FA20Sx, (c) Group FA1E0x, (d) Group FA2E0x, (e) Group FA1ESx, (f) Group FA2ESx.....	87
Figure 3.20: Schematic of the hybrid sandwich samples fabricated with vertical orientation amd photos. (a)Top view of triangular, trapiziod and square	

<p style="text-align: center;">samples with their unit cells below, (b)Perspective (c) photo of groupTRIT sample, (d) image of the FMLT sample.....</p>	89
Figure 3.21: The sample dimension of the tensile metal specimen.	91
Figure 3.22: Tensile test geometry for a composite specimen.	91
Figure 3.23: Instron 4204 universal testing machine and mechanical extensometer.	92
Figure 3.24: Ply orientation for the in-plane shear test specimens.	93
Figure 3.25: Schematic of the stacking orientations of the GFRP woven composite and cutting direction of 45° for removing the shear speciemens	93
Figure 3.26: The square foam specimen under compression testing.	94
Figure 3.27: Schematic of hybrid sandwich specimen geometry under three point bend testing.	95
Figure 3.28: Image of the compression test set-up.	96
Figure 3.29: Schematic diagram of the set-up of drop-weight impact test.	100
Figure 3.30: Photograph of the drop-weight impact tower.	101
Figure 3.31: Schematic of perforation test set-up.	102
Figure 3.32: Shows schematic of the sample used for the perforation tests. (a) Front view and section details illustrating the layers of sample group CO2/SK2 using FMLs 2/2 (Al/GFRP/Al/GFRP)to be the skin and 2/1 for the core, (b) Top view and dimensions, (c) Perspective view.	103
Figure 3.33: Schematic of specimen dimensions for the blast tests.....	104
Figure 3.34: (a) Photograph of the ballistic pendulum used for conducting the blast tests and (b) schematic of the detonator and blast tube arrangement....	108

Figure 3.35: Shows the output signal collected from the oscilloscope in the operating and control room.	109
Figure 3.36: Schematic of the ballistic pendulum oscillation following on the applied impulse.	110
Figure 3.37: Sine curve from the oscilloscope showing the amplitude in volts and time corresponding to the pendulum positions	110
Figure 3.38: Optical microscope equipment that was used in the study.....	112
Figure 4.1: Engineering stress-strain curves for the aluminium alloy 2024 T3.....	116
Figure 4.2: Typical tensile stress-strain curve for a GFRP specimen.....	120
Figure 4.3: Tensile failure modes of the woven composite (GFRP sample).	121
Figure 4.4: Typical shear stress-strain curve for a GFRP specimen.	122
Figure 4.5: Failure modes in the GFRP woven composite laminates under in-plane shear loading.	122
Figure 4.6: Load-displacement curves following a quasi-static test on the rigid foam used in this study.	123
Figure 4.7: The stress-strain traces following quasi-static tests on foams with different densities.	124
Figure 4.8: GFRP triangular corrugated-core under three-point bending test.	126
Figure 4.9: Load-displacement obtained from triangular GFRP corrugated-core under three-point bending tests.	127
Figure 4.10: GFRP trapezium corrugated-core under three-point bending test.....	128

Figure 4.11: Load-displacement obtained from Trapezium GFRP corrugated-core under three-point bending tests.	128
Figure 4.12: The hybrid square corrugated-core reinforced with foam with vertical corrugated-beam core positoin (showing x-z plane) undergone by three-point bending test.	129
Figure 4.13: The hybrid square corrugated-core reinforced with foam with side corrugated-beam core positoin (showing x-y plane) undergone by three-point bending test.	130
Figure 4.14: Load-displacement traces of the hybrid square corrugated-core based on square GFRP and reinforced PMI foam core under three-point bending test in x-y and x-z plane.	130
Figure 4.15: The plain GFRP corrugated-core undergone by three-point bending test.	131
Figure 4.16: Load-displacement traces of the plain GFRP corrugated core samples with different GFRP core thicknesses.	132
Figure 4.17: The relationship between number of ply and peak load.	132
Figure 4.18: The hybrid sandwiches reinforced with different foam core types undergone by three-point bending. Using (a) C70.55, (b) C70.130, (c) C70.200 as the reinforced foam core.	134
Figure 4.19: Load-displacement traces of the hybrid sandwiches reinforced with different foam core types under three-point bending test.	135
Figure 4.20: The hybrid sandwiches reinforced with mixed foam cores.	135

Figure 4.21: Load-displacement traces of the hybrid sandwiches reinforced with mixed foam cores under three-point bending test (MIXFBT1: C200+PMI, MIXFBT2: C50+PMI, MIXFBT3:C130+PMI)..... 136

Figure 4.22: Comparison of load-displacement curves of the hybrid sandwich structures based on FMLs reinforced with foam cores considering from the panel with FML skins in black line, without skins in red line and testing along corrugation direction(y-z plane) in dash line, x-y plane in solid line. 137

Figure 4.23: The hybrid sandwich structures based on FMLs reinforced with foam cores under three-point bending in (a) the schematic of the test plane, x-y plane, (b) y-z plane..... 138

Figure 4.24: Comparison of load-displacement curves of the hybrid sandwich structures based on multi-layers under three-point bending in different testing plane..... 139

Figure 4.25: The hybrid sandwich structure with multi-layer and reinforced foam core under three-point bending in (a) x-y plane, (b) (-y)-x plane, (c) x-z plane. 140

Figure 4.26: Comparison of load-displacement curves of the hybrid sandwich structures based on reinforced foam with different unit cell sizes under three-point bending test. 141

Figure 4.27: The hybrid sandwiches with unit cell sizes of 40 mm under three-point bending test. 142

Figure 4.28: Load-displacement trace for a corrugated-core sandwich sample GFR8P05. The error displacement is removed from the raw data and replaced by the correct data plotted in red.	143
Figure 4.29: Load-displacement traces of hybrid sandwich structures with different thicknesses of GFRP corrugated core.	144
Figure 4.30: The process of damage development of the hybrid sandwich panel based on triangular corrugated-core (GFRP) in side view.	144
Figure 4.31: Comparison of failure mode of GFRP corrugated-core between (a) the sandwich panel from [28] that used a conventional bonding technique with adhesive agents, (b) the sandwich panel in this study that the new technique to bond sandwich core and skins.	145
Figure 4.32: Load-displacement traces of hybrid sandwich structures in different core configurations.	146
Figure 4.33: (a) the process of damage development of the hybrid sandwich panel based on triangular corrugated and reinforced PMI foam core in side view, (b) the virgin panel.	147
Figure 4.34: (a) the process of damage development of the hybrid sandwich panel based on square corrugated and reinforced PMI foam core in side view, (b) the virgin panel.	148
Figure 4.35: (a) the process of damage development of the hybrid sandwich panel based on trapezoidal corrugated and reinforced PMI foam core in side view, (b) the virgin panel.	149

Figure 4.36: (a) the process of damage development of the hybrid sandwich panel based on trapezoidal corrugated core in side view, (b) the virgin panel. 149

Figure 4.37: Load-displacement traces of hybrid sandwich structures based on GFRP core reinforced PMI foam showing in different thicknesses of GFRP corrugated core. 150

Figure 4.38: Load-displacement traces of hybrid sandwich structures based on GFRP reinforced foam core showing in different types of foam core. 152

Figure 4.39: The (a) process of damage development of the hybrid sandwich panel based on triangular corrugated reinforced C70.55 foam core in side view, (b) virgin panel. 153

Figure 4.40: The (a) process of damage development of the hybrid sandwich panel based on traingular corrugated reinforced C70.55 and PMI foam core in side view, (b) virgin panel. 153

Figure 4.41: The (a) process of damage development of the hybrid sandwich panel based on traingular corrugated reinforced C70.200 and C70.55 foam core in side view, (b) virgin panel. 154

Figure 4.42: The(a) process of damage development of the hybrid sandwich panel based on traingular corrugated reinforced C70.200 and C70.55 foam core in side view, (b) virgin panel. 154

Figure 4.43: Load-displacement traces of hybrid sandwich structures based on GFRP reinforced foam core showing in different foam core densities and multi-layer. 156

Figure 4.44: The progressive damage of the hybrid sandwich panel based on traingular corrugated reinforced foam core column (a) homogeneous core density, (b) gradient core density.	157
Figure 4.45: Load-displacement traces of the hybrid sandwich panel based on triangular corrugated reinforced foam core with diffrent unit cell sizes.	158
Figure 4.46: The process of damage development of the hybrid sandwich panel based on triangular corrugated reinforced foam core with 40 mm unit cell size.	159
Figure 4.47: Load-displacement traces of hybrid sandwich structures based on GFRP reinforced foam core showing in with different core layers.	160
Figure 4.48: shows the process of damage development of the hybrid sandwich panel based on traingular corrugated reinforced foam core with different core layers(a) 1 layer. (b) 2 layers, (c) 3 layers.....	161
Figure 4.49: Load-displacement traces of the hybrid sandwich panel based on triangular corrugated FML and reinforced foam core.....	162
Figure 4.50: The process of damage development of the hybrid sandwich panel based on triangular corrugated and 1/1 FML core.	163
Figure 4.51: The process of damage development of the hybrid sandwich panel based on triangular corrugated and 2/1 FML core.	164
Figure 4.52: The process of damage development of the hybrid sandwich panel based on triangular corrugated and 1/1 FML core reinforced foam and no FML skins.....	165

Figure 4.53: shows the process of damage development of the hybrid sandwich panel based on traingular corrugated and 1/1 FML core reinforced foam and with FML skins.	166
Figure 4.54: Load-displacement traces of hybrid sandwich structures based on GFRP reinforced foam core with vertical reinforcements.	167
Figure 4.55: The hybrid sandwich structures based on GFRP reinforced foam core with the vertical reinforcement under compression. (a) the sample with skin side, (b) without skin.	168
Figure 4.56: Load-displacement response of GFRP corrugated sandwich structure without reinforced foam core.	170
Figure 4.57: Comparison of the responses of the plain GFRP sandwich structures under static and dynamic compression loads.	172
Figure 4.58: The blue area for the sample GFR8P after filtered by using Impressions software package to eliminate the oscillation factor.	173
Figure 4.59: Load-displacement responses of GFRP corrugated sandwich panels with reinforced foam core.	174
Figure 4.60: Comparison of the response of the plain GFRP sandwich structures with reinforced foam core under static and dynamic compression tests.	175
Figure 4.61: Typical load-time and displacement-time relationship of hybrid sandwich structures based on corrugated-core and FMLs under perforation test.....	177
Figure 4.62: Typical-load displacement traces of hybrid sandwich structures based on corrugated-core and FMLs under perforation tests.	178

Figure 4.63: Load-displacement traces of hybrid sandwich structures with 1 layer of triangular corrugated-core and different thicknesses of FMLs skins under perforation test.....	179
Figure 4.64:Low magnification optical micrographs of the perforated faces of the hybrid sandwich structures with CO1 group (1 layer of Aluminium core) subjected to perforation test. (a) Front faces, (b) Back faces.....	180
Figure 4.65: Low magnification optical micrographs of the cross-sections of hybrid sandwich structures with 1 layer of triangular corrugated-core and different thicknesses of FMLs skins after perforation test.....	181
Figure 4.66: Load-displacement traces of hybrid sandwich structures with 2/1 FML core and different thicknesses of FMLs skins under perforation test. ..	182
Figure 4.67: Low magnification optical micrographs of the cross-sections of hybrid sandwich structures with 2/1 FML corrugated-core and different thicknesses of FMLs skins after perforation test.....	183
Figure 4.68: Comparison of load-displacement traces of hybrid sandwich structures between 1 layer aluminium core and 2/1 FML core. Continue-line : CO1-core, dash-line: CO2-core. FML 2/1 skin shown in Black and colour FML 4/3 skin shown in Red colour.....	184
Figure 4.69: The relationship between panel thickness and specific perforation energy.....	186
Figure 4.70: Peak load and area density relationship of hybrid sandwich structures based on corrugated-core and FMLs.....	186

Figure 4.71: Perforation energy and specific perforation energy of hybrid sandwich structures based on corrugated-core and FMLs.	187
Figure 4.72: A comparison of localized damage from the blast test between (a) monolithic curvilinear corrugated core panels made of aluminium (ALC and ALC1 samples) and (e) the hybrid sandwich panels based on corrugated cores and fibre metal laminates(GFRV1 and GFRV2 samples), (b) and (f):the side view, (c)and (g): the back surface view, (d)and (h): the front surface view.....	190
Figure 4.73: Relation of impulses and explosive masses used for 4 different types of samples	191
Figure 4.74: Central deflections of the front and back faces of sample groups (a): ALC, (b): ALC1, (c): GFRV1, (d): GFRV2	192
Figure 4.75: The Progressive damage development of ALC panel from the bottom to the top.....	193
Figure 4.76: The progressive damage development of ALC1 panel from the bottom to the top.....	193
Figure 4.77: The progressive damage development of GFRV panel from the bottom to the top.....	194
Figure 4.78: The progressiv damage e development of GFRV1 panel from the bottom to the top.....	194
Figure 4.79: Stress-strain curve of triangular corrugated core sandwich structures with various plies.	195

Figure 4.80: Stress-strain curve of triangular corrugated core sandwich structures with various plies and filled with foam core.	196
Figure 4.81: The trend of number of plies and specific energy absorption of plain GFR corrugated core sandwich structures.	197
Figure 4.82: Comparison of corrugated core sandwich structures between plain GFR and filled foam structures.	198
Figure 5.1: Schematic of the cross-section of the curvilinear sandwich panel.	208
Figure 5.2: The experimental test set-up for low velocity impact testing.	209
Figure 5.3: The finite element mesh of a quarter - sized model.	214
Figure 5.4: Comparison of the experimental load-displacement trace and the predicted ones using models with different number of elements through the sheet thickness for an Alu hl /H6 panel subjected to an impact energy of 80J.	215
Figure 5.5: The process of damage development in the 6 mm thick panel.	215
Figure 5.6: The process of damage development in the 10 mm thick panel.	216
Figure 5.7: Load-displacement plots from Alu hl /H6 panels in ascending impact energy. (a) Impact energy = (a) 20 J, (b) 30 J, (c) 60 J, (g), (d) 80 J. ...	218
Figure 5.8: Load-displacement plots from Alu hl/H10 panels ascending impact energy (a) Impact energy = (a) 30 J, (b) 60 J, (c) 90 J, (d) 120 J.	220
Figure 5.9: (a) Comparison of predicted versus measured maximum force, (b) Comparison of predicted absorbed energy and measured absorbed energy.	222

Figure 5.10: Finite element predictions of the damage characteristics in the 6 mm thick Al hl/H6 panels.....	223
Figure 5.11: Finite element predictions of the damage characteristics in the 10 mm thick Al hl/H10 panels.....	224
Figure 5.12: The influence of angle of obliquity on the perforation resistance of the 6 mm thick sandwich panels.	226
Figure 5.13: Finite element predictions of damage at the perforation threshold in 6 mm thick panels impacted at angles between 90 o (normal) and 50 o..	227
Figure 5.14: The validation of perforation energy with angle of obliquely for the 2024 - T3 aluminium alloy, the stainless steel and the titanium alloy..	228
Figure 5.15: The predicted load-displacement traces of (a) the four aluminium alloys, (b) comparison of the stainless steel and titanium alloy with the 2024-T3 aluminium alloy.	229
Figure 5.16: Summary of the predicted perforation energies and specific perforation energies for the six sandwich structures.....	231
Figure 5.17: The variation of perforation energy with projectile diameter for three sandwich structures.	232
Figure 5.18: Schematic of three-point bending test suing to model the FE modelling	237
Figure 5.19: Loading and boundary conditions adopted in the finite element model	237

Figure 5.20: Mesh-sensitivity analysis showing the relationship of number of elements and fracture energy required for convergence of the FE model for GFRP corrugated panel subjected to three-point loading.....	239
Figure 5.21: Mesh-sensitivity analysis showing the number of elements required for convergence of the FE model for GFRP corrugated panel subjected to three-point loading. The mesh of model based on (b) 8,440 elements (mesh = 1 mm), (c) 20,898 elements (me	239
Figure 5.22: The progressive damage development of GFRP sandwich beam model (a) Image of the experimant, (b) FE modelling, (c)progressive damages	240
Figure 5.23: Experimental and numerical force-displacement traces for GFRP corrugated sandwich under three-point bending loading.	241
Figure 5.24: shows the FE modelling with meshes of GFRP corrugated sandwich panel under compression test.	243
Figure 5.25: Loading and boundary conditions adopted in the finite element model	243
Figure 5.26: The predicted von-Mises distribution (in Pa) of the GFRP corrugated sandwich structure.....	244
Figure 5.27: Comparison of progressive damage development between experimental (left) and FE modelling (right).	245
Figure 5.28: Comparison of load-displacement traces of GFRP corrugated sandwich structures between experimental FE data.....	245

LIST OF TABLE

Table 2.1: Energy-absorbing capacity of core structures [2]	53
Table 3.1: Material properties of the foams[134, 135]	69
Table 3.2: The plain GFRP corrugated sandwich samples made with various core thicknesses.....	79
Table 3.3: Sample ID definitions of the hybrid corrugated sandwich panels	80
Table 3.4: Samples with different GFRP core thicknesses	81
Table 3.5: Samples made with foam core of various densities	83
Table 3.6: Samples with multi-layer cores.....	84
Table 3.7: Samples with different unit sizes	85
Table 3.8: Hybrid corrugated sandwich panels with increased core layer.....	86
Table 3.9: The corrugated sandwich structures made with FML cores	88
Table 3.10: Samples of the sandwich with vertical corrugated reinforcement.....	90
Table 3.11: Summary of all specimens investigated during the quasi-static compression study.	97
Table 3.12: Details of the high speed video camera[143].....	99
Table 3.13: The sample ID definitions and dimension details of the FML core corrugated sandwiches for the projectile impact tests.....	103
Table 3.14: Specimen details on each group investigated on blast test.	105
Table 3.15: Summary of the blast conditions on the sandwich panels.	107
Table 4.1: Typical mechanical properties for aluminium alloy 2024-T3	119

Table 4.2: Material properties for the glass fibre laminates obtained from the test and [72]used in this study.....	120
Table 4.3: Mechanical properties of composite woven under in-plane shear test. .	121
Table 4.4: Mechanical properties of foam cores used in this study obtained from compression tests and Refs [2, 147].	124
Table 4.5: Drop height, peak velocity, sample thickness data related to the strain rate of dynamic compression tests on the plain GFRP corrugated sandwich panel.	171
Table 4.6: Quasi-static and dynamic specific energy absorption of plain GFRP corrugated sandwich panels.....	173
Table 4.7: Quasi-static and dynamic specific energy absorption of GFRP corrugated sandwich panels reinforced with foam core.	176
Table 4.8: Comparison of perforation energy and specific perforation energy of hybrid sandwich structures based on corrugated-core and FMLs.	185
Table 4.9: Summary of the samples ID, the explosive masses, impulses, and resulting front and back surface deflections.	188
Table 4.10: Relation between number of plies and specific energy absorption of plain GFR corrugated core sandwich structures.....	197
Table 4.11: Relation between number of plies and specific energy absorption of GFR corrugated core sandwich structures filled with foam.....	198
Table 4.12: Summary of Area density and specific energy absorption of various sandwich structures.	199

Table 4.13: Comparison of the SEA values of the best-performing corrugated core sandwich structure with those of other types of core material.	202
Table 5.1: Panel dimensions and areal density for the aluminium alloy panels.	208
Table 5.2: Isotropic hardening data for the EN AW-5182 H48 aluminium alloy....	210
Table 5.3: Materials properties and parameters for EN AW-5182 H48 aluminium alloy used in finite element modelling.	211
Table 5.4: Summary of the elasticity properties of the glass fibre/epoxy materials[72]......	236
Table 5.5: Details of mesh sensitivity analysis.	238

NOTATION

\dot{X}_0	Initial velocity
\dot{X}_0	Initial velocity in meter per second (m/s)
X_1	Distance 1 in millimetre
E_f	Flexural modulus in Mega Pascal
\ddot{X}	Acceleration vector on a trajectory of X
\dot{X}	Velocity vector on a trajectory of X
$\bar{\rho}$	The relative density of the corrugated and diamond core specimens

σ_f	Flexural stress
2024-T3	An aluminium alloy consisted of 4.9% copper and 0.9% magnesium and tempered
Al	Aluminium
ALC	Monolithic Aluminium Curvilinear corrugated core sandwich structures
ASTM	American Standard Test Method
Avg.	Average
BISRU	Blast Impact and Survivability Research Unit
BS	British Standard Test Method
C	Viscous damping coefficient
c	Average core thickness of corrugated core (mm)
C13	Airex AG PVC foams C70.130, density 130 kg/m ³
C20	Airex AG PVC foams C70.200, density 200 kg/m ³
C55	Airex AG PVC foams C70.55, density 55 kg/m ³
CO	Sandwich Core
dc	Node width
E	Impact energy in Joules
F	Force in Newton
FEA	Finite element analysis
FeCl ₃	Ferric chloride used for chemical etchant
FEM	Finite element method

FMLAT	Fibre Metal laminates core sandwich in diamond shape oriented vertically and embedded with Airex 70.130 prism PVC foam
FMLs	Fibre Metal laminates structures
G, GL	Gauge length
GFRP	Glass fibre reinforced plastic
GFRT	Glass Fibre reinforced Plastic Sandwich Panel in diamond shape oriented vertically and embedded with Airex 70.130 prism PVC foam
H	Height (mm)
L	Length, Span
Lc	Corrugation length
<i>M</i>	Total mass of the pendulum including test rig, specimen and counterbalance masses and the natural period of the pendulum
M	Mass
m_p	Mass of specimen
MPa	Mega Pascal
PC	Combined-foam core between Polymethacrylimide and Airex AG PVC foams
PE4	Plastic Explosive
PMI	Polymethacrylimide
PP	Polypropylene
PU	Polyurethane foam
PVC	Polyvinyl chloride

R, r	Radius
S	Corrugation pitch
SK	Sandwich Skins
SOD	Stand of Distance in millimetre
SQA	Square
t	Average skin thickness of sandwich panel (mm)
T, h	Thickness , Period
T6	Solution heat treated and artificially aged
T_c	Curing temperature
T_{dwell}	dwel time in minute
TRA	Trapezoid
TRI	Triangular
V.	Volt
w	Weight (g)
W, B	Width
W/mK	Thermal conductivity unit in watts per meter kelvin
δ	Displacement in millimetre
θ	Theta angle
ρ	density
I	Impulse in Newton. second (N.s)
φ	Angle of Sine wave got from oscilloscope (degree)

CHAPTER 1

INTRODUCTION

This chapter contains a brief introduction to the research project and an overview of composite materials along with their applications. The rationale behind the need for an efficient and lightweight energy-absorbing structure will be presented. Additionally, the motivation, objectives of the research and significance of the study are discussed. The chapter closes with an outline of the thesis chapters.

1.1 Overview of composite structures

Presently, there is an increasing drive to develop lightweight, energy-efficient structures for use in a wide range of engineering components. Examples include lightweight aerospace components for use in the next generation of aircraft, lightweight vehicle body work and wind turbine blades in the construction of energy-generation systems, such as wind turbines.

Sandwich structures are considered as optimal designs for a wide range of applications, including insulated structures, marine construction, transportation and aerospace vehicles. A composite sandwich panel is usually made from a lightweight foam, honeycomb or corrugated core sandwiched between two thin composite face sheets. Such a combination offers exceptional specific strength-to-weight ratio or stiffness-to-weight ratio, dimensional stability, and thermal and acoustical insulation features.

In recent years, there has been a growing interest in the research of sandwich structures, particularly in enhancing the ability of reducing self-weight and improving energy absorption such as composite sandwich structures. This is related to the increasing demand for developing better performed transportation systems with more fuel efficiency.

1.2 Composite Materials

Composite materials are widely known for having the property of a high-strength to weight ratio compared to other conventional materials. The relative ease of combination of strong fibres surrounded by a weaker matrix material serves specific purposes and exhibits desirable properties. The advantages of advanced composites out-performing the conventional materials are usually measured using specific modulus and specific strength. Figure 1.1: Shows comparison of the mechanical performance between composites and traditional light metals in terms of specific modulus and strength.

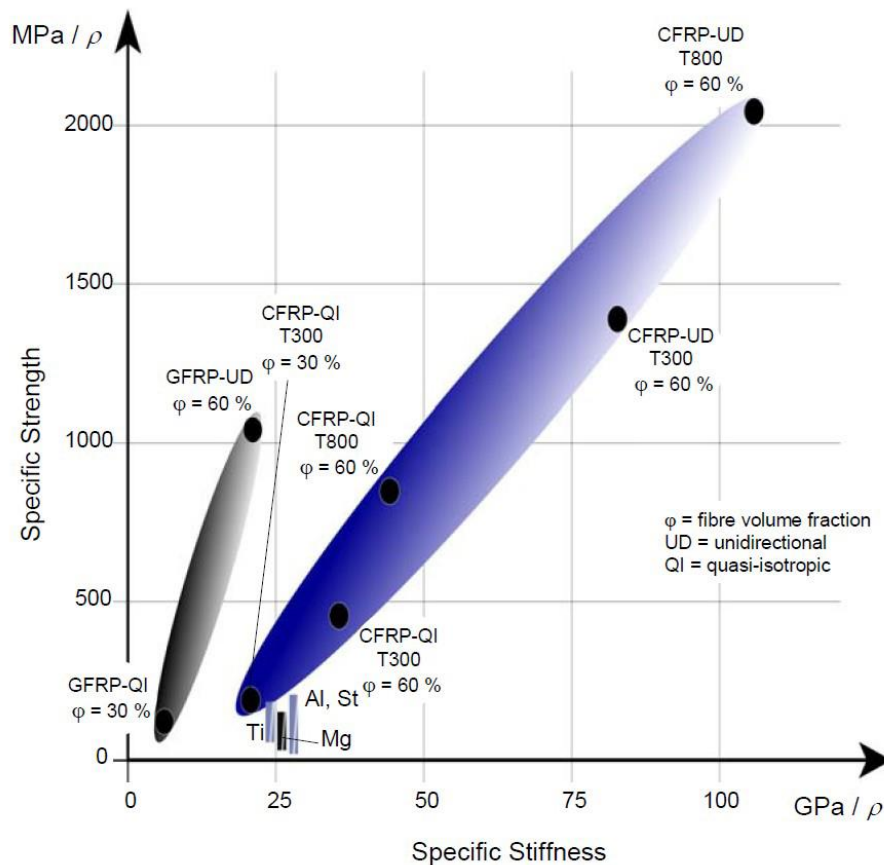


Figure 1.1: Shows comparison of the mechanical performance between composites and traditional light metals in terms of specific modulus and strength[1].

There are many advantages of using composite materials as listed below[2]:

- Light weight
- High strength and stiffness to density ratio
- High fatigue and impact resistance
- Excellent fatigue resistance
- High energy absorption
- Good corrosion resistance
- Formable to complex shape
- Improve creep-life time
- Controlled low thermal expansion
- Lower manufacturing cost and reduction of maintenance costs
- Enhanced properties via tailorable properties (Anisotropic vs. isotropic)

However, behind the excellent characteristics offered by composite materials, a few disadvantages could also be found in their uses as follows.

- Unique assembly process such as curing time, pressure and temperature requested,
- Relatively brittle with low toughness due to weak matrix,
- Manufacturing defects such as delamination, voids, inclusions and porosity,
- Environmental degradation of matrix,
- Difficulty of recycling.

1.3 Composite Sandwich Structures

A sandwich structure typically consists of two thin but stiff skins, made from a fully dense material, and separated by a thick and light core. The result of this construction is a structure with a high bending stiffness and strength but a low overall density. In fact, the bending stiffness and strength of a sandwich structure are always superior to that of a monolithic structure made from the same material and having the same weight.

Their unique properties and adaptability to different conditions offer the possibility of new solutions to challenge engineering problems. The main factors that affect their mechanical properties are properties of skins, cores and their thickness. Traditional core materials such as polymeric foams and honeycomb cores exhibit a poor air flow exchange. Sandwich structures with closed channel, cellular materials may retain air and humidity and it is one of the problems that may lead to degradation of the core properties. A corrugated core sandwich structure is fascinating to the author due to the core design that has a good strength-to-weight ratio in compression as well as in shear. An open channel of core will increase mechanical performance avoiding problems associated with humidity retention.

1.4 Applications of corrugated core sandwich structures

Composite materials have been extensively used in many military and civil applications. The following sections outline some of the existing and the potential applications for corrugated-core sandwich structures.

1.4.1 Packaging applications

A common and wide use of corrugated core sandwich structures in everyday life can be seen as a corrugated box in the packaging industry. This invention was patented in England since 1856 [3]. The design and development of packaging still has been

developed to recent days to satisfy the particular needs of the product being shipped and the hazards of the shipping surroundings, i.e. shock, compression, moisture, vibration, etc.

1.4.2 Transportation applications

Shipping containers with corrugations is a good example of transportation applications widely used around the world. A bullet train, Shinkansen 700 series, the famous Japanese invention is also an example of using corrugated structures [4].



Figure 1.2: Ship container made of corrugated sandwich structures and used for transportation industries.

1.4.3 Aerospace applications

Corrugated composites have a great potential to replace the conventional aircraft fuselage and wing. For example, a flexible morphing wing that can change its geometry by using a corrugated structure [5].

1.4.4 Marine applications

The best example to show that corrugated sandwich structures used in marine applications is the Laser Beam Welded Corrugated Core (LASCOR). This is a metallic corrugated sandwich panels used in the modern battle ships, designed to reduce the weight of a ship's deck, bulkheads and hatches without sacrificing strength and durability. LASCOR panels was used to construct in USS Mount Whitney, US Navy ship. Nowadays, new modern high performance ship has been designed to reduce weight leading to save the fuel consumption and increase cruise speed. Therefore, corrugated sandwich structures are likely to replace conventional structures in other applications for both surface ships and submarines [6].

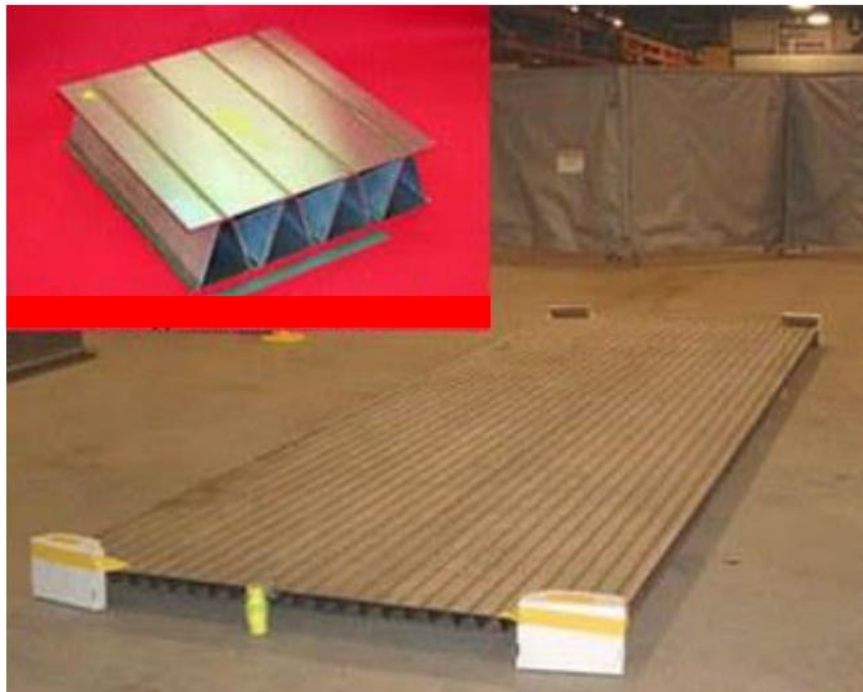


Figure 1.3: LASCOR metallic sandwich panel [6]

1.5 Motivation of the research work

The author has worked in the Royal Thai Navy for a decade and has a motivation from the career to develop a better design and build a high performance ship to be used by the Royal Thai Navy.

While composites are now being considered as a diverse range of naval applications, for many years these materials were used only in a few non-critical ship structures and in small boats.

A concept to use novel composite structures in a high performance ship is one of the most interesting approaches. As described, the conventional structures in ships are built by using steel plates that have many drawbacks such as corrosion problem due to being in contact with salt water, extremely heavy that affects the ship manoeuvre, high fuel consumption, etc. as shown in Figure 1.4. Although the low material cost is one of the main reasons that steel plates has been used to construct the ship for many decades, it was found that the maintenance to maintain ship structures in a good shape and performance lower costly.



Figure 1.4: Illustrates the battle ship experiences with a severe corrosion around the superstructures[7].

Recently, the Royal Swedish Navy is leading the design and construction of composite corvettes. The Visby class corvette, as shown in Figure 1.5, which at 72 m long, 10.4 m wide and a full-load of 620 tonnes, is the longest and nearly the heaviest all-composite naval ship. The Visby class is designed to be a multi-purpose vessel with capabilities for surveillance, combat, mine laying, mine countermeasures, and anti-submarine warfare operations. To undertake these roles, the vessel must be lightweight, strong, resistant to underwater shock loads, and stealthy by having low radar and magnetic signatures. The Royal Swedish Navy considered that these requirements could be achieved more readily by constructing the entire ship with composite materials rather than with steel, aluminium alloys or a mixture of those materials.



Figure 1.5: The image of the newest Visby class corvette that the whole superstructure was built by using composite material[8].

The Visby is the first naval ship to make significant use of carbon fibre composites in the hull that could reduce 30% of the hull weight. This makes her maximum speed to reach 35 knots.

However, using composite sandwiches to build a battle ship as seen in the Visby class, is still facing some drawbacks of the structural properties such as the impact and blast resistance. Practically, the structure of a navy ship should withstand high impact or blast loading. However, the composite sandwich structures used for Visby class still have less tolerance in terms of blast resistance. In addition, the sandwich structures with a PVC foam core experience a high level of water absorption and humidity. This could cause a degradation of the structure and reduce life span. Therefore, these aspects inspire the author to design and develop novel sandwich structures in order to build a high performance ship to serve in the Royal Thai Navy.

The new design sandwich structures have been proposed with the expectation of offering a higher impact and blast resistance, greater flexural strength to weight ratio, capability of reducing or quarantining the damage area.

It is also expected that the results of this research not only benefit marine applications as an inspiration of the author, but will also attract the attention of a range of sectors such as aerospace, automotive and construction industries where the out-performance with superior mechanical properties of newly designed sandwich structures is required.

1.6 Research aim and objectives

The primary aim of this research is to study the energy-absorbing characteristics of novel foam core sandwich structures with composite corrugated reinforcements. This research considers the influence of several parameters and concerns the crushing failure behaviour and energy absorbing capability of the sandwich structures developed.

The proposed PhD project is to investigate the mechanical behaviour of the novel hybrid sandwich structures based on corrugated-core and fibre metal laminates designs through experimental work and numerical modelling. Therefore, the project objectives can be drawn as follow:

- To improve and develop the manufacturing process of the newly developed hybrid sandwich structures with a better bonding quality between the skin and the core and reduced time consumption in the process from the previous research.
- To manufacture the sandwich structures with square, triangular, and trapezoidal corrugations following the design.
- To investigate the mechanical performance of hybrid sandwich structures based on corrugated-core and fibre metal laminates subjected to both static and dynamic

loading (tensile, three-point bending, quasi-static compression and low-velocity impact and blast)

- To model the mechanical response of hybrid sandwich structures based on corrugated-core and fibre metal laminates using the finite element techniques.
- To study the influence of varying corrugation structures, materials used, and the fibre metal laminates.

1.7 Significance of the study

The outcomes of this research have a wide significance and implications, which are stated below:

- i. The use of hybrid sandwich composite structures for the maritime applications is novel. This thesis contributes new knowledge for the designs and fabrication techniques to improve the bonding and overall mechanical properties of the hybrid sandwich corrugated structures.
- ii. This study will be highly beneficial to applications in various engineering fields, particularly in high-class naval ship super structures in order to decrease the overall ship self-weight. The composite materials proposed will enhance energy absorption significantly to reduce wave slapping effect on the ship.
- iii. Deeper understanding of the effects of geometry, material and loading parameters, such as corrugated core thickness, reinforced foam, unit cell sizes, constituent materials, impact or blast, etc., on the structural behaviour of the hybrid corrugated composite sandwich reinforced foam core.
- iv. Development of the finite element models to simulate the structural performance of the structures and further parametric studies to investigate variety of parameters.

1.8 Thesis outline

At the beginning of each chapter, an overview of the topic will be given. A summary, if relevant, will be presented at the end of each chapter to highlight the main findings.

This thesis consists of six chapters as follows:

Chapter 1: Introduction; this chapter presents the background, the motivation and the significance of the research, as well as underlining its main objectives for accomplishing the benefits of this study.

Chapter 2: Literature review; this chapter gives an overview of the experimental work, theoretical analysis and numerical modelling relevant to the topic. Attention is focused on sandwich structural response under quasi-static and dynamic loading.

Chapter 3: Experimental procedure; this chapter describes the specimen preparation that is the main development of this study and experimental tests, including tension, quasi-static compression and bending, low-velocity impact and blast, conducted in this research.

Chapter 4: Results and discussion of the experimental work; this chapter presents and discusses the results obtained following a large number of tests on the structural responses of the structures under quasi-static and dynamic loading.

Chapter 5: Finite element modelling; this chapter contains two main parts, starting with the modelling with monolithic sandwich structures, then moving to more complex corrugated sandwiches made with composite materials (GFRP). Numerical prediction values are validated and compared with experimental results.

Chapter 6: Conclusions and recommendations; this chapter summarises the overall findings and observations based on the research performed. In closing, recommendations of possible future work will also be given.

CHAPTER 2

LITERATURE REVIEW

In this chapter, a review of relevant previous research work is given on sandwich structures, composite reinforced corrugated-core sandwich structures and fibre metal laminates (FMLs) subjected to quasi-static and dynamic loading. In the beginning, a brief overview of the design and manufacture of sandwich cores, focusing on their fabrication techniques is presented. Subsequently, the background of corrugated-core sandwich and fibre metal laminates is reviewed. The geometrical parameters, such as core thickness, configurations and sizes, are discussed in relation to sandwich cores under both quasi-static and dynamic loading. Concept of energy absorption in relation to the design of novel hybrid sandwich structures is also given and followed by the review of the relevant work on finite element modelling. Finally, a summary of the main findings from the literature review and their link to the subject matter of this thesis is stated at the end of this chapter.

2.1 Overview of composite sandwich structures

Composite structures are widely known for having the property of a high-strength to weight ratio compared to other conventional structures. In general, a composite sandwich structure is fabricated by attaching two thin but stiff skins to a lightweight core. The core material is normally low strength material, but its large thickness provides the sandwich composite with a high bending stiffness in overall low density. The historical existence of sandwich structures predates mankind itself. Indeed, before the creation of foam core sandwich structures in the aerospace industry, animal s' bones provide a good example of this concept in nature. The fabrication of a sandwich structure, which is not only as light as possible but maintains its strength and integrity, is a challenging task. A natural design, from millions of years of evolution, can be seen in the skeleton of birds, with thin surfaces being stabilised to withstand tensile and compressive loads and in combination in tension, torsion and bending[9]. Sandwich panels offer a wide range of advantages over conventional monolithic materials and their use is continuously increasing in applications in the aerospace, automotive, naval and construction industries. Sandwich panels, with fibre reinforced plastic skins and a cellular core, have been shown to offer superior specific stiffness and strength properties in flexure compared to their monolithic counterparts [10] . In recent years, various core designs with improved quasi-static and dynamic properties were proposed, including those based on various foams [11, 12], honeycomb cores [13, 14], origami-type cores [15, 16] and truss cores [17-21]

2.1.1 Sandwich types

In this Section, sandwich structures are classified and categorised based on their core topologies. A number of different cellular core topologies were developed, with the particular aim to maximise the strength whilst reducing density. Cellular materials are

typically categorised as those with either stochastic cells or periodic cells. Figure 2.1, shows a classification of sandwich structures based on topologies, categorised by Zhu et al. [22]. Foam, in either a random open or closed-cellular microstructure, falls into the stochastic category [23]. In contrast, the repeated array of precision unit cells, which are assembled in either a two-dimensional open channel or three-dimensional truss, or are textile based, are typical examples of periodic structures [24].

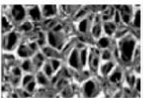
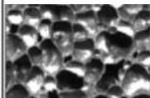




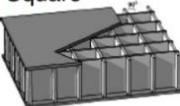



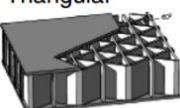

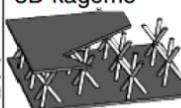

Cellular materials					
Stochastic		Periodic			
Open cell	Closed cell	2D		3D (lattice)	
		Honeycombs	Prismatic	Truss	Textile
		Hexagonal 	Triangular 	Tetrahedral 	Diamond textile 
		Square 	Diamond 	Pyramidal 	Diamond collinear 
		Triangular 	Navtruss 	3D kagome 	Square textile 

Figure 2.1: Cellular material classifications used for cores of sandwich structures [22].

2.2 Manufacturing techniques of making sandwich structures

As the aim of this study is to develop and find a new robust technique of making corrugated sandwich structures, various manufacturing techniques are stated accordingly.

While the sandwich concept is used in impressive variety of applications, the techniques employed to manufacture components tend to be few and usually involve

a large degree of manual labour. This Section will review manufacturing techniques that have been documented and also briefly covers some points of interest found in the literatures. Yan et al. [25] introduced metallic hybrid-cored sandwich constructions with aluminium foam blocks inserted into the interstices of steel corrugated plates being fabricated and tested under three-point bending. Figure 2.2 shows fabrication process of corrugated sandwich beams with unfilled and aluminium foam-filled cores. Aluminium plate was folded using hydraulic puncher. Then, laser welding technique was used to bond both face sheets to the core. Triangular foam prisms having the same shape of the interstices of the corrugated plates were cut by electro-discharge machining (EDM) from aluminium foam sheets. The triangular foam prisms were then inserted into the interstices and fixed with epoxy glue. It is interesting that the empty corrugated panel have to be cleaned before filling. Heat was applied on foam for 2 hours at 80 °C.

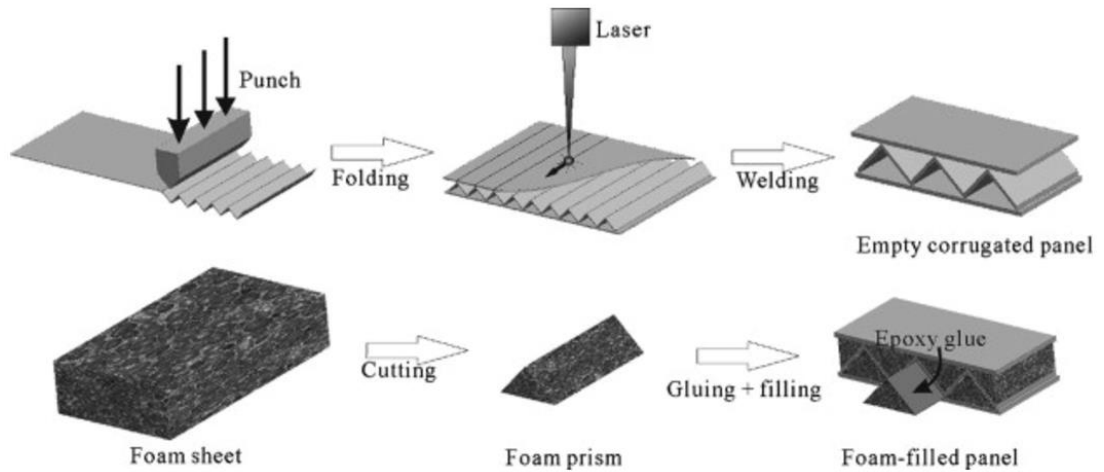


Figure 2.2: Fabrication process of corrugated sandwich beams with unfilled and aluminium foam-filled cores [25].

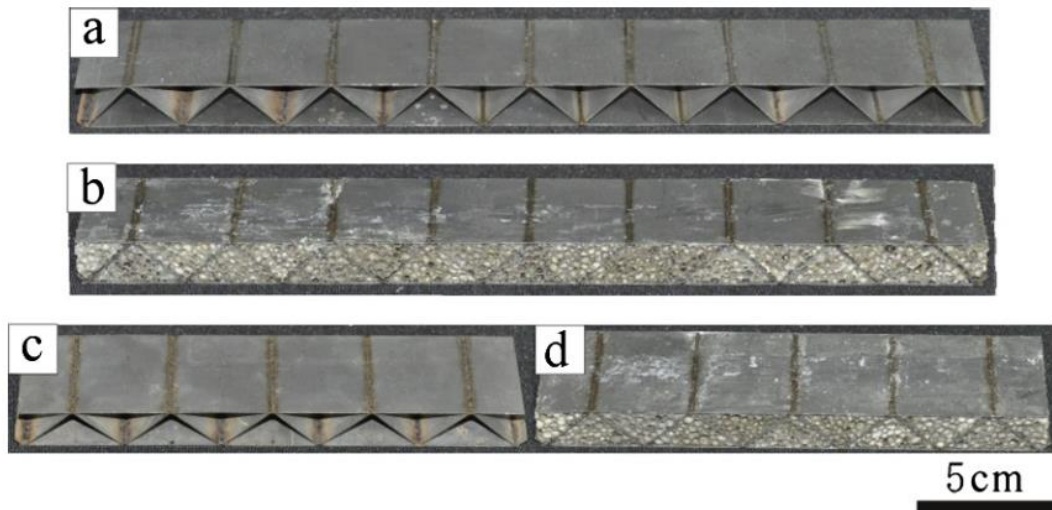


Figure 2.3: Typical as-fabricated empty and aluminum foam-filled sandwich beams with corrugated cores. Long beam: (a) empty; and (b) filled. Short beam: (c) empty; and (d) filled [25].

Wadley et al. [26] produced aluminium corrugated core sandwich panels using extrusion technique. This manufacturing process was introduced by Rimoli [27] and further developed by Wadley to study an impact response of aluminium 6061. The extruded panels were solutionised, water quenched and heat treated to a T6 condition (Solution heat treatment and artificially aging are the most common temper for 6061 aluminium). Furthermore, Wadley introduced aluminium–alumina composite core

produced by grade AD-995 alumina ceramic obtained from CoorsTek (Golden, CO, USA). Figure 2.4 shows manufacturing process of aluminium–alumina composite core. Wadley claimed that the sandwich structures could perform the best solution for resistance to single or multi-impacts near the ballistic impact area. The author found that this type of sandwich structures are too heavy and not suited for the aerospace or maritime industries. In addition, a heavy apparatuses such as extrusion and cutting machine, etc. was needed for the manufacturing process.

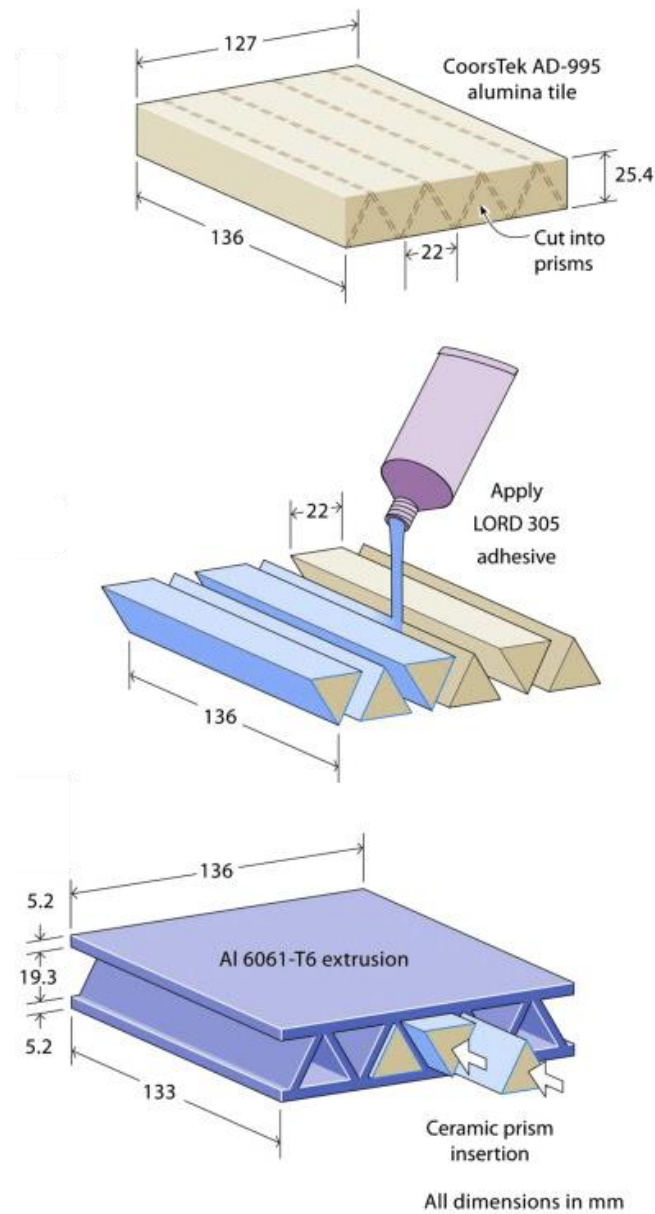


Figure 2.4: Ceramic prism integration in hybrid core sandwich panels. (a) 136 mm \times 127 mm \times 25.4 mm thick, Coorstek grade AD-995 alumina tile showing prism cuts. (b) Application of adhesive to 136 mm \times 22 mm \times 19.3 mm ceramic prisms. (c) Insertion of prisms into the [26].

Rejab et al. [28] investigated the mechanical properties of corrugated-core sandwich structures under quasi-static and dynamic loading conditions to determine the failure mechanisms and energy-absorbing characteristics of the corrugated-cores with

different cell wall thickness and filled with a foam core. In his studies, triangular corrugation structures were made from an aluminium alloy (AL), a glass fibre reinforced plastic (GFRP) and a carbon fibre reinforced plastic (CFRP) using hot press technique. Skins and core were bonded using an adhesive. It was found that the quality of gluing caused an initial weak point and led to debonding. As the result, such the unsatisfactory sandwich structure had a premature failure with poor mechanical properties. The manufacturing process was also undertaken in many steps and was a time-consuming process. This drawback was a driving motivation to extend this research in order to develop a manufacturing process providing a better solution of bonding and less time-consuming techniques. Figure 2.5 shows the GFRP triangular core manufactured using steel moulds with hot press technique. The profile of the moulds is also shown to clarify its dimensions. The mould was manufactured to a high precision using a computer-controlled numerical milling machine (CNC). The apex of each triangular unit in the mould was relatively sharp, having an average diameter of approximately 0.1 mm. This does result in a small region of resin enrichment in the corners. A 45° corrugation was selected since it gives an optimum shear modulus with respect to tensile and bending stiffness of the core structure [29].

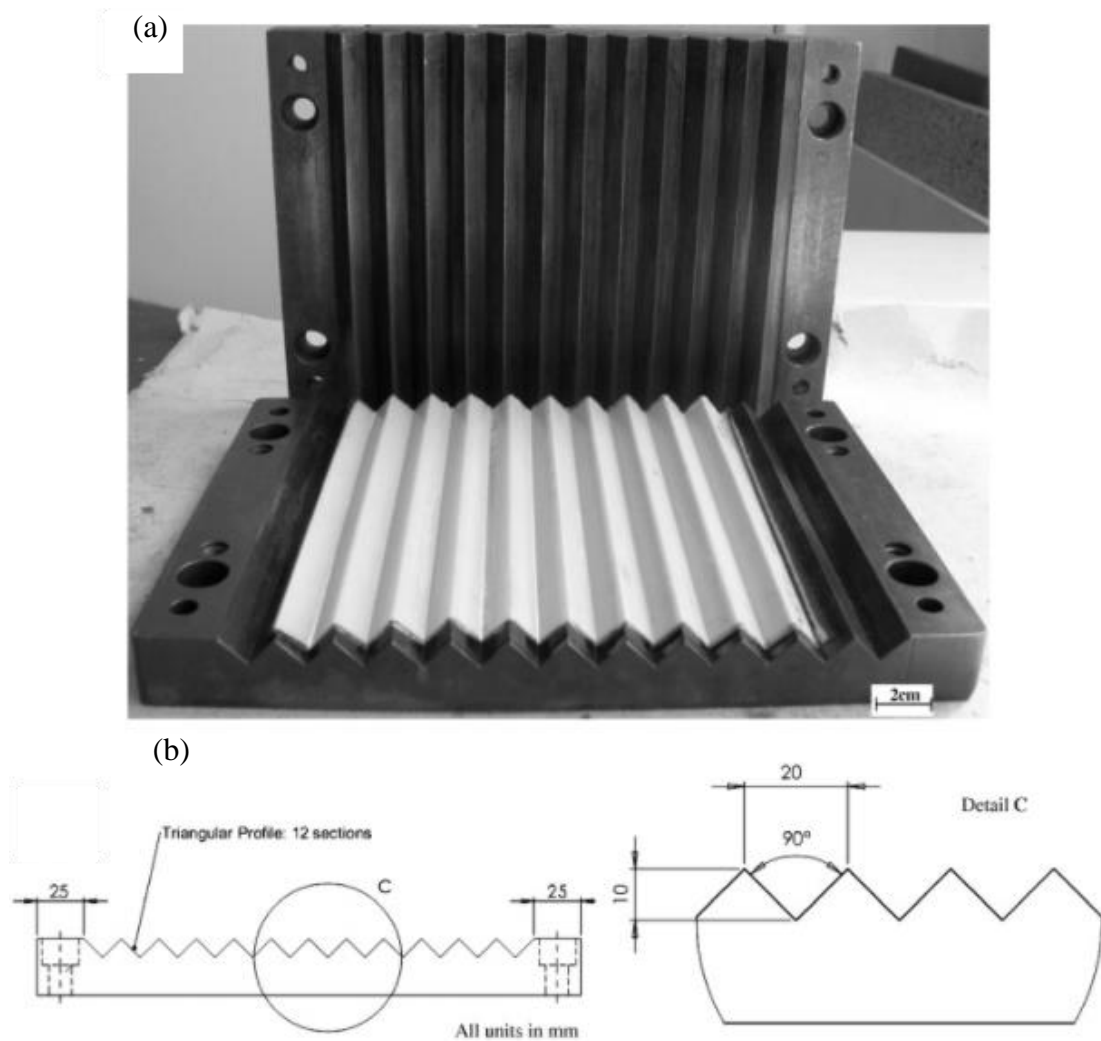


Figure 2.5: The manufacturing of triangular corrugated-core using hot press technique (a) Corrugated mould is made from steel and, (b) the profile angle of the mould [29].

Figure 2.6 presents (a) unit cell geometry of the corrugated-core sandwich panel, (b) the triangular corrugated-core samples made of aluminium, GFRP, and CFRP from top to bottom.

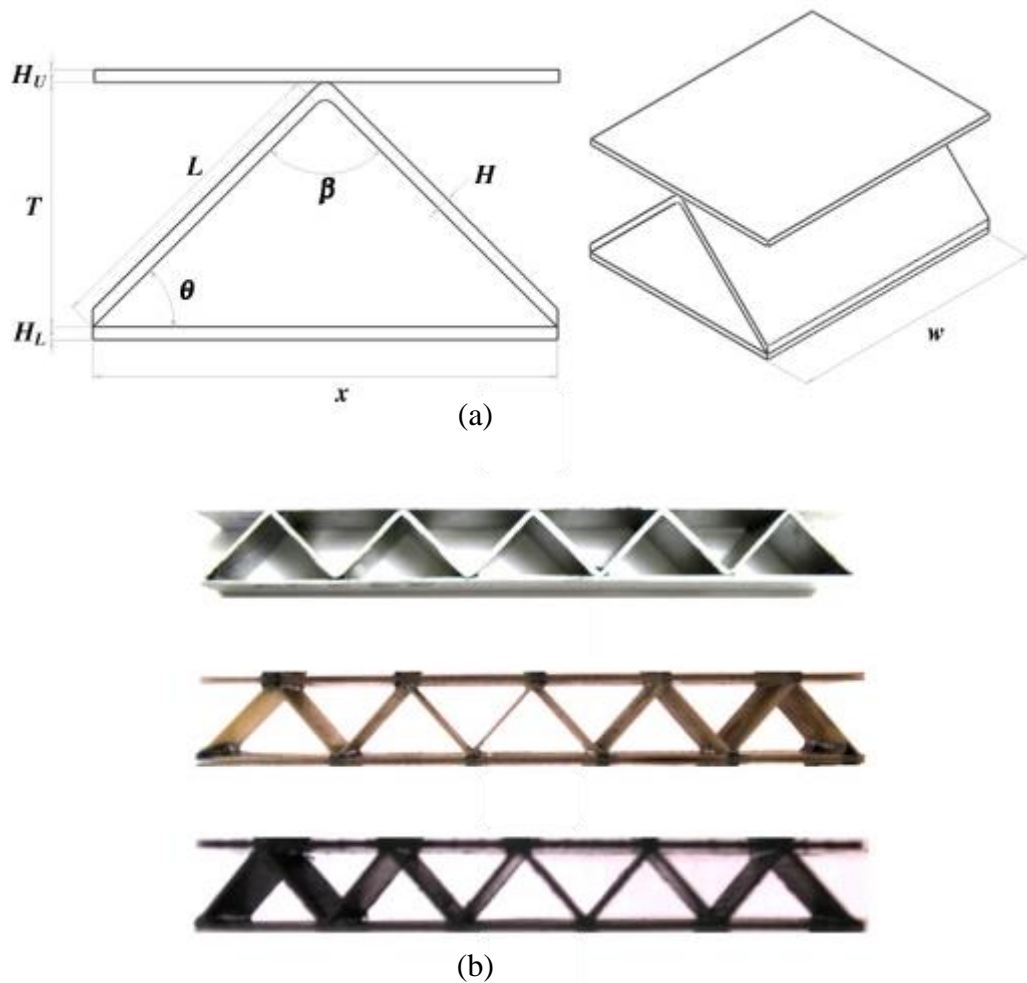


Figure 2.6: (a) Unit cell geometry of the corrugated-core sandwich panel, (b) the triangular corrugated-core samples made of aluminium, GFRP, and CFRP from top to bottom.

Rejab[28] also introduced foam filling in the composite corrugation systems using liquid polyurethane foam (PU), which expands and solidifies in the sandwich core. Figure 2.7 shows (a) expanded polyurethane foam (PU) used for filling in the corrugated-core, (b) sandwich structures using a foamless carbon fibre corrugated-core, semi-filled foam or fully-filled foam. However, the author found that this technique was not able to control the density of foam in the core. Anecdotally, it is thought that the manufacturer had to fill the liquid PU foam one by one into the corrugated-core cavity. Therefore, the density of each unit cell seemed to be dependent on the manufacturer's skill.

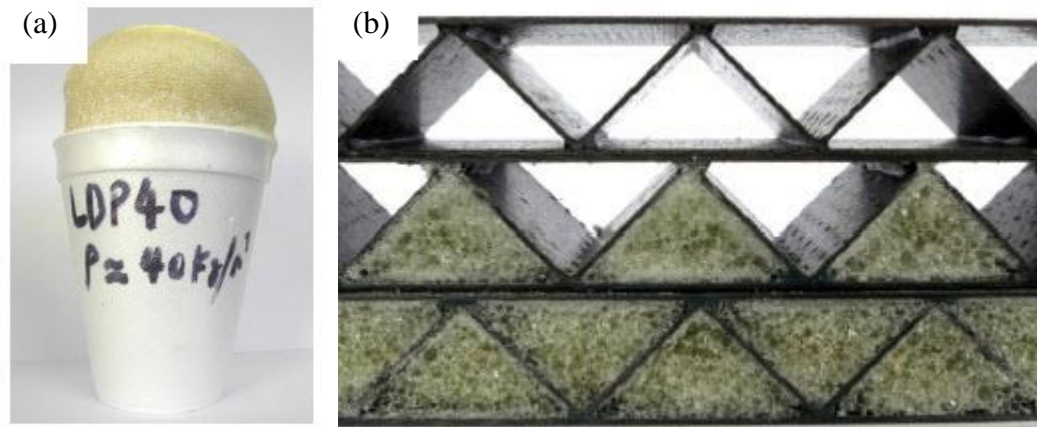


Figure 2.7: (a) Expanded polyurethane foam (PU) used for filling in the corrugated-core, (b) sandwich structures using a foamless carbon fibre corrugated-core, semi-filled foam or fully-filled foam [28]

Recently, Russell et al. [30] developed a novel triangular corrugated-core assembly fabricated from E-glass fibre using triangular prisms filled with PVC foam to form the corrugations. The points of the corrugations were stitched to the S2-glass face sheet with a Kevlar thread before the entire assembly was vacuum-bagged and cured in an autoclave at 72 °C for 6 hours. The sample was then fabricated with a strut inclination angle of approximately 64°. Once the fabrication was completed, quasi-static and dynamic loading rates were measured to assess the mechanical response of the structures.

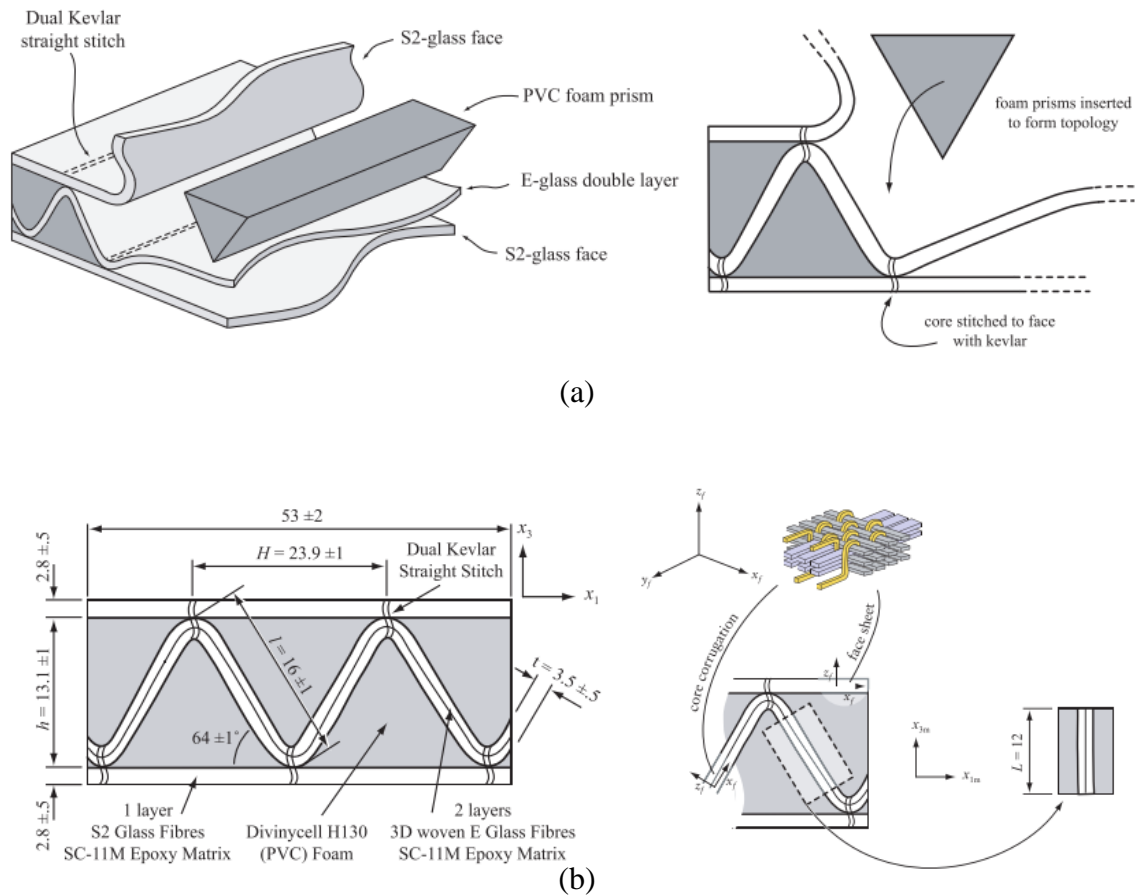


Figure 2.8: (a) dry corrugated-core assembly procedure, (b) the corrugated core test specimens with all leading dimensions and materials used for the various components labelled illustrating the 3D fibre lay-ups in the specimens and the geometry of the test coupon used to investigate material properties of the corrugated core strut material on the right [30].

2.3 Background and classification of Fibre metal laminates (FMLs)

Fibre Metal Laminates (FMLs) consists of thin alternating bonded layers of aluminium and fibre/epoxy normally. Vermeeren et al. [31], in Delft University of Technology, claimed that this type of structure offers high damage tolerance properties, and was primarily developed for aerospace applications where good fatigue properties and high strength are required. They also provided a history of Fibre Metal Laminates for example a glass fibre reinforced epoxy and also currently, GLARE (a glass

fibre/aluminium). Since 1945, the ARALL was first introduced by Rob Schliekelmann, one of the engineers, Delft University, to produce Fokker F-27 tailors. Then, Schijve et al. [32] discovered that crack growth was extremely slow because cracks only started to grow in a single layer.

In 1978, Schijve and Vogelesang started with flight simulation tests on carbon and aramid fibre reinforced laminates. The results looked promising. Roebroeks et al. [33] developed an analytical model for the prediction of fatigue crack growth in FMLs, based on fracture mechanics principles. The tests were carried out on aluminium-aramid fibre laminates baptised with the acronym Arall (Aramid Reinforced Aluminium Laminates). Glare was first produced by partnership between AKZO and ALCOA in commercial line productions. Its properties are combined with the further improved impact behaviour of Glare when high strain rates are applied (hail strike, bird impact). Glare also has a dent in the surface after impact, similar to aluminium (unlike composites), resulting in simple visual inspection for such damage. Mechanical properties of Glare after impact also appeared to be better which resulted in an application in the cargo floor in the Boeing 777 in 1990 – the first commercial application of a Glare product. A special variant, Glare 5, was developed and optimised for impact properties consisting of more glass fibre layers than regular Glare types.

Rejab [28] recommended the combined structures between fibre metal laminates and corrugated cores, as shown in Figure 2.9.

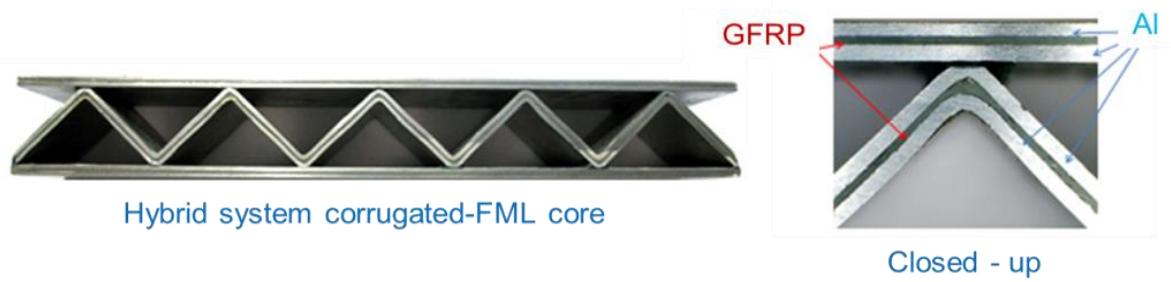


Figure 2.9: A combination of corrugated-core and fibre metal laminates[28]

The concept of constructing this structure inspired the author to develop Rejab's work much further in term of manufacturing technique in order to reduce time consumption to produce a better quality of bonding without extra adhesive.

2.4 Corrugated-core Sandwich Structures

The design of corrugated panels has been a widely used engineering application, for example, roof structures in civil engineering. Recently, corrugated laminates have been suggested as a good solution for morphing aircraft skins due to their extremely anisotropic behaviour. Corrugated-core is one of two-dimensional periodic cores, which may be classified into either straight, hat-type/trapezium, triangular or curvilinear conventional geometries, as shown in Figure 2.10 [34].

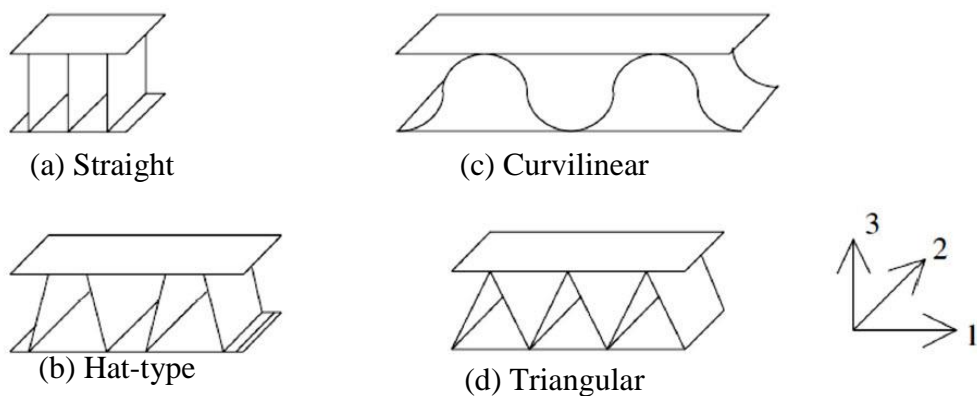


Figure 2.10: Traditional corrugated-core sandwich panels [34]

Xia et al. [35] suggested a unique method based on a simplified geometry for a unit-cell and the stiffness properties of original sheet to optimise design of corrugated-core

sandwich structures, Curvilinear and Hat-type. Their modelling strategy provided explicit expressions to calculate the equivalent material properties, and demonstrated the performance of the approach using two popular corrugation shapes. Airbus, the aircraft manufacturer [36], has developed a promising sandwich fuselage concept termed VeSCo (Ventable Shear Core), a novel design that incorporates a series of open channel structures, such as folded cores, truss cores and corrugated-cores to form the sandwich core material.

Curvilinear, Hat-type and Triangular Corrugated-core sandwich structures were chosen by the author to study in this research due to their simplicity of the design and a readiness of facilities to support manufacturing processes.

2.4.1 Curvilinear Corrugated-core

This type of structure is widely used in the packaging industry. Indeed, the curvilinear corrugated-core sandwich design has been used in the production of boxes and cardboard since the late 1800s [37]. They have been widely used in the packaging industry as a result of their low weight, recyclability and low cost. In the past, attempts have been made to predict the load-carrying capacity of corrugated box structures, most notably by McKee et al. [38]. Talbi et al. [29] analyzed the geometric and mechanical properties of corrugated board components. They also studied the behaviour of these corrugated structures when subjected to transverse shear and torsion, as shown in Figure 2.11.

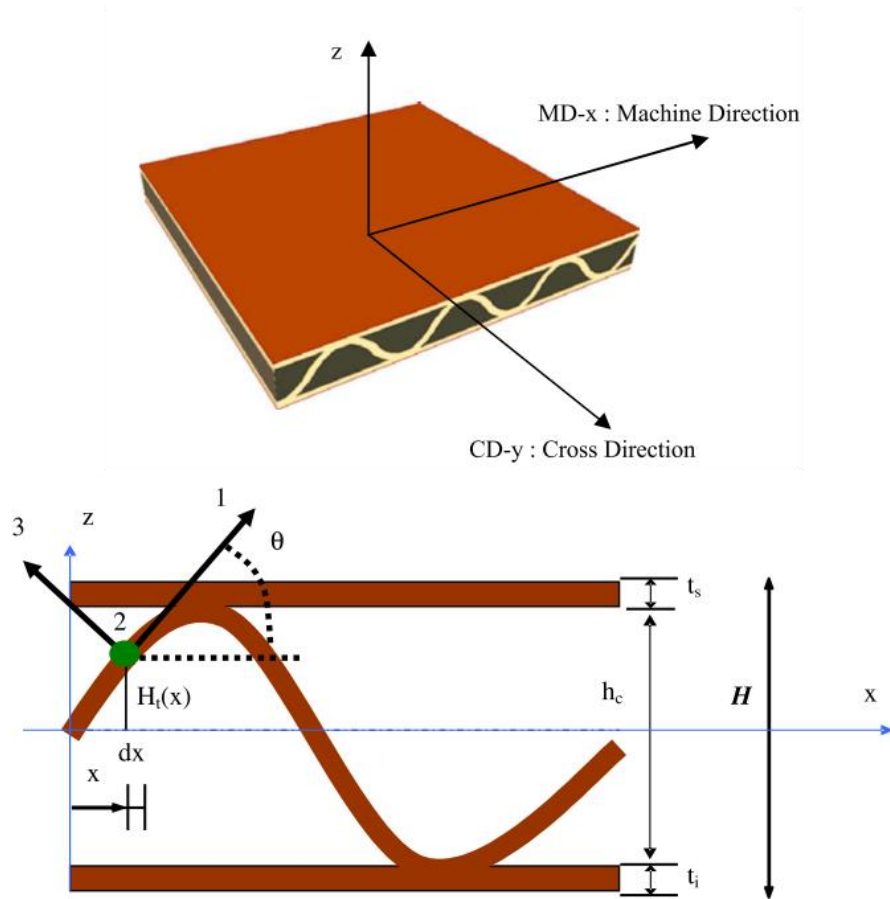


Figure 2.11: The corrugated-cardboard studied by [37]

Allaoui et al. [39] noted that corrugated cardboard is very sensitive to atmospheric conditions. Shear buckling of the core of a corrugated paperboard structure was investigated by Isaksson and Gradin [40]. It was shown that the structural strength of the panel decreases rapidly below a critical thickness of fluting. Tian and Lu [41] studied the minimum weight of a corrugated panel based on fibre reinforced composites subjected to a uniform axial compressive load in order to design an optimal corrugated panel.

Metallic corrugated core sandwich structures offer potential for use in a wide range of applications, such as those involving impact/blast load mitigation. There is a limited amount of experimental and numerical data in the literature related to the dynamic response of sandwich structures based on corrugated topologies. Recently, Mohr and

Marcadet [42] developed a phenomenological ductile fracture initiation model to predict ductile fracture in industrial practice. Here, an extended Mohr–Coulomb criterion is proposed, which makes use of the Hosford equivalent stress in combination with the normal stress acting on the plane of maximum shear. The validation with experimental results indicates that the proposed Hosford-Coulomb model can be used to accurately predict the onset of ductile fracture in advanced high strength steels. Also, Roth and Mohr [43] undertook extensive experimental and numerical work to investigate effect of strain rate on ductile fracture initiation in advanced high strength steel sheets. The extended stress-state dependent Hosford-Coulomb fracture initiation model is proposed to evaluate the strain rate effect on the onset of ductile fracture, which is also successfully validated against the experimental results. These state of the art theories could be used to simulate ductile fracture of metallic materials.

2.4.2 Straight Corrugated core

The predominant mechanical properties of straight-core sandwich panels are in the compression direction, but they are very weak in shear. Consequently, a straight corrugated-core should be designed at appropriate angles to the core trusses to ensure a good combination of compression and shear response. Kazemahvazi [20] previously reported that the shear modulus changes via increased corrugation angles as shown in Figure 2.13. A free-body diagram of the corrugated-core is shown in Figure 2.12.

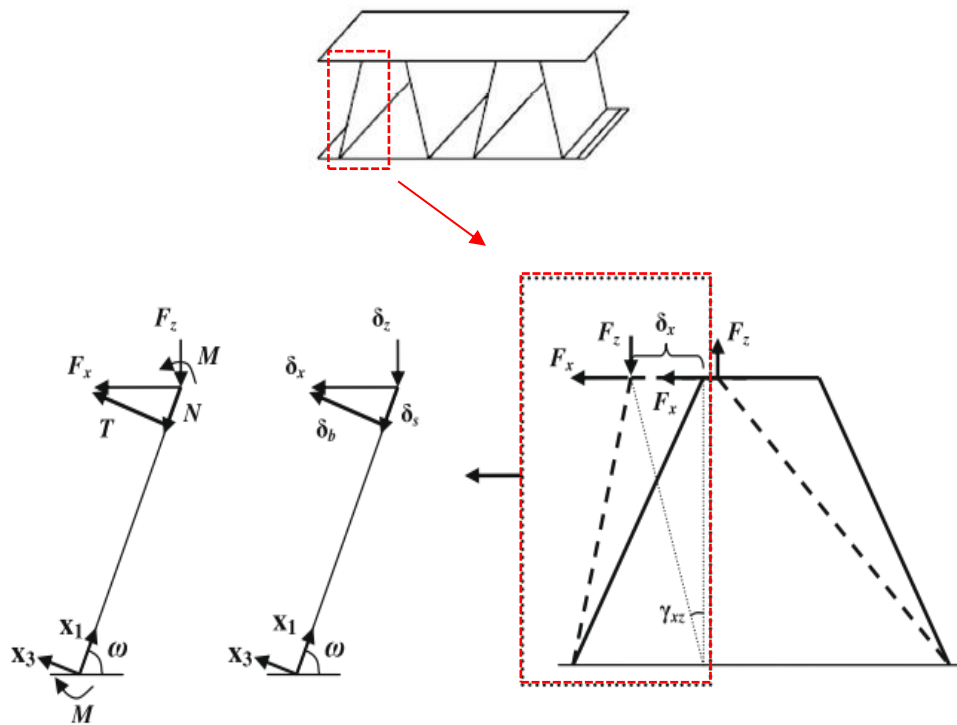


Figure 2.12: Free-body diagram of the corrugated-core[20].

In Figure 2.13, the maximum shear modulus was clearly achieved at a 45° angle, in contrast, the modulus at 0° and 90° (straight-core) angles was nearly to zero.

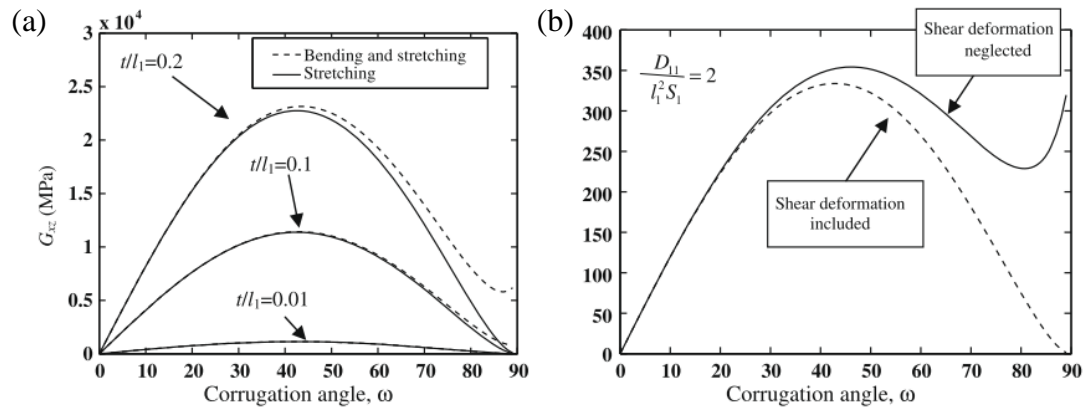
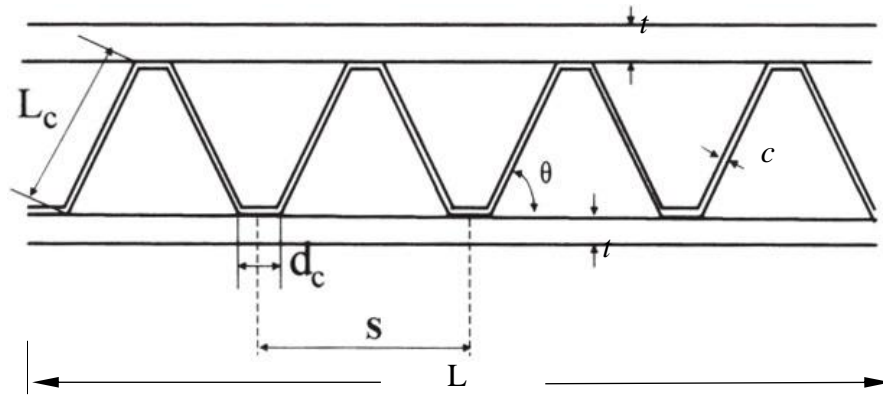


Figure 2.13: Shear modulus as function of the corrugation angle. (a) Monolithic core members and (b) sandwich core members [20].

2.4.3 Hat-type Corrugated-core

A hat-type corrugated-core or navtruss is characterized by a trapezium cross-section shape. A significant role of hat-type corrugated-core sandwich panels may be found in shipping container structures that were first built in 1950's by Malcolm McLean. Since the early 1980s, the US Navy has continued to develop and test innovative lightweight structural concepts in order to seek alternative replacements for conventional plate beam metallic structures. Wiernicki et al. [44] proposed that the concepts of corrugated core sandwich structures have the potential to offer a wide range of attractive design solutions to operational shipboard problems. They also conducted elastic and plastic analysis of lightweight metallic corrugated core sandwich panels subjected to blast loads, but they did not discuss the optimal core configurations of lightweight metallic corrugated core sandwich panels. Liang et al. [45] studied the optimal design of trapezoid metallic corrugated-core sandwich panels exposed to blast loads using combined algorithms. Figure 2.14 shows the cross section of a typical corrugated core

sandwich panel and the structural design parameters. The key core components were reported to be the corrugation leg, corrugation angles and core thickness.



L	: Space length	t	: Face sheet thickness
L_c	: Corrugation length	S	: Corrugation pitch
θ	: Corrugation angle (degree)	d_c	: Node width
c	: Core thickness		

Figure 2.14: Hat-type corrugated core sandwich panel [39]

In line with the incremental theory of plasticity, Krauthammer [46] developed an elastic-plastic analysis of trapezium corrugated-core sandwich panels, using the initial incremental plastic moments calculated by an iterative process. More recently, the author studied the effect of quasi-static and dynamic loading on a trapezium carbon fibre corrugated-core.

Dayyani et al. [47] introduced the mechanical properties of glass fibre trapezium corrugated-core for morphing skins. Prepreg laminates of glass fibre plain woven cloth were used and a heat gun and hand-layup was applied to the manufacturing technique. The corrugated panels were then manufactured by using a trapezoidal machined aluminium mould, as shown in Figure 2.15. Dayyani et al. observed that the

mechanical behaviour of the core in tension is sensitive to the variation of core height. A good degree of correlation was observed which showed the suitability of the finite element model for predicting the mechanical behaviour of corrugated laminate panels.

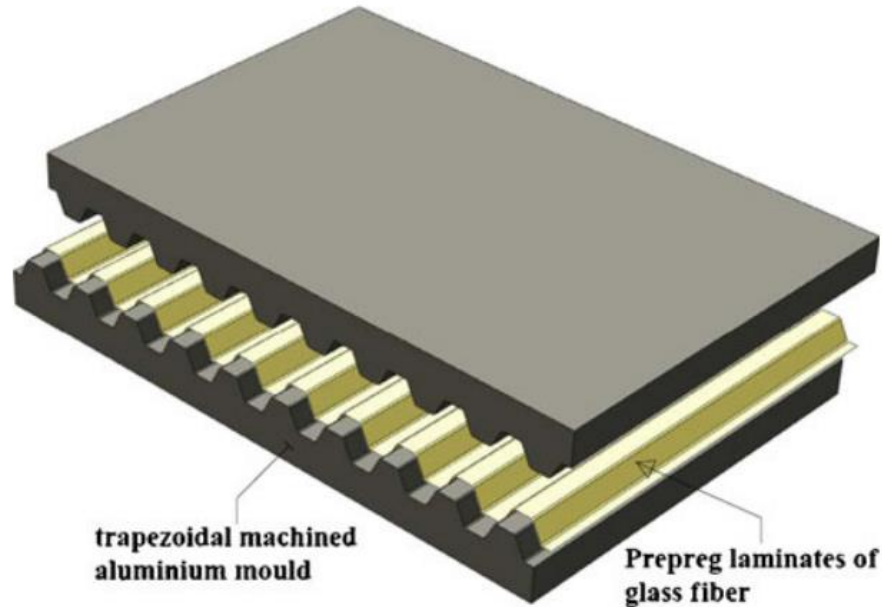


Figure 2.15: Schematic of trapezoidal machined aluminium mould and prepreg laminates of glass fibre [47]

2.4.4 Triangular Corrugated-core

To date, there has been a limited research, which has investigated triangular composite corrugated-core sandwich structures. Malcom et al. [48] extended Russell's works [30] to study further on micromechanical predictions of compressive response of glass fibre composite sandwich structures. The quasi-static compressive stress–strain response of the panels was experimentally investigated as a function of the strut width to length ratio and compared to micromechanical predictions. Good agreement was observed between experimental results and micromechanical predictions over the wide range of core densities investigated in the study.

Deshpande et al. [49] developed concept of the hierarchical corrugated-core as shown in Figure 2.16. The authors work established that the strength of the second order truss (hierarchical) was approximately ten times greater than that of a first order (monolithic) one with the similar relative density.

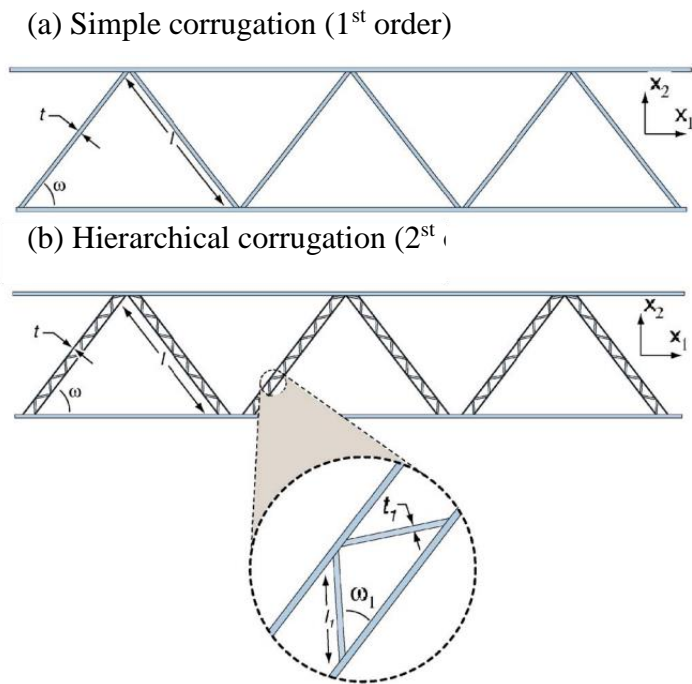


Figure 2.16: Sketches of (a) the first and (b) the second order corrugated cores sandwiched between two rigid face sheets [49].

Carlsson et al. [50] undertook an analysis on the elastic stiffness of corrugated core sandwich panels including triangular corrugated-core into the framework of first-order shear deformation laminated plate. It was found that the in-plane extensional and shear stiffness and the bending and twisting stiffness are dominated by the face sheets and that calculated values agree with the measured data.

Recently, Rejab et al [28] introduced the triangular corrugated core sandwich structures, as shown in Figure 2.17. They proposed that this configuration of sandwich structures which was designed to have 45° of the core would offer at the maximum combination of shear and nominal compressive strength. In addition, this kind of core

structures outperforms in terms of air flow exchange that could increase mechanical performance avoiding problems associated with humidity retention.



Figure 2.17: Triangular corrugated-core sandwich structures made of (a) Aluminium 2024 O (b) GFRP (c) CFRP [28].

2.5 Mechanical properties of corrugated-core sandwich structures

The mechanical response under both static and dynamic compression tests, static shear tests and under combined compression-shear loading of the corrugated-core sandwich structures are presented in this section.

2.5.1 Mechanical response under quasi-static loading

This section reviews the mechanical response under both compression and three-point bending tests.

2.5.1.1 Mechanical response under static compression test

Many researchers claimed that the overall mechanical response of a sandwich structure is largely dependent on the properties of the skin, the stiffness and strength properties of the core, as well as the strength of the bond between skin and core [2, 41, 45, 51,

52]. Ashby [53] concluded that the mechanical properties of sandwich core materials are determined by three key factors, i.e. (1) the topology of the cellular materials, (2) the parent material properties and (3) the relative density, $\bar{\rho}$, defined by the volume fraction of solid material.

Lu and Chen [54] studied the compressive responses and failure mechanisms of corrugated sandwich panels subjected to uniform lateral compression examined by a combined theoretical and experimental study. Uniaxial compression tests were conducted on two types of commercially-available corrugated board panels, FCT (Flat Crush Test) and CMT (Concorra Medium Test) to examine the validity of the analytical predictions. The authors used the effects of boundary conditions, geometrical parameters, material properties and geometrical imperfections as the parameter studies. It was found that the perfect board panel deformed in a symmetrical manner relative to the loading axis.

Côté et al. [17] investigated the compressive and shear responses of corrugated and diamond lattice materials using 304 stainless steel as the core material, as shown in Figure 2.18. The investigators conducted out-of-plane compression at the three relative densities, $\bar{\rho} = 0.036, 0.05$ and 0.10 . Figure 2.18 shows that the peak load is governed by buckling of the principal struts, whilst the subsequent softening is associated with the post-buckling response. Figure 2.19 shows a comparison of the experimental and predicted values of the out-of-plane compressive strength of the stainless steel corrugated-core panels, where an imperfection of magnitude, $\zeta = 0.25$, gives prediction of the peak stress accurately. Without imperfection, the peak stress increases systematically with increasing $\bar{\rho}$ and the analytical solutions provide an over-prediction due to the equation that does not include any imperfection. The analytical predictions were based on the Euler elastic buckling analysis and the sShanley plastic

bifurcation stresses as shown in Equation (2.6) [55].

$$\delta = \begin{cases} \frac{2\sigma_y}{\sqrt{3}} \\ \frac{k^2\pi^2 E_s}{12(1-\nu^2)_{eq}} \left(\frac{t}{l}\right)^2 \quad \text{if } \frac{t}{l} < \sqrt{\frac{8\sqrt{3}(1-\nu^2)\sigma_y}{k^2\pi^2 E_s}} \end{cases} \quad (2.1)$$

where k is a boundary condition factor ($k = 2$ if built-in), E_s is the Young's modulus, σ_y is the yield stress, ν is a Poisson's ratio and (t/l) is an aspect ratio of thickness and a length of a strut. The buckling response under quasi-static loading is a common means of failure in metallic truss structures [56].

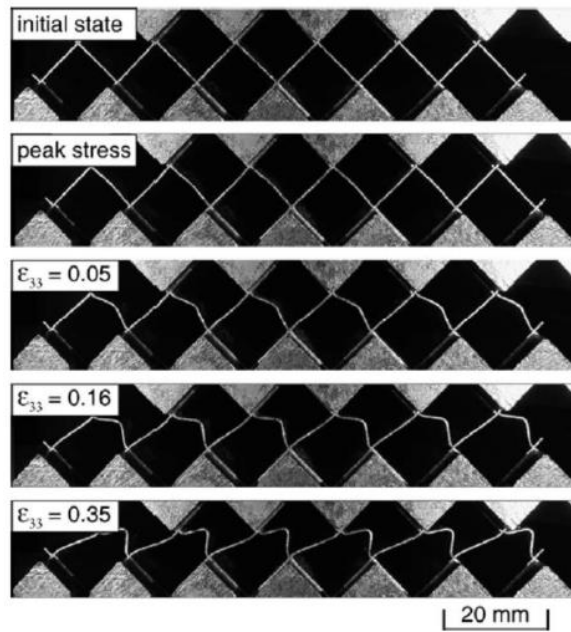


Figure 2.18: Deformation images of the $\bar{\rho} = 0.05$ corrugated-core in out-of-plane compression [17]

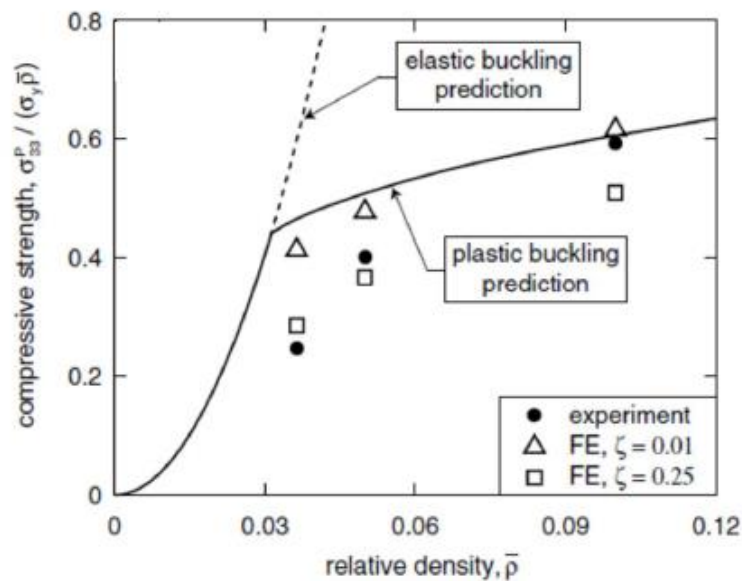


Figure 2.19: A comparison of the experimental and predicted values of out-of-plane compressive strength of stainless steel corrugated-core panels [17]

Rejab et al. [29] presented the mechanical behaviour of corrugated-core sandwich panels. The experimental investigations and numerical analyses were carried out into the compression response. Subsequent failure modes were obtained in corrugated-core

sandwich panels based on an aluminium alloy, a glass fibre reinforced plastic (GFRP) and a carbon fibre reinforced plastic (CFRP).

2.5.1.2 Mechanical response under three-point bending

For an empty or foam-filled corrugated sandwich beam loaded in 3-point bending, the total deflection δ at its mid-span may be given as the sum of the deflections due to bending of the face sheets and shear of the core[25]:

$$\delta = \frac{FL^3}{48(EI)_{eq}} + \frac{FL}{4(GA)_{eq}} \quad (2.2)$$

where $(EI)_{eq}$ and $(GA)_{eq}$ were the equivalent flexural rigidity and shear rigidity, respectively, that may be expressed as:

$$(EI)_{eq} = \frac{Ebt_f d^2}{2} + \frac{Ebt_f^3}{6} + \frac{C_{22}^H bc^3}{12} \quad (2.3)$$

$$(GA)_{eq} = \frac{bd^2}{c} C_{44}^H \approx bcC_{44}^H \quad (2.4)$$

Here, C_{22}^H is the in-plane elastic modulus of the core in the 2-direction, and C_{44}^H is the out-of-plane shear modulus of the core in the 2–3 direction. By using the homogenization method, these two elastic constants may be obtained as [57]:

$$\begin{aligned}
C_{22}^H = & \frac{E}{(1-\nu^2)} \left(\frac{t}{l}\right) \frac{\cos^3 \theta}{\sin \theta} + \frac{E}{(1-\nu^2)} \left(\frac{t}{l}\right)^3 \sin \theta \cos \theta \\
& + \frac{2kE}{(1-\nu^2)} \left(\frac{t}{l}\right) \frac{\cos \theta}{\sin \theta} + (1-\nu_s) C_{11}^f
\end{aligned} \tag{2.5}$$

2.5.2 Mechanical response under dynamic loading

Many studies have been carried out to help understand and improve the impact resistance of composite materials and structures [58-62]. This section focuses on the mechanical responses of corrugated-core sandwich structures under low velocity impact, perforation and blast loading and the related subjects of dynamic effects and impact testing.

2.5.2.1 Dynamic Effects

The periodic cellular core dynamic response has been proposed to be significantly different from its quasi-static loading response, due to three key effects [28]:

a) Material strain-rate sensitivity

The core constituent material may demonstrate a strain-rate dependence, i.e. the yield strength of mild steel increases with increasing strain-rate [63].

b) Inertia stabilisation

Cellular cores are buckling-dominated, consequently the inertial effects can delay the onset of buckling and change the wavelength of the buckling mode. However, these propagation effects are deemed negligible [64]

c) Wave propagation

As impact velocity increases, wave propagation effects become important. The propagation of elastic, plastic and bending waves can be transmitted through the core and affect structure macroscopic properties. For example, if

dynamically loaded a metal column in compression, the impact velocity becomes greater than the plastic wave speed and the column does not buckle. Instead, the material accumulates at the impacted end [65].

2.5.2.2 Mechanical response under low velocity impact loading

Analysis of composite sandwich panels subject to impact loads has been of much interest in recent years, because of the sensitivity of advanced composite materials to impact damage [66-76]. Christoforou et al. [77] published an analytical solution to solve an impact response in composite plates, based on the usual Fourier series expansion for simply-supported plates, combined with Laplace transform techniques for the impact problem solution.

Two criteria for the classification of impact response were presented by Chai and Zhu [78], as shown in Figure 2.20. From the chart, M is mass of impactor, m_p is mass of specimen and (M/m_p) is impactor mass ratio, E is impact energy, h is height of mass. For low velocity impact, the deformation of a sandwich panel subjected to impact load can be divided into two parts as following equation;

$$f = w + \alpha \quad (2.6)$$

where w is the global deflection and α is the indentation. The global deflection w depends on the boundary conditions and highly dependent on the impact duration. If the impact duration (t) is long enough, global deflection will be in the phase with the motion of the impactor, thus dominating deformation.

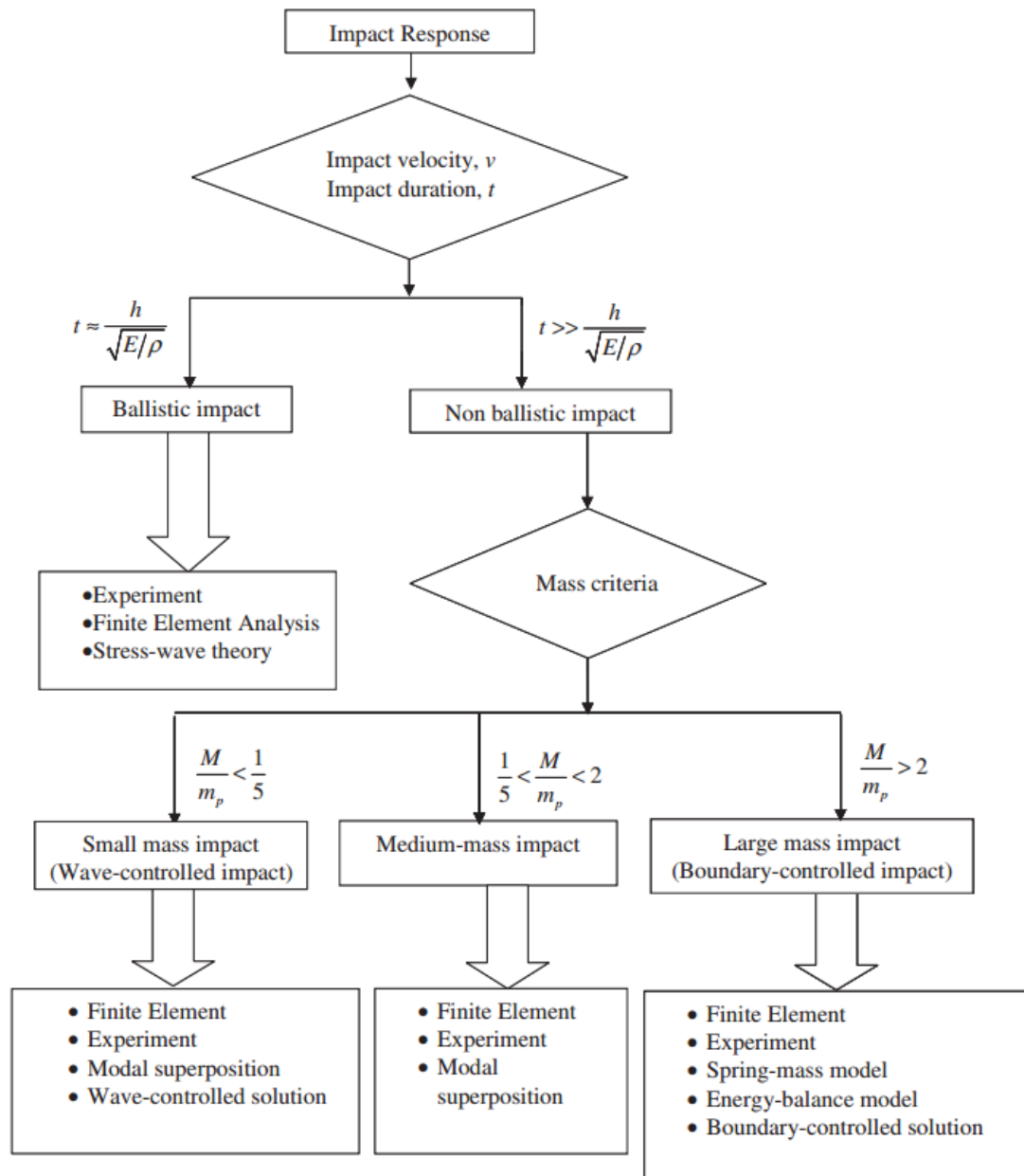


Figure 2.20: Solution methods for different categories of impact [78]

Stronge [79] highlighted the difference of deformation or damage between low velocity impact and high velocity impact. It was explained that plastic deformation is localised around the contact area where the low velocity impact occurs, whereas a large deformation or damage occurs for high velocity impact. In this criterion, the impact mass, M , and time duration, t , are taken into account as key parameters [80, 81]. Olsson [81] concluded that long impacts cause a quasi-static response influenced by the plate size and boundary conditions. Short impacts cause a response governed by wave

propagation unaffected by plate size and boundary conditions. Cantwell and Morton [82] classified the impact response using velocity up to 10 m/s for the low velocity impact. Rubino et al. [83] investigated the impact response of clamped stainless steel Y-framed and corrugated core sandwich plates loaded by aluminium foam projectiles. At low values of projectile momentum, the sandwich panels deflected less than their monolithic counterparts. However, at higher values of projectile momentum, the sandwich panels failed in a tearing mode, whereas the monolithic panels remained intact. Kılıçaslan et al. [84] conducted an experimental and numerical study on the impact response of layered trapezoidal corrugated aluminium core and aluminium sheet interlayer sandwich structures. Here, strain rate effects were attributed to micro-inertial effects that increased the critical buckling load of the fin at high rates of loading. Radford et al. [85] conducted impact tests on triangular corrugated, pyramidal and aluminium foam core sandwich plates. It was observed that the corrugated and metal foam core sandwich plates offered the best dynamic performance. Tilbrook et al. [56] investigated the dynamic crushing characteristics of sandwich panels based on prismatic lattice cores. Here, the quasi-static and dynamic compression deformation behaviour of stainless steel corrugated and Y-frame sandwich cores were tested. At velocities below 30 m/s, micro-inertial stabilization against elastic buckling was observed to occur. At higher velocities the propagation of plastic waves within the core resulted in the front face stresses increasing with velocity, whilst the rear surface stresses remained roughly constant.

2.5.2.3 Mechanical response under perforation

The various deformation mechanisms that occur when a projectile strikes a target at normal incidence are discussed in this section. Penetration by projectiles is influenced by variables such as material properties, impact velocity, projectile shape, target support position and relative dimensions of the target and projectile [86]. Cantwell and Morton [75] conducted a series of low and high velocity impact tests on a number of CFRP laminates. The influence of the projectile mass upon the impact response and subsequent load-bearing capability of a composite structure were studied. The first damage threshold energy with impactor mass is shown in Figure 2.21. Light, fast-moving projectiles induced a much localised mode of target response. Furthermore, they compared the influence of low and high velocity impact response of CFRP and found that the size and shape of the target determined its energy-absorbing capability and therefore its impact response for velocity impact loading. Fast moving projectile from high velocity impact loading did not induce a localized mode of target response and the size of damage [74].

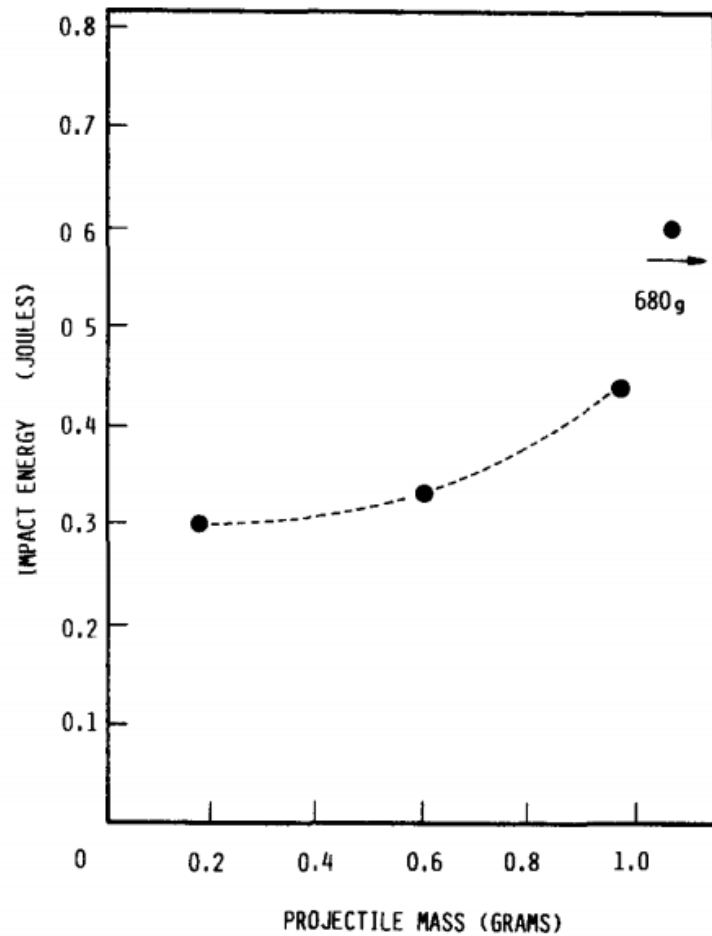
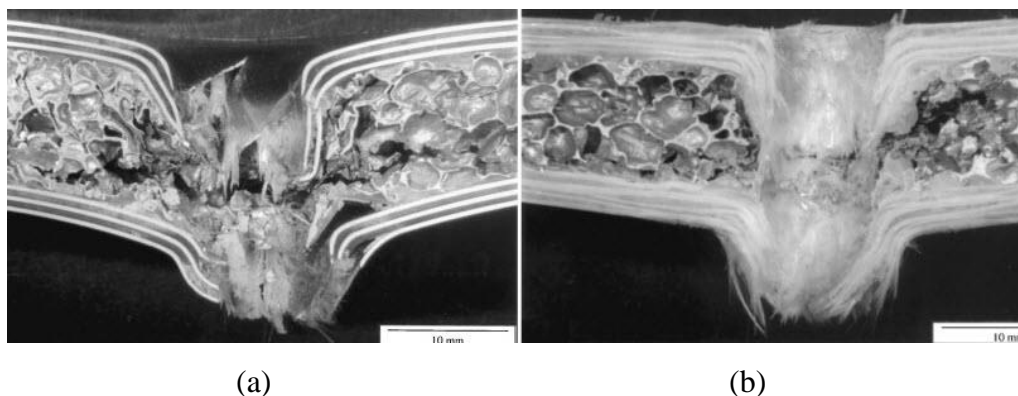


Figure 2.21: The variation of the first damage threshold energy with impactor mass for the eight-ply ($\pm 45^\circ$) laminate [75].

Aktas et al. [87] conducted the experimental investigation of the impact response of unidirectional glass/epoxy laminates by considering energy profile diagrams and associated load–deflection curves. They found that the primary damage mode was fibre fracture for higher impact energies; whereas, it was indentation, which resulted in delamination and matrix cracks, for smaller impact energies. Contour plots of the overall damage areas were also depicted for several impact energies.

Villanueva and Cantwell [69] studied the high velocity impact response of composite and FML-reinforced sandwich structures using a nitrogen gas gun. Using a 10 mm diameter projectile, impact testing was conducted on sandwich structures, which had plain composite and fibre-metal laminate (FML) skins and a range of aluminium foam

cores. It was reported that the composite skins were delaminated and split longitudinally in the unidirectional glass fibre/polypropylene-based systems. In contrast, the sandwich structures which were woven glass fibre/polypropylene-based, had less delamination. Figure 2.22 compares the cross-sections of (a) unidirectional FML and (b) woven FML-reinforced sandwich specimens after being subjected to impact energies at 120 J. Figure 2.23 shows perforation and specific perforation energies of the composite and FML skinned aluminium foam sandwich structures.



(a) (b)
Figure 2.22: Low magnification optical micrographs of the cross-sections of (a) unidirectional FML and (b) woven FML-reinforced sandwich specimens after being subjected to impact energies at 120 J [69].

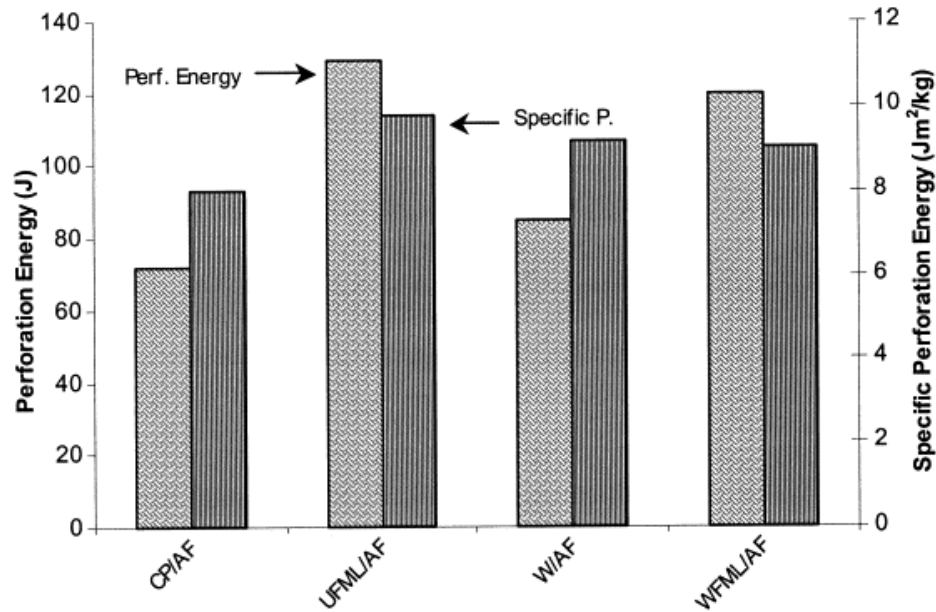


Figure 2.23: Perforation and specific perforation energies of the composite and FML skinned aluminium foam sandwich structures [69].

2.5.2.4 Mechanical response under blast loading

Military and civilian structures can be exposed to intentional or accidental blasts. Composite sandwich structures are being considered for energy absorption applications in blast resistant cargo containers, ordnance boxes, transformer box pads, etc. [88]. A superior performance was confirmed by Yuen et al. [89] by investigating ability of sandwich panels to resist dynamic loading. The cellular microstructure of composite sandwich structures allows them to undergo large deformation at nearly constant nominal stress and thus absorb more energy [90-92].

Sandwich structures have various energy dissipation mechanisms, such as bending and stretching of the face sheet, as well as compression and shear of the core, especially in the case of impulsive loading [93-97]. Under blast loading, core plays a significant role to absorb blast energy more than one half of the initial kinetic energy imparted to face sheet of the sandwich plate due to crushing in the early stages of deformation,

prior to significant overall bending and stretching. The high crushing strength and energy absorption per unit mass of the core is therefore important [98-102]. Yazici et al. [103] carried out both experimental and numerical study of foam filled corrugated core steel sandwich structures subjected to blast loading using a shock tube facility and high speed photography.

Langdon et al. [104] observed behaviour of fibre-metal laminates subjected to localised blast loading. They studied the behaviour of aluminium alloy-glass fibre-reinforced polypropylene-based fibre-metal laminates (FMLs) subjected to localised explosive blast loading. Figure 2.24(a) shows the schematic of loading arrangement and Figure 2.24(b) shows the photograph of ballistic pendulum.

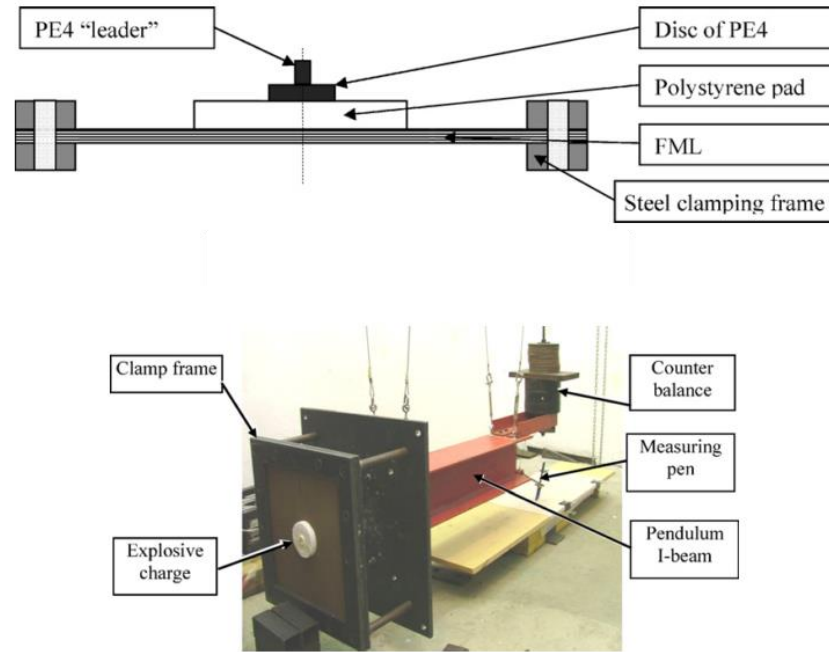


Figure 2.24: (a) Schematic of loading arrangement, (b) photograph of ballistic pendulum setup [104]

Langdon focused on varying thickness and material distribution, and investigated the influence of stacking configuration. The threshold impulse for the onset of tearing was found to increase linearly with panel thickness [105, 106].

2.6 Concept of energy absorption

Energy absorption is an energy required to fracture a part subjected to shock loading as in an impact test. Alternative terms are impact value, impact strength or impact resistance. A structure which has high energy absorption will be able to deform extensively in order to dissipate the force. During the impact test, the energy of the motion or the kinetic energy to crush the sample, E_{crush} , is expressed by the following relationship [107-109]:

$$E_{crush} = \frac{1}{2}mv^2 \quad (2.7)$$

where m and v , are the mass and the critical velocity of the body respectively.

The Law of Conservation of Energy states that the total amount of energy never changes. Figure 2.25 illustrates the transformation of energy. The potential energy can be expressed by [110]:

$$E_{potential} = mgh \quad (2.8)$$

where a carriage has a mass (m) kg, without movement ($u = 0$ m/s) under the gravity (g). When the carriage is released and travel down nearly touch the sample surface, the energy transforms to another form as kinetic energy as described in Equation (2.7), where the carriage has maximum velocity (v). During impact, a force does work, W_{crush} , on the sample. The product of the force, F_{crush} , exerted and the distance travelled, L_{crush} , is equal to the energy transmitted to a system and can be expressed by [110]:

$$W_{crush} = \int_0^{\delta_{max}} Fd(\delta) \quad (2.9)$$

An ideal energy-absorbing structure transforms all of the work input to work output. Efficiency is defined as the ratio of the work input into a system to the useful work output [107, 111, 112]

$$Efficiency = \frac{Work\ done}{Energy\ used} \quad (2.10)$$

Load-displacement curve obtained from quasi-static or dynamic loading is commonly used to study characteristics of the performance of a particular energy-absorbing structure as shown in Figure 2.26 [113-115].

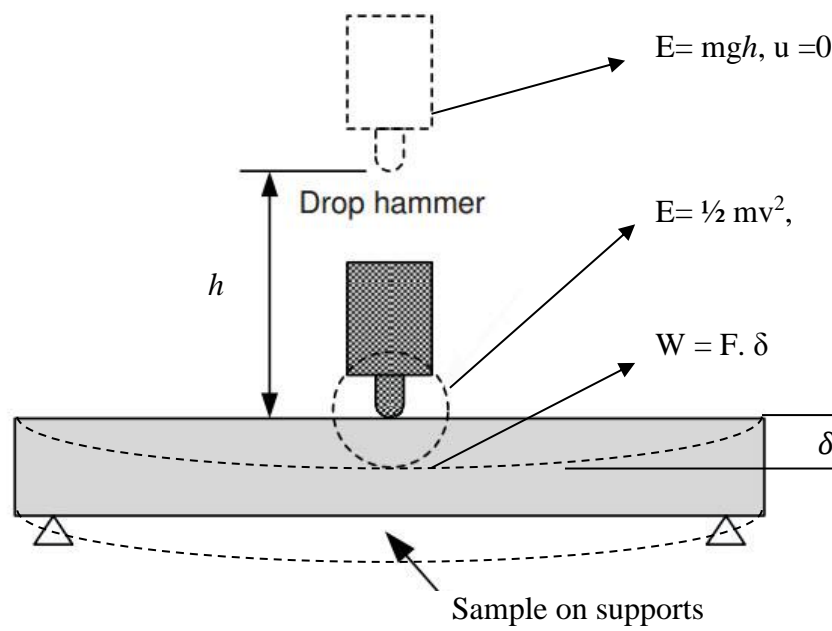


Figure 2.25: The transformaiton of energy[110]

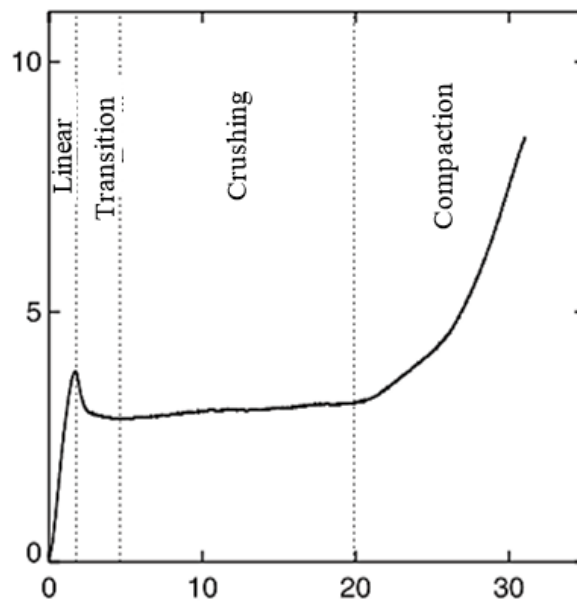


Figure 2.26: Typical load-displacement regions of a specimen tested under quasi-static compression [114].

2.6.1 Energy-absorbing capacities of core structures

The performance of energy absorption capacity of lightweight sandwich structures is generally determined by using a specific energy absorption value (SEA) in kJ/kg to compare the energy absorption to weight ratio. The area under the load-displacement traces as shown in Figure 2.29 presents the absorbed energy of the structure. Laurin [114] carried out a number of experimental tests to evaluate the specific energy absorption of sandwich cores, with summarised the energy-absorbing features being listed in Table 2.1.

Table 2.1: Energy-absorbing capacity of core structures [2]

Core types	Density (kg/m³)	SEA (kJ/kg)	Author
PVC, PET, Linear Foam	40-200	8-15	Hassan et al. [116]
PMI foam, PVC foam	52–250	11–18	Heimbs [117]
PI/PU/PE foam	69.2- 104.2	2-9	Heimbs [118]
Aluminium foam	n/a	12.3-28.5	Altenaiji et al. [119]
Aluminium foam	270 -313	4.98- 5.5	Ochelski et al, [120]
Aluminium matrix syntactic foam	1640	50.6	Tao and Zhao [121]
Aluminium honeycomb	27–192	9–45	Heimbs [118]
Nature fibre honeycomb	0.1-0.4	0.6-6.5	Zuhri et al.[122]
Chiral CFRP honeycomb	n/a	96.5	Airoldi et al. [123]
Polypropylene honeycomb	40	3.1	Alia et al. [124]
Bamboo tube foam core	40-200	19-53	Umer et al, [125]
CFRP tubes embedded PVC foam	40-280	21-155	Alia et al. [124]
CFRP tubes embedded in PS foam	107.8	86	Heimbs [118]
GFRP tubes supported by PS foam	n/a	17.7–32.6	Tarlochan et al. [126]
Corrugated-cores	205-363	31.5-63.5	Ruzaimi and Cantwell [127]

Carbon foldcore	103–114	4.5–22.5	Heimbs [118]
Kevlar foldcore	48–113	2–7.5	Heimbs [118]
Nomex	29–48	8–18	Heimbs [118]
Lattice structure	3.5–13.9	0.6–6.4	Smith et al. [128]
Composite pyramidal truss cores	20–35	0.75–8	Xiong et al. [129]

2.7 Review of modelling of sandwich structures

In this section, the background of the finite element method, the modelling of corrugated-core sandwich structures and the related issues associated with static and dynamic FE modelling are discussed.

2.7.1 Background of the finite element method

The finite element method (FEM), also referred as the finite element analysis (FEA), is a numerical method for solving complex problems in engineering and physics. Alternatively, FEM can be used to analyse complicated structural behaviour where experimental analyses either may not be feasible and/or when the expense of experimental testing is considered a limitation. More recently, the use of FEM as a computer-aided engineering (CAE) tool for technical analysis has become the most popular method. There are several commercial FE packages available, e.g. Abaqus, LS-Dyna, ANSYS, CosmosM, ALGOR, MSC.Nastran, etc.

Researchers and industry are typically the end-users of commercial FE packages. An appropriate level of understanding, to fully optimise its capability, is required by the operator. For example, the end-user with a good understanding of FEM has the ability to produce detailed visualisations in CAE, to show the stresses and strains and

deformation of the structural components. Therefore, FEM gives a high level of assurance in the performance of the structural components pre-manufacturing.

2.7.2 Modelling of Corrugated-core Sandwich Structures

Rejab [29] simulated the compression response, and subsequent failure modes in corrugated-core sandwich panels based on an aluminium alloy, a glass fibre reinforced plastic (GFRP) and a carbon fibre reinforced plastic (CFRP) using numerical analyses. Abaqus/Explicit software package was used with four-noded shell elements (S4R). The study extend further to analyse the failure modes such as buckling of the cell walls and imperfections method was applied to FEA models. The predictions of FEA generally show reasonably good agreement with the experimental measurements.

Haj-Ali et al. [130] presented a refined nonlinear finite element approach for analysing corrugated fibreboards. In their work, the anisotropic and nonlinear material stress–strain behaviour of the corrugated structured was modelled. It was found that the proposed refined modelling approach was able to accurately predict the overall mechanical behaviour and ultimate failure in a wide range of corrugated systems.

Buannic et al. [34] studied the homogenization of corrugated core sandwich panels using finite element modelling. Their work was devoted to the computation of the effective properties of corrugated core sandwich panels. The homogenization theory is used, based on the asymptotic expansion method to determine the equivalent membrane and pure bending characteristics of periodic plates. This study allows to compare different types of alveolar structures with traditional stiffened structures, with a view to their applications in shipbuilding.

Zhou et al. [131] reported the numerical modelling of perforation impact damage of fibre metal laminates using a commercial finite element code Abaqus/Explicit

software package with the implementation of a user-defined subroutine. A vectorised user-defined material subroutine (VUMAT) was developed to define Hashin's 3D rate-dependant damage criteria for the GFRP. Good agreement was obtained between the simulations and the experimental results, in terms of the load–displacement traces, the deformation and failure modes.

Noor et al. [51] studied the hierarchy of computational models for sandwich panels and shells, predictor-corrector procedures, and the sensitivity of the sandwich response to variations in the different geometric and material parameters. Extensive numerical results are presented for thermally stressed sandwich panels with composite face sheets. The study showed the effects of variation in their geometric and material parameters on the accuracy of the free vibration response, and the sensitivity coefficients predicted by eight different modelling approaches (based on two-dimensional theories).

Côtéa et al. [17] predicted the quasi-static response of the triangular corrugated and diamond lattice cores. Modelling a single corrugation using a three-dimensional linear shell element (S4R), alongside an input of the elastic-plastic property of the stainless steel, enabled the authors to ascertain a prediction of the mechanical response of the core. The researchers, subsequently, imposed an imperfection in the shape of the buckling mode onto the corrugation unit cell, at the location where the Eigen mode and the maximum amplitude equal to 25% of the sheet thickness was specified in the FE model. Figure 2.27 (a) displays photographs of the $\bar{\rho} = 0.05$ corrugated core showing the deformation mode during tests in out-of-plane compression. Figure 2.27(b) displays the measured responses and finite element predictions of the corrugated core specimens in out-of-plane compression of $\bar{\rho} = 0.036$ (top), $\bar{\rho} = 0.05$ (bottom).

Liang et al. [45] developed lightweight structural concepts for naval applications, with a view to replacing traditional designs with optimized metallic corrugated core sandwich panels. The optimum designs of metallic corrugated core sandwich panels were modelled under blast loading. The authors showed that parameters, such as the corrugation angle and core thickness, are important when designing the core structure.

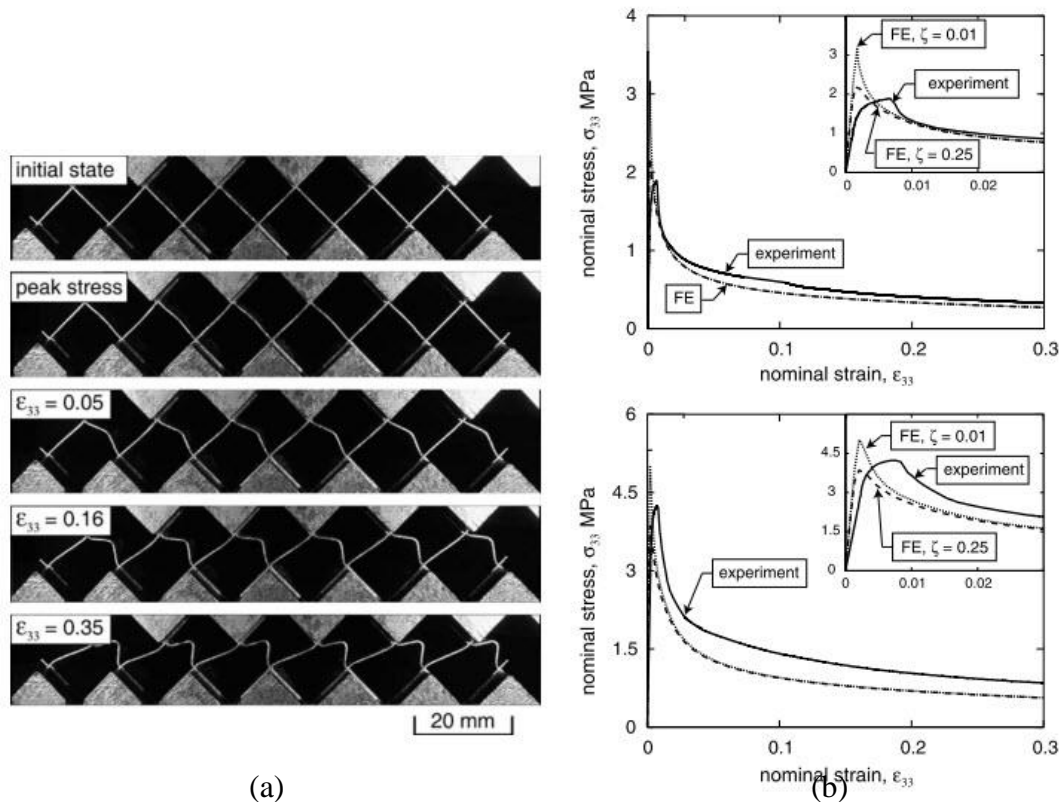


Figure 2.27: Photographs of the $\bar{\rho} = 0.05$ corrugated core showing the deformation mode during tests in out-of-plane compression and (b) measured responses and finite element predictions of the corrugated core specimens in out-of-plane compression of $\bar{\rho} = 0.05$ (top), $\bar{\rho} = 0.10$ (bottom) [17].

Tilbrook et al. [56] simulated quasi-static and dynamic crushing of sandwich panels with prismatic lattice and Y-frame sandwich cores using a commercial finite element code Abaqus/Explicit. Two-dimensional four-noded plane strain quadrilateral element with reduced integration (CPE4R) was used. Figure 2.28 (a) shows comparisons of the measured results and numerical predictions of the quasi-static response, with good

agreement throughout the collapse response. In Figure 2.28 (b), the finite element calculations also demonstrated that material strain-rate effects have a negligible effect upon the dynamic compressive response of laboratory-scale and full-scale sandwich cores.

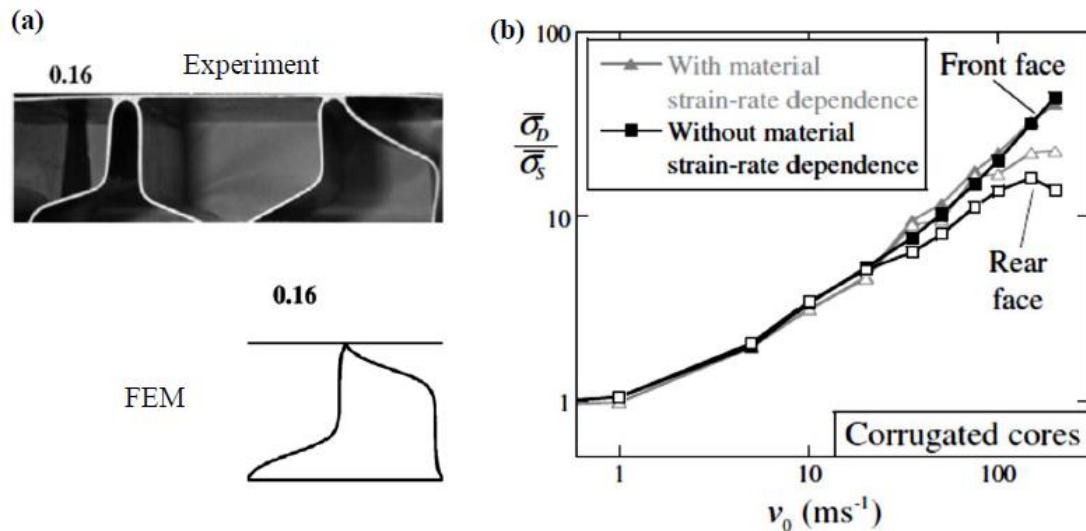


Figure 2.28: (a) A comparison between the observed and FE predictions of the quasistatic deformation mode of the corrugated-core specimens and (b) FE predictions of the dynamic strength enhancement with and without material strain-rate sensitivity [56].

Recently, Han et al. [57] studied the design optimization of foam-reinforced corrugated sandwich beams. They carried out a combined analytical and numerical study for the structural stiffness, collapse strength and minimum mass design of foam-filled corrugated sandwich beams under transverse three-point bending. Using an Abaqus software package version 6.10 with 2D finite element simulations to predict the initial collapse strength, six different failure modes were considered, with the effect of loading platen width being accounted. Finite element simulations were performed to validate the analytical predictions, with a good agreement obtained. There were six different failure modes identified, i.e. (1) face yielding (FY), (2) face wrinkling (FW),

(3) core shear with corrugated member buckling (CSB), (4) core shear with corrugated member yielding (CSY), (5) indentation with corrugated member buckling (INDB), and (6) indentation with corrugated member yielding (INDY).

Blast impact response of aluminium foam sandwich composites were conducted by Rajan et al. [53]. The study examined the modelling of aluminium foam sandwich composites subjected to blast loads using LS-DYNA software. The sandwich composite was designed using laminated face sheets (S2 glass/epoxy and aluminium foam core). The aluminium foam core was modelled using an anisotropic material model. The laminated face sheets were modelled using material models that implement the Tsai-Wu and Hashin failure theories. Blast load was applied using the CONWEP blast equations (*LOAD_BLAST) in LS-DYNA. They found that the blast loads excited at the geometric center of the plate and the box resulted in outward radial wave propagation. The damage progression of the sandwich composite occurred by ‘dishing’, which increased with increasing magnitude of the blast. These findings are consistent with studies in [54-56].

He et al. [132] designed the lightweight concept of corrugated-core sandwich structures fabricated with carbon fibre reinforced polymer (CFRP) face sheets and aluminium alloy cores enabling sandwich structures to maximize the specific bending stiffness/strength and improve the energy absorption capability. The low velocity impact behaviour of such structures is investigated experimentally and numerically. A user subroutine VUMAT is developed to model the composite face sheet behavior, in which a progressive damage model based on the Hashin failure criteria and Yeh delamination failure criteria is implemented in ABAQUS/Explicit. A good agreement was obtained between the experimental and predicted results in terms of impact force,

absorbed energy, and failure modes of sandwich structures. They revealed that fibre and matrix damage, delamination of face sheets as well as buckling of core members occur under varied impact energies. The predicted impact damage of specimen is shown in Figure 2.36.

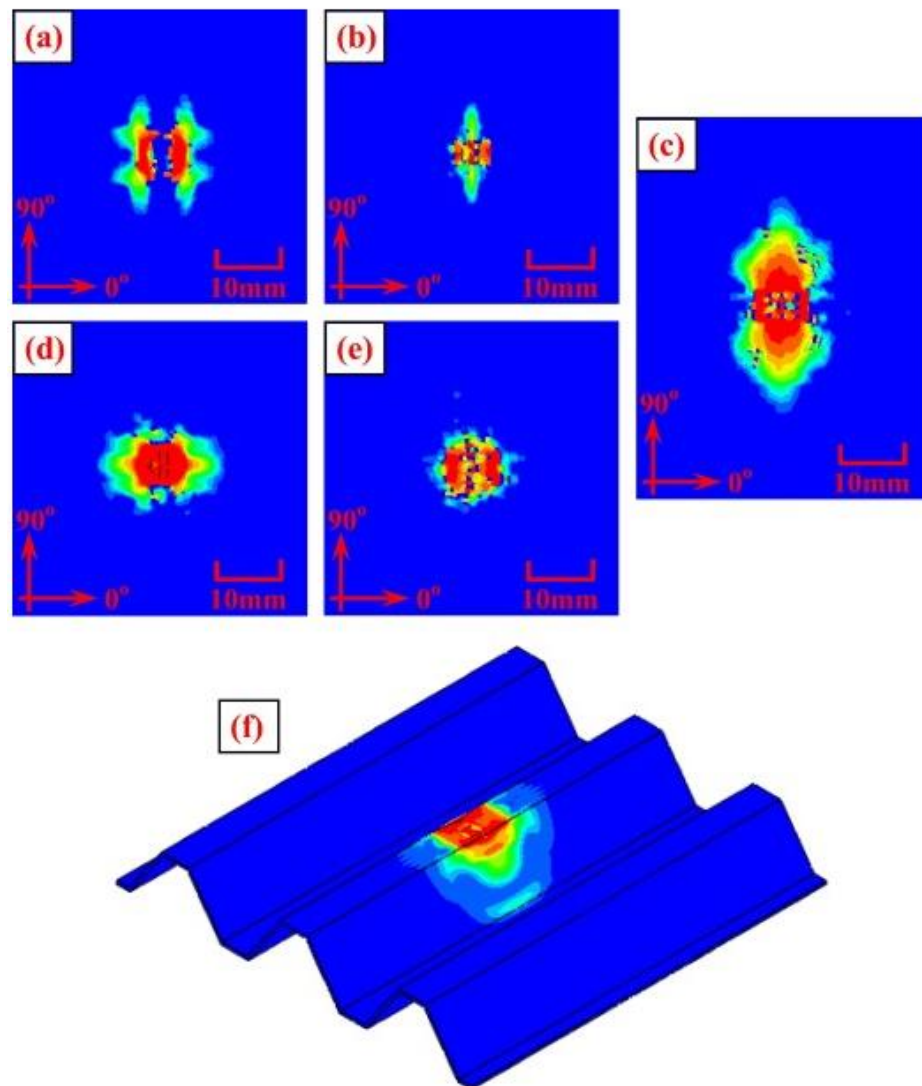


Figure 2.29: The predicted impact damage of specimen C for the 10 J case: (a) the fiber tensile failure; (b) the fiber compressive failure; (c) the matrix tensile failure; (d) the matrix compressive failure; (e) the delamination failure; and (f) the corrugated core failure [132].

Nemeth et al. [133] studied the buckling and post buckling behaviour of thin plates with a cut-out and made of advanced composite materials.

2.8 Failure mechanisms of corrugated-core sandwich structures

In this section, failure mechanisms of corrugated-core sandwich structures are reviewed with relevant work in the past and in the recent studies.

2.8.1 Failure mechanisms from quasi-static loading

In their recent work, Rejab et al. [28] investigated the failure modes of the CFRP triangular corrugated-cores, as shown in Figure 2.30. The delamination, fibre breaking and debonding failure modes were found under quasi-static loading.

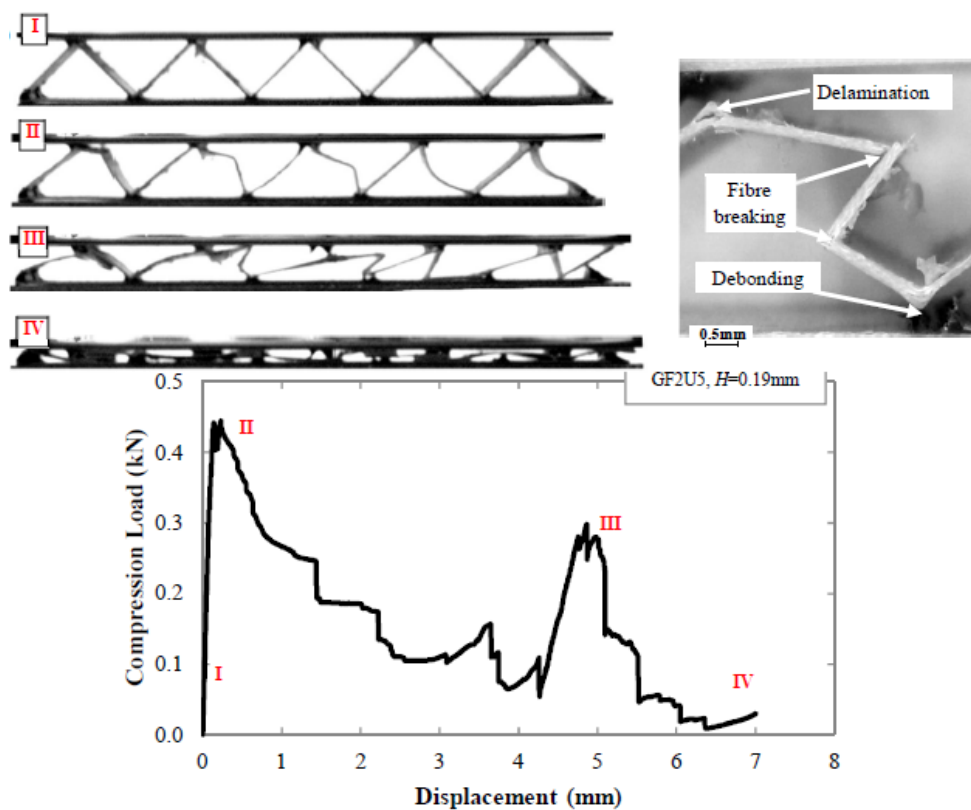


Figure 2.30: (a) Photographs of progressive damage development beside with (b) failure mode related to (c) load-displacement curve for a GFRP sandwich corrugated-core structure [28].

Notably, Figure 2.30 reveals that the debonding between core and skins occurred firstly, which led to the failure of corrugated-core sandwich structure. This evidence indicates that the bonding between skins and core needs to be improved. The bonding using adhesive agent introduced by Rejab et al. [28] was applied to all the corrugated-

cores sandwich structures. Figure 2.31 shows the debonding failure of the AL corrugated-core sandwich structures under quasi static compression as well as the failure of sandwich structures using GFRP material.

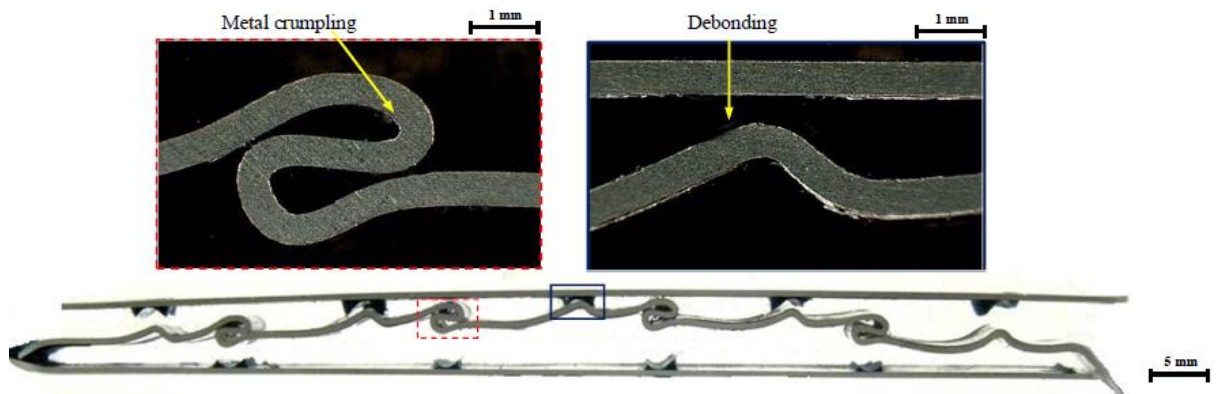


Figure 2.31: Post-damage photos of the AL corrugated-core sandwich structures [28]

The failure modes in the corrugated-core specimens were further investigated in the corresponding semi-filled and fully-filled specimens, as shown in Figure 2.32 and Figure 2.33. An examination of the filled specimens indicated that the foam was compressed and became thinner and left the cavities after crushed.

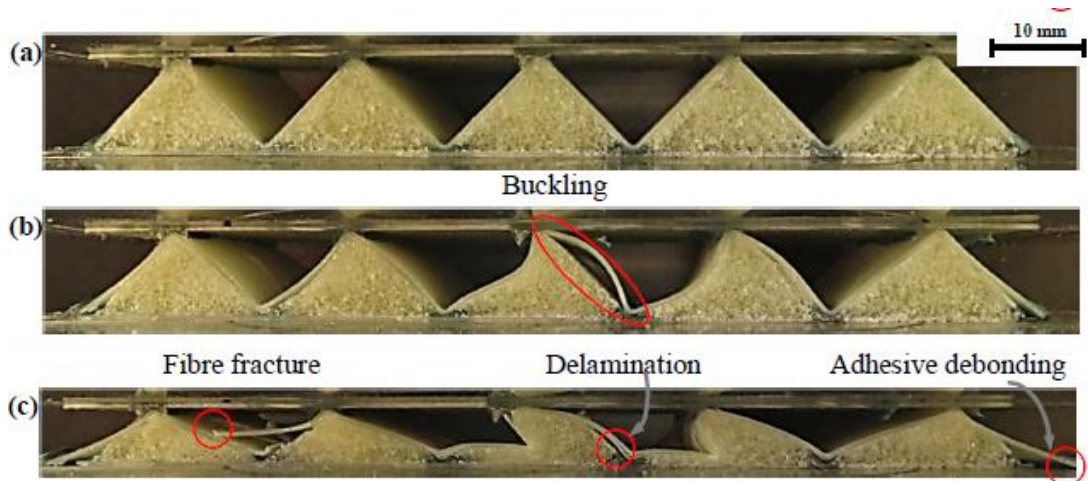


Figure 2.32: Photographs of progressive damage development in the GFPUS sandwich structure during (a) initial compression, (b) the buckling process and (c) the final stages of testing.

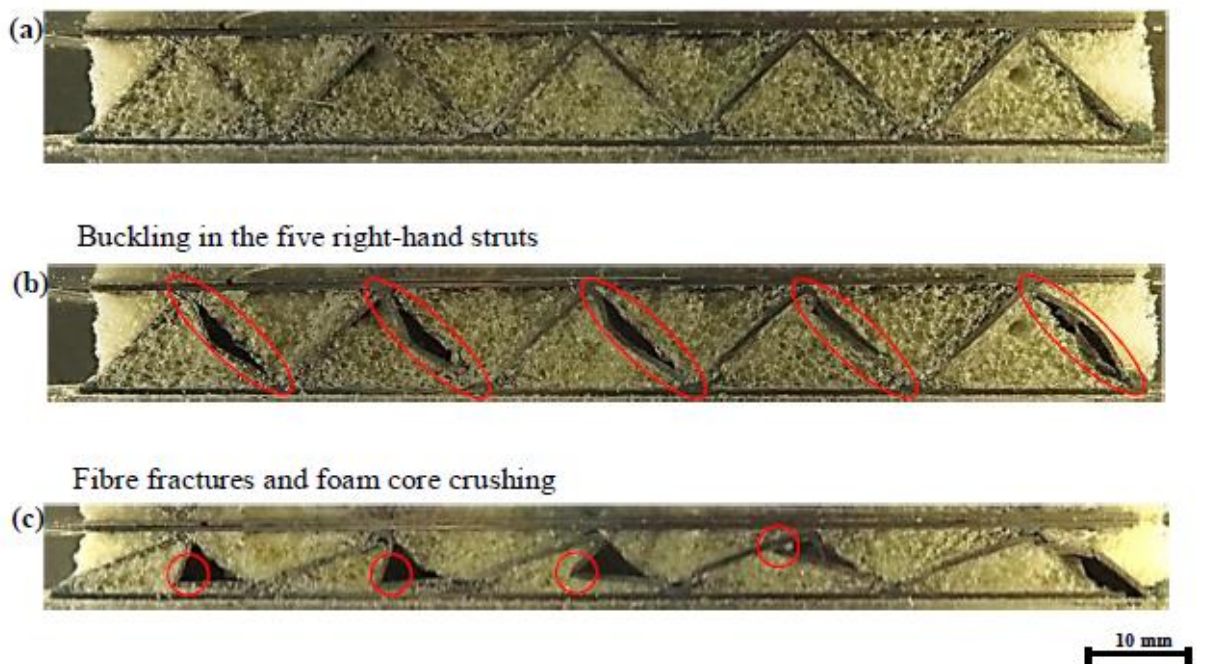


Figure 2.33: Photographs of progressive damage development showing the buckling failure from (a) initial compression, (b) buckling in the cell wall structure and (c) core crushing [28]

2.8.2 Failure mechanisms from dynamic loading

Russell et al. [30] revealed the micro-buckling failure mode of the E-glass composite sandwich structures, as shown in Figure 2.34. At higher applied strain rates the

response was reasonably rate insensitive with compressive crushing of the glass fibres being the dominant failure mode. They found that the foam filling did not have any significant effect on the measured responses.

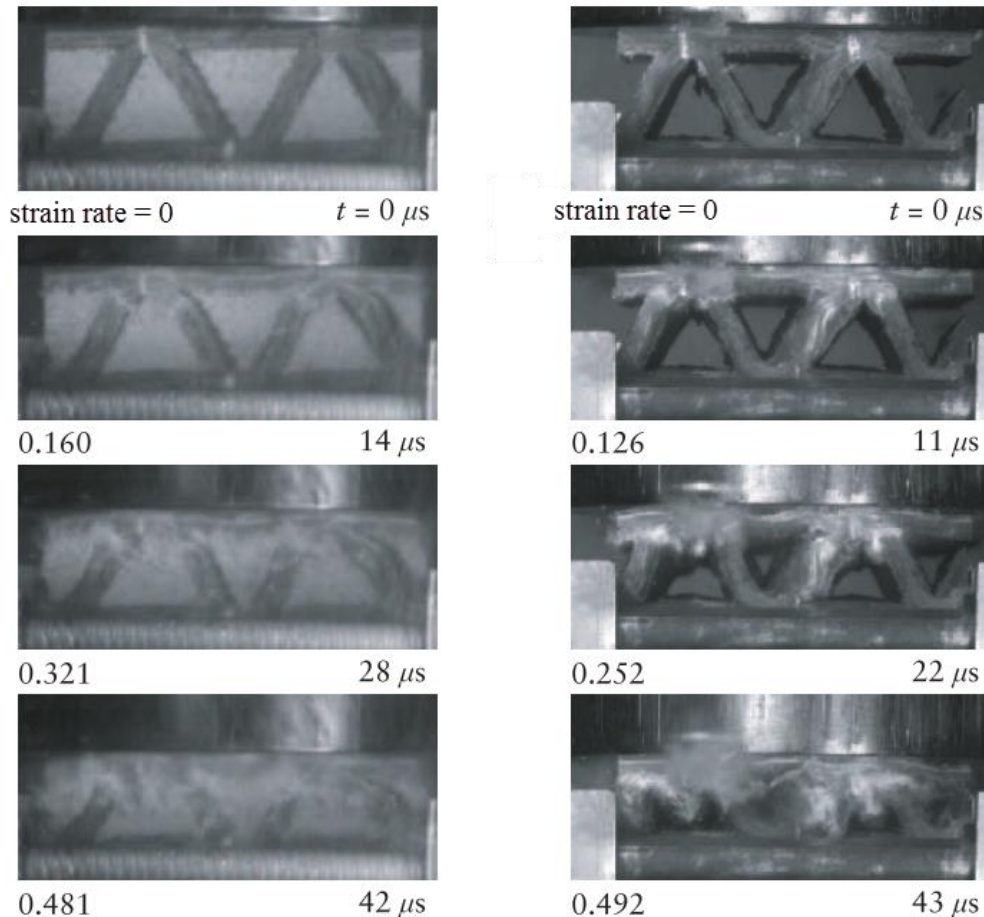


Figure 2.34: Deformation sequences in the filled (left) and unfilled (right) corrugated core specimens impacted at a velocity $v_0 = 150\text{ms}^{-1}$. Impact occurs on the top face of the specimens in the photographs [30].

Aktaş et al. [87] reported the experimental investigation of the impact response of composite laminates. They revealed the damage modes and the damage process of laminates under varied impact energies, as shown in Figure 2.35 and Figure 2.36. The primary damage mode was found to be fibre fracture for higher impact energies; whereas, it was indentation resulting in delamination and matrix cracks for smaller impact energies.



Figure 2.35: Bottom layer delamination and fiber failures [87]

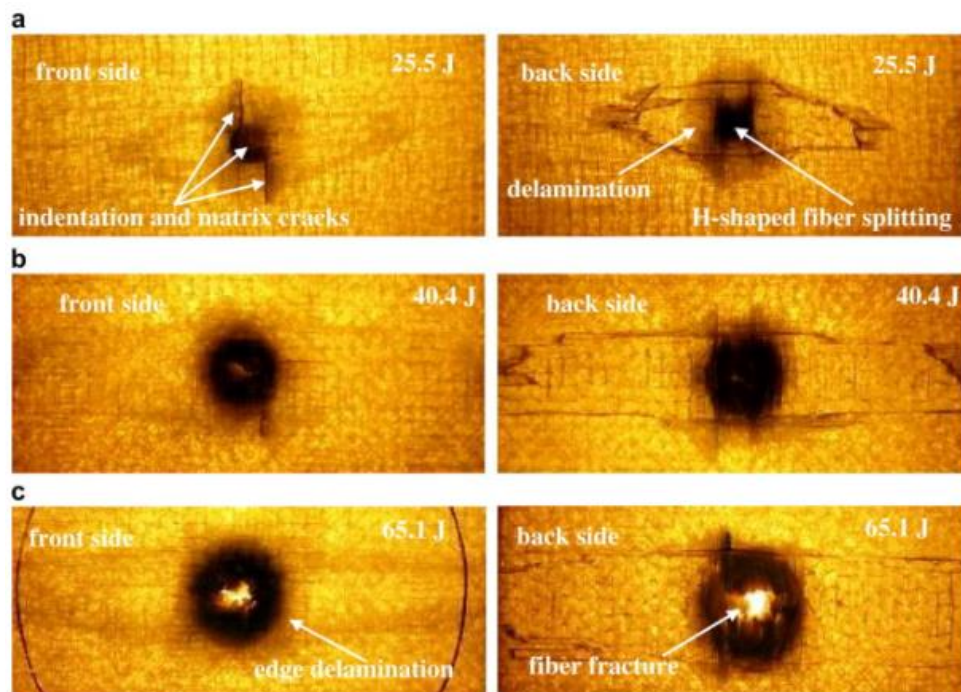


Figure 2.36: Some representative photographs of damaged samples taken with strong backlighting [87].

2.9 Summary of literature review

This chapter has presented a review of past and current research work relevant to this thesis. A brief overview is given on composite sandwich structures and classification using their core topology and cellular materials, e.g. foams, periodic cores. To make clear the understanding of the new hybrid sandwich structures, the background of corrugated-cores sandwich and fibre metal laminates was provided. Four main corrugated-core sandwich structures, i.e. Curvilinear, Straight, Hat-type and Triangular corrugated cores, have been reviewed, followed by the background and classification of fibre metal laminates. The mechanical response of corrugated-core sandwich structures under quasi-static and dynamic loadings has been discussed, alongside relevant research studies. Subsequently, the impact responses of the corrugated-core sandwich structures have been discussed. Finally, the procedures of modelling sandwich structural responses using commercially-available codes, and numerical modelling techniques have been reviewed, with examples of published numerical work.

The experimental work to be presented in the next chapter will cover a new technique of manufacturing and evaluation of the mechanical properties of hybrid corrugated-core sandwich structures reinforced with foam and designed with various core configurations. A number of tests, ranging from quasi-static compression to dynamic loading are presented, with the aim to understand the mechanical response, energy absorption and failure modes in these structures. Using analytical models and the finite element models, the predictions of the strength and stiffness of the structures are developed both in quasi-static as well as dynamic loading using parametric studies.

CHAPTER 3

EXPERIMENTAL PROCEDURE

This chapter gives a brief introduction on composite materials used to produce hybrid sandwich structures. The details of the manufacturing processes for producing the novel hybrid sandwich structures based on corrugated cores and fibre metal laminates (FMLs) are presented. Subsequently, the experimental work on compression, 3-point bending, dynamic perforation, flat-head compression, flat-head impact, hemisphere projectile impact and blast tests are reported. The final part of the chapter focuses on describing the optical microscopy techniques used to investigate the failure mechanisms in the hybrid sandwich structures subjected to various loading conditions.

3.1 Materials examined

In this section, the materials used in this study are described, which consist of aluminium alloy sheet, woven glass fibre prepregs and PVC foam to produce the hybrid sandwich structure specimens.

3.1.1 Aluminium 2024-T3

Aluminium alloy 2024 is an aluminium alloy consisted of 4.9% copper and 0.9% magnesium. It was introduced by Alcoa in 1931 as an AL clad sheet. T3 means using temper process. Aluminium alloy 2024-T3 is widely utilized in aircraft applications since it has superior mechanical properties and good machining characteristics when compared to other series. For this reason, aluminium alloy 2024-T3 has been selected for use in this study to produce the hybrid sandwich panels. It was supplied by Aerocom Metals Limited, Coventry, UK. When using aluminium alloy 2024-T3 to fabricate fibre metal laminates (FMLs) structures, the aluminium sheet surfaces were etched by well-known chemical etchant, ferric chloride (FeCl_3). This was done at Anodisers Runcorn Ltd, Runcorn, UK.

3.1.2 Glass fibre reinforced plastic (GFRP)

The glass fibre reinforced plastic (GFRP) used here was supplied by Gurit AG (Stesapreg EHG250-44-55). The density of the laminated GFRP is 1750 kg/m^3 . Prior to manufacture, the woven prepreg (four harness satin or Crowfoot) was cut to dimensions of 200 mm x 200 mm and then laid up, to give the required thickness. Sheets of thin (PP) films were then placed on each surface of the prepreg. The prepreg was subsequently placed in a Meyer hot press and heated to a temperature of 145°C under a pressure of 6 bar (0.6 MPa) for 90 minutes.

3.1.3 Core materials

Novel hybrid sandwich cores were designed uniquely by using embedded foams and corrugated composite beams. Four different types of cross-linked polymer foam that combine excellent stiffness and strength to weight ratios with superior toughness were used in this study. The PVC foams were supplied by Airex AG and Evonik Industry. Table 3.1 provides a summary of the relevant mechanical properties of the foams with a mass range of 55 to 200 kg/m³. Figure 3.1 shows the cross-linked polymer foam specimens and their appearance used for material tests.

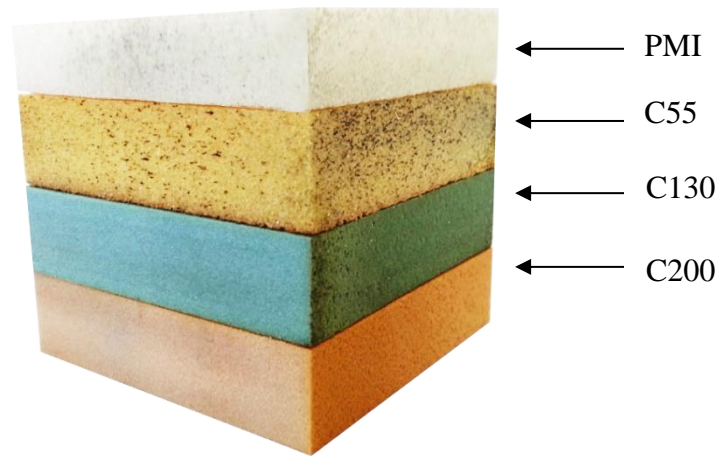


Figure 3.1: Cross-linked polymer foam specimens.

Table 3.1: Material properties of the foams [134, 135]

Properties	ROHACELL51 (PMI)	C70.55 (C55)	C70.130 (C130)	C70.200 (C200)
Density (kg/m ³)	52	60	130	200
Thickness (mm)	20	20	20	20
Compressive strength (MPa)	0.8	0.90	3.0	5.2
Compressive modulus (MPa)	75	69	170	280
Shear strength (MPa)	0.8	0.85	2.4	3.5
Shear modulus (MPa)	24	22	54	75
Thermal conductivity (W/mK)	0.031	0.031	0.039	0.048
Colour	White	Yellow	Blue	Brown

3.1.4 Fibre metal laminates (FMLs)

Fibre metal laminates (FMLs) consist of several thin metal layers bonded with layers of composite material, which form a laminated structure [136]. The aluminium 2024-T3 and woven glass fibre resin plastic prepregs were used. In this study, the FMLs were manufactured to be a pair of skins and beam core of hybrid sandwich structures by using hot press technique under a pressure of 2.5 bar and heated to a temperature of 125 °C, at a rate of 3°C/min. Stacking sequences of multilayer configurations were ranged from a simple 2/1 (Al-GFRP-Al) to a 4/3 (Al-GFRP-Al-GFRP-Al-GFRP-Al) laminate. For example, a lay-up of FMLs 3/2 as shown in Figure 3.2 [68].

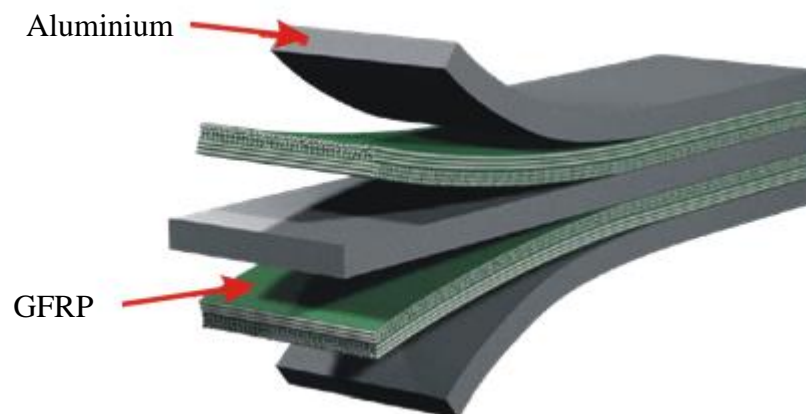


Figure 3.2: A typical fibre metal laminates 3/2 [4]

3.2 Manufacturing methods

This study has been undertaken on the basis of the previous research, entitled ‘The mechanical properties of novel lightweight structures based on corrugated-cores’, by Dr R. Rajab [28]. New manufacturing and fabrication techniques have been proposed and developed in the current study. The previous research had used the Alradite 420 adhesive as a bonding agent between the sandwich core and its skins. It was found that the quality of gluing caused an initial weak point and led debonding. As a result, such an unsatisfactory sandwich structure had a premature failure with weak mechanical

properties. Furthermore, the previous conventional manufacturing technique had many fabrications and was a time-consuming process. Therefore, the new fabrication technique has been developed in order to reduce processing time by using one- go fabrication by hot press machine. The highlight of the new technique is to bond the sandwich skins and its core to form one piece homogeneously under appropriate pressure and temperature. The improved bonding quality could be revealed by showing better mechanical properties and bonding strength between sandwich skins and core.

3.2.1 Design of corrugated cores

The preceding literature review has highlighted the fact that most of the previous studies have used a 45° triangular profile in the corrugated structure. Therefore, a similar triangular corrugated core has been chosen for the sandwich structures in this research.

The corrugated-cores were prepared using a mould with a 45° triangular profile. The mould has dimensions of 210x240 mm. Figure 3.3 shows the moulds which were made from mild steel. Each unit cell has a nominal height of 10 mm and a base of 20 mm. The female mould (the lower profile) was used to hold the composite prepreg (or flat material) and the male mould (the upper profile) pressed the material to form the shape of a triangular profile.

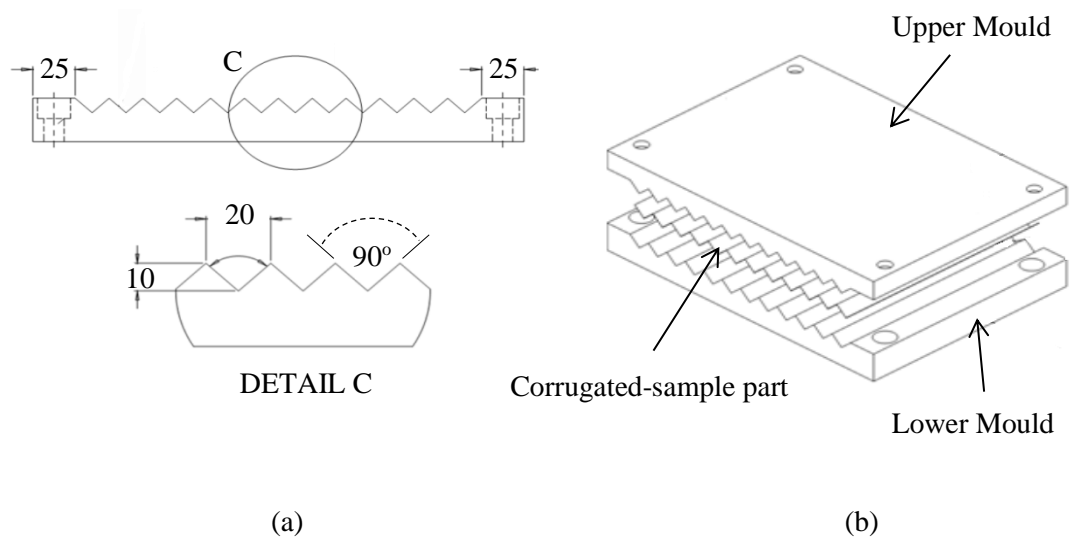


Figure 3.3: The triangular corrugated core moulds. (a) Drawing design with dimensions, (b) Assembly showing the core sample, (c) Images of the lower and upper moulds

3.2.2 Fabrication processes

The fabrication processes of the designed corrugated structures are listed as follows.

- Prism foam cores were prepared by cutting the foam panel using a band saw machine to the required dimensions, depend on type of sample; for example, 20x200 mm (base x length of prism) as shown in Figure 3.4.
- The glass fibre reinforced plastic (GFRP) prepreg as described in Section 3.1.2



Figure 3.4: Foam core elements cut into a prism shape.

was cut to a smaller piece (200x1200 mm) from the roll. Its width and length were the same as the dimensions of the foam prism and the roll's height respectively.

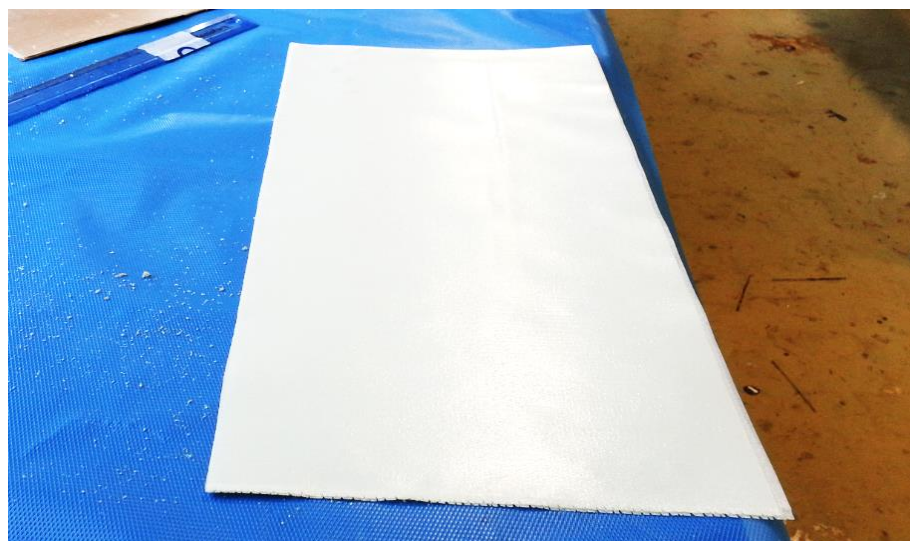


Figure 3.5: The prepared GFRP cut into a required dimension.

- Each prism was then wrapped by GFRP prepreg along the GFRP's length direction until meet the dimension of the hot press platen area. Figure 3.6 shows how the foam core prisms were wrapped by the GFRP woven prepreg

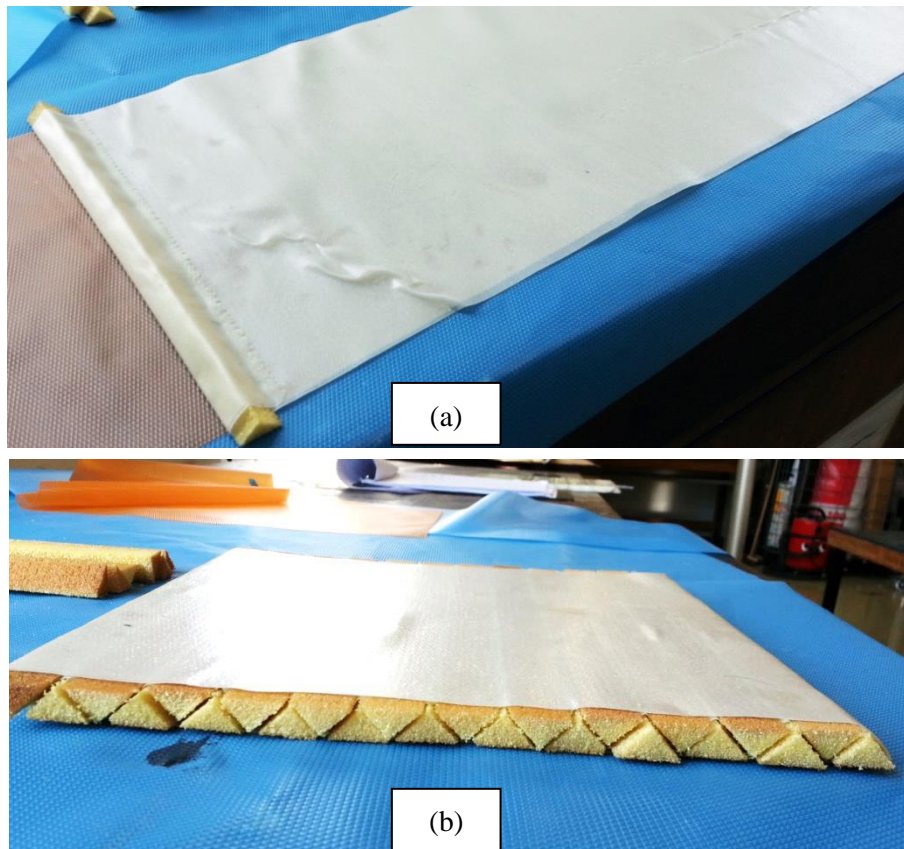


Figure 3.6: The prism foam core elements are wrapped into GFRP woven along the 0/90° direction. (a) The first prism was wrapped, (b) become a panel.

- The panel was then placed between the upper and lower platens of the hot press. The surfaces of sample panel were separated from the mould platens by using polytetrafluoroethylene (PTFE) coated glass cloth heat sealing tape from PAR-group Ltd [137] to ensure that the samples could be easily demoulded after curing. Figure 3.7 shows the sample panel placed between the upper and lower platens of Meyer hot press machine. A thermocouple was used to

monitor the operating temperature in the middle of the panel to ensure that the curing process followed the manufacturer's recommendations.

- The curing cycle is shown in Figure 3.9. The GFRP woven prepreg was cured

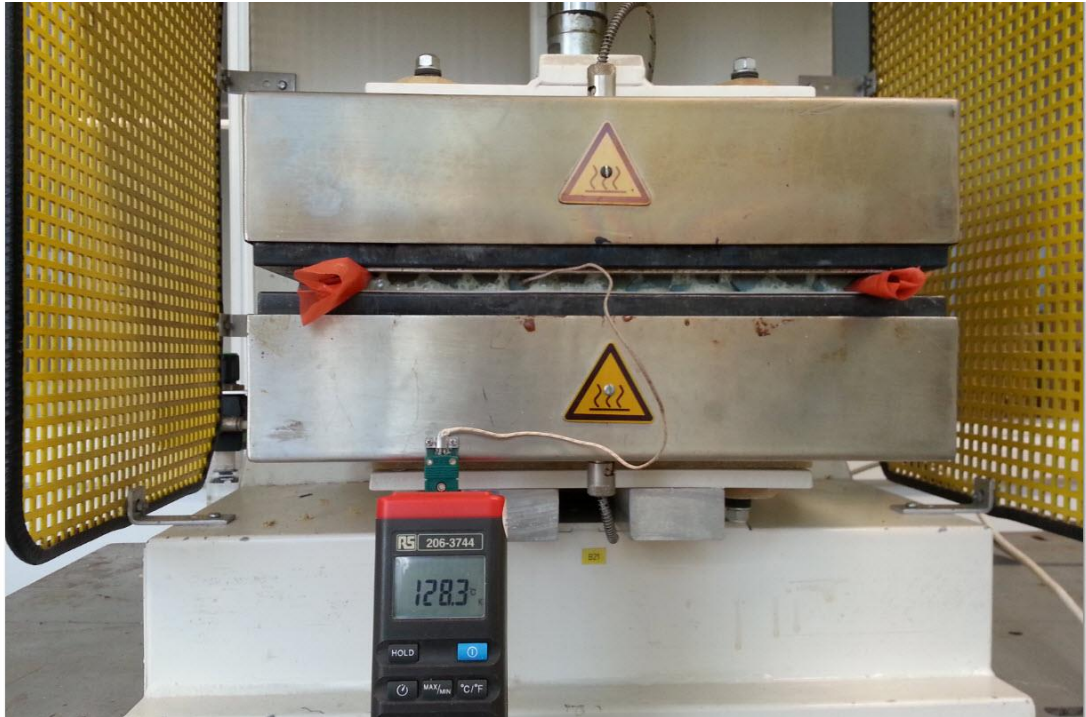


Figure 3.7: Shows the sample panel placed between upper and lower platens of Meyer hot press machine and the thermocouple displaying the operating temperature on the screen.

under an applied constant pressure between 2.5 and 3 bar and a curing temperature (T_c) between 120 and 160 °C with a dwell time (T_{dwell}) of 90 minutes. A heating rate of 3 °C/min was used, before cooling down to the room temperature at the cooling rate of 4 °C/min. The panel was removed after the temperature was below 60 °C. Figure 3.8 shows the corrugated light-weight panels after cured from hot press.

- The sample panel was then cut to the required sample dimensions for testing as shown in Figure 3.10.



Figure 3.8: The sample panels after cured from hot press process.

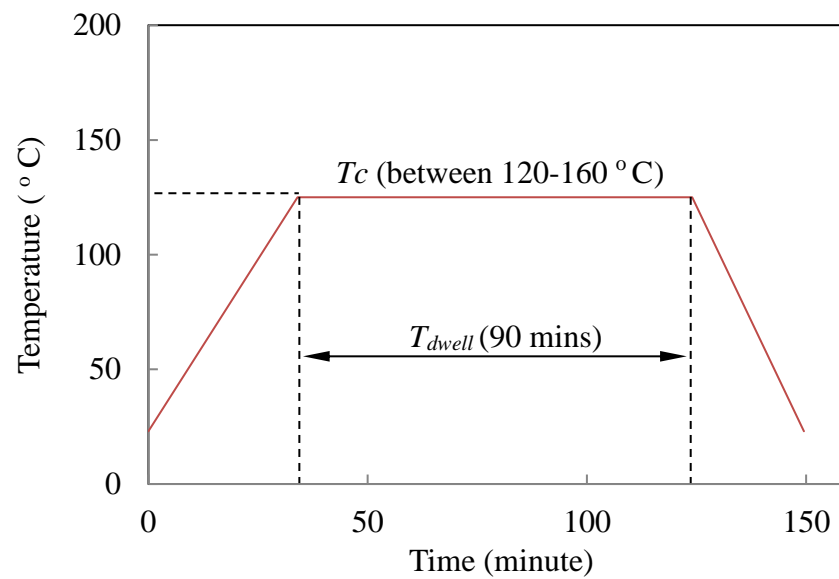


Figure 3.9: Time and temperature of curing profile during hot press process.



Figure 3.10: The samples ready for testing.

3.3 Test specimens and configurations

In order to study the potential of hybrid sandwich structures in particular for use in the maritime, aerospace and infrastructure industries, a number of design parameters, such as the structural configuration, the GFRP core thickness, the type of foam core and the unit cell size, have been studied to investigate their effects on the structural response related to quasi-static and dynamic loading. In the initial part of this section, the basic sample dimensions are illustrated as shown in Figure 3.11. Then the next section describes in detail of the parameters studied. Notably, there are at least 8 samples for each group being prepared. Therefore, at least 3 identical samples were tested for each case under the quasi-static and dynamic loading, respectively.

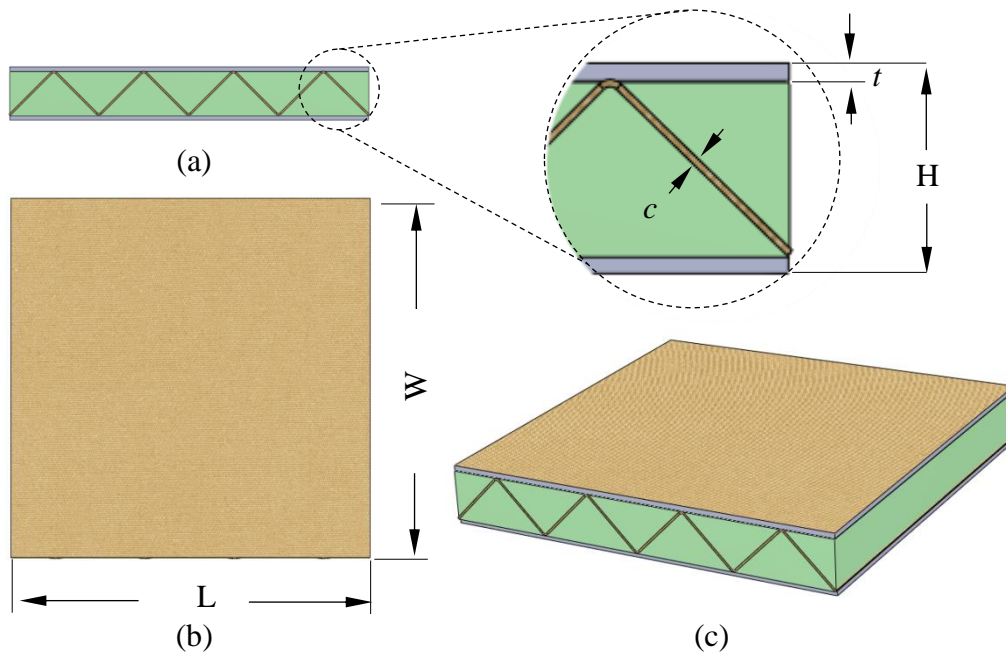


Figure 3.11: Dimensions of a typical specimen (a)Front, (b) Top, (c) perspective.

3.3.1 The effect of the core thickness of plain GFRP corrugated sandwich structures

GFRP triangular corrugated sandwich structures without embedded foam were produced to have different core sheet thickness by increasing the number of plies. Here, four core thicknesses, 0.23, 0.45, 0.71 and 1.05 mm were fabricated from 2, 4, 6, 8 plies respectively. There were again 8 samples for each group prepared including two spare samples. All the sample skins were manufactured using 4 plies of GFRP with a total thickness of 0.5 mm. In order to manufacture the GFRP corrugated sandwiches, the triangular corrugated core moulds (Figure 3.3) were used. The plain GFRP core was then fabricated with the GFRP woven prepreg which were cured to be the top and bottom skins between hot press platens. Figure 3.12 shows an image of a GFRP triangular corrugated sandwich sample with its ID definition show in Table 3.2.



Figure 3.12: Photograph of a plain GFRP triangular corrugated sandwich structure without an embedded foam.

Table 3.2: The plain GFRP corrugated sandwich samples made with various core thicknesses.

Sample ID		Sample ID definition and dimensions					
GFR 2P 01		GFRP triangular corrugated sandwich structure without foam					
		Glass Fibre reinforced plastic					
		Number of plies					
		Sample number					
No.	Samples ID	Dimensions			Weight (w)	Avg core thickness (c)	Avg skin thickness (t)
		Length (L)	Width (W)	Thickness (H)			
		(mm)	(mm)	(mm)	(g)	(mm)	(mm)
1	GFR2P	81.61	80.90	10.07	17.95	0.23	0.50
2	GFR4P	78.72	80.14	10.40	20.45	0.45	0.50
3	GFR6P	80.11	79.24	10.12	22.70	0.71	0.50
4	GFR8P	80.17	79.78	10.77	41.50	1.05	0.50

3.3.2 Different core configurations

Three types of core configurations, i.e. triangular, trapezoid and square shapes, were considered in the study. Here, using a hybrid core means the corrugated beam core would be combined with the embedded prism foam or FML structures. Using foam prisms embedded with GFRP sheets as the whole core could accelerate time with a good advantage on the fabrication. To produce the core, the steel moulds were needed

3.3.3 Various core thickness of GFRP corrugated reinforced foam core

The samples as discussed in Section 3.3.1 were examined. However, the samples in this section contained embedded PMI foam, as shown in Figure 3.14. The embedded foam core sandwich samples were then compared to the pure conventional foam core sandwich samples in group PMIOP. The details of samples in each group are shown in Table 3.4.

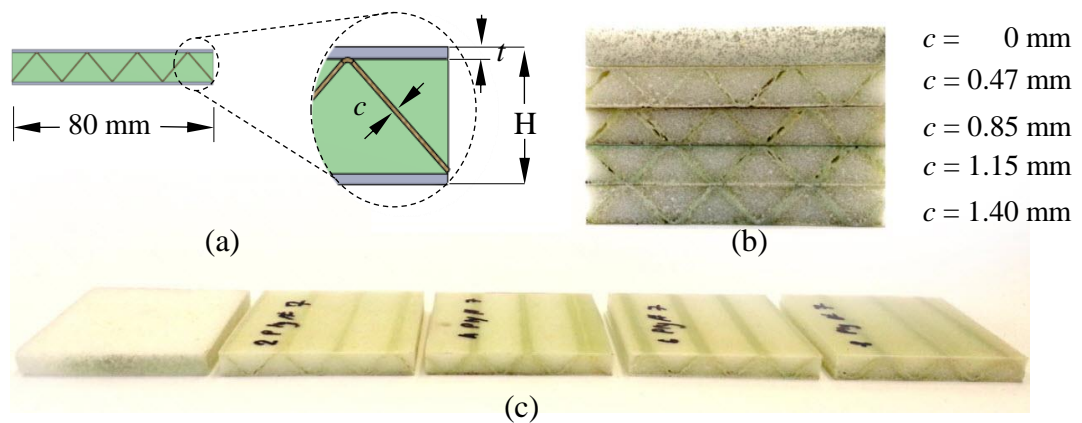


Figure 3.14 : The hybrid sandwich samples in different GFRP corrugated core thickness. (a) Schematic in side view, (b) GFRP core hickness values, (c)The samples in perspaective

Table 3.4: Samples with different GFRP core thicknesses

Sample ID	Sample ID definition and dimensions						
<u>PMI 2P 01</u>	GFRP corrugated sandwich structure embedded with foam core						
	Embedded core using PMI foam						
	Number of ply						
	Sample number						
No.	Samples ID	Dimensions			Weight (w) (g)	Avg core thickness (c) (mm)	Avg skin thickness (t) (mm)
		Length (L)	Width (W)	Thickness (H)			
		(mm)	(mm)	(mm)			
8	PMIOP	80.63	78.47	10.09	3.55	0.00	0.57
9	PMI2P	80.53	80.32	10.52	14.80	0.47	0.53
10	PMI4P	80.31	80.18	10.03	19.30	0.85	0.53
11	PMI6P	80.45	80.04	10.34	27.90	1.15	0.57
12	PMI8P	80.33	79.53	10.96	30.10	1.40	0.58

3.3.4 Different types of foam cores

Six types of samples were investigated to assess the effect of different types of foam cores on the corresponding structural performance. Figure 3.15 shows the images of the hybrid sandwich samples based on those foam cores with their sample ID definitions being given in Table 3.5. The control variables in this study contain the design of 4 plies of GFRP corrugated core and their skins as before.

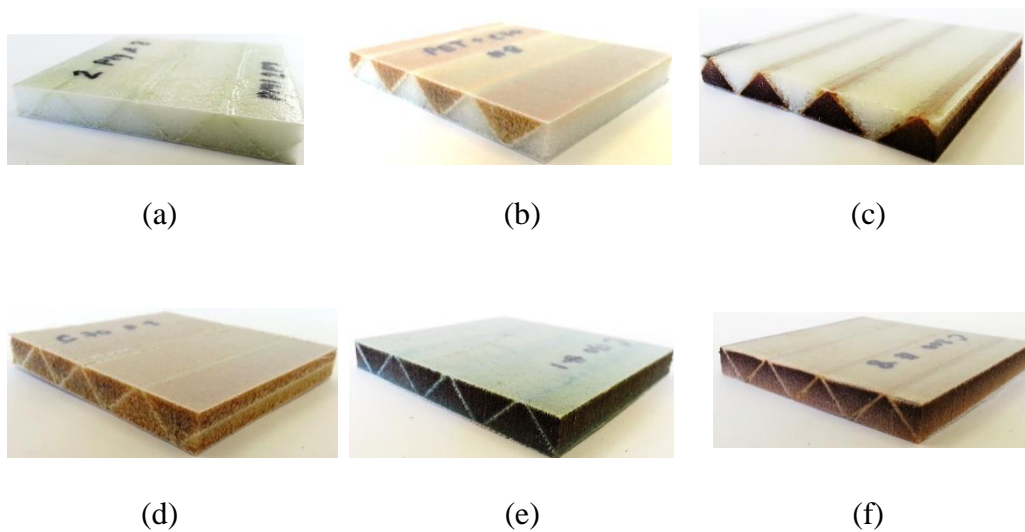


Figure 3.15: Hybrid sandwich samples with different types of foam cores. Foam cores using (a) PMI used in group PMI4P, (b) combination of PMI and C70.55 used in group PC54P, (c) combination of PMI and C70.200 used in group PC24P, (d) C70.55 used in group C554P, (e) C70.130 used in group C134P, (f) C70.200 used in group C204P.

Table 3.5: Samples made with foam core of various densities

Sample ID		Sample dimensions					
PMI 2P 01 		GFRP triangular corrugated sandwich structure embedded foam core					
		Embedded core using PMI= PMI foam, PC5= combine PMI+C70.55, PC2 = combine PMI+ C70.200, C55 = C70.55, C13 = C70.130, C20 = C70.200.					
		Number of ply					
		Sample number					
No.	Samples ID	Dimensions			Weight (<i>w</i>)	Avg core thickness (<i>c</i>)	Avg skin thickness (<i>t</i>)
		Length (L)	Width (W)	Thickness (H)			
		(mm)	(mm)	(mm)	(g)	(mm)	(mm)
13	PMI4P	80.32	80.19	10.15	19.04	0.44	0.57
14	PC54P	80.32	80.48	9.58	15.85	0.41	0.56
15	PC24P	80.44	80.19	9.98	18.55	0.50	0.56
16	C554P	80.32	80.20	10.20	15.10	0.45	0.60
17	C134P	79.57	80.37	9.87	19.60	0.42	0.54
18	C204P	80.43	80.40	9.91	21.90	0.42	0.51

3.3.5 Samples with different foam core densities and multi-layer

A range of hybrid sandwich panels was designed to investigate the effect of different foam core densities and multi-layer designs on their structural response. There were two sample types, homogeneous and graded core density, as shown in Figure 3.16 and their details are given in Table 3.6. The multi-layer with homogenous density samples were created using foam type C70.55 as the core which has the density of 60 kg/m^3 . Each layer was oriented and referenced by corrugated direction ($0^\circ/90^\circ/0^\circ$). The multi-layer with graded core density samples were created using 3 different foam core densities with foam type C70.55 at the top surface, C.130 at the middle, and C.200 at the bottom surface. The core density is 60 kg/m^3 from the top surface where the impact load from impactor would first interaction with the sample and 200 kg/m^3 at the bottom.

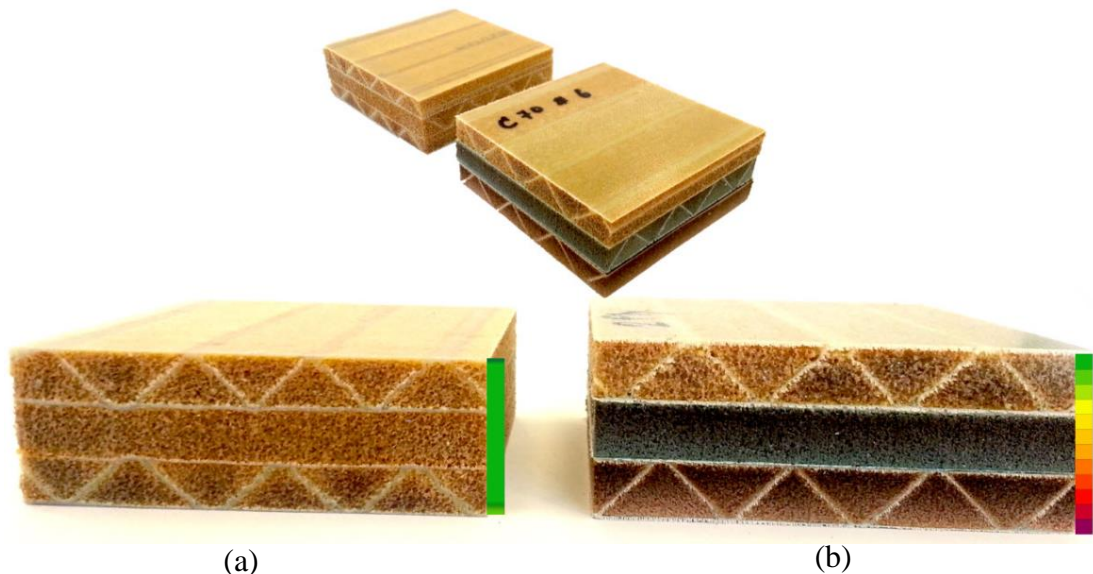


Figure 3.16: Photographs of the hybrid sandwich samples showing in different foam core densities. (a) Multi-layers with homogeneous density, (b) Multi-layers with graded foam core created using foam types, C70.55, 130, 200, from the top surface to bottom.

Table 3.6: Samples with multi-layer cores

Sample ID		Sample ID definition and dimensions					
C55 H 01 → → → →		Hybrid sandwich panel with multi-layer and core density					
		Embedded foam core using C55=Airex C70.55, CMX= combine C70.55, 130, 200, from top to bottom					
		Type of core density (H= Homogeneous, G= Gradient)					
		Sample number					
No.	Samples ID	Dimensions			Weight (w)	Avg core thickness (c)	Avg skin thickness (t)
		Length (L)	Width (W)	Thickness (H)			
		(mm)	(mm)	(mm)	(g)	(mm)	(mm)
19	C55H	79.79	79.36	27.10	50.35	0.43	0.55
20	CMXG	80.00	79.25	33.78	79.05	0.48	0.58

3.3.6 Samples with different unit cell sizes

This section gives the details of the samples used to study the effect of the unit cell size, as shown in Figure 3.17 and Table 3.7. Due to their different sizes, the performance of the panels was assessed by considering their specific energy absorption. The Airex C70.55 foam was used for all samples. The technique used to fabricate the samples was to cut different sized prism foams having heights of 10, 14 and 20 mm and base line of 20, 28 and 40 mm, respectively.

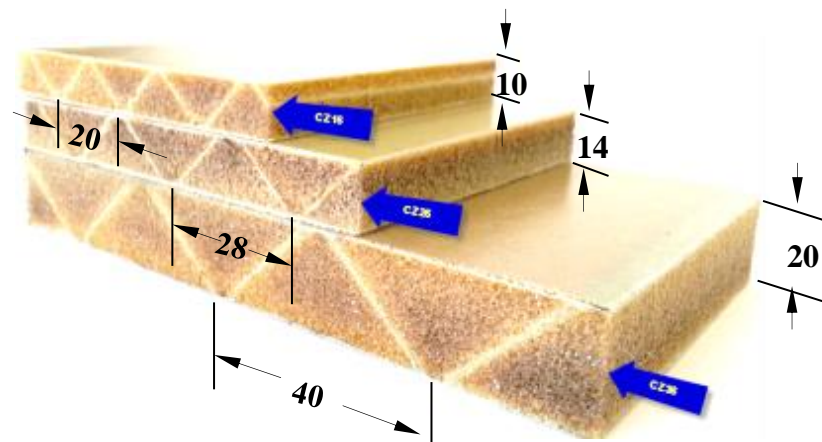


Figure 3.17: Photograph of the hybrid sandwich samples showing the different sizes of the unit in mm.

Table 3.7: Samples with different unit sizes

Sample ID	Sample ID definition and dimensions						
C55 Z2 01	Hybrid Sandwich GFR triangular core + prism Foam						
	Foam core embedded using Airex C70.55						
	Group size						
	Sample number						
No.	Samples ID	Dimensions			Weight (w) (g)	Avg core thickness (c) (mm)	Avg skin thickness (t) (mm)
		Length (L) (mm)	Width (W) (mm)	Thickness (W) (mm)			
21	C55Z1	80.44	79.86	10.24	15.20	0.43	0.55
22	C55Z2	80.38	100.16	15.47	33.50	0.40	0.51
23	C55Z3	80.74	140.86	20.12	53.20	0.40	0.56

3.3.7 Samples with different number of core layers

Three types of sample based on 1, 2 and 3 layers are described in this section. The manufacturing method used to produce the samples involved placing corrugated core on each layer as $0^\circ/90^\circ/0^\circ$. Airex C70.55 foam was used for the entire structure. Figure 3.18 shows the images of the samples. The sample dimensions and other details are displayed in Table 3.8.

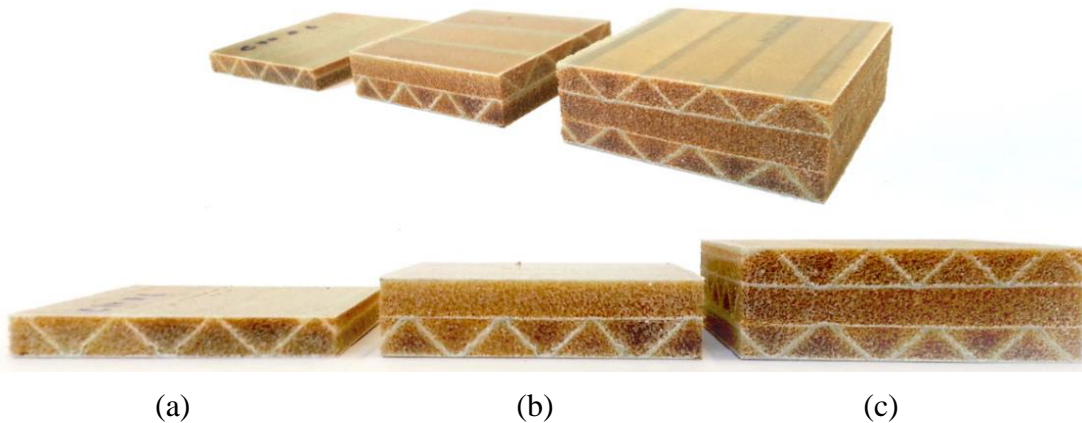


Figure 3.18: Images of the hybrid sandwich samples in different layers. (a) 1, (b) 2, (c) 3 layers.

Table 3.8: Hybrid corrugated sandwich panels with increased core layer.

Sample ID		Sample ID definition and dimensions					
C55 L2 01		Hybrid Sandwich GFR triangular core + prism Foam					
		Foam core embedded using Airex C70.55					
		Number of layer					
		Sample number					
No.	Samples ID	Dimensions			Weight (w) (g)	Avg. core thicknes s (c) (mm)	Avg. skin thicknes s (t) (mm)
		Length (L)	Width (W)	Thickness (H)			
		(mm)	(mm)	(mm)			
24	C55L1	80.32	80.20	10.20	15.10	0.48	0.58
25	C55L2	79.66	79.89	19.26	34.70	0.50	0.55
26	C55L3	79.82	79.74	27.77	52.75	0.43	0.59

3.3.8 Sandwich structures based on FML cores

Six types of samples were prepared to investigate the potential offered by using FML cores with and without foam embedded as shown in Figure 3.19. The sample dimensions and other details are shown in Table 3.9. In order to produce FML samples, firstly, corrugated aluminium 2024 T3 sheet was pressed to form the corrugated shape, which was then fabricated with the other constituent parts using the developed technique method as described in Section 3.2.2.

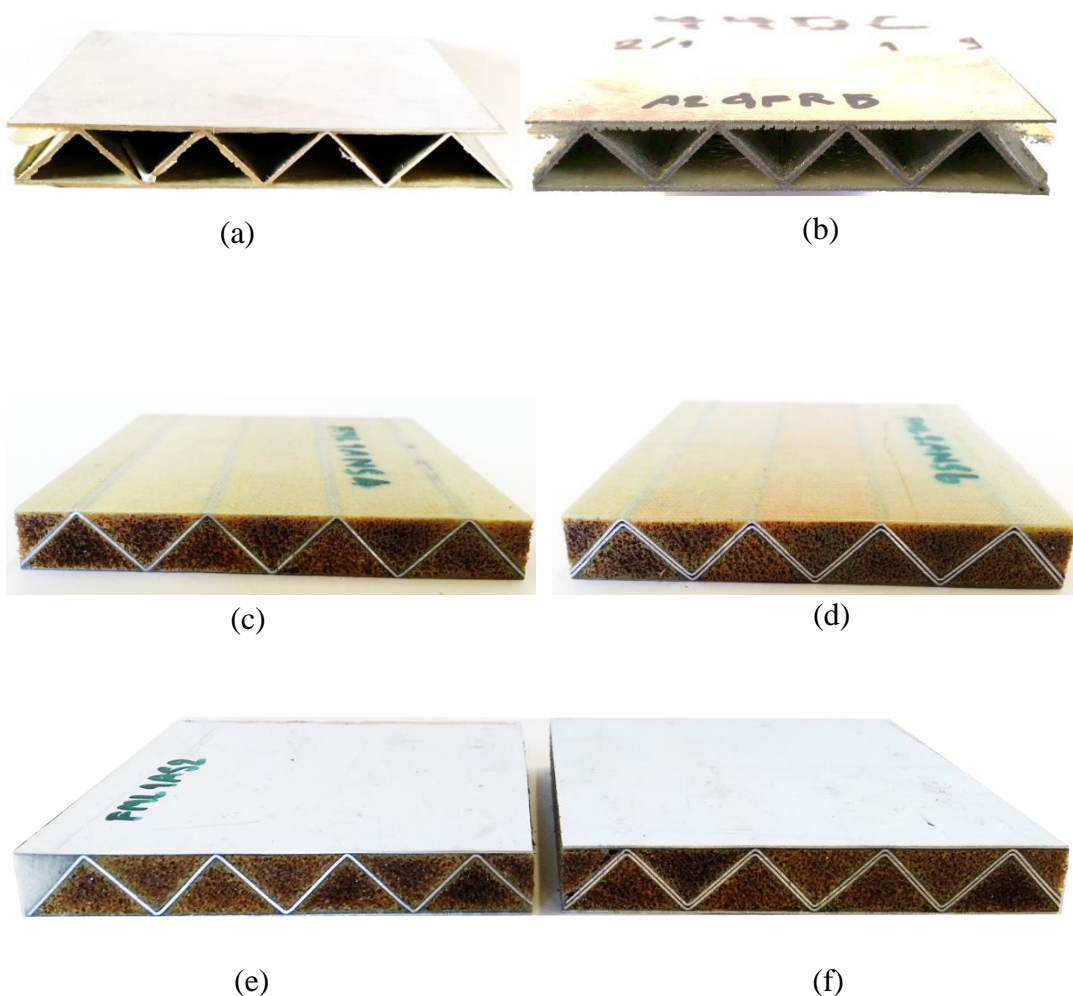


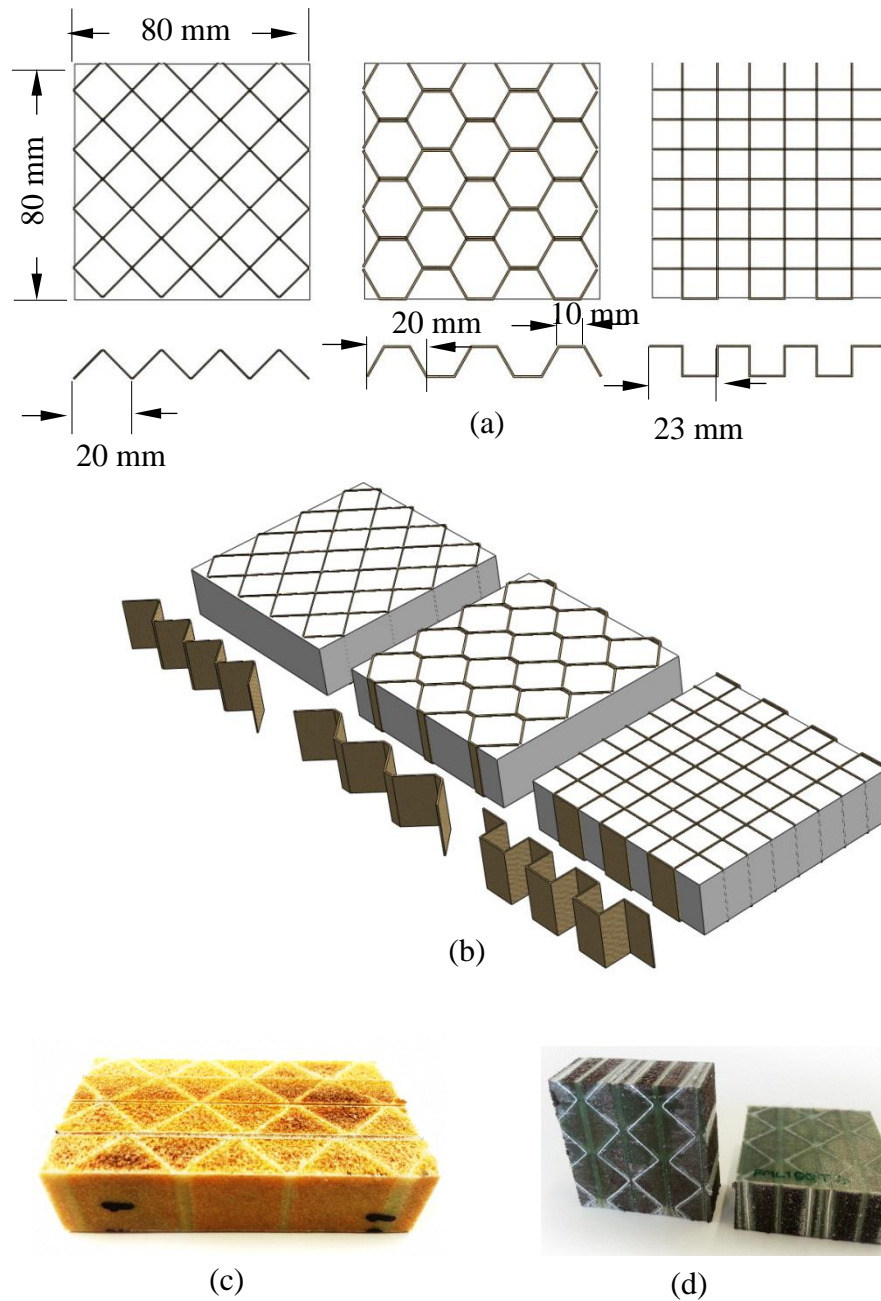
Figure 3.19: Photographs of the hybrid sandwich samples using FMLs as core or skins. (a) Group FA10Sx, (b) Group FA20Sx, (c) Group FA1E0x, (d) Group FA2E0x, (e) Group FA1ESx, (f) Group FA2ESx

Table 3.9: The corrugated sandwich structures made with FML cores

Sample ID		Sample ID definition and dimensions					
F A1 E S 1							
		Type of core(A1= 1 layer of Al, A2= FML 2/1)					
		Core embedded Foam(E= Yes, 0= No)					
		Skin type (S= FML 1/1, N= Only 4 Plies GFRP)					
		Sample number					
No.	Samples ID	Dimensions			Weight (w) (g)	Avg core thicknes s (c) (mm)	Avg skin thicknes s (t) (mm)
		Length (L)	Width (W)	Thickness (H)			
		(mm)	(mm)	(mm)			
27	FA10SX	78.07	79.56	10.56	31.30	0.40	0.85
28	FA20SX	83.42	79.35	11.61	45.10	1.12	0.85
29	FA1E0X	79.61	78.34	10.43	27.70	0.67	0.59
30	FA2E0X	79.69	79.80	11.33	42.50	1.50	0.55
31	FA1ESX	79.85	79.65	11.10	44.75	0.80	1.20
32	FA2ESX	79.69	78.93	12.07	55.20	1.50	1.20

3.3.9 Cores with vertical reinforcements

The literature review has highlighted the fact that the sandwich structures which consist of a vertical orientation core, for example honey comb core sandwich structures, would offer good energy absorption. Therefore, the behaviour of cores with a vertical orientation is to be investigated in the study. Here, three types of sample shape similar to that shown in Section 3.3.2 were fabricated. Figure 3.20(a) shows the constituent parts containing different configurations of the core, i.e. triangular, trapezoid and square shapes. Then parts were fabricated by orienting the GFRP core in the vertical direction. An additional technique was applied in this fabrication by using the square steel frame to apply the pressure at four edges of the panel during hot press process. The finished samples are shown in Figure 3.20 and sample dimensions in Table 3.10



(c) (d)
 Figure 3.20: Schematic of the hybrid sandwich samples fabricated with vertical orientation and photos. (a) Top view of triangular, trapezoidal and square samples with their unit cells below, (b) Perspective (c) photo of groupTRIT sample, (d) image of the FMLT sample

Table 3.10: Samples of the sandwich with vertical corrugated reinforcement.

Sample ID		Sample ID definition and dimensions					
TRI T 01							
No.	Samples ID	Dimensions			Weight (w)	Avg core thicknes s (c)	Avg skin thicknes s (t)
		Length (L)	Width (W)	Thickness (H)			
		(mm)	(mm)	(mm)	(g)	(mm)	(mm)
33	TRIT	79.86	80.15	20.14	15.25	0.46	0.52
34	TRAT	79.89	80.10	20.19	19.18	0.48	0.55
35	SQAT	79.89	80.14	20.17	21.14	0.40	0.59
36	FMLT	50.44	50.26	20.12	24.55	0.86	0.50

3.4 Mechanical tests of the plain composite, metal and FMLs

3.4.1 Tensile tests on the aluminium alloy

A series of quasi-static tensile tests were conducted using a screw-driven universal Instron 4204 testing machine. A standard dog-bone shaped aluminium specimen was prepared based on the standard methods for tension testing of metallic materials ASTM E8/E8M – 16a [138], as illustrated in Figure 3.21. The dimensions of the specimen were 20 mm x 150 mm and a nominal thickness of 0.4 mm. The tensile tests were carried out at a crosshead speed of 1 mm per minute until fracture. An extensometer with the original gauge length, $GL = 50$ mm, was attached onto the specimen to record the extension. At least three repeated tests were performed in order to obtain reliable data.

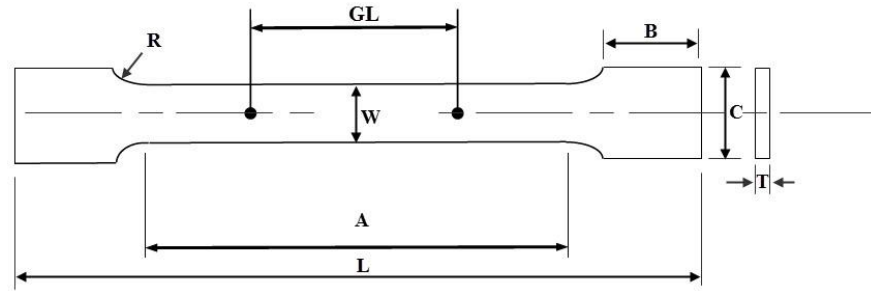


Figure 3.21: The sample dimension of the tensile metal specimen.

3.4.2 Tensile tests on the composites

Woven GFRP samples were also tested in tension in accordance with the standard BS 527-4 [139]. The dimensions of the specimen were 25 mm x 250 mm and a nominal thickness of 5 mm, as shown in Figure 3.22. Aluminium end-tabs were bonded to the specimen for proper gripping and to ensure failure in the gauge length.

Figure 3.23 shows the tensile test set-up on the GFRP composite sample. Again the same extensometer with a gauge length, $GL = 50$ mm was attached to the specimen in the longitudinal direction. Tests were undertaken at a constant crosshead moment of 1 mm per minute.

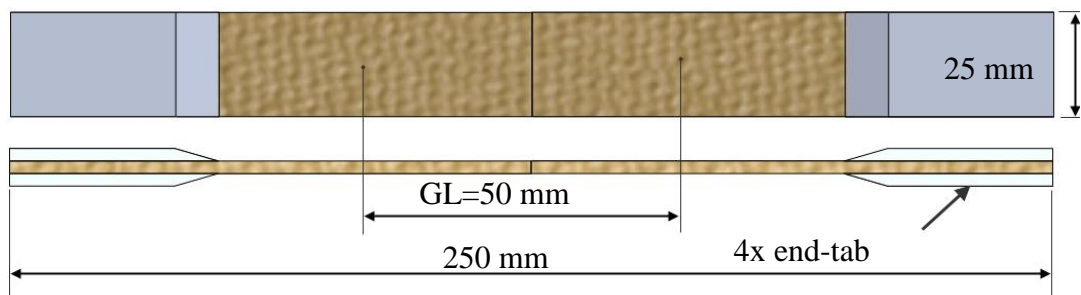


Figure 3.22: Tensile test geometry for a composite specimen.



Figure 3.23: Instron 4204 universal testing machine and mechanical extensometer.

3.4.3 In-plane shear tests on composites

To obtain the shear strength and shear modulus values, a series of in-plane shear tests were undertaken on the composites. The tests were carried out using the Instron 4204 tensile testing machine on the composite specimens with the same sample dimensions, set-up and procedure outlined in Section 3.4.2. The specimens were prepared by orientating the plies at $\pm 45^\circ$, as shown in Figure 3.24 and Figure 3.25, then cutting to the dimensions of the standard test, BS 527-4 discussed above.

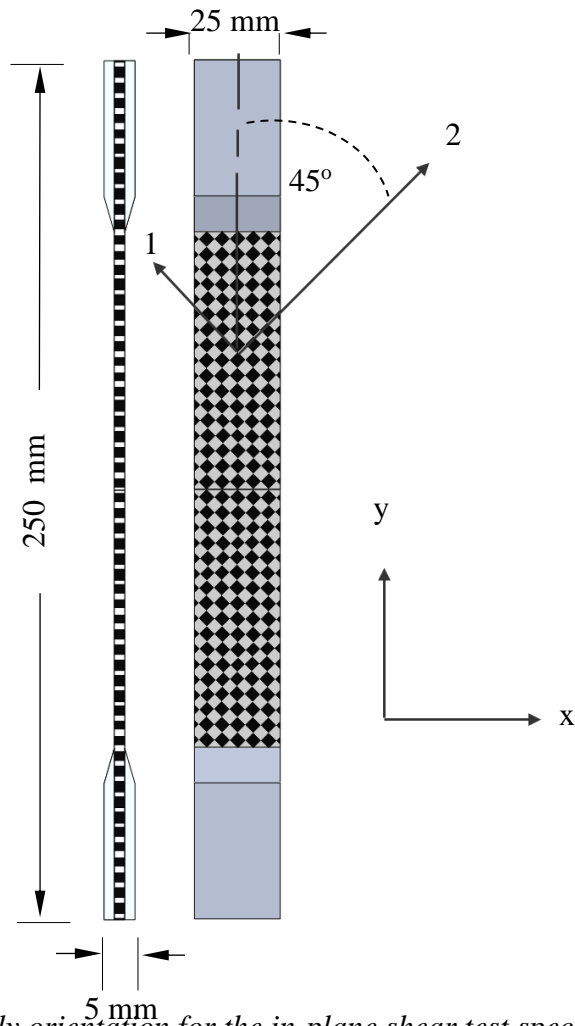


Figure 3.24: Ply orientation for the in-plane shear test specimens.

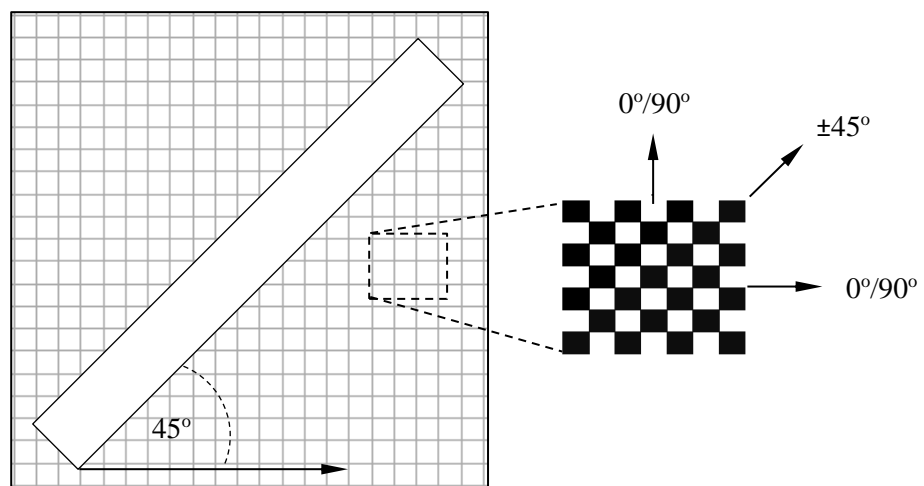


Figure 3.25: Schematic of the stacking orientations of the GFRP woven composite and cutting direction of 45° for removing the shear specimens

The shear stress-strain values can be calculated according to the following equations:

$$\tau_{12} = \frac{\sigma_y}{2} \quad (3.1)$$

$$\gamma_{12} = \varepsilon_y - \varepsilon_x \quad (3.2)$$

where τ_{12} is the shear stress, σ_y is the tensile stress in the specimen, γ_{12} is the shear strain, ε_y is the strain in the loading direction and ε_x is the strain at 90° to the loading direction. The in-plane shear-stress versus strain curves exhibit a non-linear response throughout the loading range [28].

3.4.4 Compression tests on rigid foams

All the foam specimens were prepared with the overall dimensions of 50x50x20 mm and tested by using Instron 4204 testing machine according to the ASTM D1621 standard [140]. Figure 3.26 shows the compression test set up where the square foam is placed between the platens of the test machine. The specimens were again tested at a quasi-static compression loading rate of 1 mm per minute. The load-displacement trace was recorded until approximately 10 % of densification was achieved.



Figure 3.26: The square foam specimen under compression testing.

3.5 Quasi-static structural tests

3.5.1 Three-point bending tests

Three-point bending tests were conducted on the hybrid sandwich specimens to investigate their flexural behaviour. The tests were done using an Instron 4505 universal testing machine according to the ASTM D790 Flexural Testing Standard [141]. Beams having length, width and height dimensions of 140, 20, and 13 mm

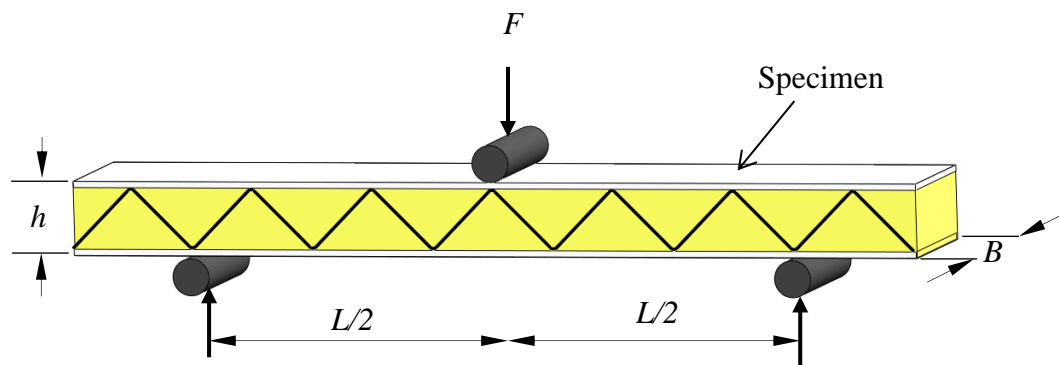


Figure 3.27: Schematic of hybrid sandwich specimen geometry under three point bend testing.

respectively were supported on two 10 mm diameter steel cylinders with a span of 100 mm. The crosshead displacement rate of 1.0 mm/minute was operated to the 10 mm diameter upper cylindrical bar pressing on the specimen. The load versus bending displacement trace was recorded. Figure 3.27 shows a schematic of the hybrid sandwich specimen geometry under three-point bending loading.

3.5.2 Static compression tests

A series of axial quasi-static tests on the hybrid sandwich structures were conducted using an Instron 4204 testing machine with a 100 kN load cell, at a constant crosshead

displacement rate of 1.0 mm/minute and some specimens could withstand higher forces, therefore the Instron 5989, with a capacity of 600 kN, located at University of Manchester, was used employing at the same crosshead displacement rate.

The test procedure was started by placing a specimen on the lower platen (driven part) that is able to control the up-down movement and axial crushing between the parallel steel platens, as shown in Figure 3.28. The quasi-static tests were continued beyond the densification threshold of the specimen. For each of the test configurations, at least three specimens were tested. Table 3.11 shows summary of all 36 groups of specimens investigated during the quasi-static compression study.

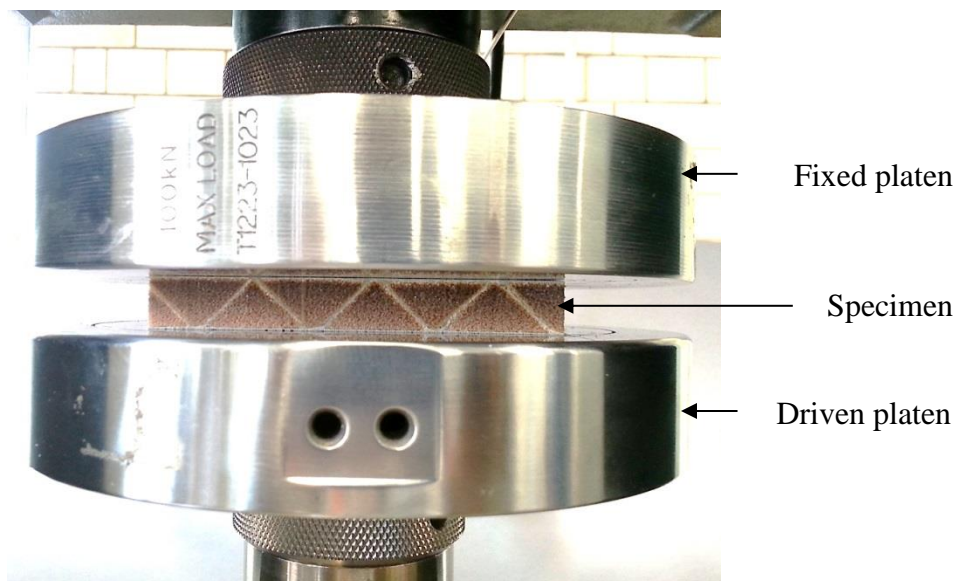


Figure 3.28: Image of the compression test set-up.

Table 3.11: Summary of all specimens investigated during the quasi-static compression study.

No.	Samples ID	Dimension			Weight	Avg. core	Avg. skin
		Length	Width	Thickness		Thickness	Thickness
		(mm)	(mm)	(mm)	(g)	(mm)	(mm)
1	GFR2P	81.61	80.90	10.07	17.95	0.23	0.50
2	GFR4P	78.72	80.14	10.40	20.45	0.45	0.50
3	GFR6P	80.11	79.24	10.12	22.70	0.71	0.50
4	GFR8P	80.17	79.78	10.77	41.50	1.05	0.50
5	TRI4P	80.41	80.07	10.11	19.75	0.49	0.51
6	TRA4P	79.97	80.01	10.93	20.50	0.42	0.52
7	SQA4P	79.80	79.86	10.36	22.05	0.48	0.59
8	PMI0P	80.63	78.47	10.09	3.55	0.00	0.57
9	PMI2P	80.53	80.32	10.52	14.80	0.23	0.53
10	PMI4P	80.31	80.18	10.03	19.30	0.49	0.53
11	PMI6P	80.45	80.04	10.34	27.90	0.49	0.57
12	PMI8P	80.33	79.53	10.96	30.10	1.02	0.58
13	PMI4P	80.32	80.19	10.15	19.04	0.40	0.54
14	PC54P	80.32	80.48	9.58	15.85	0.48	0.53
15	PC24P	80.44	80.19	9.98	18.55	0.43	0.59
16	C554P	80.32	80.20	10.20	15.10	0.42	0.59
17	C134P	79.57	80.37	9.87	19.60	0.45	0.59
18	C204P	80.43	80.40	9.91	21.90	0.40	0.58
19	C55H	79.79	79.36	27.10	50.35	0.43	0.55
20	CMXG	80.00	79.25	33.78	79.05	0.48	0.58
21	C55Z1	80.44	79.86	10.24	15.20	0.43	0.55
22	C55Z2	80.38	100.16	11.88	33.50	0.40	0.51
23	C55Z3	80.74	140.86	19.20	53.20	0.40	0.56
24	C55L1	80.32	80.20	10.20	15.10	0.48	0.58
25	C55L2	79.66	79.89	19.26	34.70	0.50	0.55
26	C55L3	79.82	79.74	27.77	52.75	0.43	0.59
27	FA10S	78.07	79.56	10.56	31.30	0.40	0.85
28	FA20S	83.42	79.35	11.61	45.10	1.12	0.85
29	FA1E0	79.61	78.34	10.43	27.70	0.67	0.59
30	FA2E0	79.69	79.80	11.33	42.50	1.50	0.55
31	FA1ES	79.85	79.65	11.10	44.75	0.80	1.20
32	FA2ES	79.69	78.93	12.07	55.20	1.50	1.20
33	TRIT	79.86	80.15	20.14	15.25	0.46	0.52
34	TRAT	79.89	80.10	20.19	19.18	0.48	0.55
35	SQAT	79.89	80.14	20.17	21.14	0.40	0.59
36	FMLT	50.44	50.26	20.12	24.55	0.86	0.50

3.6 Dynamic testing

Low velocity impact tests using a flat projectile, perforation tests using a spherical projectile and blast tests are described in detail in this section. These tests were undertaken to investigate the dynamic response of the hybrid sandwich structures.

3.6.1 Low velocity impact tests with a flat head impactor

An instrumented drop-weight tower with a flat head projectile and a high speed camera were used to record the dynamic compression response of the hybrid sandwich structures, as shown in Figure 3.29 (schematic diagram) and Figure 3.30 (image). The low velocity impact tests were conducted using the same sample groups listed in Table 3.13, in order to compare the response of the hybrid sandwich structures to both quasi-static and dynamic testing. Here, the impact force was measured directly using a piezoelectric load cell from the Kistler Ltd, type 9363A [142], connected to a charge amplifier using an insulated co-axial cable. The load cell was positioned under the lower platen as shown in Figure 3.29. The measuring capacity of the load cell was up to 120 kN. The displacement was monitored using a high speed video camera (INC, M/N: X4C-U-4, S/N: 24-0507-0875). Details of the high speed video camera system are given in

Table 3.12. During the test, the sample was placed on the lower platen. The carriage was released using a trigger. Before a free-fall of the carriage, a reference target located in the front of the mass surface was tracked by the high speed camera. The raw data

from the video camera was then analysed using the Proanalyst Software package in order to convert the images to a displacement-time relationship. The signal from the load cell transducer was sent to the amplifier (in volts) and transformed to a digital signal by a digitiser device. This information was finally fed to a software package on the PC. The data from the high speed video camera and the load cell were synchronised using Excel software.

The mass and height of the impactor were adjusted to obtain the desired impact energy, E , based on the test requirements. This can be calculated using the expression:

$$E = mgh \quad (3.3)$$

Table 3.12: Details of the high speed video camera[143].

Camera- motionPro X4	Make: integrated design tools, INC. M/N: X4C-U-4 S/N: 24-0507-0875
PROANALYST SOFTWARE	Make: Xcitex Edition: Professional Version: Workstation
Motion Pro software	Make: Redcake Alliance 24-0507-02075

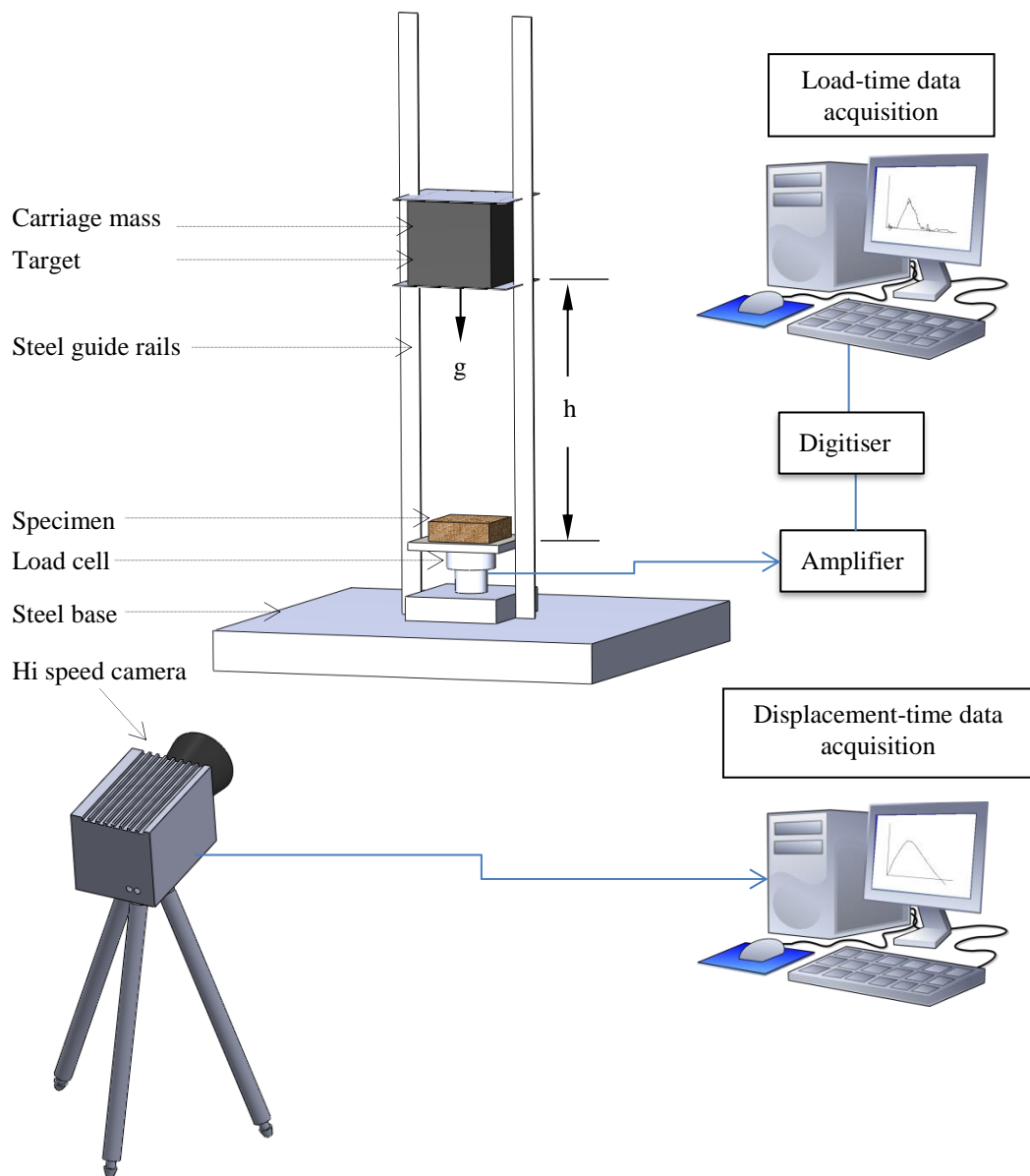


Figure 3.29: Schematic diagram of the set-up of drop-weight impact test.

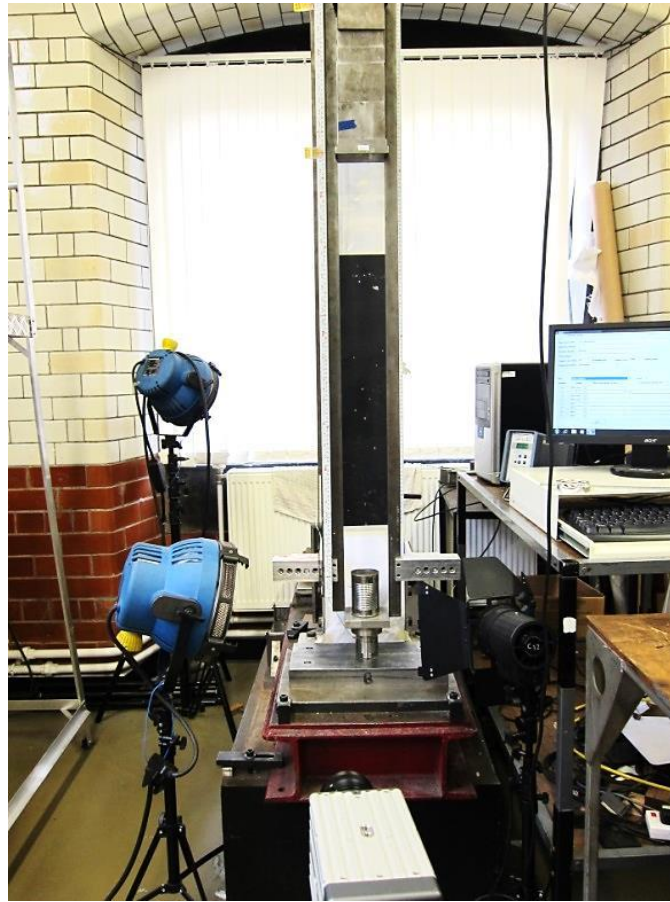


Figure 3.30: Photograph of the drop-weight impact tower.

3.6.2 Perforation tests

Low velocity perforation tests were carried out on hybrid sandwich panels with dimensions of 140 x 140 mm using the drop-weight impact tower shown in Figure 3.30. The test set-up is similar to the drop-weight impact test undertaken using the flat head impactor as described in Section 3.6.1. Figure 3.31 shows a schematic of the perforation test set-up, including details of the clamping arrangement. Here, a half spherical projectile with 10 mm of diameter was used to replace the flat head impactor. The load cell was placed between the carriage and the cylindrical projectile with spherical shape at the bottom tip. The sample was clamped in a frame that was tightened by bolts at the corners and placed on the steel supporter with a square opening. Figure 3.32 shows schematic of the sample consisted of FML skins and core

used for the perforation tests. The synthesis of this study is that the hybrid sandwich structures with FML skins and core would offer a higher performance compared to the other sandwich structures. Here, two different cores, i.e. 1 layer of Al sheet and 2/1 (AL/GFRP/Al) of the samples were produced with four different thicknesses of FML skins (1/1-4/4) as shown in Table 3.13.

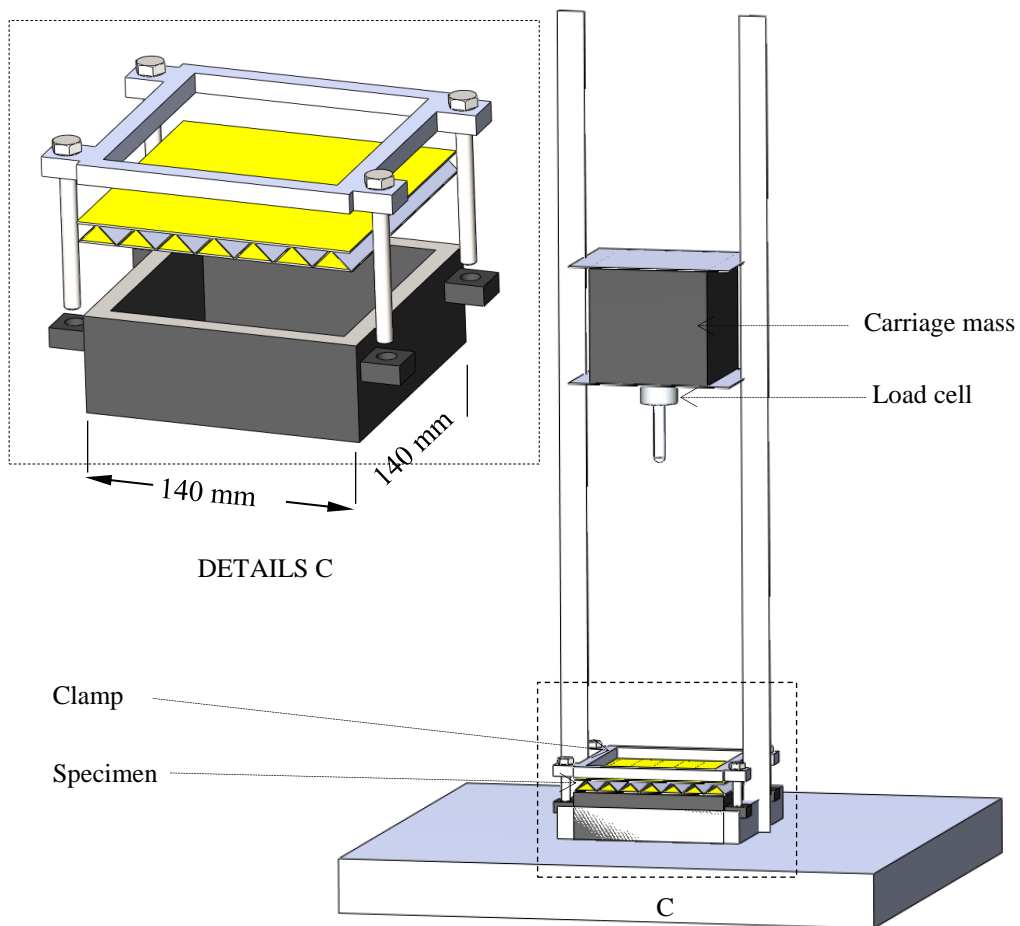


Figure 3.31: Schematic of perforation test set-up.

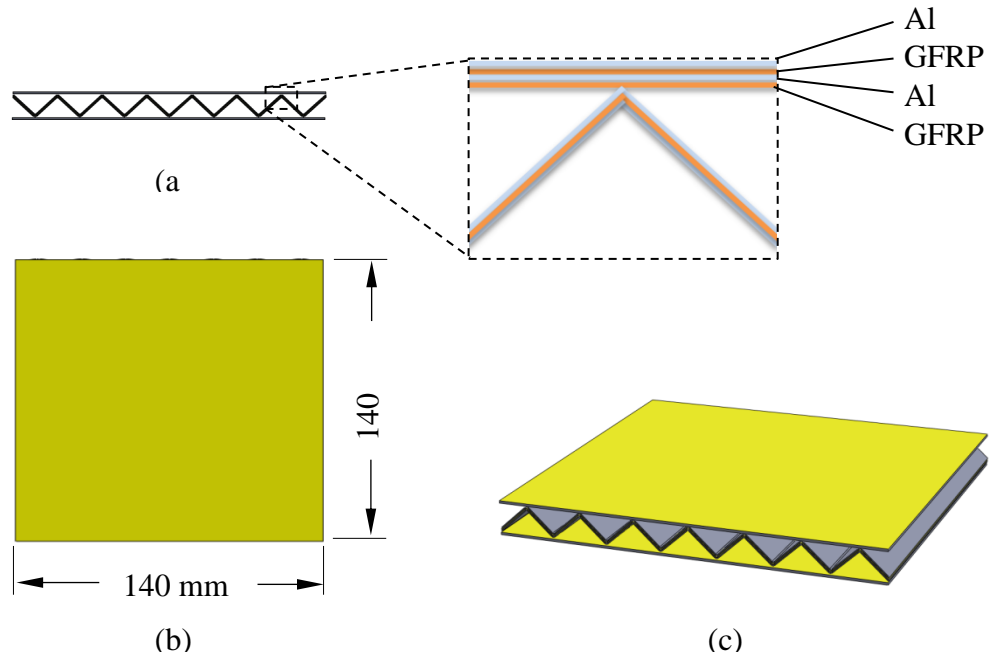


Figure 3.32: Shows schematic of the sample used for the perforation tests. (a) Front view and section details illustrating the layers of sample group CO2/SK2 using FMLs 2/2 (Al/GFRP/Al/GFRP) to be the skin and 2/1 for the core, (b) Top view and dimensions, (c) Perspective view.

Table 3.13: The sample ID definitions and dimension details of the FML core corrugated sandwiches for the projectile impact tests

Sample ID		Sample dimensions					
<u>CO1/SK1</u>							
		FMLs Triangular Core					
		FMLs core type (1= 1 layer Al, 2=2/1)					
		FMLs skin					
		FMLs skin type (1=1/1, 2=2/2, 3=3/3, 4=4/4)					
No.	Samples ID	Dimension			Weight	Avg. core Thickness	Avg. skin Thickness
		Length	Width	Thickness			
		(mm)	(mm)	(mm)	(g)	(mm)	(mm)
37	CO1/SK1	140	140	10.05	54.2	0.40	1.00
38	CO1/SK2	140	140	13.03	87.6	0.40	2.24
39	CO1/SK3	140	140	17.45	93.5	0.40	3.40
40	CO1/SK4	140	140	18.55	105.2	0.40	4.17
41	CO2/SK1	140	140	11.1	98.6	1.50	1.20
42	CO2/SK2	140	140	13.3	109.0	1.50	1.20
43	CO2/SK3	140	140	15.72	120.3	1.50	3.40
44	CO2/SK4	140	140	19.47	175.0	1.50	4.69

3.6.3 Blast tests

The panels could be used to make a fuel tank or bulk head of ship or for maritime applications that may experience an explosion. In order to evaluate such the high strain-rate dynamic response of hybrid sandwich structures, blast tests were conducted on a ballistic pendulum in the Blast Impact and Survivability Research Unit (BISRU) at the University of Cape Town, South Africa. Eight types of specimens listed in Table 3.14 were tested with at least 4 different explosive masses for each configuration. The samples selected were designed to offer a higher energy absorption in order to reduce the damage area of the core structure to be protected. Therefore, most of the samples were the FML sandwich structures developed especially for these tests. However, two types of monolithic curvilinear sandwich structures in group ALCX, ALC1X manufactured by Metawell® [144] and triangular cores in group FML shown in Table 3.14 were included for purposes of comparison. Figure 3.33 shows a schematic of the specimen geometry.

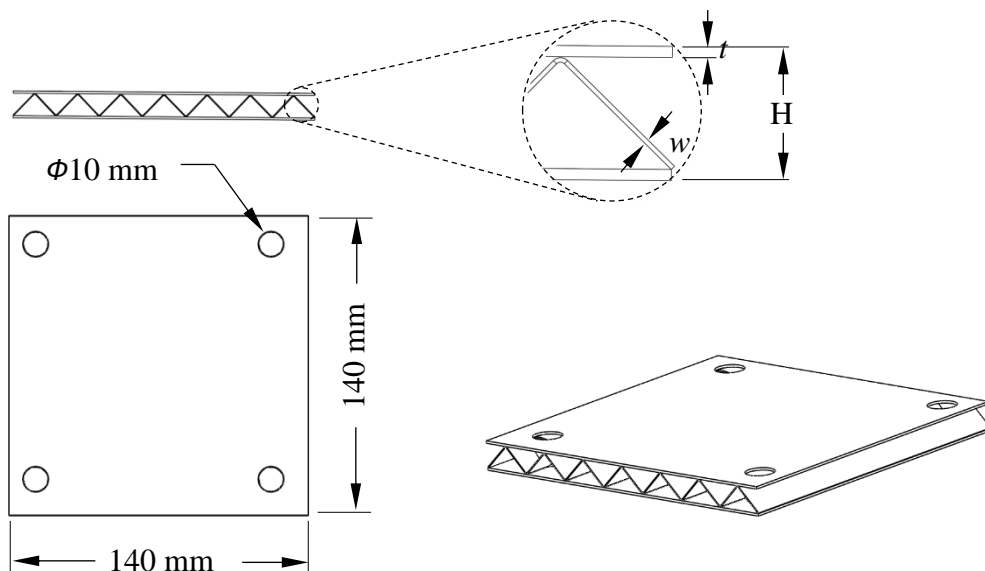

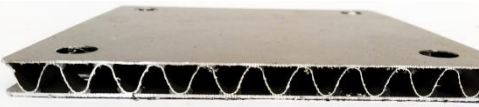
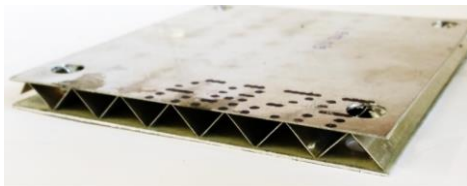


Figure 3.33: Schematic of specimen dimensions for the blast tests.

All of the samples had 4 holes (10 mm in diameter) drilled, near the 4 corners of the sample. The sample was placed between the front and the back support plates shown

in Figure 3.34(b). The plates were then was tightened by bolts to the ballistic pendulum as shown in Figure 3.34(a). A circular polystyrene foam with 10 mm thick 90 mm diameter was placed inside a cylindrical steel tube with the same inner diameter as the foam. Blast loading was applied to the specimens by detonating a 20 mm diameter disc of PE4 explosive attached to the centre of the cylindrical foam using double-sided adhesive tape. The stand-off distance (SOD) between the PE4 explosive and the sample was 90 mm. The detonator used was one gram of PE4 explosive, connected to the cable, and attached to the centre of the 20 mm diameter PE4 explosive discs. The impulse was determined from the measured swing of the pendulum using the oscilloscope connected to laser sensor and received voltage signal as shown in Figure 3.35. Table 3.14 gives a summary of the blast conditions used to test the sandwich panels.

Table 3.14: Specimen details on each group investigated on blast test.

No.	Sample group	Photograph	Details
1	ALC		Monolithic curvilinear corrugated core sandwich structures 6 mm thick, made of aluminium EN AW-5182 H48, produced by Metawell, Germany.
2	ALC1		Monolithic curvilinear corrugated core sandwich structures, the same as ALC samples, but 10 mm thick, made of aluminium EN AW-5182 H48.
3	FML1/1		Triangular corrugated core, made of Al 2024 T3 sheet + 1/1 (Al/GFRP) skins (4 plies of GFRP used).

4	GFRV1		4 plies of GFRP triangular corrugated core containing embedded Airex 70.130 prism PVC foam + 1/1 (Al/GFRP) skins (4 plies of GFRP used), 20 mm unit cell base line.
5	GFRV2		8 plies of GFRP triangular corrugated core containing embedded Airex 70.130 prism PVC foam + 1/1 (Al/GFRP) skins (4 plies of GFRP used), 40 mm unit cell base line.
6	FMLV		2/1 (GFRP/Al/GFRP), using 0.6 mm Al triangular core containing embedded Airex 70.130 prism PVC foam + 1/1 (Al/GFRP) skins (4 plies of GFRP used), 40 mm unit cell base line.
7	GFRT		4 plies of GFRP oriented in a diamond shape and embedded in Airex 70.130 PVC foam + 1/1 (Al/GFRP) skins (4 plies of GFRP used).
8	FMLAT		FML 2/1 (GFRP/Al/GFRP) core oriented in diamond shape and embedded in Airex 70.130 PVC foam + 1/1 (Al/GFRP) skins (4 plies of GFRP used).

Table 3.15: Summary of the blast conditions on the sandwich panels.

No.	Samples ID	Dimension			Avg. core thickness (t) (mm)	Avg. skin thickness (w) (mm)	Weight (g)	Mass of PE4 (g)	
		Length	Width	Thickness (H)					
		(mm)	(mm)	(mm)					
1	ALC1	140x140		5.9	0.2	0.5	82.55	1	
2	ALC2			5.9			82.15	3	
3	ALC3			5.9			82.01	4	
4	ALC4			5.9			80.20	5	
5	ALC101			10.2			118.50	0.5	0.5/0.8
6	ALC102			10.2	120.05	2			
7	ALC103			10.2	119.70	3			
8	ALC104			10.2	121.05	5			
9	FML1/1			11.4	131.85	0.4	1.2	131.85	3
10	FML1/2			11.5				131.25	4
11	FML1/3			11.4				133.15	5
12	FML1/4			11.5				133.40	6
13	GFRV101			12.1	205.65	0.8	1.2	205.65	7
14	GFRV102			11.8				206.75	9
15	GFRV103			11.8				204.00	11
16	GFRV104			11.8				199.95	12
17	GFRV201			21.4	223.60	1.3	0.8	223.60	7
18	GFRV202			21.5				228.90	9
19	GFRV203			21.4				234.40	11
20	GFRV204			21.4				235.10	12
21	FMLV201			21.9	268.05	0.6	1.0	268.05	4
22	FMLV202			22.0				262.10	5
23	FMLV203			22.1				267.15	7
24	FMLV204			22.1				267.55	8
25	GFRT1			21.7	372.05	1.3	0.8	372.05	8
26	GFRT2			21.6				371.40	9
27	GFRT3			21.4				373.60	11
28	GFRT4			21.4				367.50	12
29	FMLAT1			19.1	328.45	1.1	1.2	328.45	5
30	FMLAT2			19.7				332.70	6
31	FMLAT3			19.8				324.40	10
32	FMLAT4			19.9				333.50	12

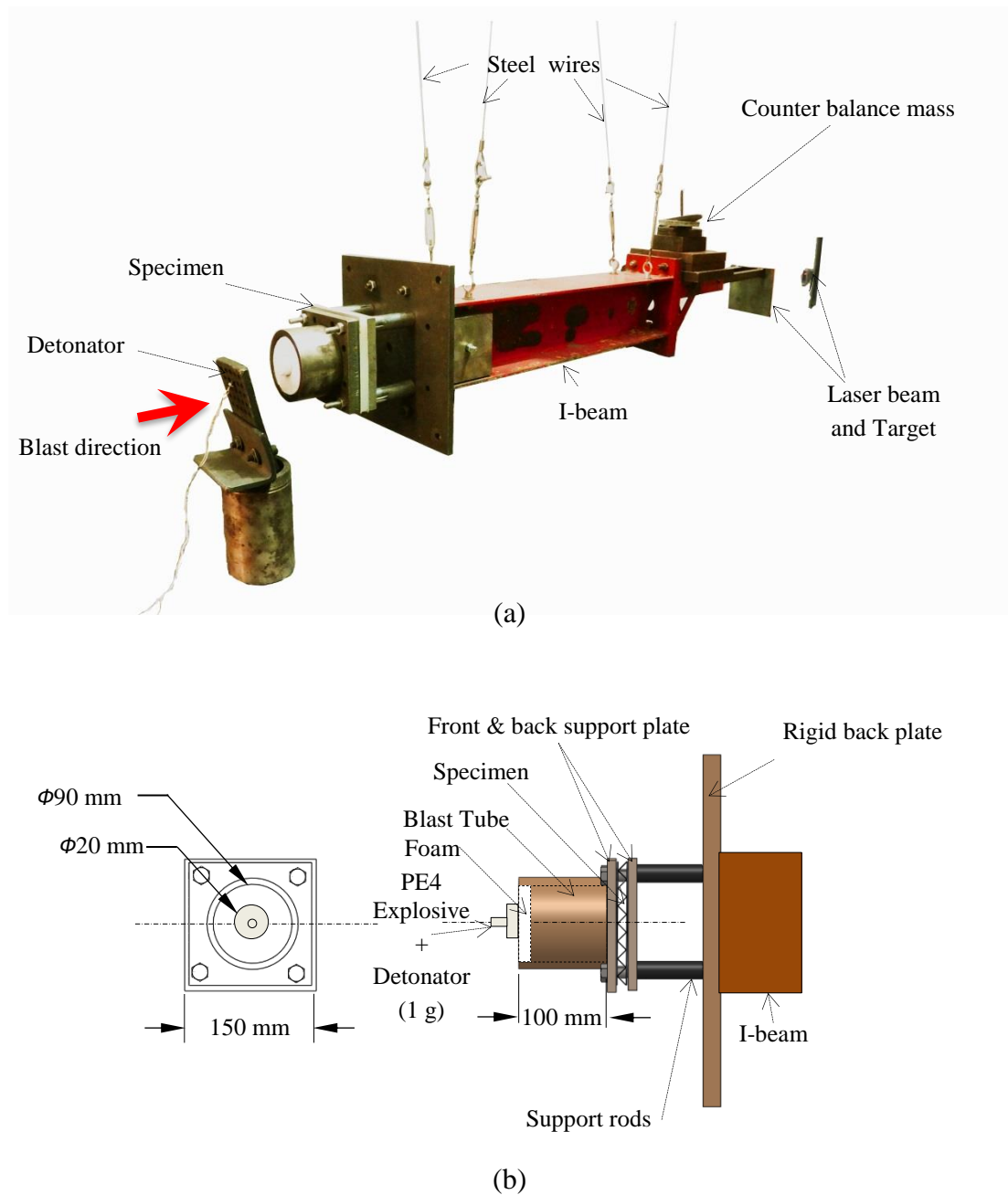


Figure 3.34: (a) Photograph of the ballistic pendulum used for conducting the blast tests and (b) schematic of the detonator and blast tube arrangement.

Figure 3.35 shows the oscilloscope displaying the sine curve on the screen in the control room.



Figure 3.35: Shows the output signal collected from the oscilloscope in the operating and control room.

The impulse is calculated using the geometry, natural period of the system taken from the oscilloscope using a laser sensor measured the displacement at the back of the ballistic pendulum. Figure 3.36 shows a schematic representation of the ballistic pendulum and the associated geometry of the system. The red and blue lines represent the maximum position after blast loading [145].

Figure 3.37 shows a sine curve produced by the oscilloscope showing the amplitude in volts and period of time corresponding to the pendulum positions.

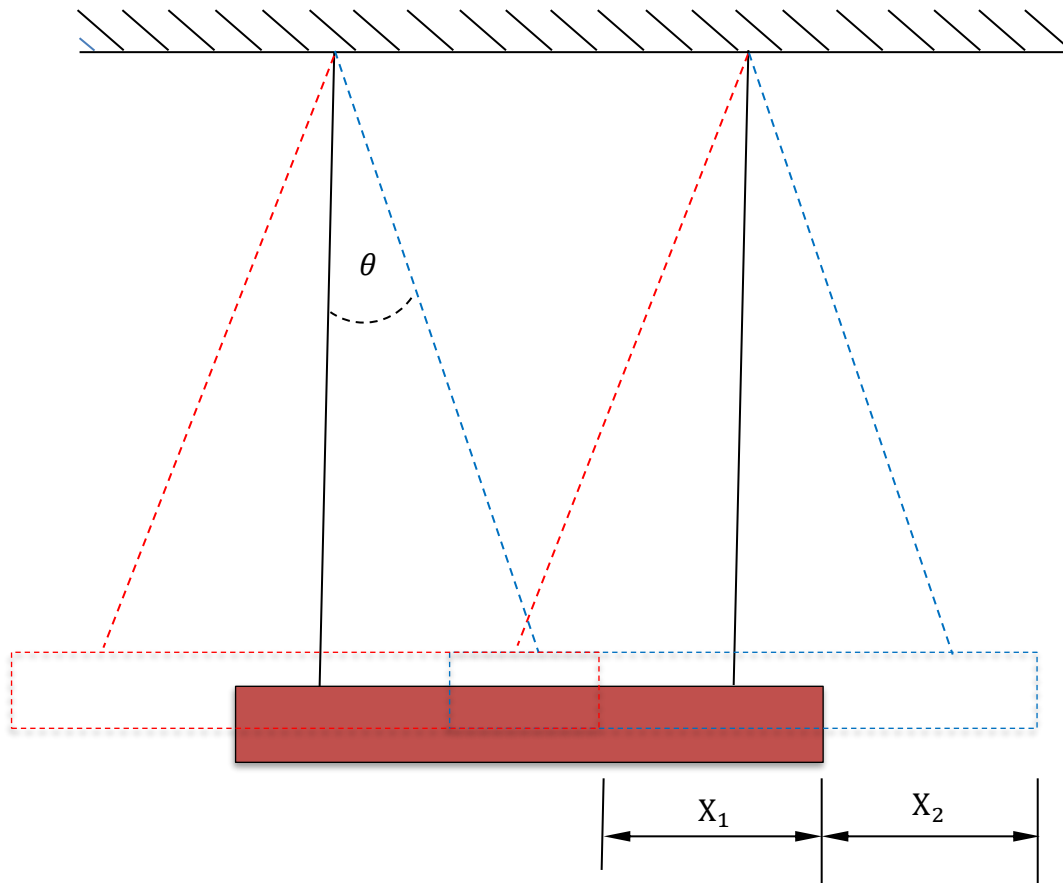


Figure 3.36: Schematic of the ballistic pendulum oscillation following on the applied impulse.

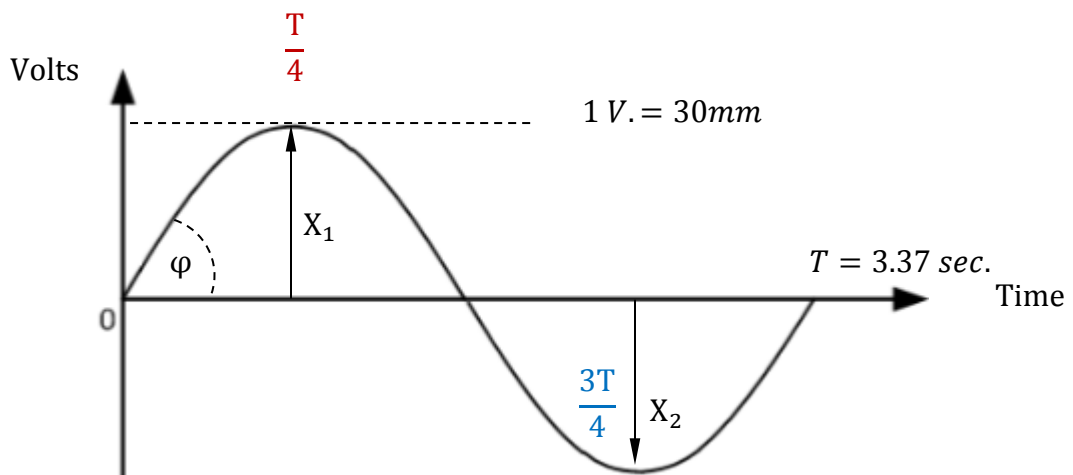


Figure 3.37: Sine curve from the oscilloscope showing the amplitude in volts and time corresponding to the pendulum positions

The linear motion of the ballistic pendulum is expressed by [145]:

$$\ddot{X} + 2\beta\dot{X} + \omega_n^2 = 0 \quad (3.4)$$

where

$$\beta = \frac{C}{2M} \quad \text{and} \quad \omega_n = \frac{2\pi}{T} \quad (3.5)$$

where the constants C , M and T are defined as the viscous damping coefficient, the total mass of the pendulum including the test rig, the specimen and counterbalance masses and the natural period of the pendulum respectively.

Equation (3.4) can be written in the X form as:

$$X = \frac{e^{-\beta t} \dot{x}_0 \sin(\omega_d t)}{\omega_d} \quad (3.6)$$

where the initial velocity of the pendulum is \dot{x}_0 and

$$\omega_d = \sqrt{\omega_n^2 - \beta^2} \quad (3.7)$$

Assuming that X_1 and X_2 are the maximum forward and backward of the pendulum and $t = \frac{T}{4}$ and $\frac{3T}{4}$ respectively. Therefore, equation (3.6) can be changed to:

$$X_1 = \frac{\dot{x}_0 T e^{-\beta \frac{T}{4}}}{2\pi} \quad (3.8)$$

$$X_2 = \frac{\dot{x}_0 T e^{-\beta \frac{3T}{4}}}{2\pi} \quad (3.9)$$

Equations (3.8) and (3.9), β can be solved as:

$$\beta = \frac{2}{T} \ln\left(\frac{X_1}{X_2}\right) \quad (3.10)$$

Substitute Equation (3.10) into Equation (3.8) the initial pendulum velocity can be found to be:

$$\dot{X}_0 = \frac{2\pi}{T} X_1 e^{\beta \frac{T}{4}} \quad (3.11)$$

Therefore, the impulse can then be calculated by:

$$I = M\dot{X}_0 \quad (3.12)$$

In addition, a simplicity of an initial velocity, \dot{X}_0 , can also be calculated using the result from oscilloscope as:

$$\dot{X}_0 = \tan \varphi \quad (3.13)$$

3.7 Failure mechanisms and damage observations

An optical microscope camera (Infinity 2, Lumenera Corporation) as shown in Figure 3.38 was used to examine the failure mode of the samples after testing. The crushed samples from both the quasi-static and dynamic experiments were polished to a 1200 grit finish using a silicon carbide paper and then placed on the optical microscope to investigate the failure mechanisms.

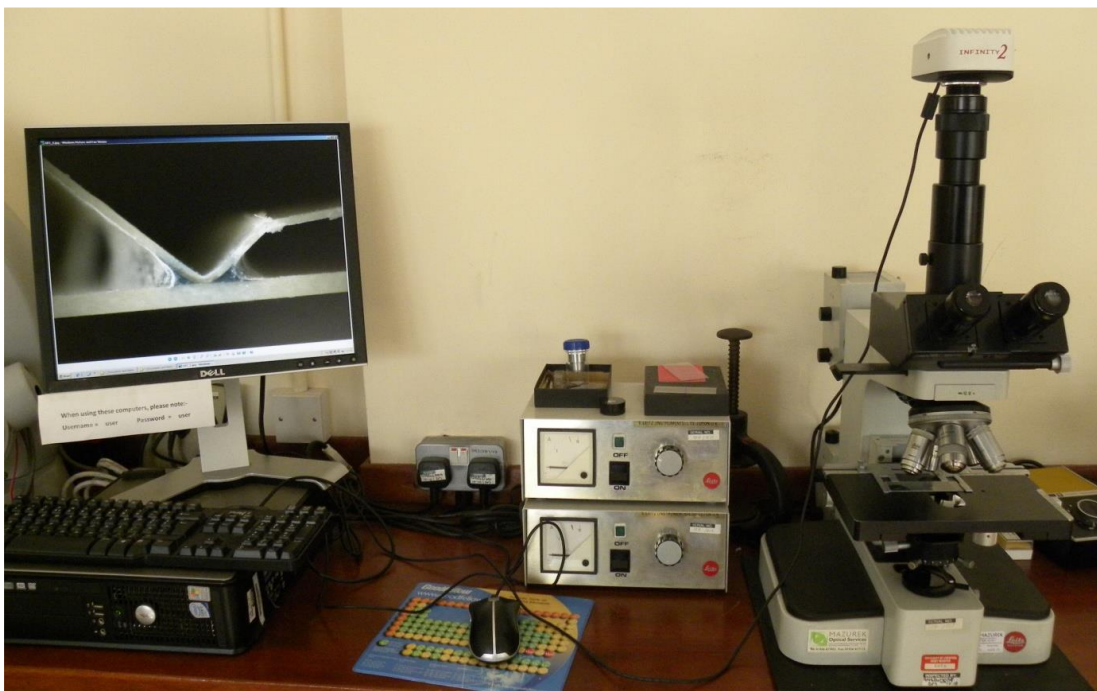


Figure 3.38: Optical microscope equipment that was used in the study.

3.8 Summary

Chapter 3 highlights the details of the novel manufacturing and the fabrication techniques used to produce the hybrid corrugated-core sandwiches. Details of the sample preparation and the parameters studied are given. The experimental set-up and testing procedure for both the quasi-static and dynamic loading are also described. Finally, the failure modes of the samples were obtained using optical microscopy.

CHAPTER 4

RESULTS AND DISCUSSION

In this chapter, the experimental results obtained will be presented and discussed. Firstly, the mechanical response of each material tested was characterised based on the results throughout a series of tensile and compression tests. Subsequently, the test results of the sandwich structures under quasi-static three-point bending and compression tests are presented. Following this, the dynamic behaviour of the structures under low velocity impact with flat-head projectile, low velocity impact perforation with hemisphere projectile and blast will be presented. Finally, the failure mechanisms observed in the structures during and after the tests will be characterised and discussed.

4.1 Mechanical properties of materials

This section presents and discusses the results obtained from a series of tensile tests on the Al 2024 T3 and GFRP, in-plane shear on the GFRP laminates, and compression tests on rigid foams to obtain the related material properties.

4.1.1 Tensile tests of aluminium alloy

In order to obtain the material properties of aluminium alloy 2024-T3 used in this research, the standard tensile tests following ASTM E8/E8M – 16a [138] were carried out. Under tensile loading, the aluminium alloy samples were deformed and elongated pass through elastic and plastic deformation phases. Within the elastic region, a linear relationship part between the stress and strain can be found to be used to work out the modulus of elasticity, as shown in Figure 4.1. Based on the stress-strain curve following the elastic stage, the yield stress, ultimate tensile strength and fracture strain can be obtained.

Here, the simple equations of the engineering stress and strain can be calculated using the following equations:

$$\sigma = \frac{F}{A_0} \quad (4.1)$$

$$\varepsilon = \frac{L_f - L_0}{L_0} \quad (4.2)$$

where σ is the engineering stress, ε is the engineering strain, F is the external axial load, A_0 is the original cross-sectional area of the specimen, L_0 is the original length of the specimen and L_f is the ultimate length of the specimen.

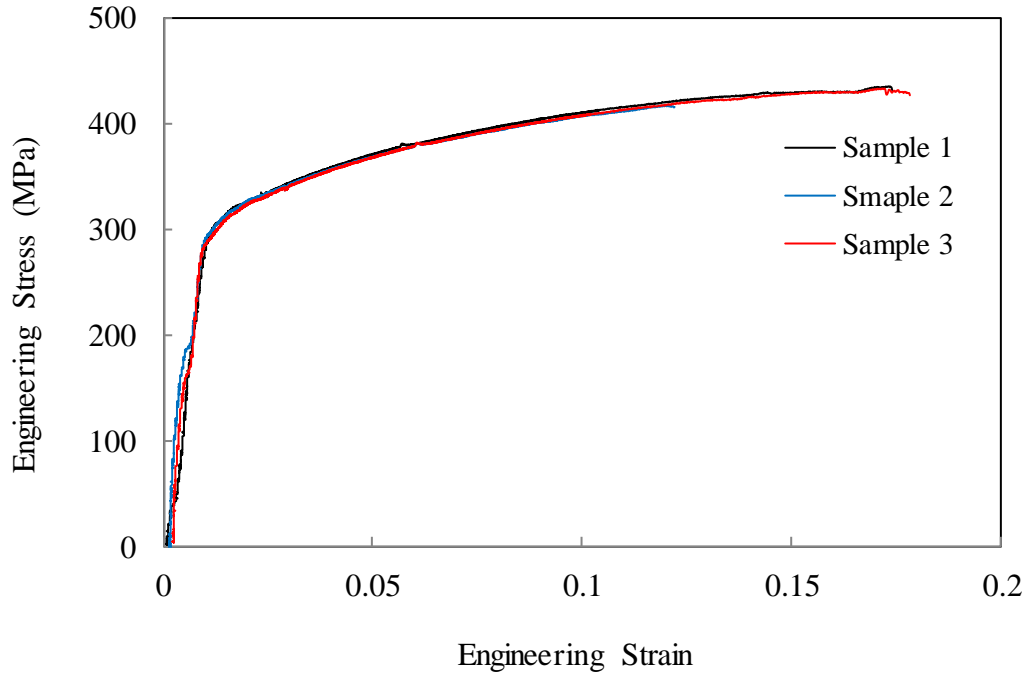


Figure 4.1: Engineering stress-strain curves for the aluminium alloy 2024 T3

However, during the test under tension loading, the sample dimensions and its cross-sectional area are dynamically changed from the original values. Therefore, the true stress and true strain would be considered a more direct measure of the material response in the plastic flow range.

True stress is related to engineering stress. Assuming material volume remains constant, there is:

$$A_0 l_0 = Al, \quad \frac{A_0}{A} = \frac{l}{l_0} \quad (4.3)$$

Using $\frac{A_0}{A}$ to reform the equation

$$\sigma = \frac{F}{A} = \frac{F}{A} * \frac{A_0}{A_0} = \frac{F}{A_0} * \frac{A_0}{A} \quad (4.4)$$

From Equation (4.3), the strain form can be derived as:

$$\frac{A_0}{A} = \frac{l}{l_0} = \frac{(l_0 + \delta)}{l_0} = 1 + \frac{\delta}{l_0} = (1 + \varepsilon) \quad (4.5)$$

Substitute Equation (4.5) into Equation (4.4), one has

$$\sigma_T = \frac{F}{A_0} (1 + \varepsilon) \quad (4.6)$$

$\frac{F}{A_0}$ is known as the nominal stress (σ) in Equation (4.1), which can be used to replace it in

Equation (4.6). Then the true stress can be calculated by using the following equation:

$$\sigma_T = \sigma (1 + \varepsilon) \quad (4.7)$$

True strain also can be calculated when the rate of instantaneous increase in the instantaneous gauge length, i.e.

$$\varepsilon_T = \int \frac{dl}{l} = \ln\left(\frac{l}{l_0}\right) \quad (4.8)$$

$$\varepsilon_T = \ln\left(\frac{l_0 + \Delta l}{l_0}\right) = \ln\left(\frac{l_0}{l_0} + \frac{\Delta l}{l_0}\right) \quad (4.9)$$

Therefore, the true strain can be written in the following form:

$$\varepsilon_T = \ln(1 + \varepsilon) \quad (4.10)$$

A summary of material properties of aluminium 2024-T3 is shown in

Table 4.1. Some of them could not be obtained by the tensile tests carried out, which were obtained from reference [2, 3].

Table 4.1: Typical mechanical properties for aluminium alloy 2024-T3

Properties	Aluminium 2024 T3
Density [kg/m ³]	2800
Modulus of elasticity [GPa]	70
Tensile yield strength [MPa]	315
Ultimate tensile strength [MPa]	435
Elongation at break [%]	18
Shear modulus [GPa]	25.8 [2]
Poisson's Ratio	0.33 [146]
Shear Modulus[GPa]	28[2]
Shear strength [MPa]	290[3]

4.1.2 Tensile tests on the composites

Typical stress-strain curves for the GFRP are given in Figure 4.2. Here, the composite laminates under tensile loading behave more or less in a linear fashion up to the maximum stress value. Modulus of elasticity and ultimate tensile stress can be obtained using stress-strain relationship shown Figure 4.2, Material properties of the glass fibre laminates tested are shown in Table 4.2.

Table 4.2: Material properties for the glass fibre laminates obtained from the test and [72] used in this study.

Properties	GFRP woven (EHG250-44-55)
Density [kg/m ³]	2,550
Modulus of elasticity [GPa]	23
Ultimate tensile strength [MPa]	320
Elongation at break [%]	2
Shear modulus [GPa]	5[3]
Poisson's Ratio	0.15[3]
Shear strength [MPa]	320[3]

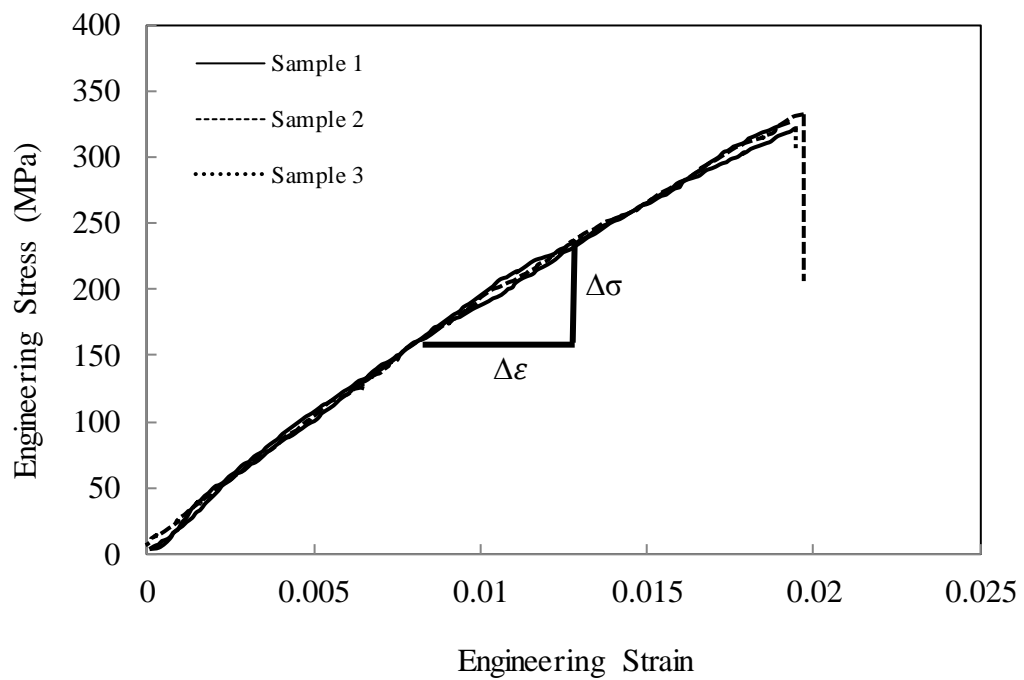


Figure 4.2: Typical tensile stress-strain curve for a GFRP specimen.

Figure 4.3 shows a damaged sample of under tensile test, in which the composite laminates failed in a catastrophic manner across the width of the sample.

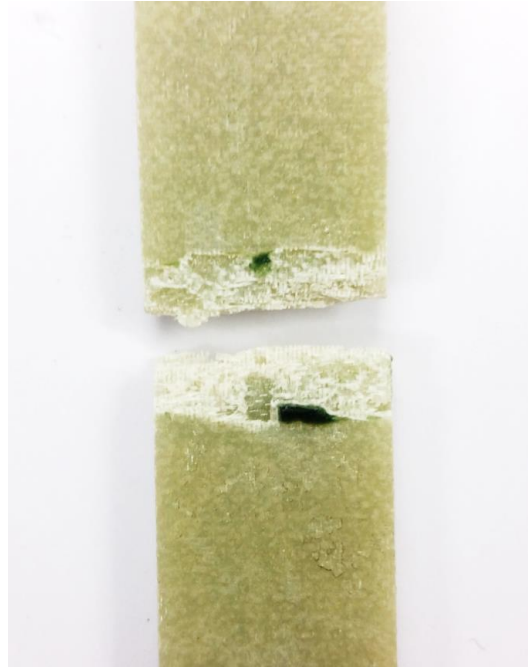


Figure 4.3: Tensile failure modes of the woven composite (GFRP sample).

4.1.3 In-plane shear tests on the composites

Here, the mechanical properties of the composite woven under the in-plane shear test are shown in Table 4.3 and shear stress-strain curve of a GFRP specimen is shown in Figure 4.4.

Table 4.3: Mechanical properties of composite woven under in-plane shear test.

Properties	GFRP woven (EHG250-44-55)
Density [kg/m ³]	2,550
Shear strength [MPa]	105
Ultimate Shear strain[%]	8.1

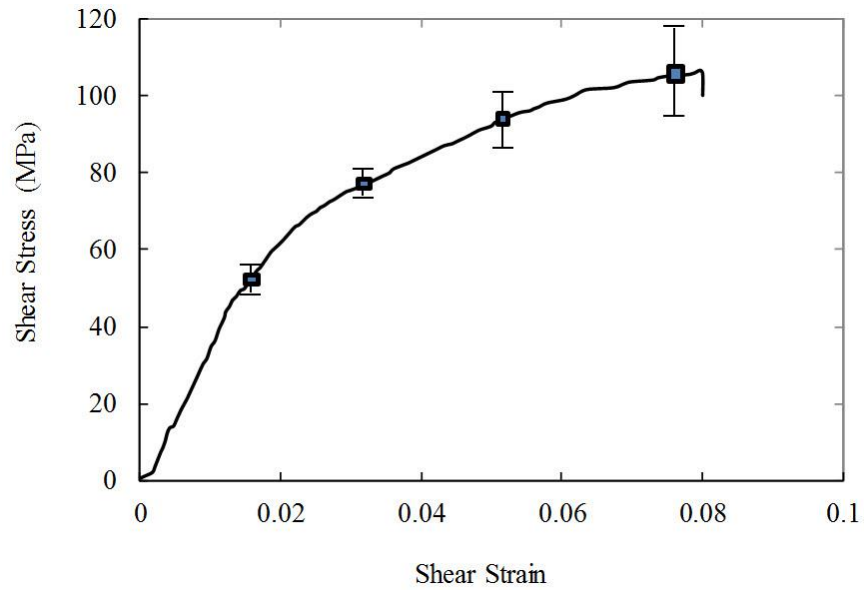


Figure 4.4: Typical shear stress-strain curve for a GFRP specimen.

Figure 4.5 shows the damaged sample of under in-plane shear test, which indicates the composite also failed in a catastrophic manner across the width of the sample.

However, the crack propagation reveals as a zig-zag pattern.



Figure 4.5: Failure modes in the GFRP woven composite laminates under in-plane shear loading.

4.1.4 Compression tests on the rigid foam

This section investigates the mechanical properties of the foam materials by conducting quasi-static compression tests on four different densities, ranging from 52 to 200 kg/m³, as described in Section 3.3.4. Tests were undertaken at a crosshead displacement rate of 1 mm/min and the crushing process was interrupted when the crosshead had travelled until reaching to the densification zone that could be judged by the compressive force begin to increase dramatically. All tests were performed at room temperature, i.e. 23°C. Figure 4.6 shows load-displacement curves following quasi-static tests on the rigid foam used in this study. Figure 4.7: The stress-strain traces following quasi-static tests on foams with different densities. Table 4.4 shows the mechanical properties of foam cores used in this study obtained from the compression tests and references [5, 6].

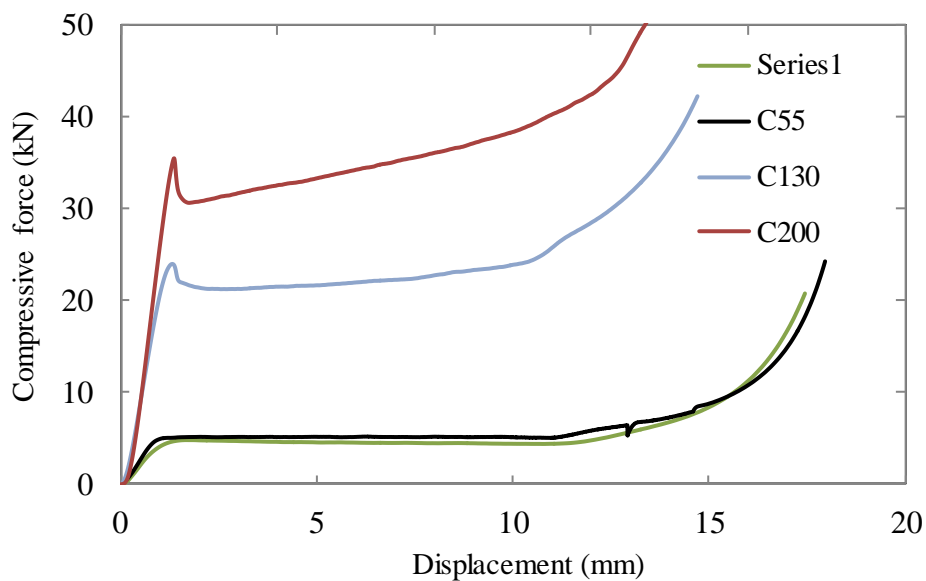


Figure 4.6: Load-displacement curves following a quasi-static test on the rigid foam used in this study.

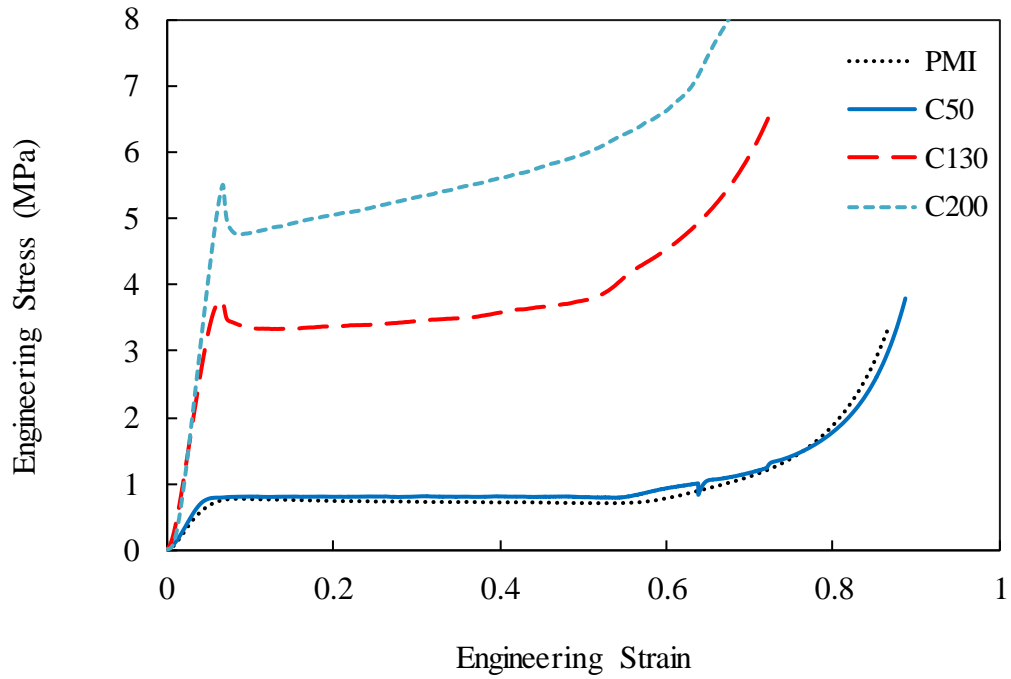


Figure 4.7: The stress-strain traces following quasi-static tests on foams with different densities.

Table 4.4: Mechanical properties of foam cores used in this study obtained from compression tests and Refs [2, 147].

Mechanical properties	PMI	C55	C130[2]	C200[2]
Density (kg/m ³)	52	60	130	200
Poisson's ratio	0.32	0.32	0.32	0.32
Compressive modulus (MPa)	37	69	160	280
Compressive strength (MPa)	0.8	0.9	2.6	4.8
Compressive fracture strain	0.68	0.7	0.7	0.7
Tensile modulus (MPa)	21	45	110	175
Tensile strength (MPa)	0.6	1.3	3.8	6
Shear modulus (MPa)	24	22	47	75
Shear strength (MPa)	0.8	0.8	2.3	3.5
Shear fracture strain	0.08	0.16	0.3	0.3

4.2 Quasi-static test results of various corrugated sandwich beams

This section presents the results of comprehensive tests of hybrid sandwich structures under three-point bending and compression with flat loading platens.

4.2.1 Three point bending tests to determine the structural stiffness

High performance lightweight sandwich structures require the cores to have high stiffness and strength as well as energy absorption capacities. Three-point bending tests were conducted on the hybrid sandwich samples to investigate their flexural behaviour. As described in Section 3.5.1, the flexural modulus was calculated using the following equation:

$$E_f = \frac{FL^3}{4B\delta h^3} \quad (4.11)$$

where F is the applied load, δ is the mid-span deflection, L is the span, B is the beam width and h is the height or thickness of the specimen. The flexural strength was calculated at the maximum force using the following equation:

$$\sigma_f = \frac{3FL}{2Bh^2} \quad (4.12)$$

Most of data are presented with the relation of load against displacement in this section. The images were presented to reveal the failure modes of various structures. Observed failure modes were labelled as: Skin yielding (SY); Plastic Skin Buckling (P-SB); Elastic Skin wrinkling (E-SW); Elastic core buckling (E-CB); Indentation (ID); Debonding (DB). At the end of this section, all the data presented will be summarised.

4.2.1.1 Effect of the core configuration under three-point bending

This section presents experimental results of corrugated sandwich beams made with various types of core.

4.2.1.1.1 Responses of plain GFRP triangular corrugated cores

The typical failure mode of plain GFRP triangular corrugated sandwich beam under three-point bending is shown in *Figure 4.8*. The initial failure occurred at the top skin. The skin buckled near the mid-span where the load was applied. There were three identical samples tested, with the load-deflection curves being shown in *Figure 4.9*.



Figure 4.8: GFRP triangular corrugated-core under three-point bending test.

The average maximum peak load is approximately 340 N. The sandwich sample exhibited slightly flexible behaviour beyond elastic deformation. However, the samples suddenly snapped at their top skins that led to the compressive force dramatically dropped at around 1 mm of the bending deflection (δ) and remained constant at around 50 N till the ultimate failure.

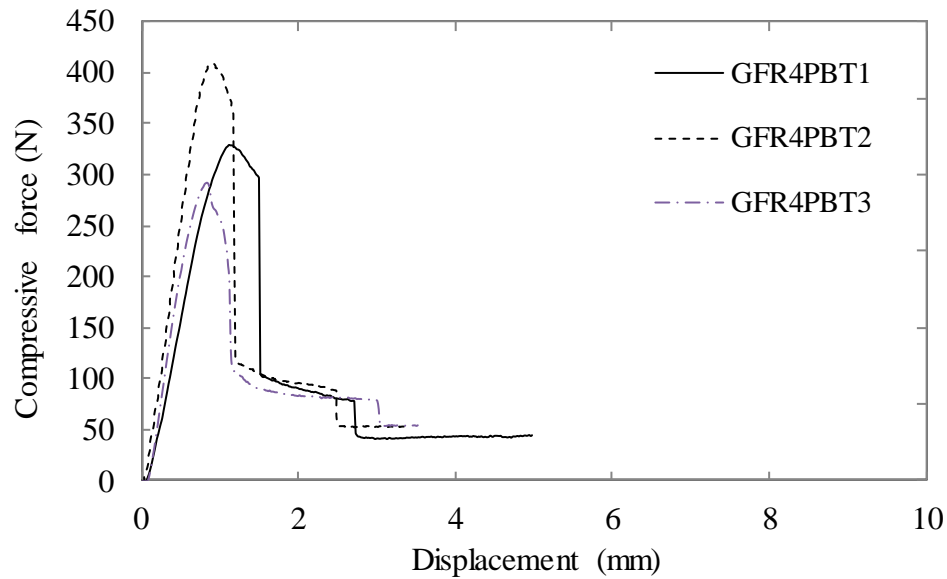


Figure 4.9: Load-displacement obtained from triangular GFRP corrugated-core under three-point bending tests.

4.2.1.1.2 GFRP trapezium corrugated core

For the plain GFRP trapezium corrugated core, the deformation and failure modes of the sandwich beam under three-point bending show the similar features as the triangular corrugated core sandwich beam, i.e. the top skin buckling failure adjacent to the loading point as shown in Figure 4.10. Figure 4.11 shows the load-displacement relationships obtained from three repeated tests, which indicate a much lower stiffness in comparison to the triangular core beam as the former core shape is more robust than the latter. The average maximum peak load is around 250 N with a sudden drop of the load due to buckling at the top skin corresponding to 5 mm bending displacement.

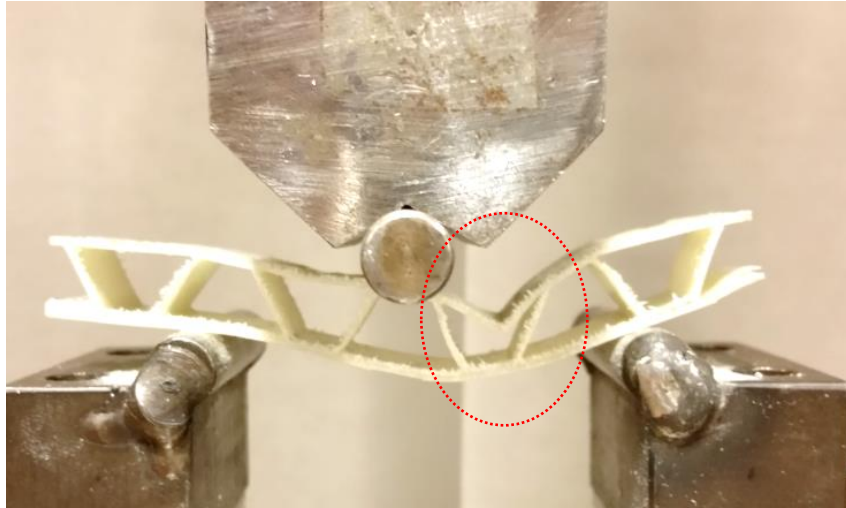


Figure 4.10: GFRP trapezium corrugated-core under three-point bending test.

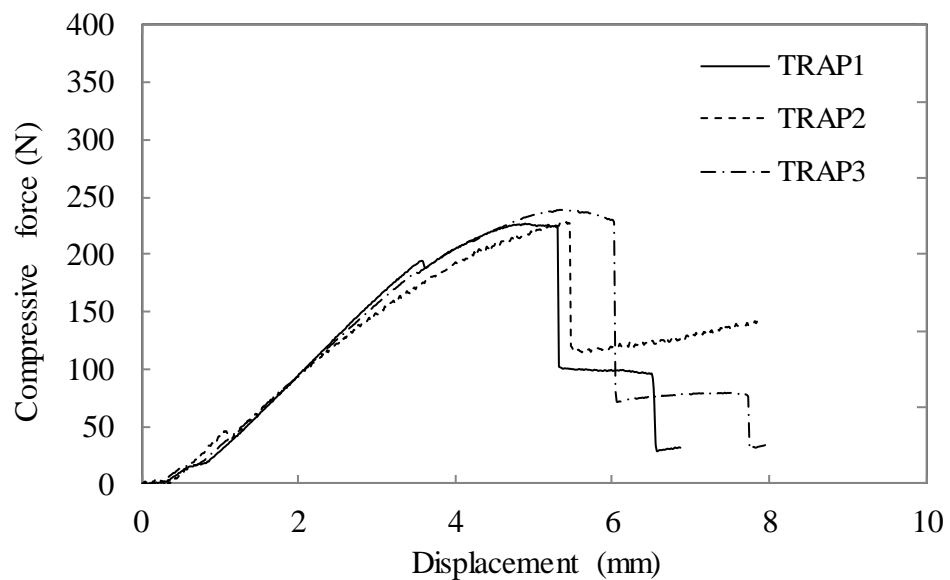


Figure 4.11: Load-displacement obtained from Trapezium GFRP corrugated-core under three-point bending tests.

4.2.1.1.3 Hybrid square corrugated foam core

As the author could not produce a plain GFRP square corrugated core due to the limitation of machinery to form the square mould, a hybrid GFRP square corrugated

frame was produced to reinforce a foam core. This is a very light corrugated sandwich structure with a one-go fabrication process, which gives a good integration between the core and the skins. *Figure 4.12* and *Figure 4.13* show the hybrid GFRP square corrugated-core reinforced with PMI foam core under three-point bending in x-z plane and x-y plane, respectively. It can be clearly seen at bottom of the mid-span in x-z plane of sample SQ3BT1 that the crack propagation starts to grow across the width of the sample. It also reveals that the debonding failure occurred between the skin and the foam core. However, the plastic buckling and debonding failure occurred at the top skin when tested in x-y plane. *Figure 4.14* shows load-displacement results of the samples tested in the two planes. Apparently, the flexural stiffness of the sample placed vertically or along x-z plane is greater than that of the sample placed flatly or along x-y plane due to a greater beam depth (H). However, the peak force of the former is clearly lower than the latter. Notably, both sample types have a sudden drop of the load due to buckling and debonding failure. However, the plateau level of the former is again lower than the latter. This is likely caused by more effective of the flat GFRP corrugation to resist the post failure loading.

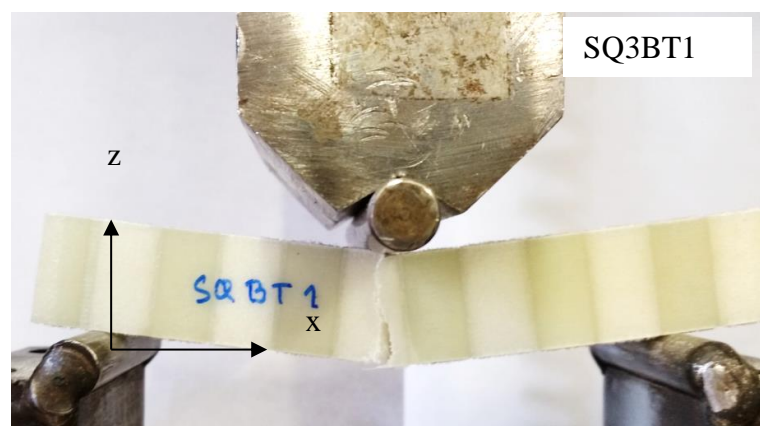


Figure 4.12: The hybrid square corrugated-core reinforced with foam with vertical corrugated-beam core position (showing x-z plane) undergone by three-point bending test.

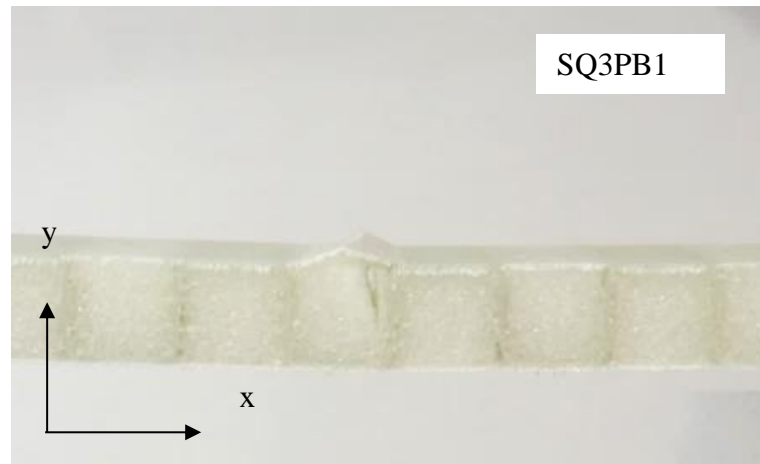


Figure 4.13: The hybrid square corrugated-core reinforced with foam with side corrugated-beam core position (showing x - y plane) undergone by three-point bending test.

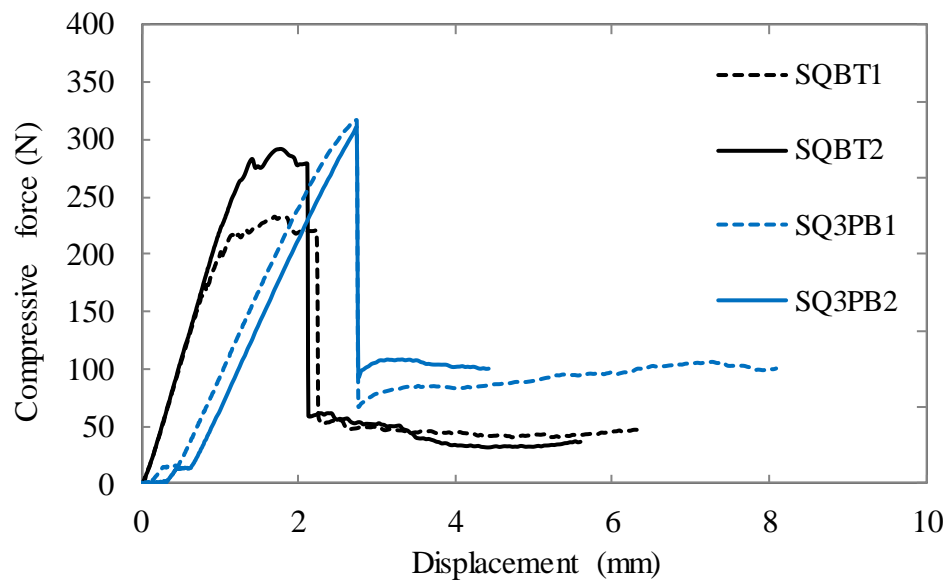


Figure 4.14: Load-displacement traces of the hybrid square corrugated-core based on square GFRP and reinforced PMI foam core under three-point bending test in x - y and x - z plane.

4.2.1.2 Effects of the thickness of plain GFRP corrugated core and skin

The effect of the thickness of plain GFRP triangular corrugated core under three-point bending load were investigated. There were 4 different thicknesses of GFRP triangular corrugated sandwich beams tested, i.e. 0.23, 0.45, 0.71 and 1.05 mm fabricated from 2, 4, 6, 8 plies respectively. *Figure 4.15* shows the plain GFRP corrugated core sandwich beam with a thickness of 1.05 mm undergone by three-point bending test. Clearly, the similar deformation and failure modes are exhibited to that mention in Section 4.2.1.1.1. Load-displacement traces of the plain GFRP corrugated core samples with different GFRP core thicknesses are shown in *Figure 4.16*. The relation between number of ply and peak load is depicted in *Figure 4.17*. It can be seen that relationship between the peak load and the number of ply follows almost an exponential fashion.



Figure 4.15: The plain GFRP corrugated-core undergone by three-point bending test.

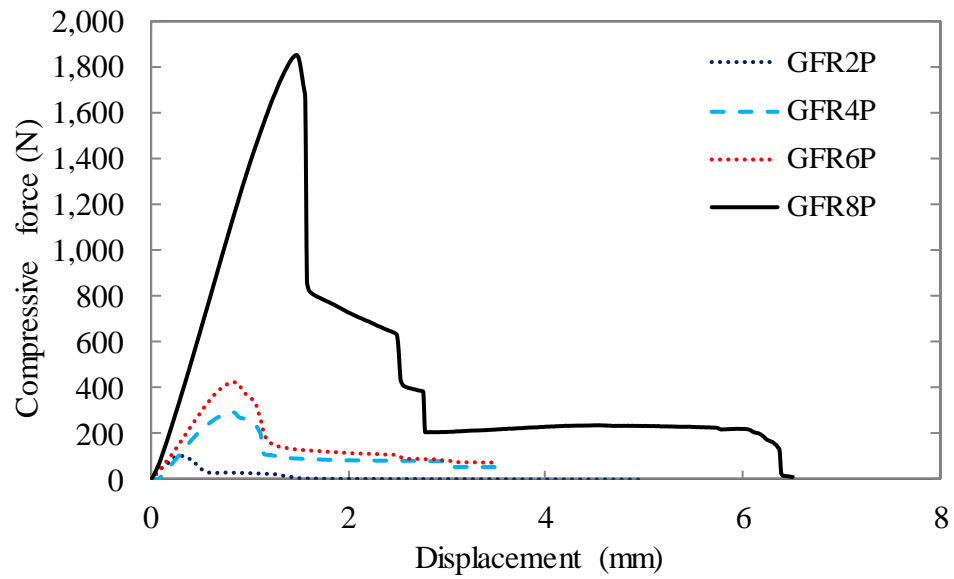


Figure 4.16: Load-displacement traces of the plain GFRP corrugated core samples with different GFRP core thicknesses.

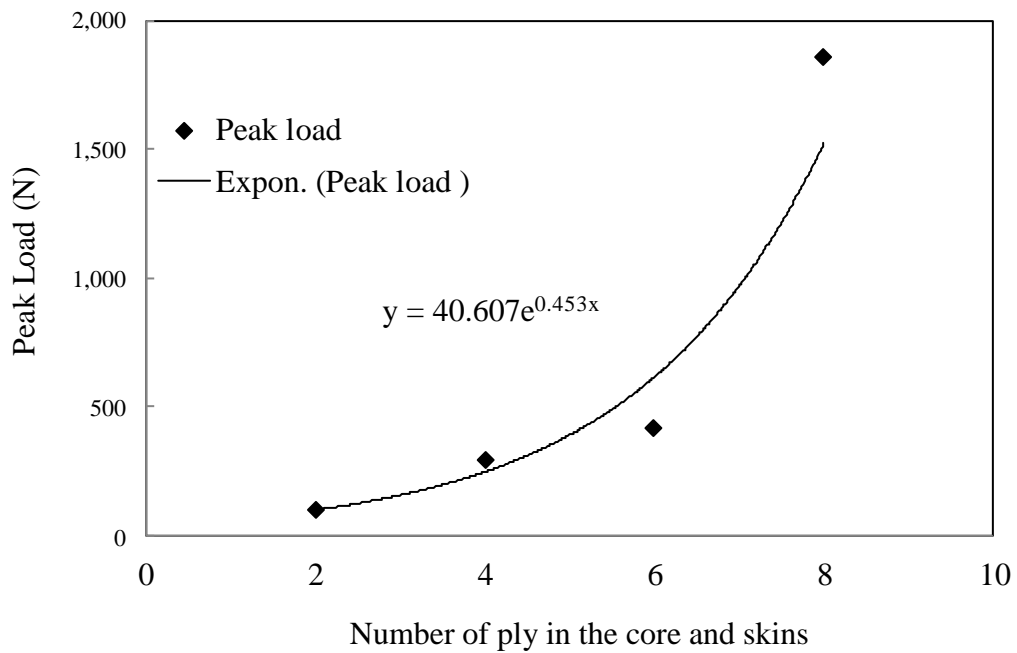


Figure 4.17: The relationship between number of ply and peak load.

4.2.1.3 Hybrid sandwiches reinforced with different types foam core

In this section, results of the hybrid sandwich structures reinforced with different types of foam core under three-point bending will be presented. *Figure 4.18* shows the failure modes of hybrid sandwiches reinforced with different foam core types, i.e. (a) C70.55, (b) C70.130, (c) C70.200. With the same conditions of the GFRP core and skin thickness, the structures with the lower density foam core such as C70.55 and C70.130 withstand the loading reasonably well. Both of them have wrinkles on the top skin surface and also the debonding failure between the foam core and the top skin. In contrast, the foam core with the highest density, i.e. C70.200 shown in *Figure 4.18(c)*, experienced with a crack in the mid-span where the tension and shear failure initiated from the bottom skin at the mid-span. *Figure 4.19* shows load-displacement traces of the hybrid sandwiches reinforced with different foam cores under three-point bending. All of the samples have the similar initial flexural stiffness and the first peak load. Sample C70BT1 with the lowest foam core density indicates a big drop on the load (more than 50%), followed by a stable plateau loading resistance. Interestingly, other two samples, C130BT1 and C200BT1, show some drop of the load after the first peak, then increasing the plateau load to a much higher level until the ultimate failure. This means that the foam density needs to be above a certain level (likely above 100 kg/m^3) to make such the sandwich structure effective to resist bending load.

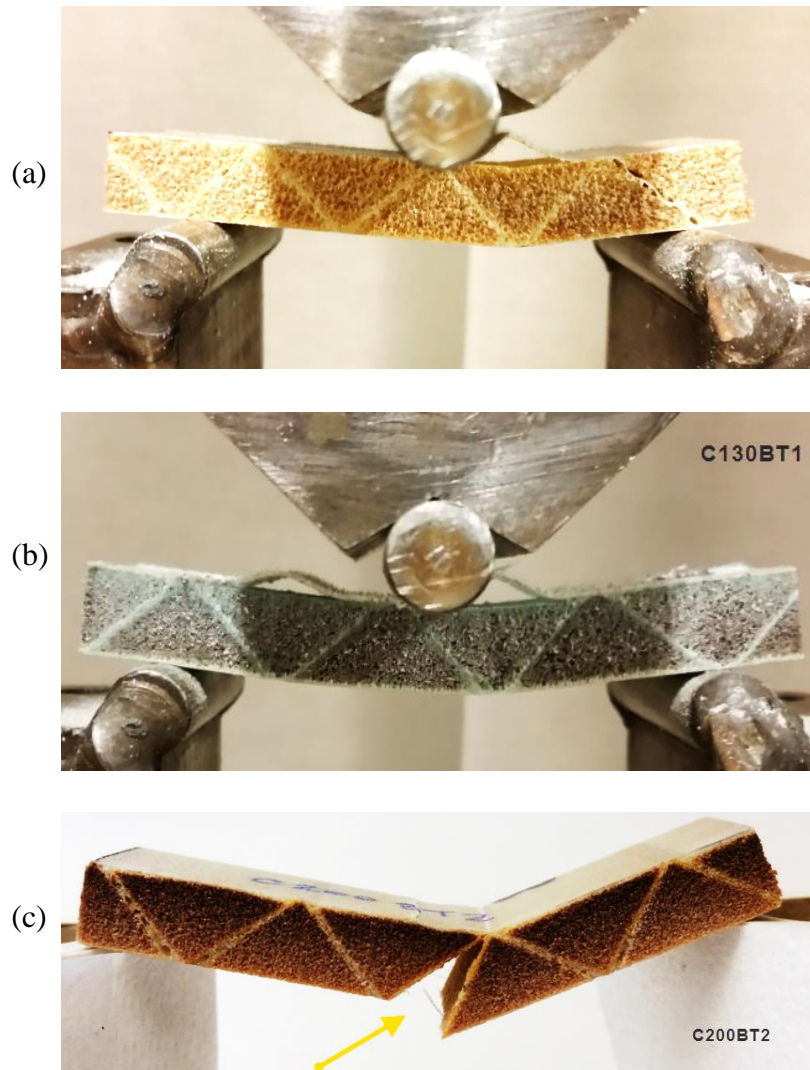


Figure 4.18: The hybrid sandwiches reinforced with different foam core types undergone by three-point bending. Using (a) C70.55, (b) C70.130, (c) C70.200 as the reinforced foam core.

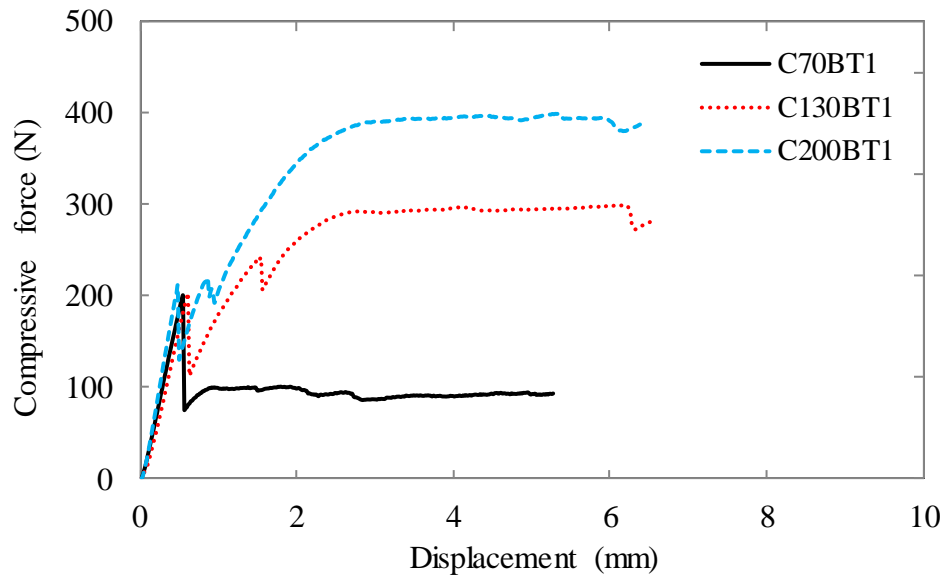


Figure 4.19: Load-displacement traces of the hybrid sandwiches reinforced with different foam core types under three-point bending test.

4.2.1.4 Hybrid composite sandwich beams with mixed foam cores

This section aims to investigate the influence of using mixed prism foam cores under three-point bending. For example, mixing the highest density foam as C70.200 with the lowest density of 52 kg/m^3 as PMI foam. Figure 4.20 shows the deformed shape of MIXFBT1 sample. All the values of flexural stiffness, flexural strength and the peak load seem lower than the other scenarios. No debonding or cracking failure occurred during the test. Only a small elastic buckling revealed on the top skin.

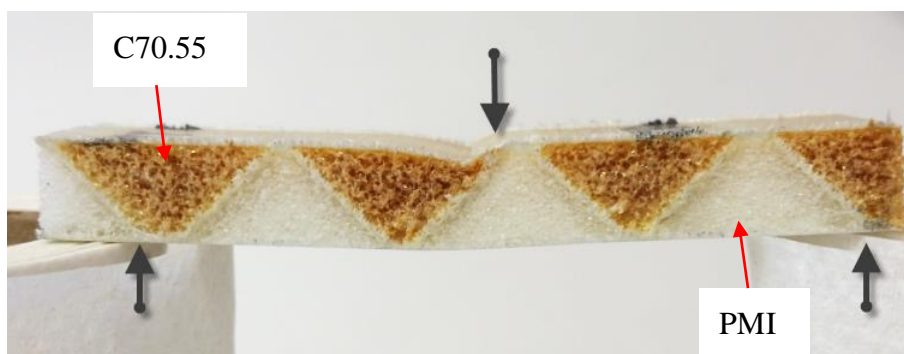


Figure 4.20: The hybrid sandwiches reinforced with mixed foam cores (C70.55 and PMI) under three-point bending test.

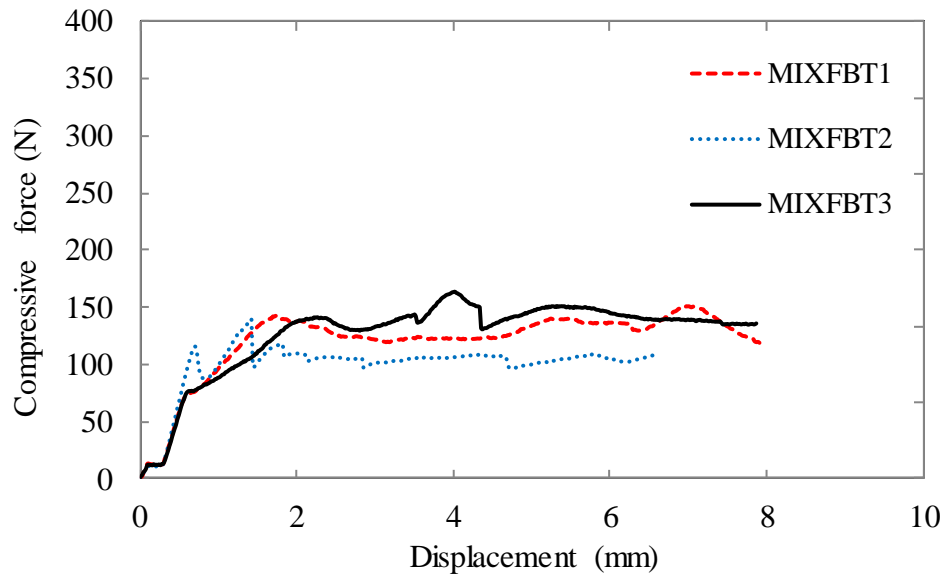


Figure 4.21: Load-displacement traces of the hybrid sandwiches reinforced with mixed foam cores under three-point bending test (MIXFBT1: C200+PMI, MIXFBT2: C50+PMI, MIXFBT3: C130+PMI)

4.2.1.5 Hybrid sandwich structures based on FMLs reinforced with foam cores

The influence of using FMLs reinforced foam core is presented in this section. This study focusses on bending in both x-y and y-z planes, as shown in Figure 4.23(a) and (b). Figure 4.22 shows a comparison of load-displacement curves of the hybrid sandwich structures based on FMLs reinforced with foam cores. Here, the panel with FML skins is expressed in black line, without skins in red line and testing along corrugation direction (y-z plane) in dash line, along x-y plane in solid line. Clearly, the hybrid sandwich structures have a greater flexural modulus when using the FML skin (the black curves in Figure 4.22). The load-displacement traces in x-y plane show slightly greater than that in y-z plane and however, the traces suddenly drop due to crack initiation as shown in Figure 4.23 (a). The hybrid sandwich structure with reinforced FMLs could offer a higher performance under flexural loading along the

longitudinal corrugated core direction or in y-z plane as shown in dash line in Figure 4.22.

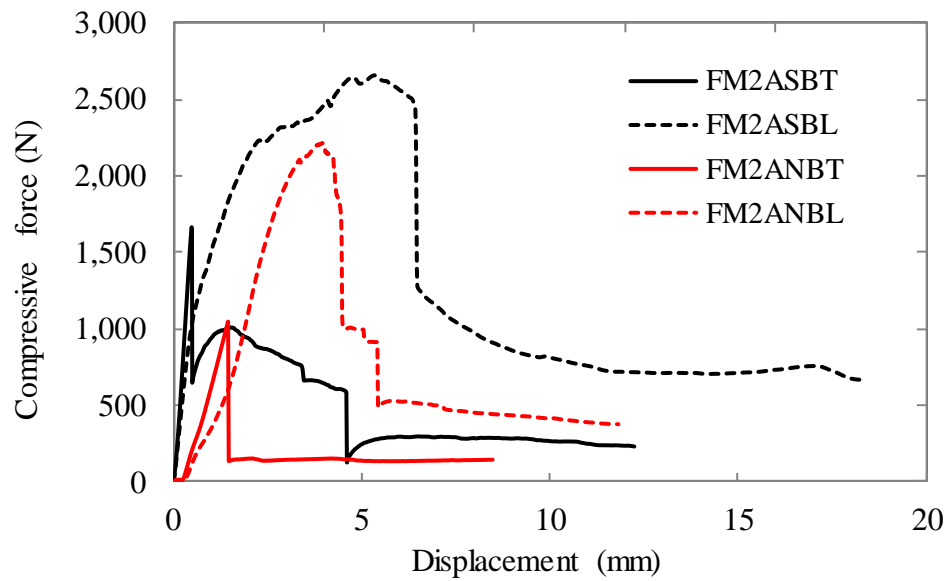


Figure 4.22: Comparison of load-displacement curves of the hybrid sandwich structures based on FMLs reinforced with foam cores considering from the panel with FML skins in black line, without skins in red line and testing along corrugation direction(y-z plane) in dash line, x-y plane in solid line.

It was found that the cracking failure occurred when the hybrid sandwich structure was undergone by three-point bending that applied load at the corrugated core apex (Figure 4.23 (a)). On the other hand, when applied opposite to the corrugated core apex, the skin would start to fail.

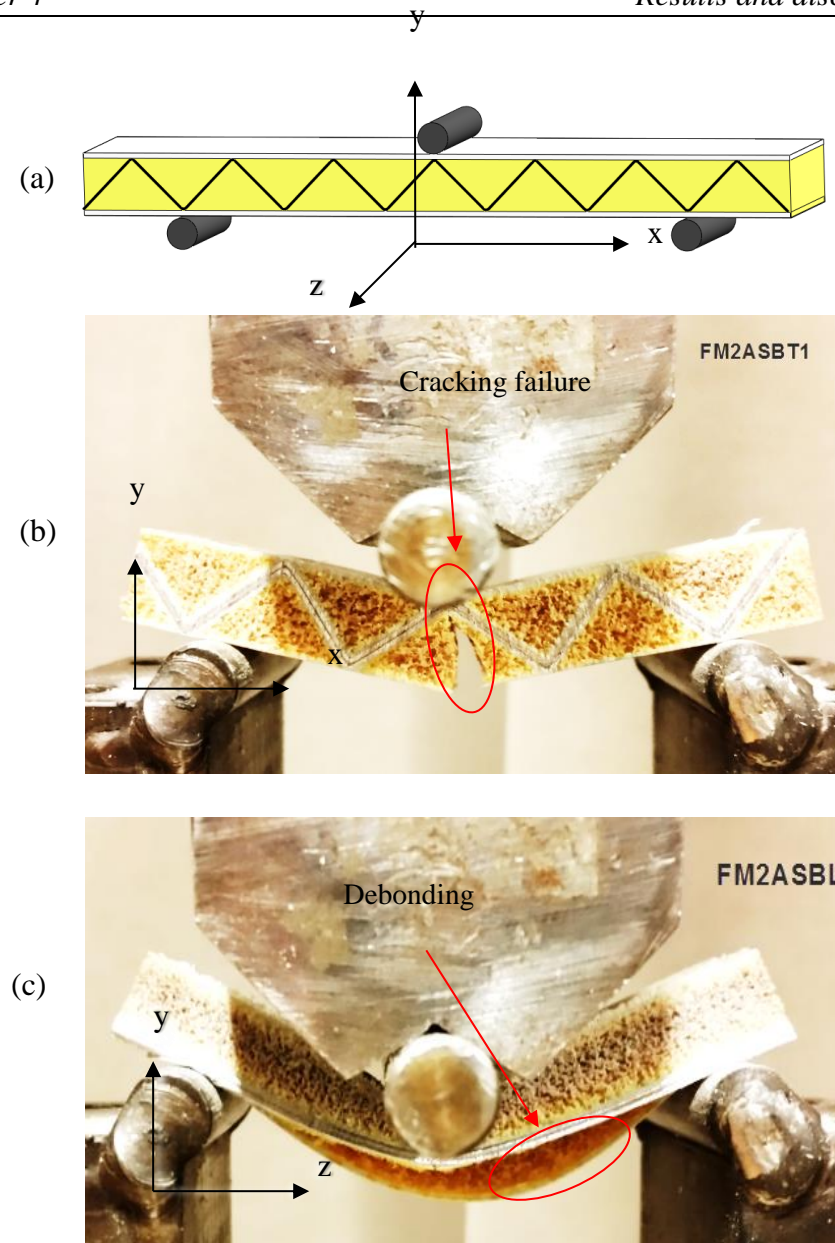


Figure 4.23: The hybrid sandwich structures based on FMLs reinforced with foam cores under three-point bending in (a) the schematic of the test plane, x - y plane, (b) y - z plane.

4.2.1.6 Hybrid sandwich structure with multi-layer and reinforced foam core

Figure 4.24 shows the comparison of load-displacement curves of the hybrid sandwich structures based on multi-layers under three-point bending in different testing planes. The load-displacement curve (red line in Fig. 24) of the hybrid sandwich structure loaded in x - z plane, in which the corrugated-core is up right to the loading direction,

offers a higher flexural modulus, but with a significantly drop on the load after the peak. The crack propagation begin to start across the skin (Fig. 4.25c).

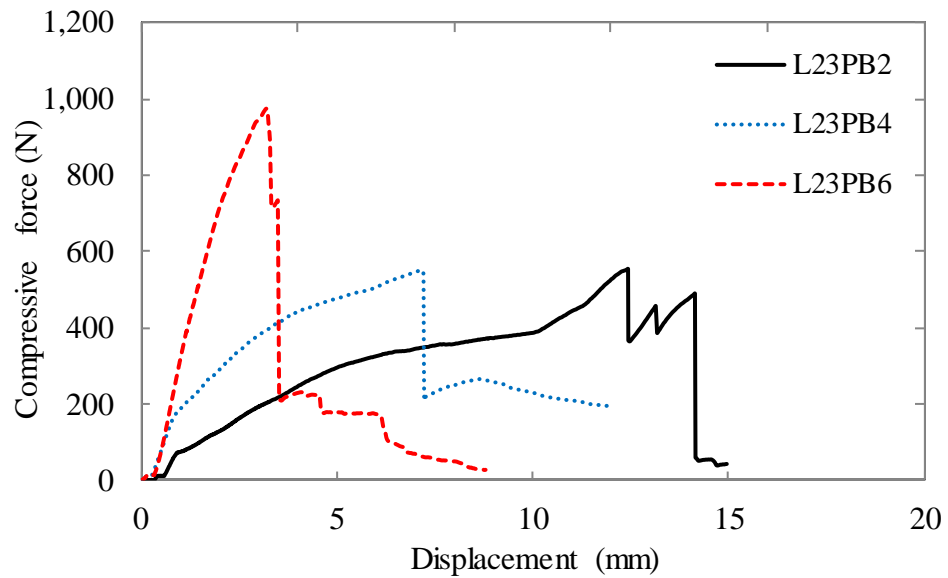


Figure 4.24: Comparison of load-displacement curves of the hybrid sandwich structures based on multi-layers under three-point bending in different testing plane.

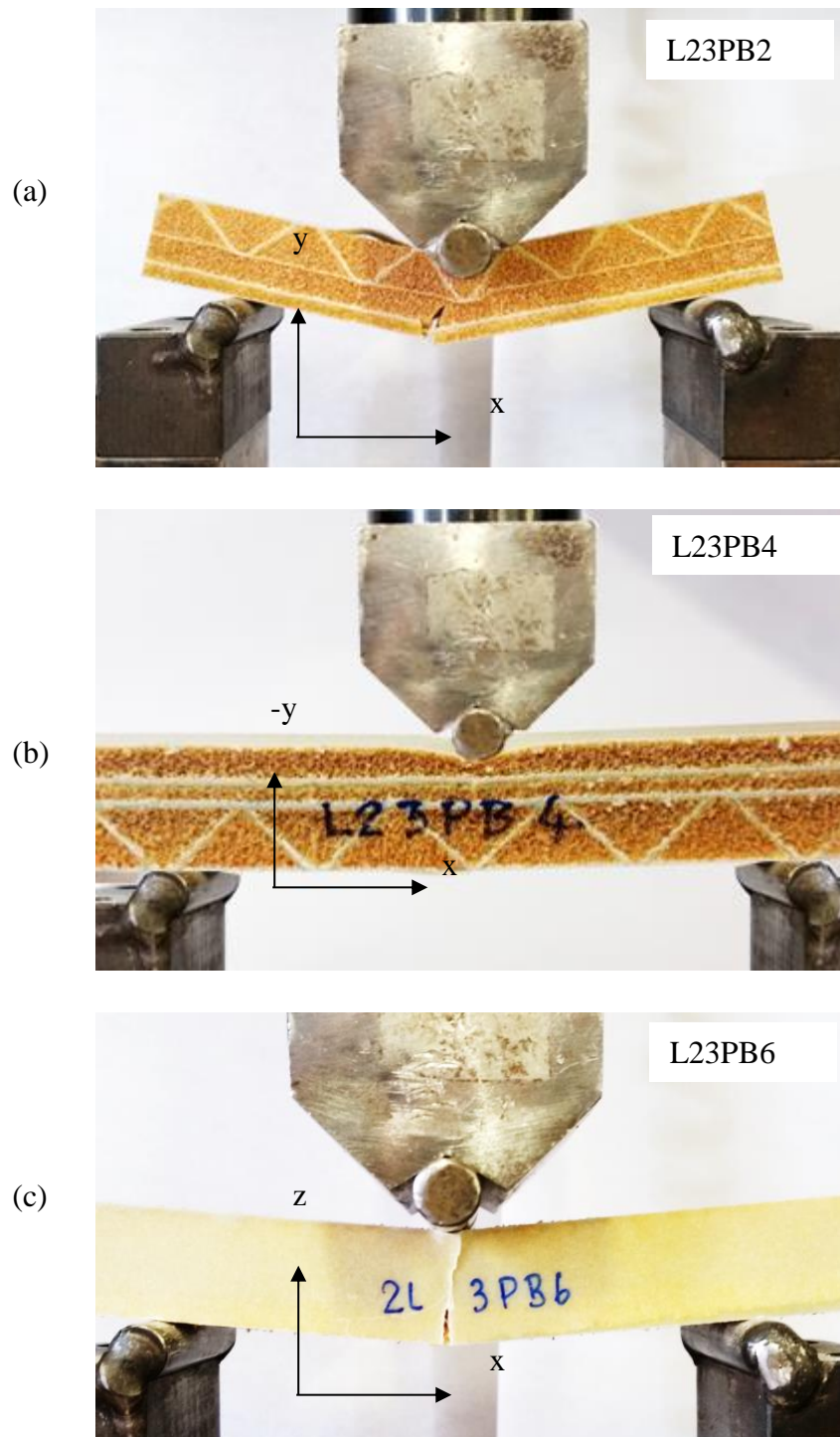


Figure 4.25: The hybrid sandwich structure with multi-layer and reinforced foam core under three-point bending in (a) x - y plane, (b) $(-y)$ - x plane, (c) x - z plane.

4.2.1.7 Hybrid sandwiches with different unit cell size

Figure 4.26 shows the comparison of load-displacement curves of the hybrid sandwich structures based on reinforced foam with different unit cell sizes (unit cell base line 10, 20 and 40 mm) under three-point bending. Their traces reveal the similar trend of the initial flexural stiffness. A smaller unit cell size has a lower flexural strength. The sandwich samples seem initiating the fail at the support points with large embedment deformations, as shown in Figure 4.27. This was caused by using a low density foam core. The sandwich structure will likely fail by cracking at the bottom of the mid-span other than the embedment failure if use a higher density foam core.

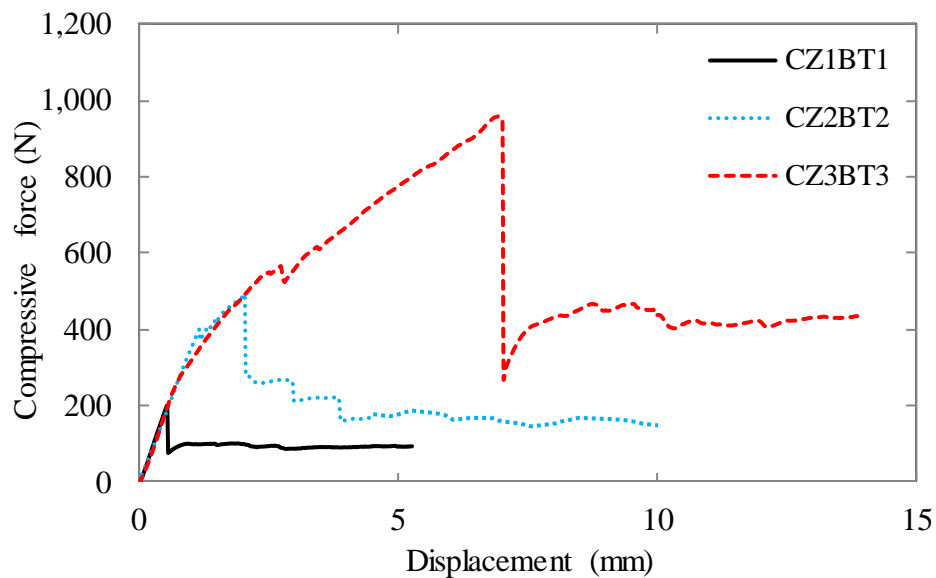


Figure 4.26: Comparison of load-displacement curves of the hybrid sandwich structures based on reinforced foam with different unit cell sizes under three-point bending test.

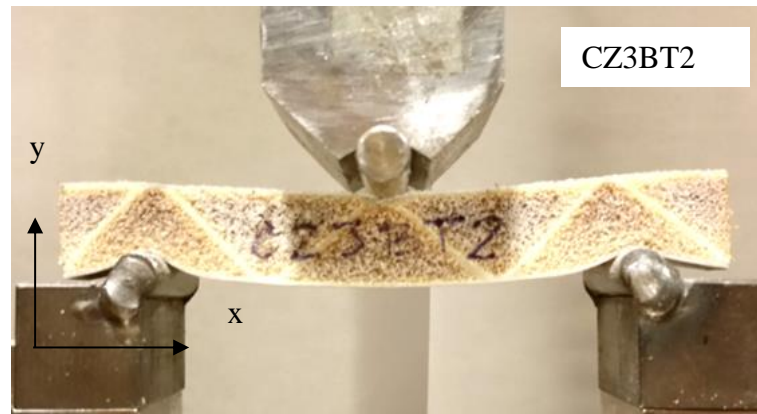


Figure 4.27: The hybrid sandwiches with unit cell sizes of 40 mm under three-point bending test.

4.2.2 Static compression behaviour of hybrid corrugated sandwiches

In order to find out the compression strength and stiffness of various hybrid sandwich structures under lateral compression loading, quasi-static compression tests were conducted.

4.2.2.1 Compression test compliance

In order to obtain a high degree of accuracy in the overall compression test results, a calibration test was conducted to correct the raw data. Prior compression test, the hyper-rigid steel plate were placed instead of the sample. The testing result was revealed the compliance. *Figure 4.28* shows typical raw data in black line, a compliance curve in black-dash line and the corrected curve for a compression test on a corrugated-core structure in red line. Here, the example of using compliance curve taken from the results of compression test on sample GFR8P05 to correct the data.

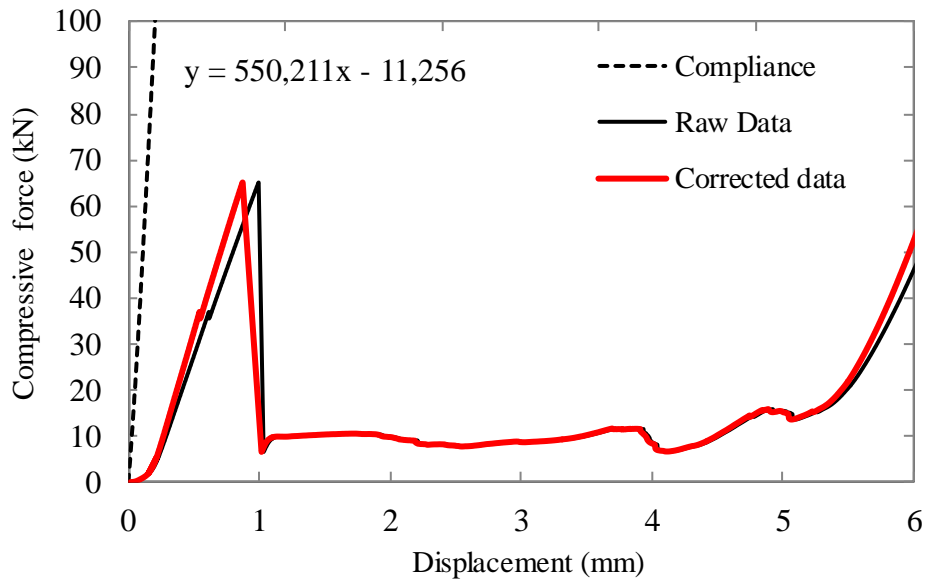


Figure 4.28: Load-displacement trace for a corrugated-core sandwich sample GFR8P05. The error displacement is removed from the raw data and replaced by the correct data plotted in red.

4.2.2.2 The effect of core thickness of plain GFRP corrugated sandwich structures under compressive loading

Typically, the load-displacement traces for the plain GFRP corrugated sandwich structures exhibited brittle behaviour, involving extensive crushing associated with a huge load drop, as shown in Figure 4.29. Figure 4.30 shows the process of damage development of the hybrid sandwich panel based on triangular corrugated-core (GFRP) in side view. From the starting point to the peak load in the stage I, the compressive load increases linearly (Fig. 4.30) until followed by the drastic load drop beyond the elastic deformation. At the peak point, the compressive strength is indicated. The gradient of the curve in the linear region can be used to determine the compressive modulus of the sandwich structure based on the corresponding stress and strain curve. After the peak point, the compressive load consequently drops almost

80%. This indicates that strength of the sandwich structure has decreased by approximately 80%. The stage II is simply a plateau one with a progressive crushing on the core. The fibres begin to fracture in the middle of individual corrugations. Consequently, the formation of hinges occurs in the middle of the cell wall where the breaking begins. Finally, the structure experienced densification (the stage III) at the cell wall close to the lower skin, as evidenced in Region III (*Figure 4.29*).

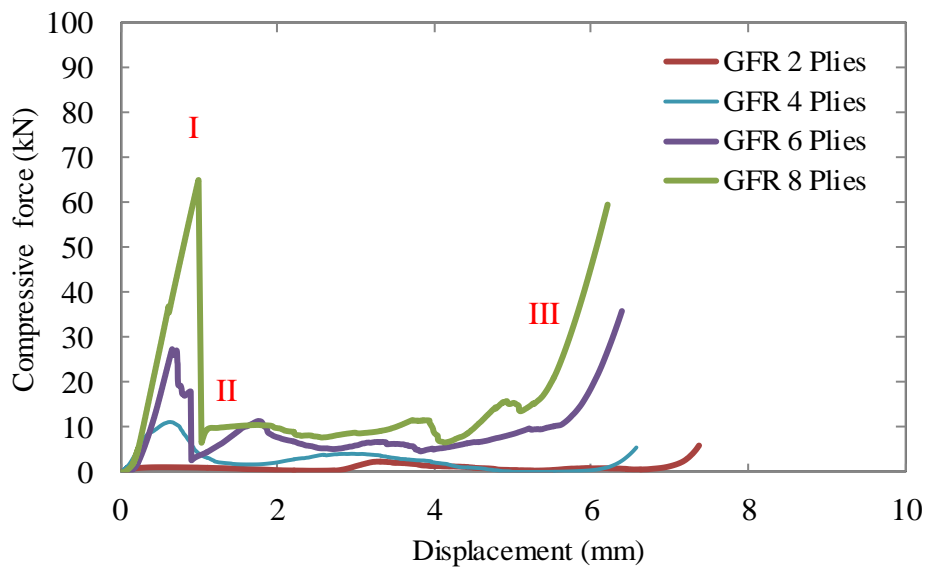


Figure 4.29: Load-displacement traces of hybrid sandwich structures with different thicknesses of GFRP corrugated core.

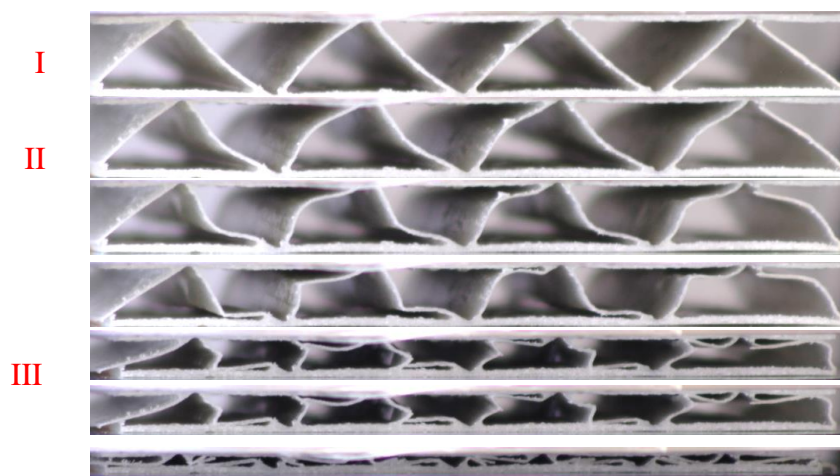


Figure 4.30: The process of damage development of the hybrid sandwich panel based on triangular corrugated-core (GFRP) in side view.

It was found that the relationship between peak load and GFRP core thickness increases exponentially when increasing the number of plies (Fig. 4.17).

Considering the failure mode, Figure 4.31 reveals the failure modes of GFRP corrugated-core between (a) the sandwich panel from [5] that used a conventional bonding technique with adhesive agents and (b) the sandwich panel in this study that the new technique is used to bond sandwich core and skins. It can be clearly seen that the debonding failure mode occurred when using the conventional technique. On the other hand, the new bonding technique could eliminate this type of failure mode.

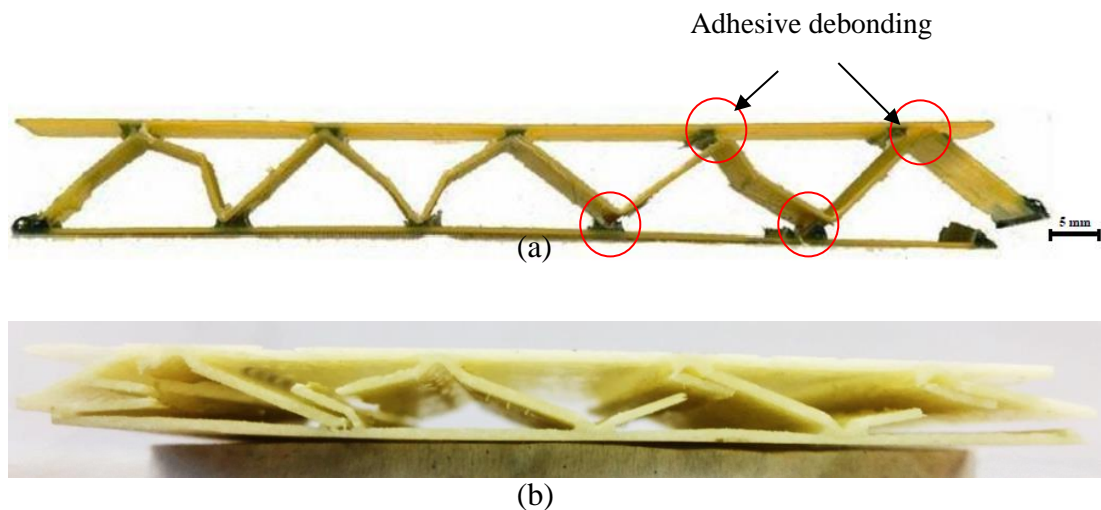


Figure 4.31: Comparison of failure mode of GFRP corrugated-core between (a) the sandwich panel from [28] that used a conventional bonding technique with adhesive agents, (b) the sandwich panel in this study that the new technique to bond sandwich core and skins.

4.2.2.3 The effect of different core configurations

Figure 4.32 shows load-displacement traces of hybrid sandwich structures in different core configurations. It can be clearly seen that the hybrid corrugated-core sandwich structures outperforms other structures in terms of peak load or compressive strength and their compressive stiffness. For the sandwich structures with no reinforced foam

core such as trapezoidal and triangular core, their compressive modulus are also similar to the other sandwich structures. However, there is a sudden drop of the load carrying capacity as the cell wall fracture, which is reflected in the load-displacement traces. Consequently, the compressive load decreased approximately 80% until densification has been reached. However, the sandwich structures reinforced with foam core have their load-displacement traces gradually dropped after reaching the yield point. The sandwich structure with the square foam configuration has an outperformed characteristic under compressive loading. Its energy absorption, estimated by the area under load-displacement curve, is also the highest, followed by the trapezoidal and triangular foam configuration respectively.

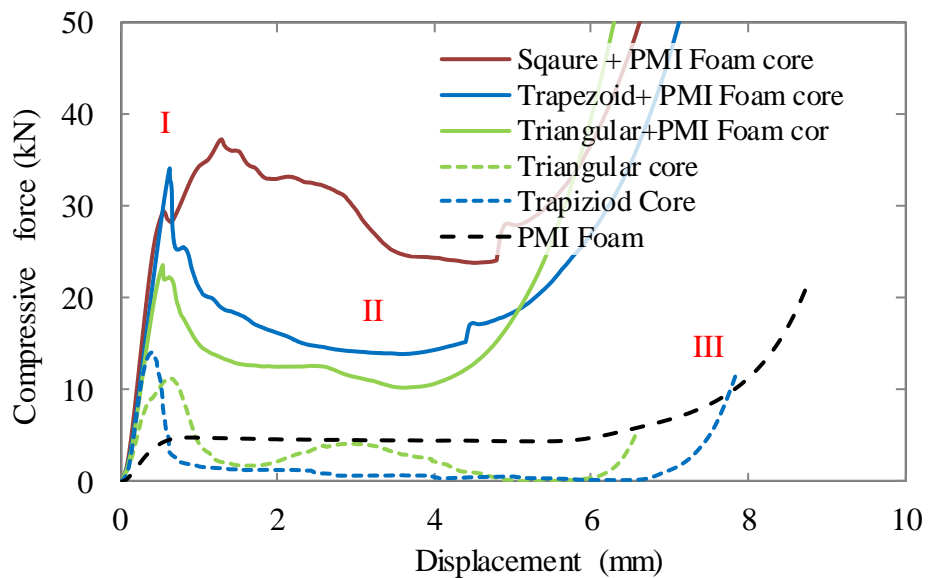


Figure 4.32: Load-displacement traces of hybrid sandwich structures in different core configurations.

Figure 4.33 (a) shows the damage development of the hybrid sandwich panel based on triangular GFRP corrugated and reinforced PMI foam core in side view. The stage I is simply related to the linear elastic deformation till the peak load and then the sudden

drop of the loading level. This is followed by buckling and debonding failure during the stage II, characterised as a plateau stage. The foam core plays an important role to support both sides of the cell wall. Therefore, the foam reacts against cell wall deflation. However, when the externally applied load at the cell wall builds up and becomes greater than the strength of foam core or interface bonding strength, buckling and/or debonding failure will occur. The prolonged stage II with a reasonably high plateau will be crucial to absorb more energy. Once the structure under compression gets into the stage III, i.e. densification, the energy absorbed will be limited.

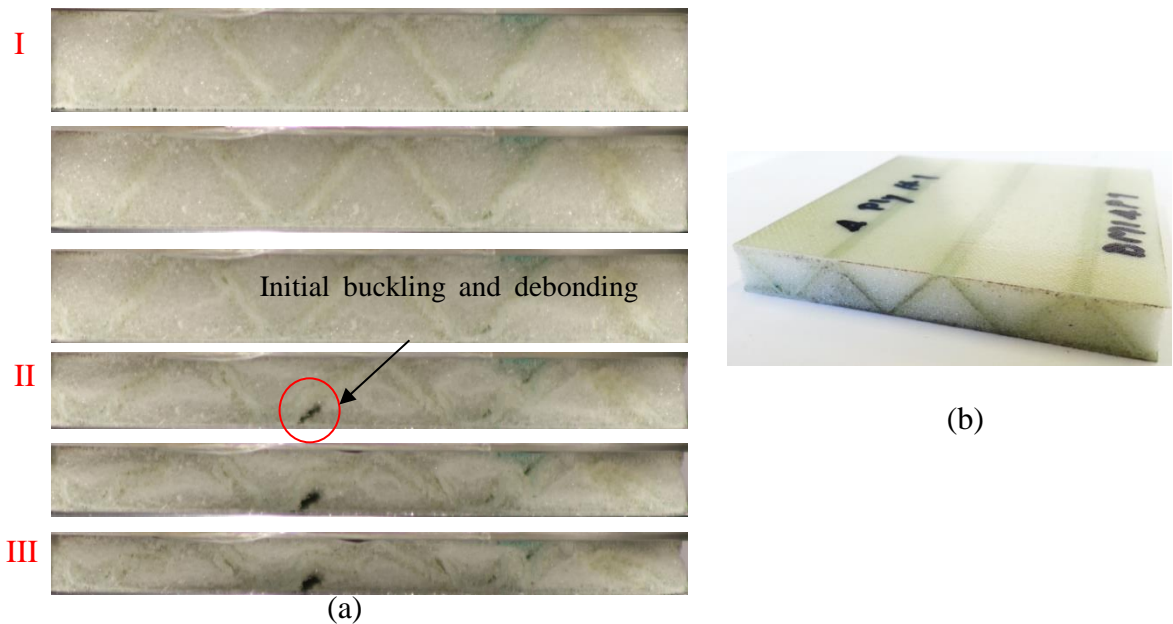


Figure 4.33: (a) the process of damage development of the hybrid sandwich panel based on triangular corrugated and reinforced PMI foam core in side view, (b) the virgin panel.

Figure 4.34 (a) shows the progressive damage development of the hybrid sandwich panel based on square corrugated and reinforced PMI foam core. Each cell wall of this sandwich structure is straight up right or perpendicular against both its skins.

Therefore, the square configuration has a higher tolerance when subjected to compressive loading, but has a lower tolerance when experiencing with shear loading as described in the literature review chapter.

Notably, the imperfect bonding is found in Figure 4.34(a). Unlike the other types, the additional horizontal pressure was applied to rig during the fabrication process in order bond each foam block with the molten GFRP prepreg. However, the lateral restraints applied may not be uniform due to the simplified mould when the hot press applies the load in the vertical direction. Therefore, the imperfect bonding left inside the structure by this reason. During the stage II, the buckling and debonding failure occur almost at every unit cell wall.

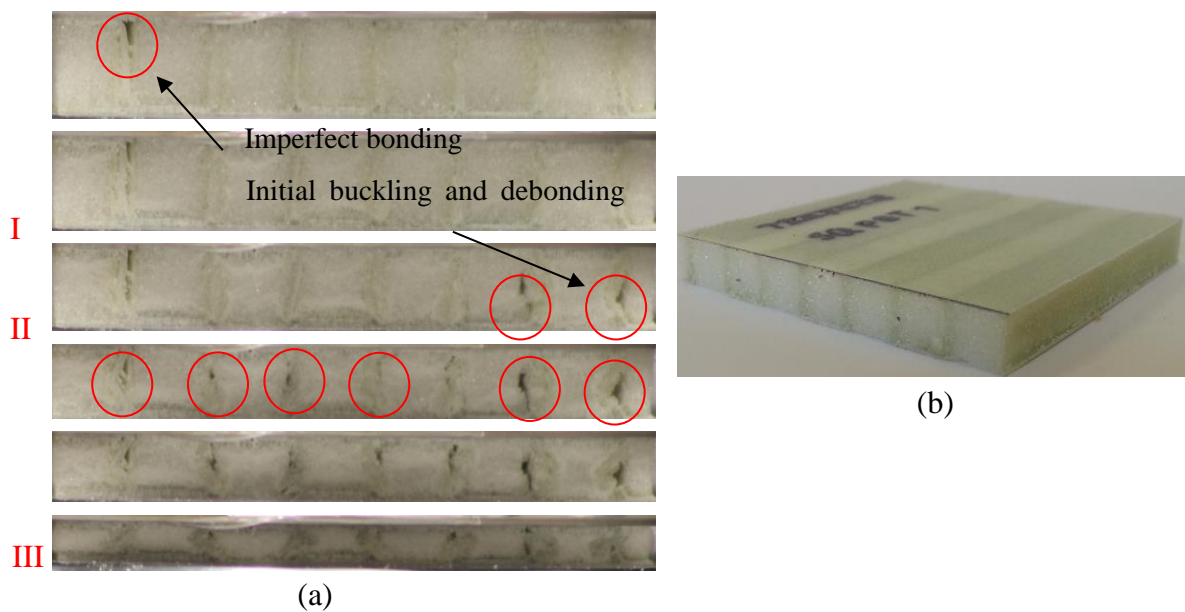


Figure 4.34: (a) the process of damage development of the hybrid sandwich panel based on square corrugated and reinforced PMI foam core in side view, (b) the virgin panel.

Figure 4.36 shows the progressive damage of the hybrid sandwich panels based on trapezoidal corrugated and reinforced PMI foam core. The similar behaviour as

triangular or square sandwich types was shown in the figure. An initial buckling and debonding failure mainly happens in the stage II.

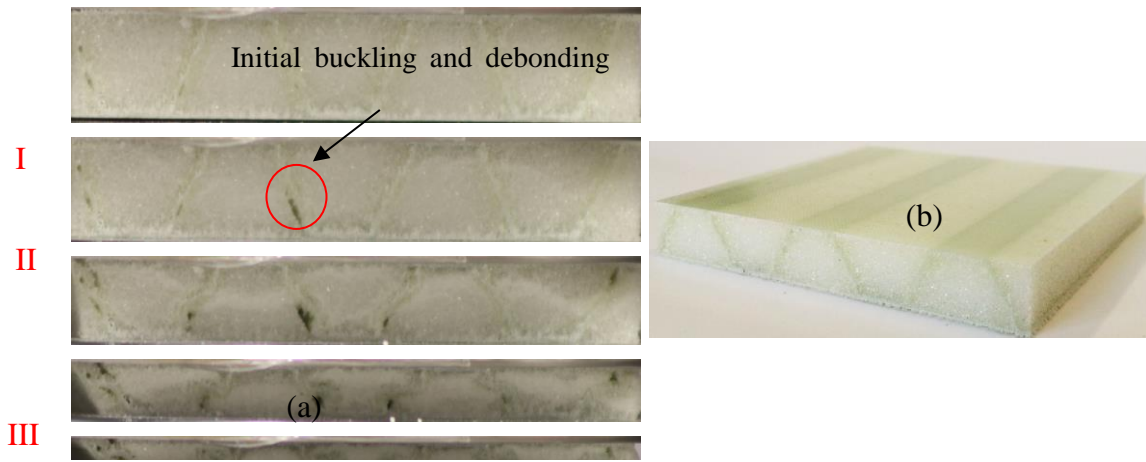


Figure 4.35: (a) the process of damage development of the hybrid sandwich panel based on trapezoidal corrugated and reinforced PMI foam core in side view, (b) the virgin panel.

Figure 4.36 (a) shows the process of damage development of the hybrid sandwich panel based on trapezoidal corrugated core without reinforced foam. It is clearly seen that the initial buckling failure is developed in the stage I, followed by post buckling failure in the stage II, further to the breaking and crunching into the densification stage III.

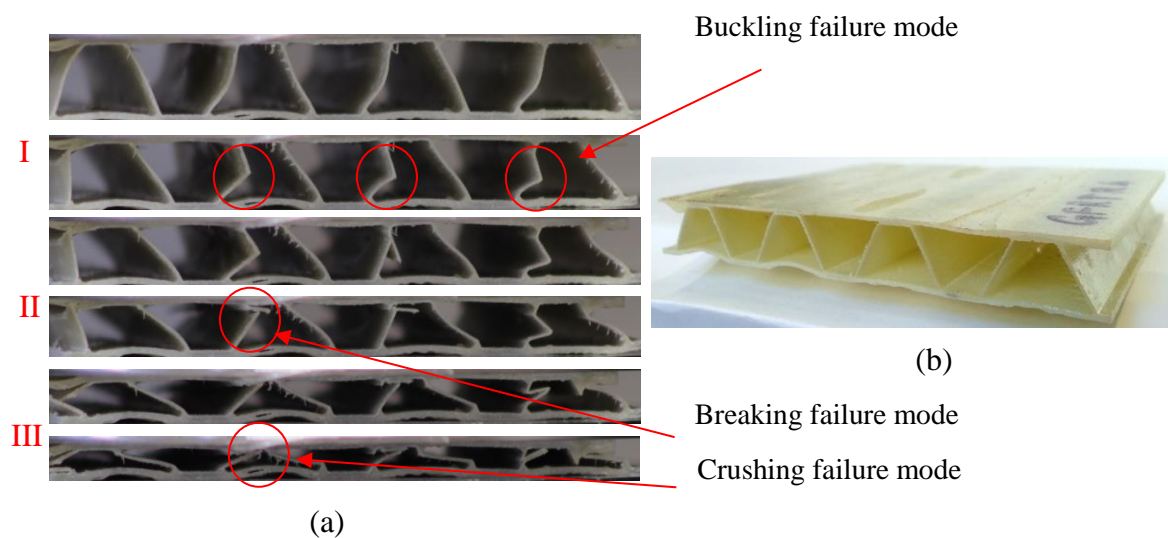


Figure 4.36: (a) the process of damage development of the hybrid sandwich panel based on trapezoidal corrugated core in side view, (b) the virgin panel.

4.2.2.4 The effects of thickness of GFRP corrugated core sandwich structure reinforced foam cores under compression

Figure 4.37 compares the effects of thickness of the GFRP triangular hybrid core sandwich panels, with reinforced PMI foam core. The force-displacement traces indicate that the overall features are similar to the corresponding triangular core specimens without the foam core, but with much higher plateau resistance. It is observed that with the increasing of ply number and therefore the increase in the GFRP core thickness, the compressive energy absorption capabilities of the sandwich panels increase, with the higher plateau level and longer plateau stage for the higher number of ply.

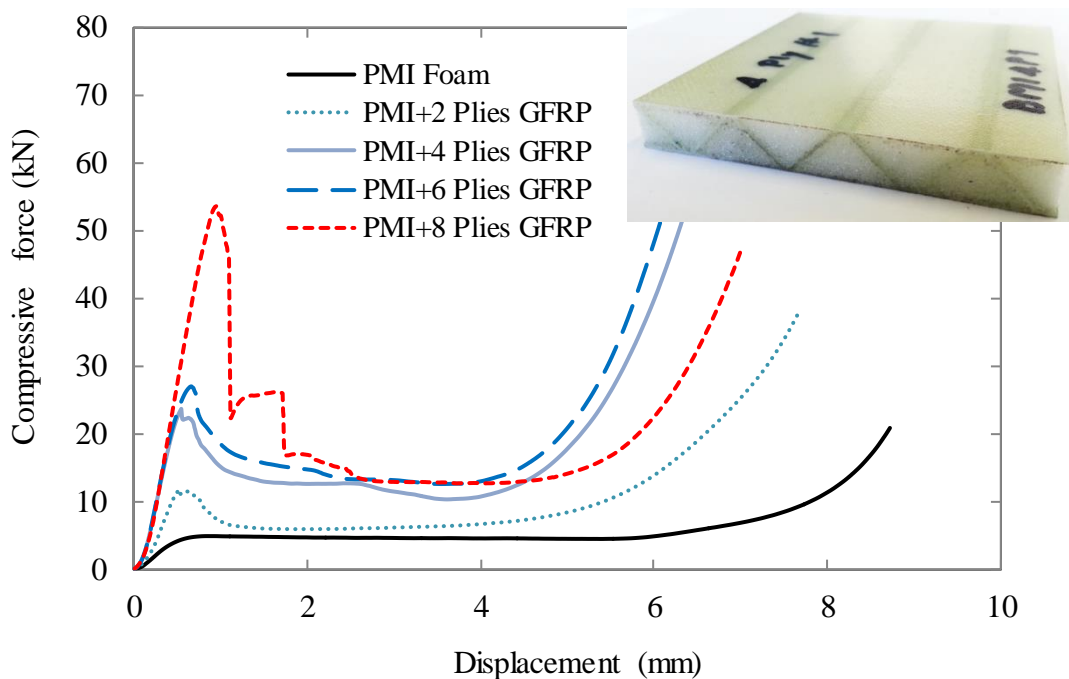


Figure 4.37: Load-displacement traces of hybrid sandwich structures based on GFRP core reinforced PMI foam showing in different thicknesses of GFRP corrugated core.

4.2.2.5 The effects of different types of foam cores

In this section, the effects of different types of foam core were investigated on the compression behaviour of the sandwich panels. Figure 4.39 shows load-displacement traces of hybrid sandwich structures based on GFRP reinforced foam core with different types of the foam. From this investigation, it was proved that a higher density of reinforced foam core would offer a higher structural performance under compressive loading, in terms of higher plateau level with increasing resistance.

The results from combination of reinforced form cores reveal that the sandwich structural performance is dependent on the overall density and foam core characteristics. For example, if both foam cores have the same density, the response of sandwich structure under compressive loading is likely similar to mono-type foam core. If the foam core is made with combined densities, the response of the sandwich structure under compressive loading will appear in a different manner. This can be noticed at the combination core of C200+PMI+GFRP that the response in its load-displacement trace shows a clear hardening after the elastic limit. The prism shape leads the foam core fails at the tip first, then the tip will be flattened by the increased compressive force. The flattened area then gradually expands out from the middle. These characteristics could be used to design this kind of sandwich structure to optimise the energy absorption energy.

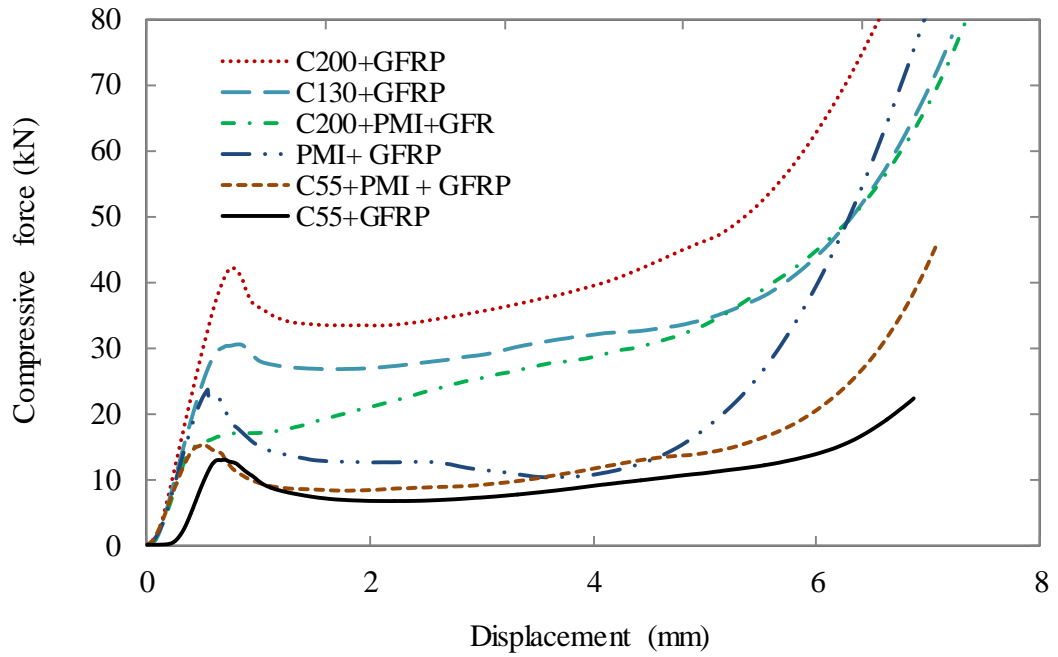


Figure 4.38: Load-displacement traces of hybrid sandwich structures based on GFRP reinforced foam core showing in different types of foam core.

Figure 4.39(a) - Figure 4.42(a) show the progressive damage of the hybrid sandwich panels based on triangular corrugated reinforced with C70.55 foam core (Figure 4.39(b)), with C70.55 and PMI foam core (Figure 4.40(b)), C70.200 and C70.55 foam core (Figure 4.41(b)) and C70.130 (Figure 4.42(b)). Notably, the buckling failure mode occurred with mostly asymmetric deformations when the same density of foam core combined. Otherwise, the buckling direction would expand to the foam core with lower density, for example in Figure 4.40(a) and Figure 4.41(a).

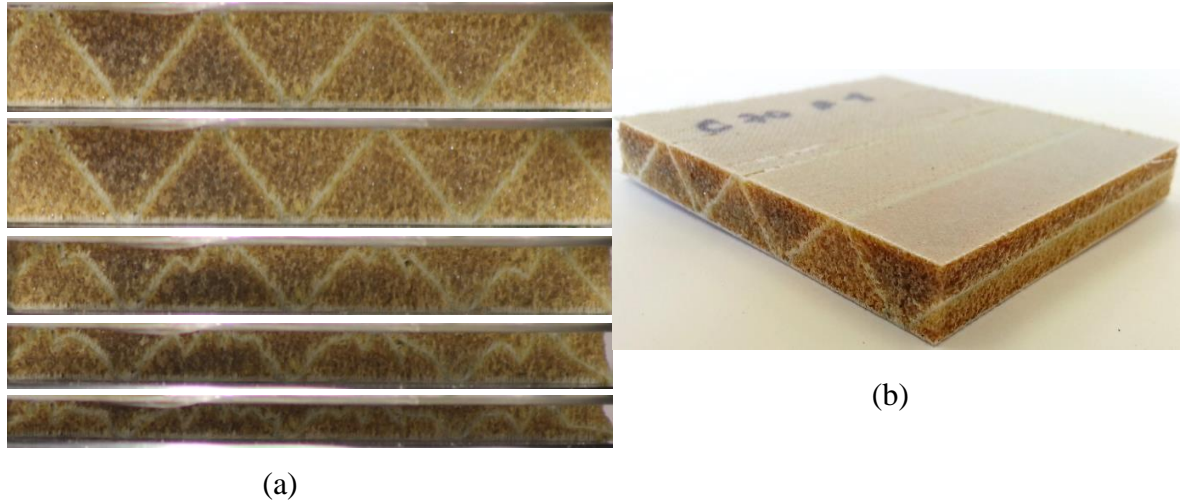


Figure 4.39: The (a) process of damage development of the hybrid sandwich panel based on triangular corrugated reinforced C70.55 foam core in side view, (b) virgin panel.

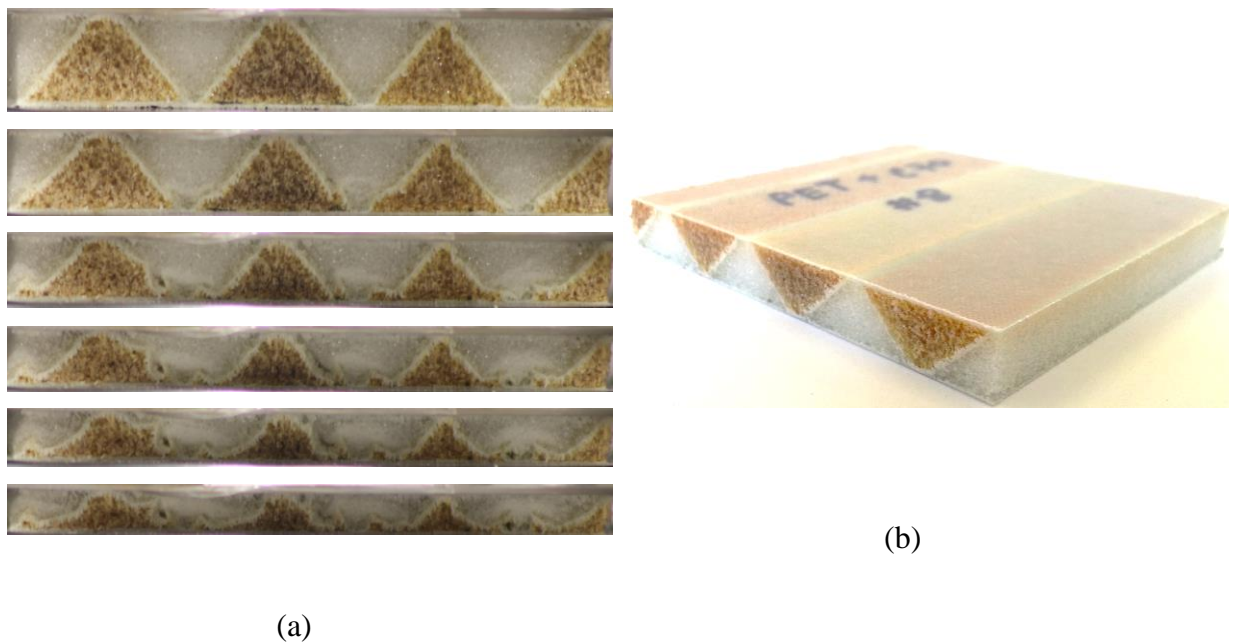


Figure 4.40: The (a) process of damage development of the hybrid sandwich panel based on triangular corrugated reinforced C70.55 and PMI foam core in side view, (b) virgin panel.

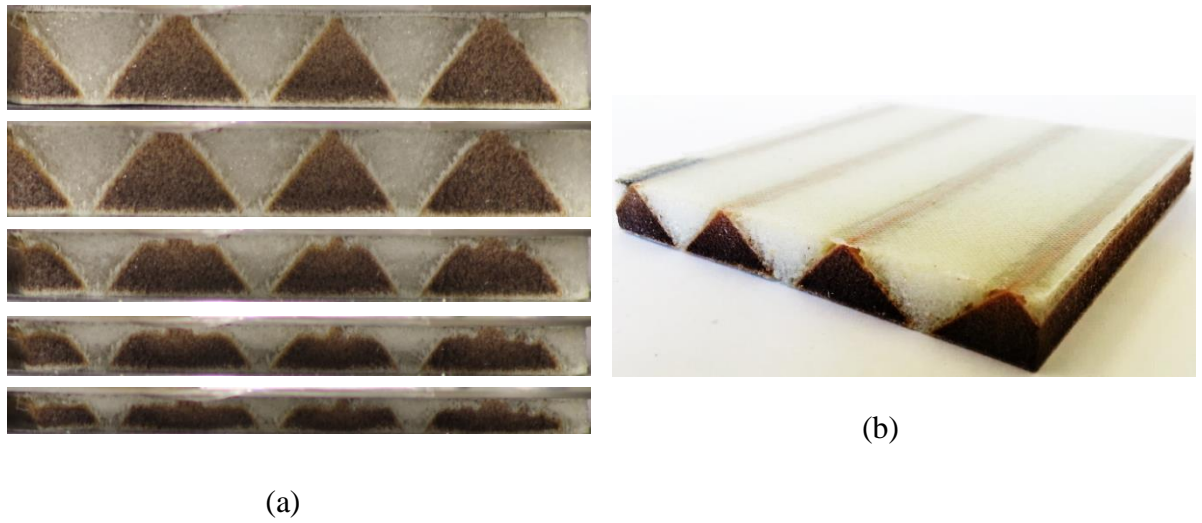


Figure 4.41: The (a) process of damage development of the hybrid sandwich panel based on traingular corrugated reinforced C70.200 and C70.55 foam core in side view, (b) virgin panel.

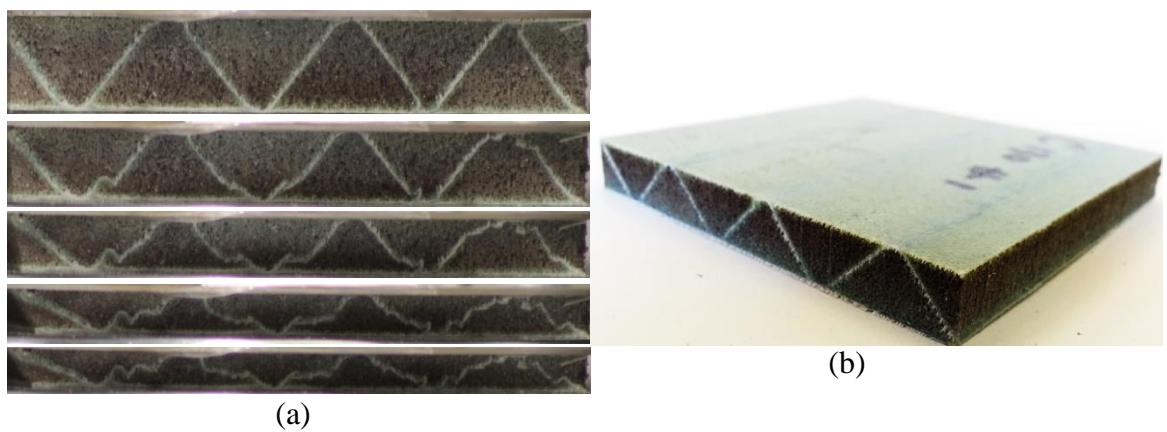


Figure 4.42: The(a) process of damage development of the hybrid sandwich panel based on traingular corrugated reinforced C70.200 and C70.55 foam core in side view, (b) virgin panel.

4.2.2.6 The effects of different foam core densities and multi-layer

Figure 4.43 shows the relationship between crosshead displacement over the sample and their compressive force response for homogenous and gradient foam core type. Initially, the compressive force increases linearly with a very small displacement less than 1 mm and thereafter with a series of non-linear responses. The homogeneous foam core exhibited a steep linear response with their peak compressive force yielded at approximately of 15 kN. After having the first peak force, the homogenous foam core seems demonstrating couple of non-linear plateau force regions, followed by densification. Along the plateau region of force – displacement curves it was noticed series of fluctuated forces with respect to the crosshead displacement, which is likely attributed to series of failures on the structure. There was also evidence of foam separation from the triangular corrugated structures with embedded homogeneous foam (Figure 4.44(a)). In contrast, there was close contact in place between gradient foam and corrugated structures as the crosshead displacement continues. The structure deforms continuously as the increased compression loading applied on the sample. The progressive deformation modes of are shown in the Figure 4.44(a).

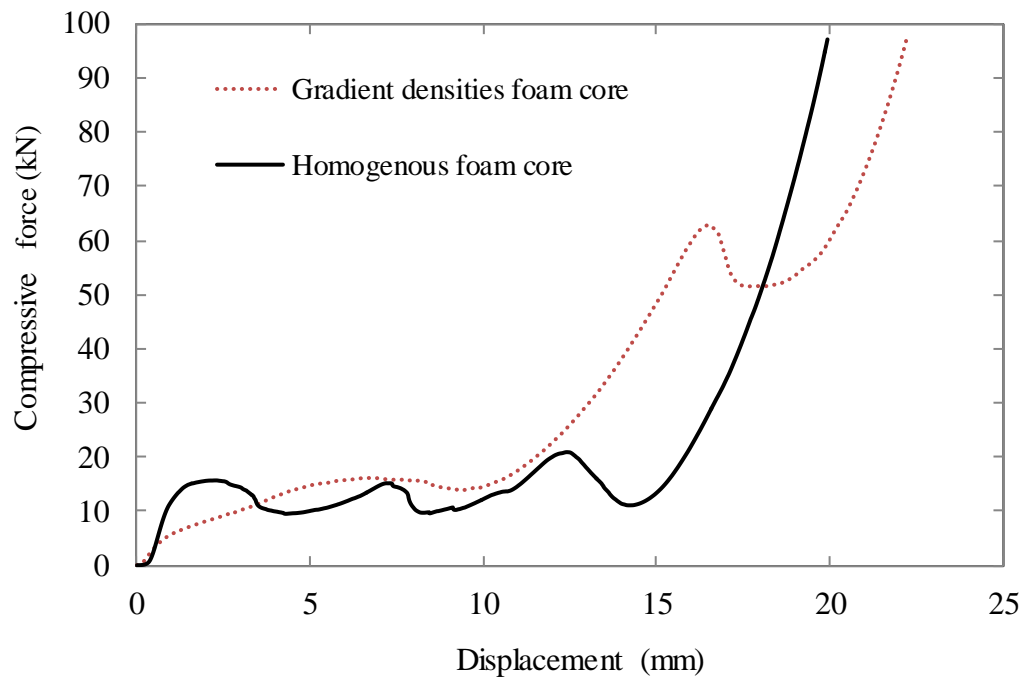


Figure 4.43: Load-displacement traces of hybrid sandwich structures based on GFRP reinforced foam core showing in different foam core densities and multi-layer.

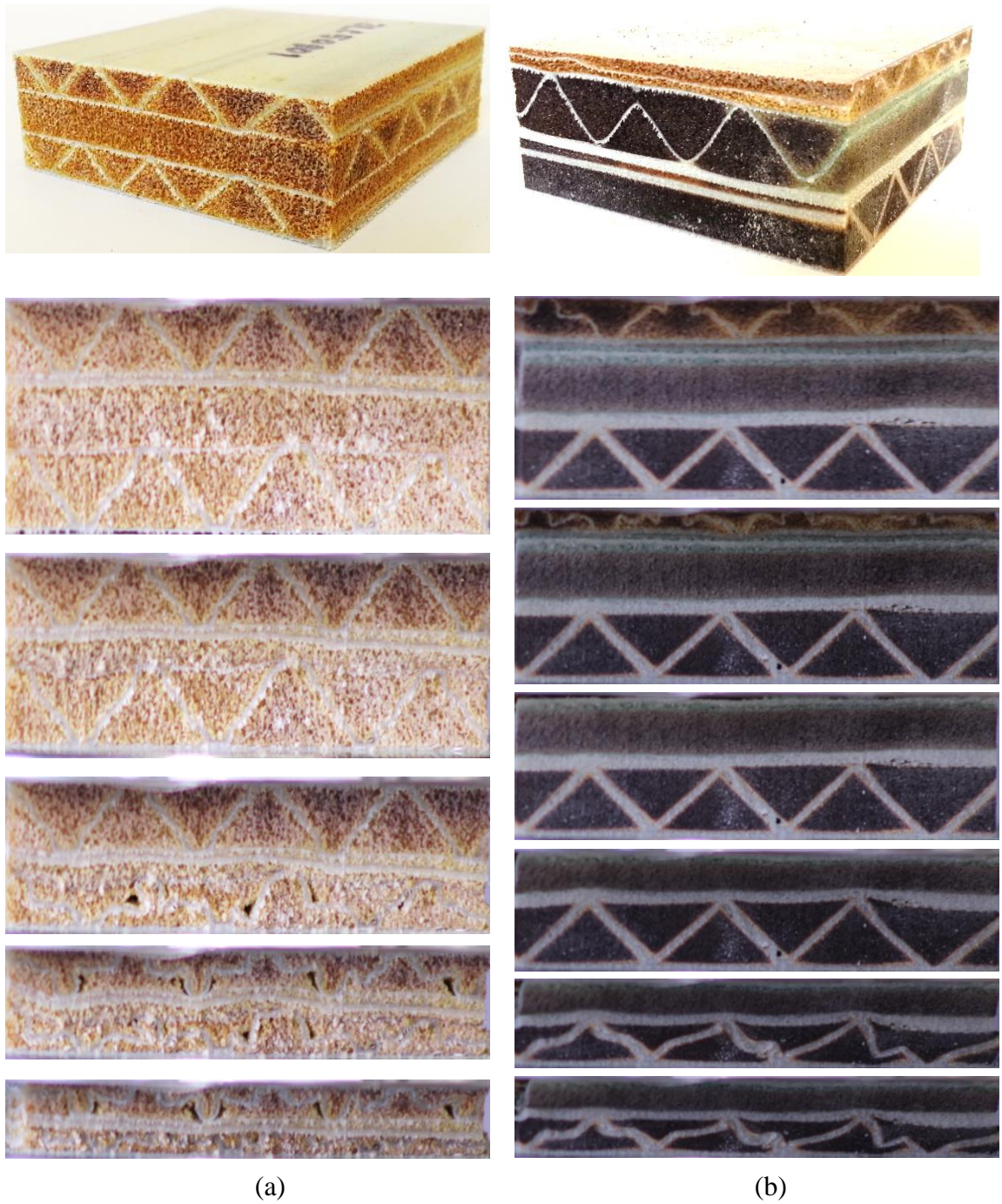


Figure 4.44: The progressive damage of the hybrid sandwich panel based on triangular corrugated reinforced foam core column (a) homogeneous core density, (b) gradient core density.

4.2.2.7 The effects of unit cell size

It is expected that the performance of the corrugated sandwich structures is influenced by the size of the unit cell of the sample. Figure 4.45 shows that the peak force of the structures increases with respect to the unit cell size. The force versus displacement trace indicates a linear response until the peak load, followed by a steep drop in load. This drop corresponds to the preliminary failure on the sample and the load seems exhibiting a plateau region over displacement as it continues to crush. After the plateau region, it follows with a sharp densification. The peak force of the sample with smaller unit cell size (20 mm) results at 12.5 kN. For the samples with medium (30 mm) and large (40 mm) unit cell sizes, the peak load yields in two and three times of that smaller unit cell size, respectively. These results highlight the influence of unit cell size cells on the compressive strength of the structures.

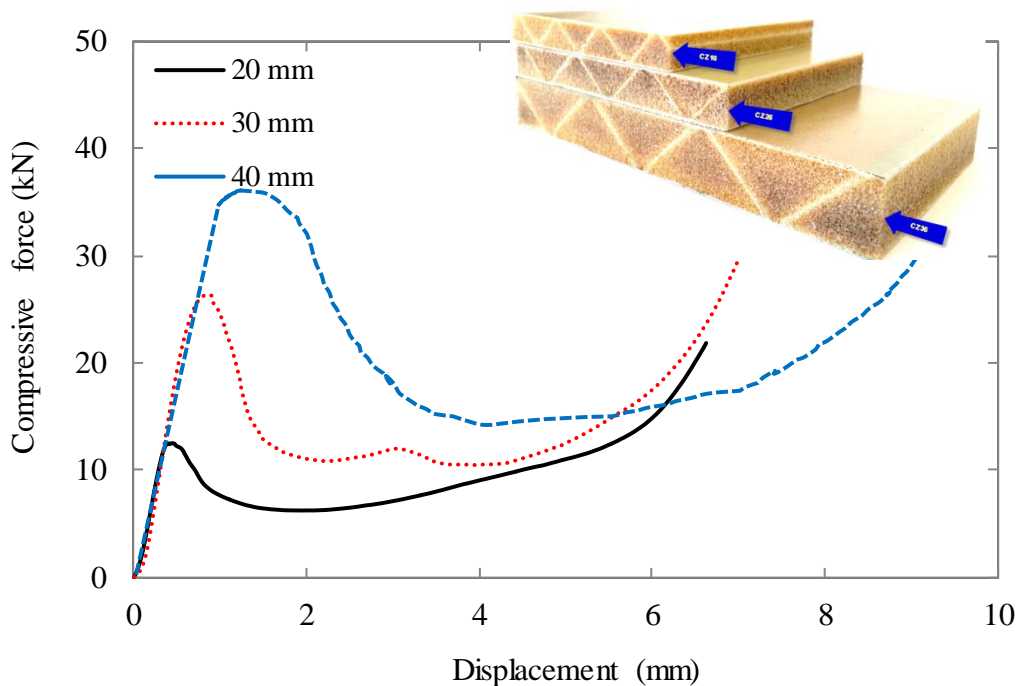


Figure 4.45: Load-displacement traces of the hybrid sandwich panel based on triangular corrugated reinforced foam core with different unit cell sizes.

Figure 4.46 shows the damage development of the hybrid sandwich panel based on triangular corrugated reinforced foam core with 40 mm unit cell size. The buckling failure can be seen after the elastic limit and also the debonding failure found at the same location.

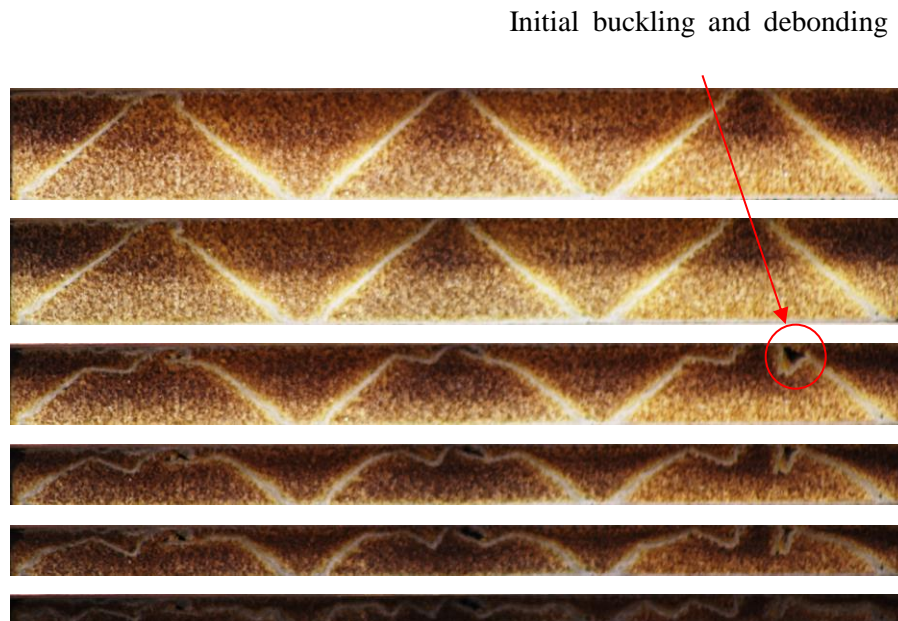


Figure 4.46: The process of damage development of the hybrid sandwich panel based on triangular corrugated reinforced foam core with 40 mm unit cell size.

4.2.2.8 The effects of different core layers

Compression tests were then carried out on the hybrid sandwich panels based on triangular corrugated reinforced foam cores as a function of core layer. The sandwich panels respond in a drastic linear manner up to the peak force, as shown in Figure 4.47. Based on observations, it was evident that just after the first peak force, the structure starts to deform and the crushing process continues until densification occurs, as shown in step-wise crushing images, Figure 4.48. With increasing core layers, the compressive force seems not changing significantly, however there is still a slight increase on the peak force

for panel with 2 layers, i.e. approximately 15%. The core with three layers shows another slight increase on the first peak force when compared to that of the panel with 2 layer core. Nevertheless, the core with three layers exhibits much longer plateau region, indicating a much higher energy absorbing capacity. The effects of core layers are evident on the plateau region of the force-displacement traces.

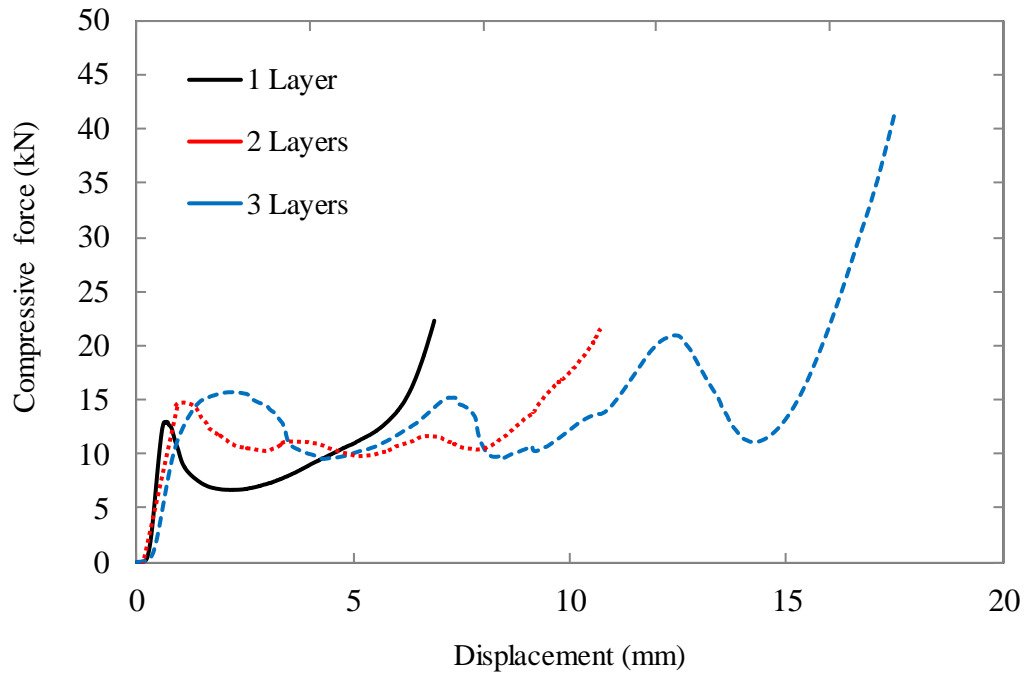


Figure 4.47: Load-displacement traces of hybrid sandwich structures based on GFRP reinforced foam core showing in with different core layers.

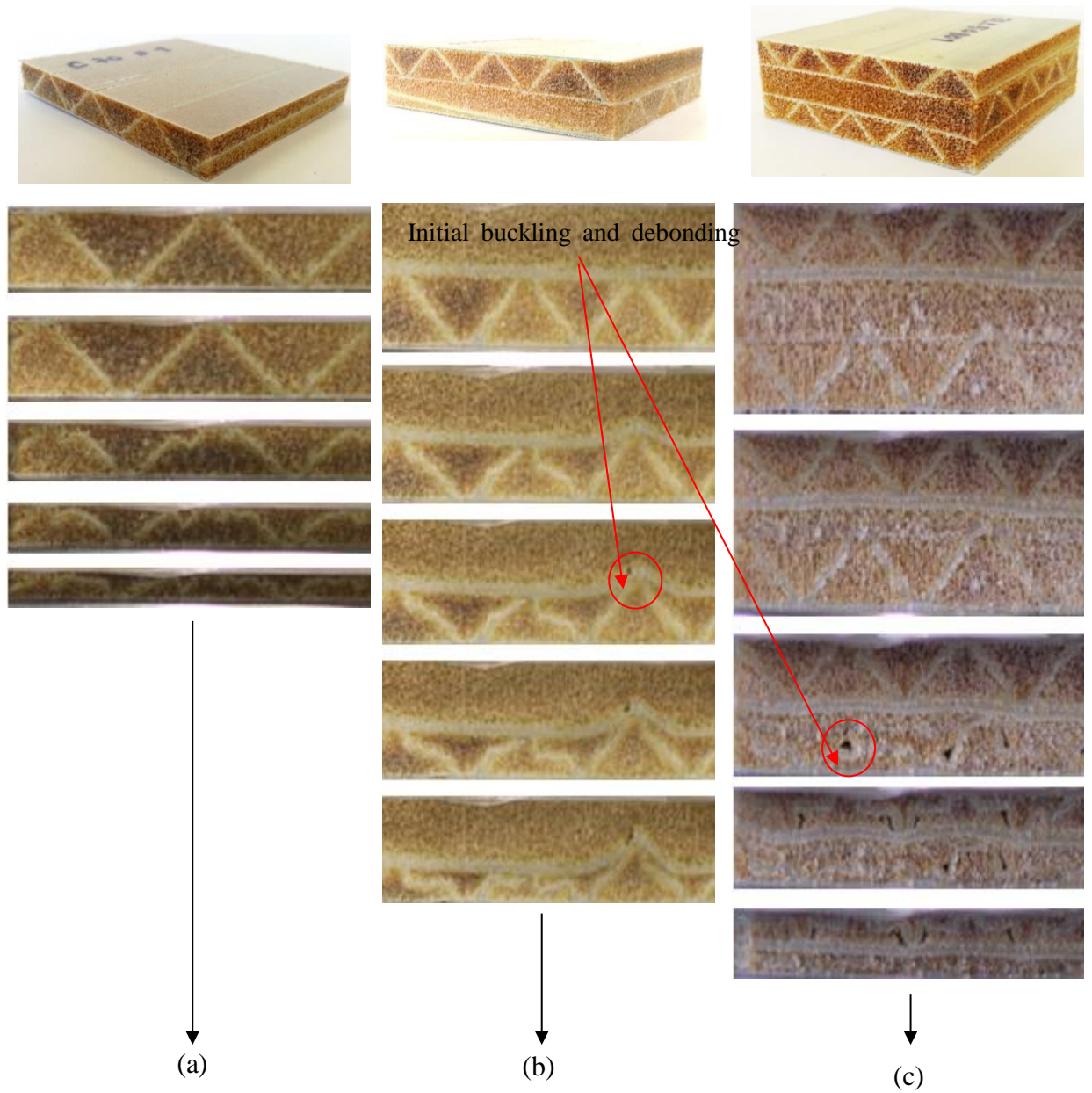


Figure 4.48: shows the process of damage development of the hybrid sandwich panel based on triangular corrugated reinforced foam core with different core layers (a) 1 layer, (b) 2 layers, (c) 3 layers.

4.2.2.9 The effects of using FMLs cores and skins

Figure 4.49 shows load-displacement traces of the hybrid sandwich panel based on triangular corrugated FMLs with reinforced foam core. Apparently, using FML as a core and skins could offer high compressive stiffness. The hybrid sandwich structures have a predominant elastic deformation due to a high rigidity as well as a high compressive modulus. The compressive strength is dependent on the core thickness and reinforced foam as shown in Figure 4.49. However, there is a catastrophic drop on load in the load-displacement traces after reach the elastic limit when the initial failure of the sandwich structures is triggered. Nevertheless, all those sandwich structures demonstrate various plateau resistance levels.

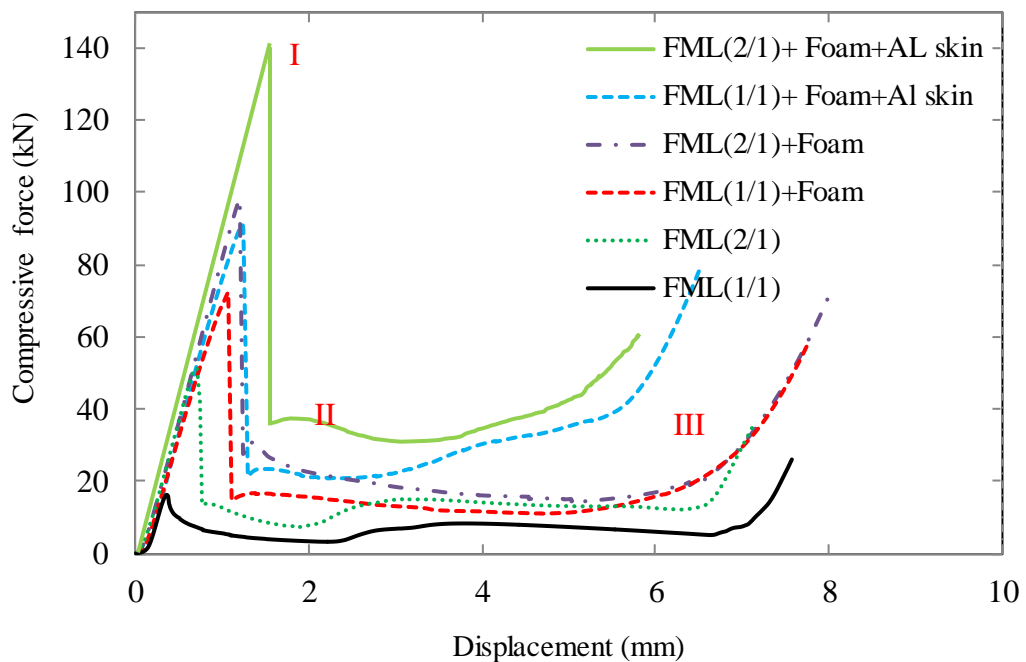


Figure 4.49: Load-displacement traces of the hybrid sandwich panel based on triangular corrugated FML and reinforced foam core.

Figure 4.50 shows the progressive damage of the hybrid sandwich panel based on triangular corrugated and 1/1 FML core. As aluminium has a ductile property, there was progressive elasto-plastic buckling failure with increased loading. The FML core was then crumpling until the corrugated-core was almost completely flattened.



Figure 4.50: The process of damage development of the hybrid sandwich panel based on triangular corrugated and 1/1 FML core.

Figure 4.51 shows the process of damage development of the hybrid sandwich panel based on triangular corrugated and 2/1 FML core. The behaviour of this sandwich type

was revealed the same manner as 1/1 FML core as mentioned above. Furthermore, the delamination failure mode occurred beyond the mid-span. Both FML skins were not torn apart under compressive loading. The FML core then experienced with crumpling after the corrugated-core has been almost completely flattened.

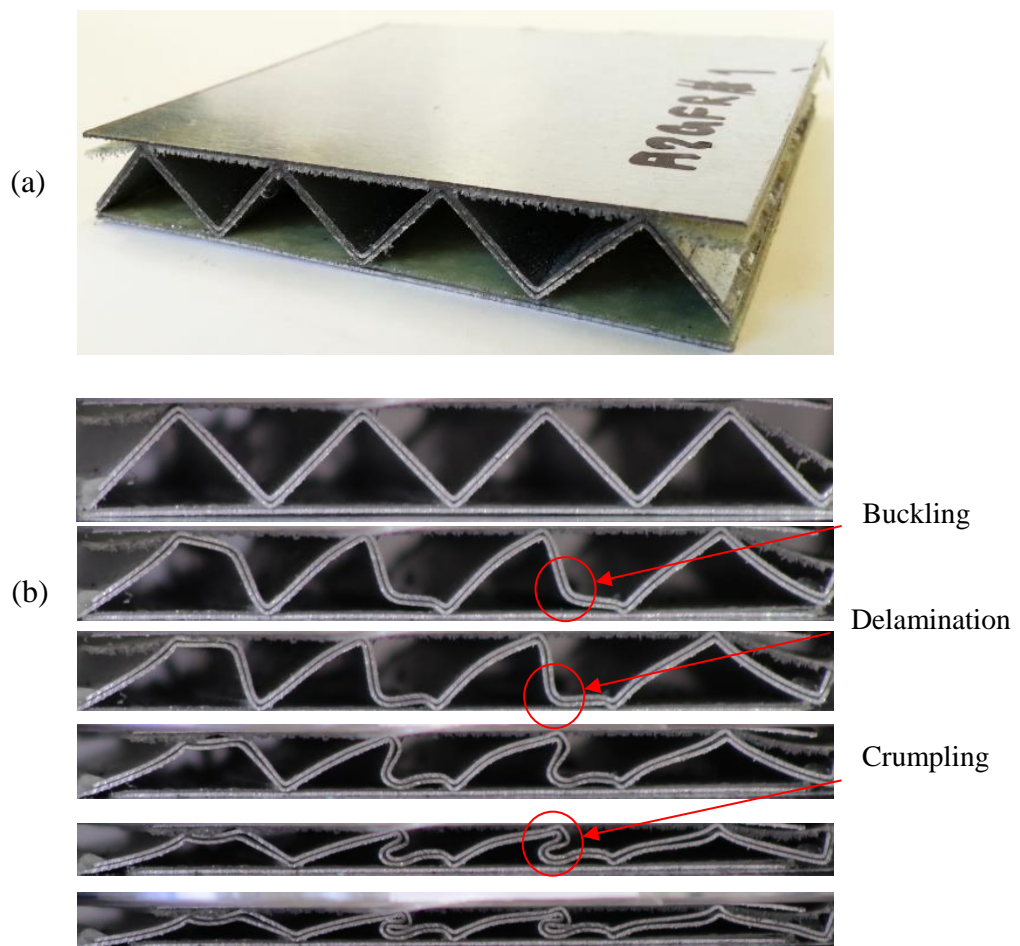


Figure 4.51: The process of damage development of the hybrid sandwich panel based on triangular corrugated and 2/1 FML core.

Figure 4.52 shows the process of damage development of the hybrid sandwich panel based on triangular corrugated and 1/1 FML core reinforced foam and no FML skins. Without the FML skins, the sandwich structure seemed to be expanded to both sides horizontally. Both FML skins were torn apart under compressive loading following with the buckling failure of aluminium core and initial cracking of foam core.

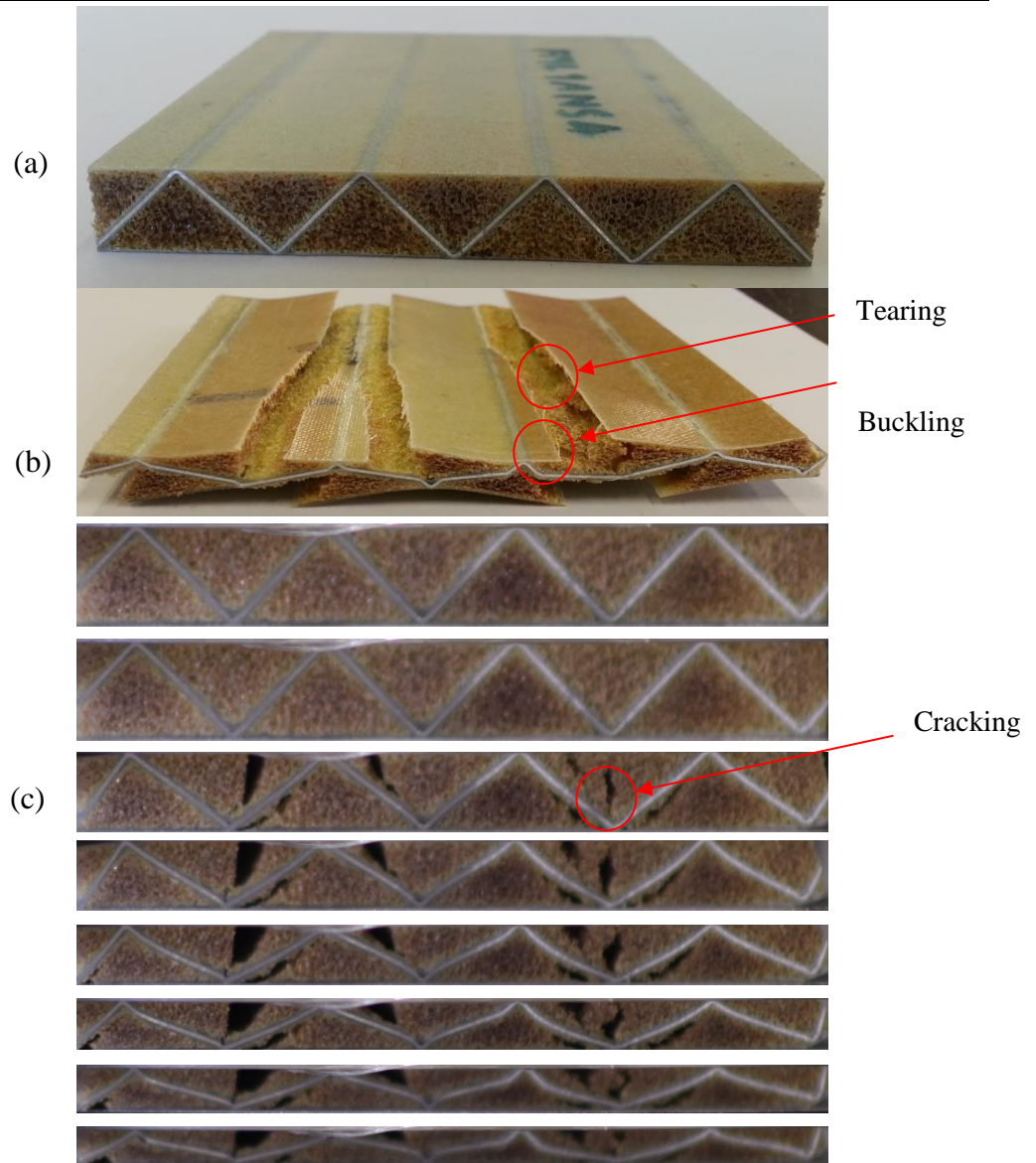


Figure 4.52: The process of damage development of the hybrid sandwich panel based on triangular corrugated and 1/1 FML core reinforced foam and no FML skins.

Figure 4.53 shows the process of damage development of the hybrid sandwich panel based on triangular corrugated and 1/1 FML core reinforced foam and with FML skins. The behaviour of this sandwich type was revealed the same manner as 1/1 FML core without FML skins as mentioned above. However, instead of expanded sideways, the sandwich samples buckled and crumpled before they were fully crushed.

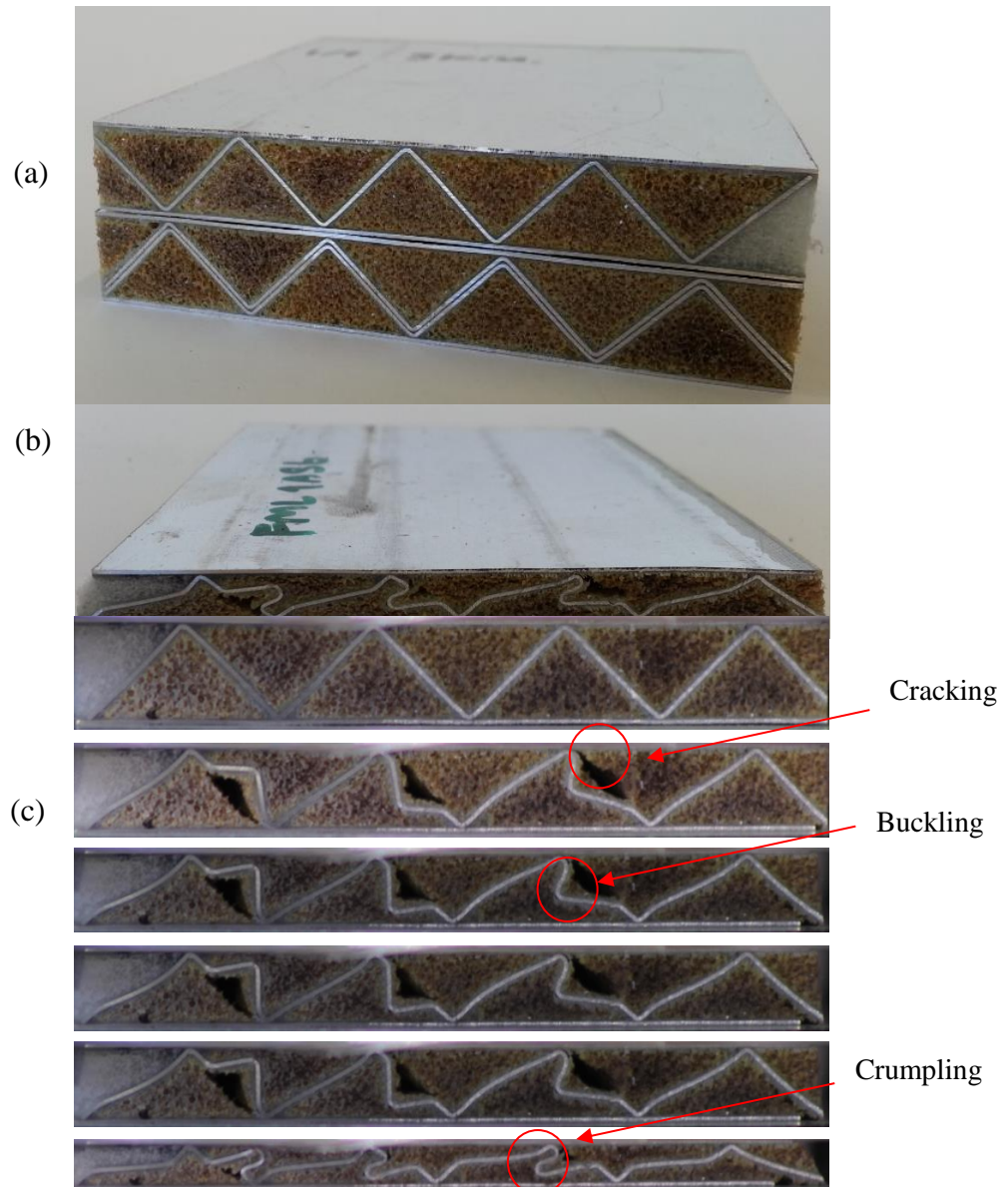


Figure 4.53: shows the process of damage development of the hybrid sandwich panel based on triangular corrugated and 1/1 FML core reinforced foam and with FML skins.

4.2.2.10 The effects of the cores with vertical reinforcements

Figure 4.54 shows load-displacement traces of hybrid sandwich structures based on GFRP reinforced foam core with the vertical corrugation reinforcements subjected to compression. It is clearly seen that using the vertical reinforcements can offer an enhanced compressive strength. The load-displacement traces also undergo a gradual decrease until reaching the densification region. Interestingly, when using FML as the vertical reinforcement, the peak load was predominantly higher than the others, but the compressive load drops sharply around 40 %, then remains constant until reaching the densification point.

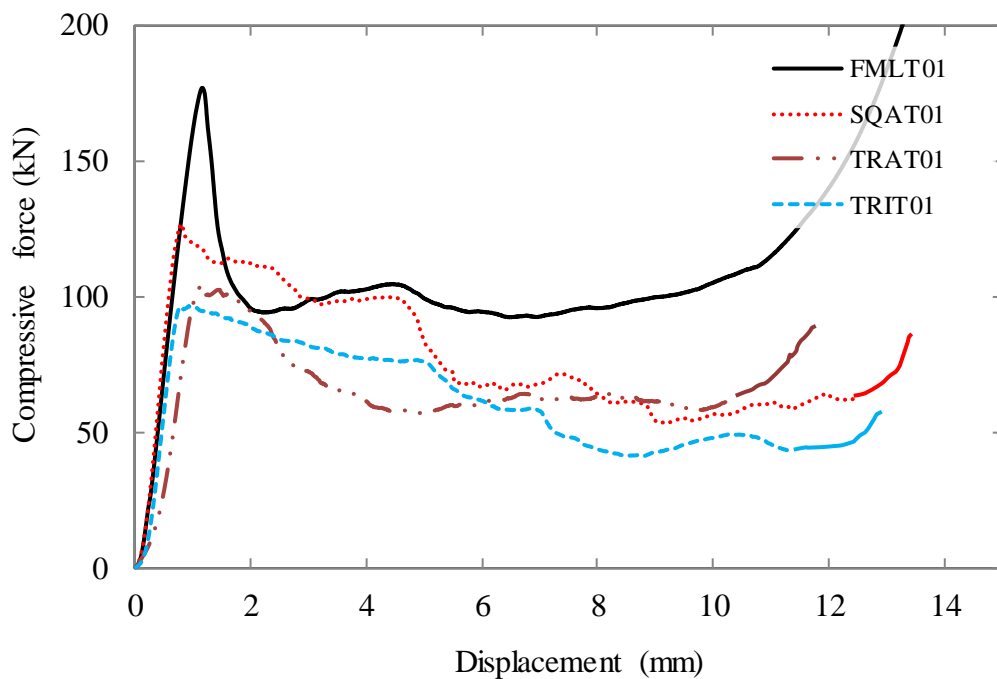


Figure 4.54: Load-displacement traces of hybrid sandwich structures based on GFRP reinforced foam core with vertical reinforcements.

Figure 4.55 shows the crushed sample of hybrid sandwich structures based on GFRP reinforced foam core with the vertical reinforcement under compression. The crushing process started from one side to another and led one side of the skin peeled off from the core. Another skin still remained until the sandwich was fully crushed.

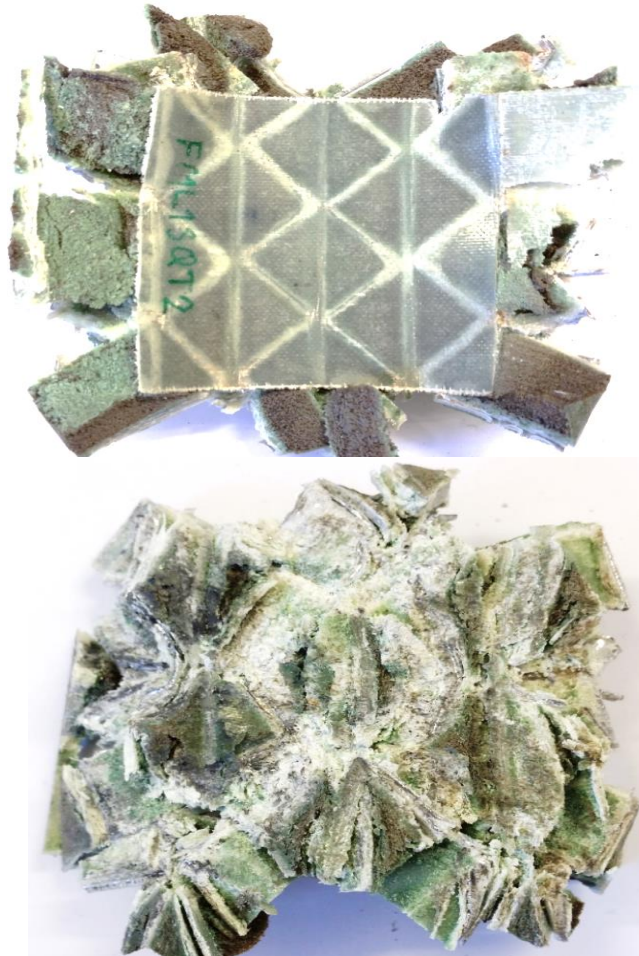


Figure 4.55: The hybrid sandwich structures based on GFRP reinforced foam core with the vertical reinforcement under compression. (a) the sample with skin side, (b) without skin.

4.3 Dynamic response

This section presents the response of various hybrid sandwich structures subjected to low velocity impact with flat platen crosshead and perforation tests as well as blast.

4.3.1 Compressive behaviour of hybrid sandwich structures subjected to impact loading

Crush tests at a high strain rate were performed using a drop-weight impact tower. In this section, the parameters investigated include the effects of GFRP core thickness, reinforcement with foam core, multi-layer and using FML, to study the response of the systems under low velocity impact loading with the flat platen cross head. The results shown here are based on the averaged value of three repeated tests. The response curves are represented in terms of the dynamic compressive loading and displacement (in mm) in order to find the energy absorption which is the area under the load-displacement curve. The strain is determined by the displacement divided by the original specimen height. Therefore the strain rate can be estimated by:

$$\dot{\varepsilon}(t) = \frac{d\varepsilon}{dt} = \frac{d}{dt} \left(\frac{L(t) - L_0}{L_0} \right) = \frac{1}{L_0} \frac{dL}{dt}(t) = \frac{v(t)}{L_0} \quad (4.13)$$

where L_0 is the original thickness of the sample and $L(t)$ is its length at each time t . Then the strain rate can be calculated by the velocity of cross-head before the impact to the sample divided by the original specimen height.

The author found that the behaviour of hybrid sandwich panels respond to both quasi-static and dynamic compressive loading in a similar manner regardless the core density, multi-layer, FML, etc. Therefore, only two cases are analysed in this section, i.e. the effect of core thickness of the plain GFRP corrugated sandwich structures and the effect of core thickness of GFRP corrugated sandwich structure reinforced foam core.

4.3.1.1 The effect of core thickness on the plain GFRP corrugated sandwich structures under dynamic compressive loading

Compressive behaviour of the plain GFRP corrugated sandwich structures without reinforced foam core under dynamic compressive loading was investigated. Figure 4.56 presents the corresponding load-displacement traces.

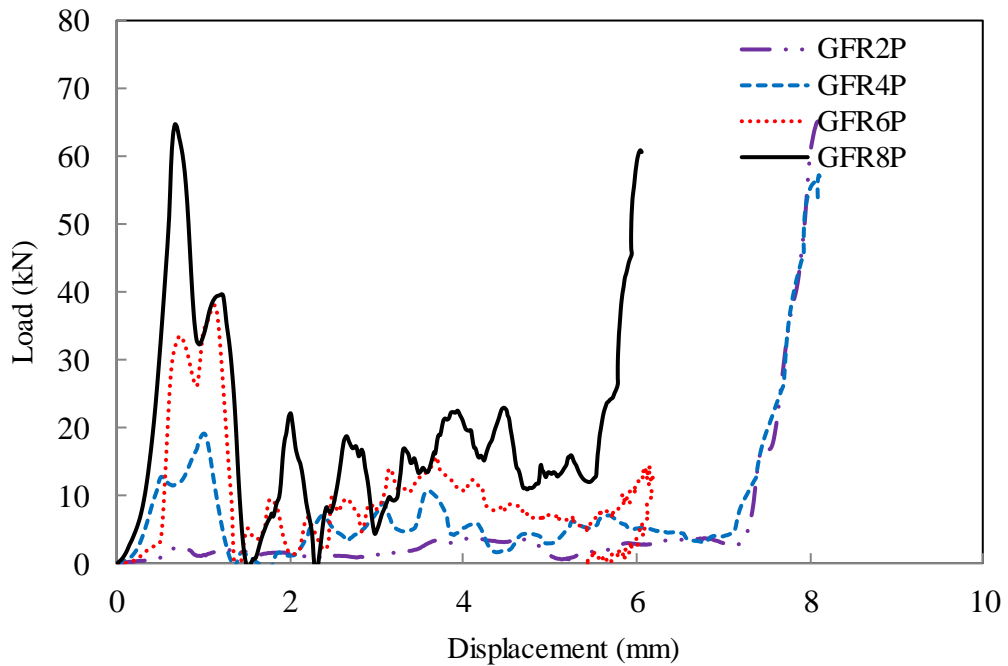


Figure 4.56: Load-displacement response of GFRP corrugated sandwich structure without reinforced foam core.

Typically, the experimental traces show a similar trend. When a flat head projectile strikes the sample, the impact force goes up almost linearly to reach the peak load. Then, the sample started to be damaged that leads the impact load to drop drastically. This is followed by oscillatory behaviour due to the up-down vibration effect as well as the fracture of the cell. Here, the zero reaction force is corresponding to the projectile temporarily bounced off the target. During this stage, the sample experiences a full crush, until the densification.

It is worth noting that the static and dynamic compressive tests experience different strain rates. As using a constant cross-head speed of 1 mm/minute for the quasi-static compression tests, the strain rate is approximately 10^{-6} s^{-1} . For the dynamic compression test, the strain rate was calculated by using Equation (4.13). Table 4.5 shows the strain rates of dynamic compression tests conducted on the plain GFRP corrugated sandwich panels compared to the constant strain rate from the static tests.

Table 4.5: Drop height, peak velocity, sample thickness data related to the strain rate of dynamic compression tests on the plain GFRP corrugated sandwich panel.

Sample type	Drop height (m)	Peak Velocity (m/s)	Thickness (mm)	Strain rate (s-1)	
				Static	Dynamic
GFR2P	0.25	2.21	9.97	1.6×10^{-6}	2.2×10^{-1}
GFR4P	0.30	2.43	9.61	1.6×10^{-6}	2.5×10^{-1}
GFR6P	0.42	2.87	10.52	1.6×10^{-6}	2.7×10^{-1}
GFR8P	0.60	3.43	10.79	1.6×10^{-6}	3.2×10^{-1}

To evaluate the influence of strain rate, the results from both static and dynamic compression tests are plotted together as shown in Figure 4.57. Only the load-displacement curves of GFR8P panels are presented, as all of the rest behave with the similar trend. It is clearly seen that the response of the plain GFRP sandwich structures under static and dynamic compression loading reveals a similar peak load and trend, with the dynamic response showing a higher stiffness. There seems no significant strain rate effect on the plain GFRP sandwich structures in the sense of the peak load. However, the areas under the load-displacement curves are quite different for both loading cases, the dynamic loading is approximate 10% greater than static loading

which will affect the energy absorption values. In addition, it was found that the impact loading dropped to zero caused by the projectile vibration as mentioned before.

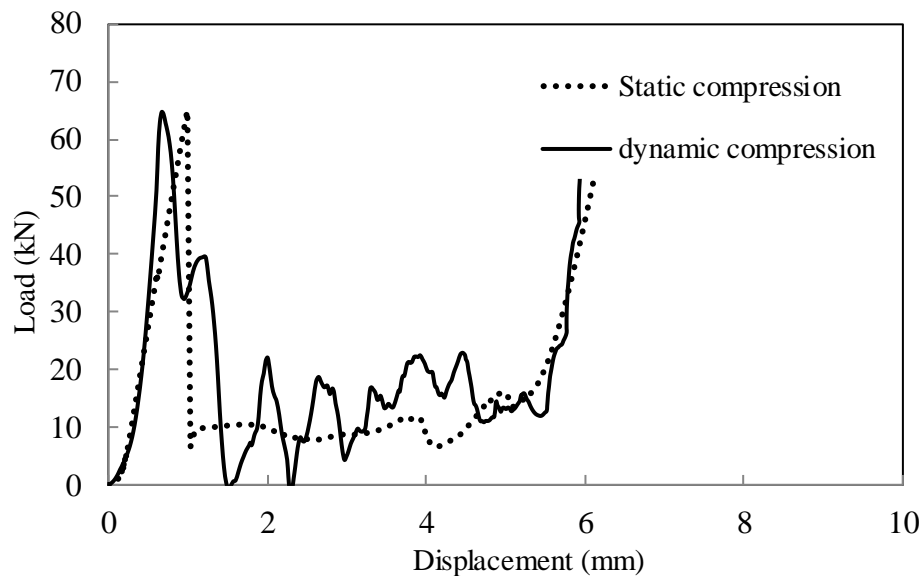


Figure 4.57: Comparison of the responses of the plain GFRP sandwich structures under static and dynamic compression loads.

The energy absorption of the panel was determined from the area under the load-displacement trace up to the densification point. Due to the oscillation as mentioned before, the energy absorption can be determined by the area under the curve (Figure 4.58). However, the oscillation factor may affect the energy absorption value. In order to obtain an accurate estimation, the data from the piezoelectric load cell were filtered using the Impressions software package. After re-plotting, the area under curve is shown in Figure 4.58 in the grey shade.

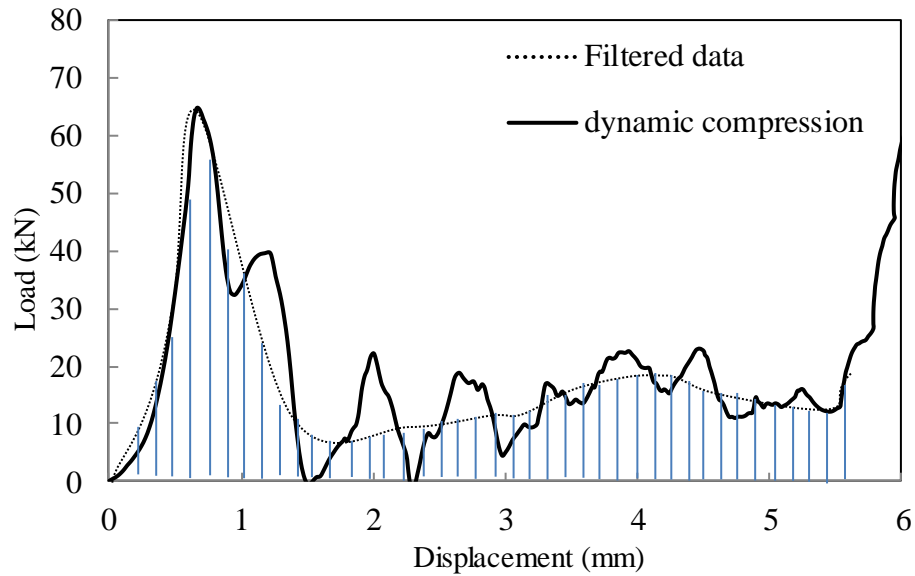


Figure 4.58: The blue area for the sample GFR8P after filtered by using Impressions software package to eliminate the oscillation factor.

Quasi-static and dynamic specific energy absorption of plain GFRP corrugated sandwich panels are presented in Table 4.6. In general, the dynamic specific energy absorption (SEA) values are significantly higher than the static counterparts.

Table 4.6: Quasi-static and dynamic specific energy absorption of plain GFRP corrugated sandwich panels.

Sample type	Density [kg/m ³]	Quasi-static SEA [kJ/kg]	Dynamic SEA [kJ/kg]
GFR2P	2.65	2.93	6.19
GFR4P	3.63	5.10	9.21
GFR6P	3.86	15.16	15.20
GFR8P	6.38	16.10	16.88

4.3.1.2 The effect of core thickness of GFRP corrugated sandwich structure reinforced foam core

Compressive behaviour of the plain GFRP corrugated sandwich structure with reinforced foam core under dynamic compressive loading is shown in Figure 4.59.

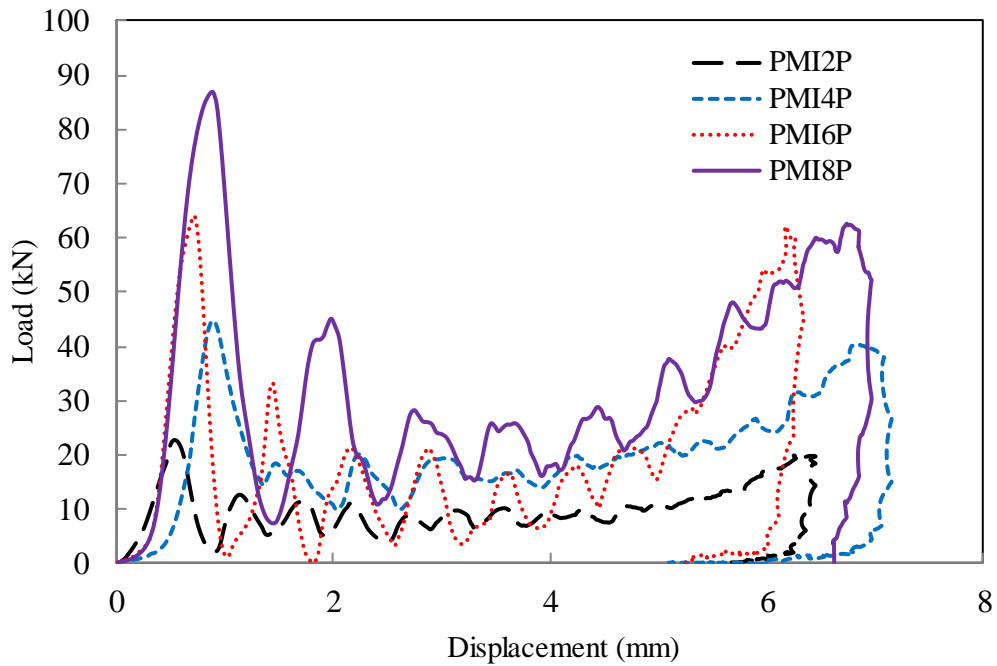


Figure 4.59: Load-displacement responses of GFRP corrugated sandwich panels with reinforced foam core.

The behaviour of GFRP corrugated sandwich panels with reinforced foam core under dynamic compressive loading has the similar features, i.e. quickly reaching the peak load, then sharp drop of the resistance, followed by oscillated plateau stage. Increasing of ply numbers indeed increases the peak load, as expected. By using the reinforced foam core a higher impact resistance is obtained. It can be seen that the oscillation increases as a function of the number of plies, as it occurred with PMI8P panel which experienced with a high level of oscillation. Figure 4.60 shows that the loading rate affects the results in term of the peak load and the level of plateau stage. As the responses from other samples are in the similar manner, here only one pair of PMI8P samples from both the quasi-static and dynamic compression tests are presented. The hybrid sandwich panels with reinforced foam core under impact loading offers a much higher peak load (up more than 60%) and plateau resistance, in comparison to the static

counterpart. From Figure 4.60, the peak load from the quasi-static data is around 54 kN, whilst the peak load from the dynamic impact test is almost 90 kN.

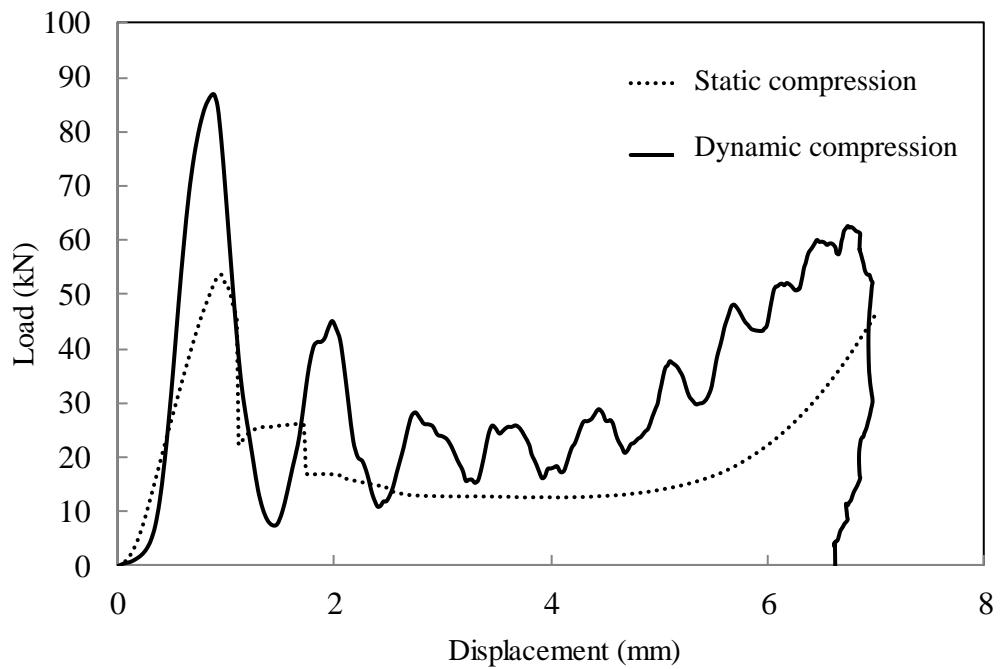


Figure 4.60: Comparison of the response of the plain GFRP sandwich structures with reinforced foam core under static and dynamic compression tests.

Table 4.7 shows quasi-static and dynamic specific energy absorption of GFRP corrugated sandwich panels with reinforced foam core. As can be seen, the dynamic specific energy absorption values are much higher than the quasi-static counterparts.

Table 4.7: Quasi-static and dynamic specific energy absorption of GFRP corrugated sandwich panels reinforced with foam core.

Sample type	Density [kg/m ³]	Quasi-static SEA [kJ/kg]	Dynamic SEA [kJ/kg]
PMI2P	2.29	7.51	13.12
PMI4P	3.00	9.44	15.30
PMI6P	4.15	14.35	22.10
PMI8P	4.67	18.22	25.00

4.3.2 Perforation behaviour

This section presents the experimental data obtained from perforation tests using the drop-weight impact tower as described in Section 3.6.2. The results from two different cores of hybrid corrugated sandwich panels based on FML cores and skins, i.e. 1 layer of Al sheet and 2/1 (AL/GFRP/Al) with four different thicknesses of FML skins (1/1-4/4) are analysed and compared. In all cases, the perforation process involves local plastic deformation and perforation.

Figure 4.61 shows typical load-time and displacement-time relationships of hybrid sandwich structures based on corrugated-core and FMLs.

These types of sandwich structures have a unique design with a 2/2 stacking sequence of FML skins and 1/1 FML corrugated core that allow air flow along the corrugation direction. The best outcome of this scenario is a high perforation resistance from FML skins. It can be seen that there are two peak loads due to the interaction between the projectile impactor and both FML skins shown in the load-displacement trace.

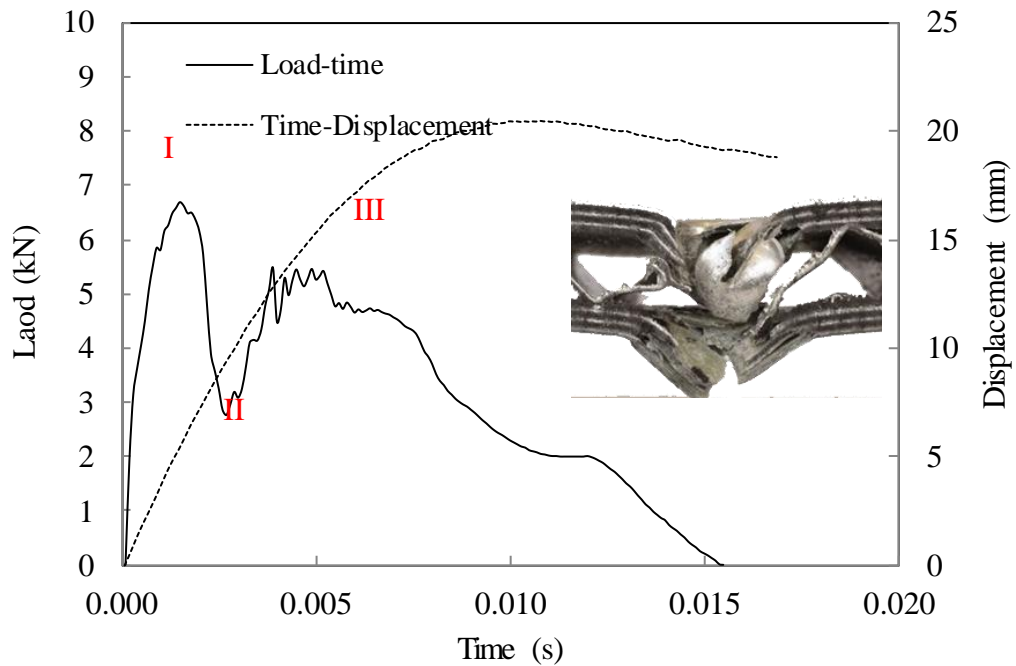


Figure 4.61: Typical load-time and displacement-time relationship of hybrid sandwich structures based on corrugated-core and FMLs under perforation test.

Figure 4.62 shows typical load-displacement traces of hybrid sandwich structures based on corrugated-core and FMLs under perforation test. The input impact energy, controlled by changing the carriage height, could govern the pattern of load-displacement trace. If the impact energy is not sufficient to penetrate through the panel, the displacement will travel backward in the later stage of the test. Both curves have the similar area under the curve that means they have the similar energy absorption capability. However, the resistance offered by the upper skin is clearly higher than the lower skin (stage I) due to higher velocity. Also, there is a bouncing back, which means the lower skin was not fully perforated. Therefore, it is expected that the localised damage of the upper and lower skins is different.

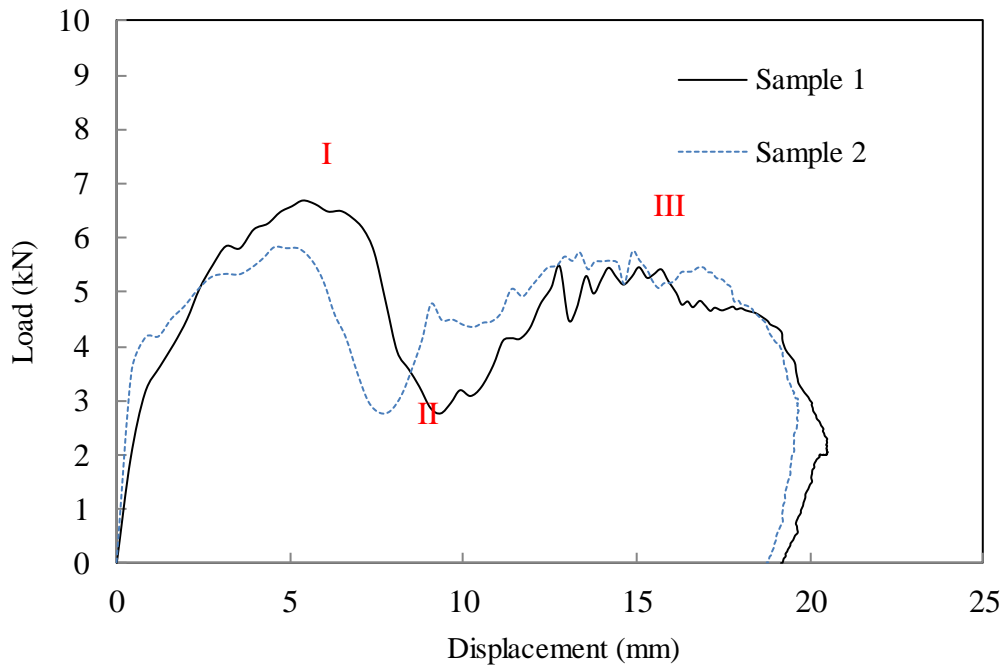


Figure 4.62: Typical-load displacement traces of hybrid sandwich structures based on corrugated-core and FMLs under perforation tests.

Figure 4.63 shows load-displacement traces of hybrid sandwich structures based on FML core and skin with 1 layer of triangular corrugated-core and different thicknesses of FMLs skins under perforation tests. For examples, the panel CO1/SK1 means CO1 (core with one aluminium sheet layer) and SK1(1/1 FML skin (AL/ GFRP)) and so on. The peak load of CO1/SK1 panel under perforation testing is approximately 2.7 kN with a gradual decrease of the impact load until the panel was perforated. The impact load resistance of CO1/SK2 core is around 4 kN in average. The different level of the load at the sandwich core can be explained by the position of the perforation area as shown in Figure 4.65. The position of the perforation was attempted to pass through the apex of the corrugated core. However, the angle of the corrugation altered the direction of perforation slightly, which led to an oblique impact, as shown in Figure 4.65 for the sample CO1/SK3.

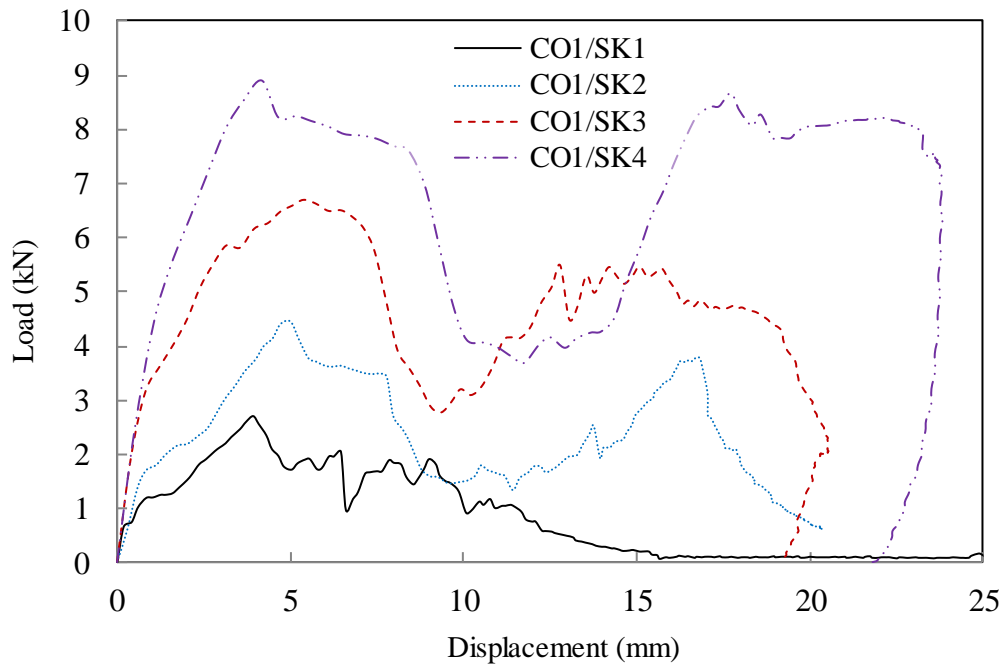


Figure 4.63: Load-displacement traces of hybrid sandwich structures with 1 layer of triangular corrugated-core and different thicknesses of FMLs skins under perforation test.

Failure in the test samples involved tensile fracture on the lower skin of the sample, leading to a cross-shaped fracture pattern as shown in Figure 4.65(b). These cracks tended to propagate through the thickness of the laminate, enabling the projectile to finally push through the plate and leading to the formation of a hole, as shown in the front and rear images. Figure 4.66 shows the cross-sections of damaged samples tested. As can be seen, the buckling damage of the core was more severe when the number of FML skin layer increased, which, in contrast, makes the core weaker.

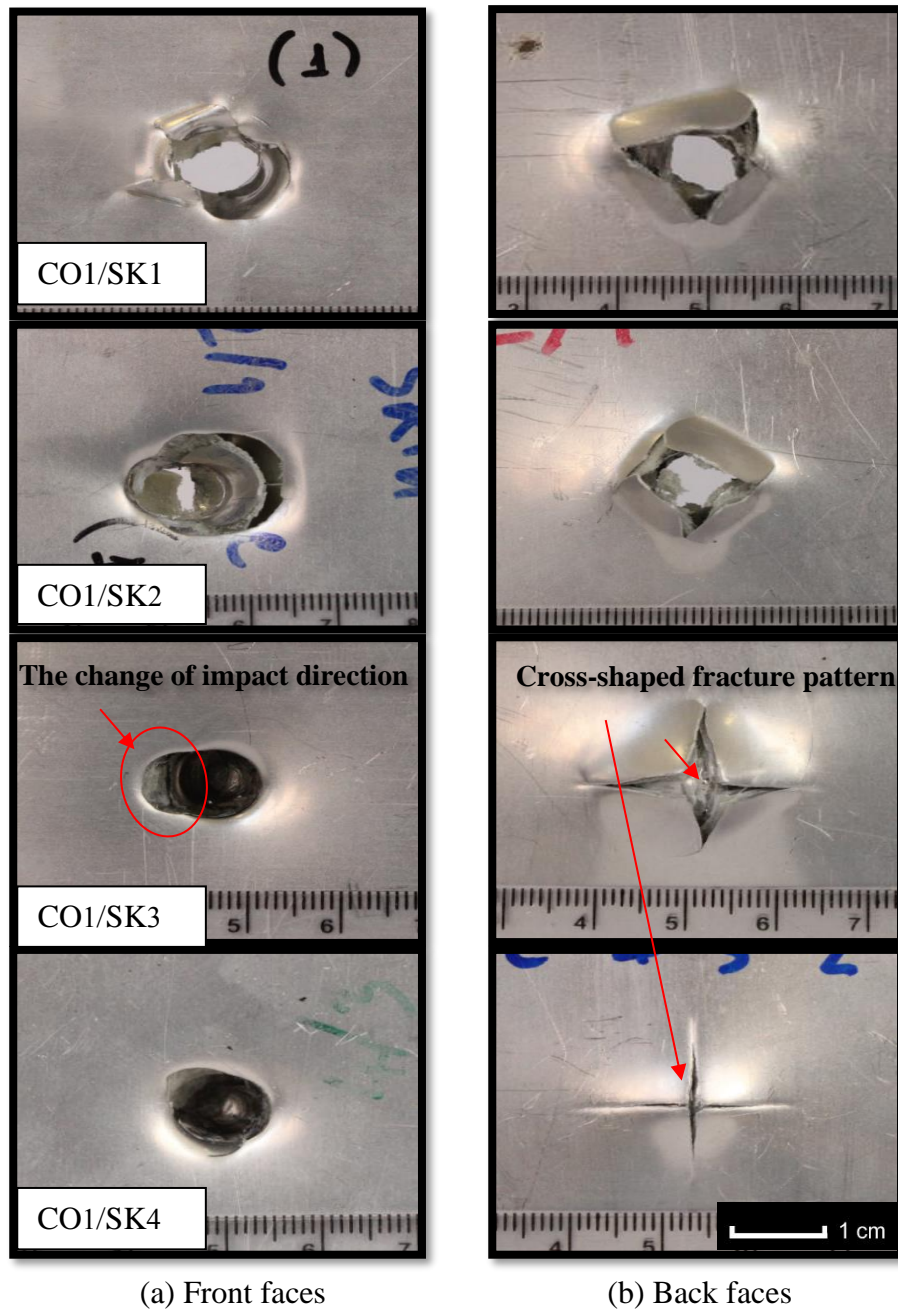


Figure 4.64: Low magnification optical micrographs of the perforated faces of the hybrid sandwich structures with CO1 group (1 layer of Aluminium core) subjected to perforation test. (a) Front faces, (b) Back faces.

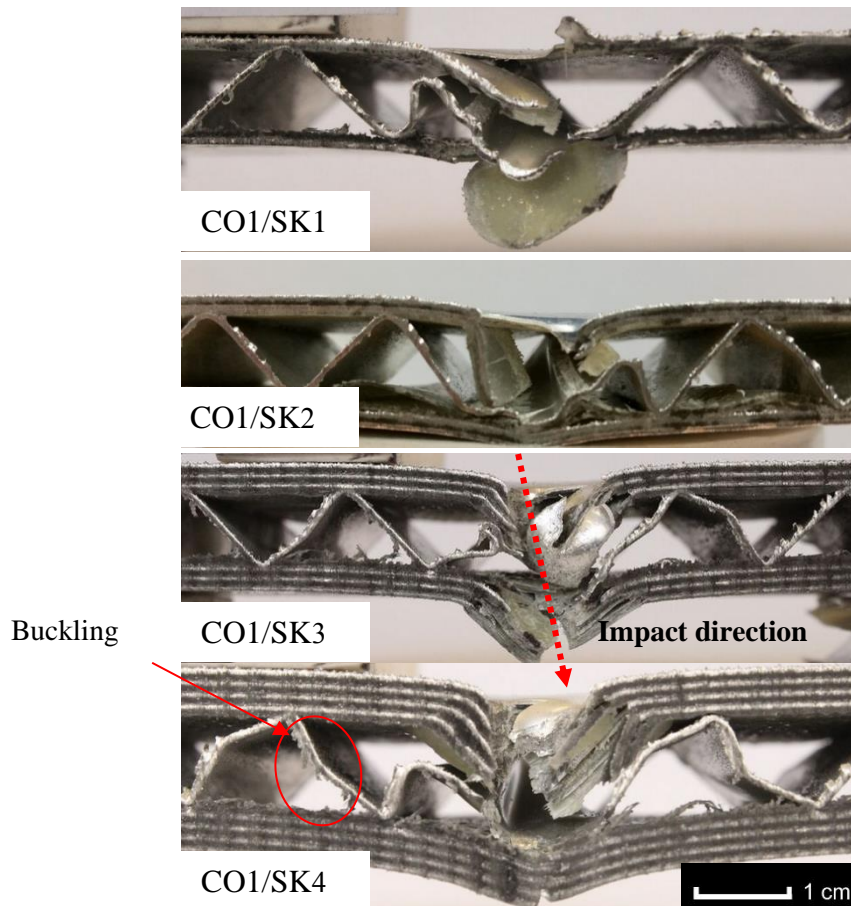


Figure 4.65: Low magnification optical micrographs of the cross-sections of hybrid sandwich structures with 1 layer of triangular corrugated-core and different thicknesses of FMLs skins after perforation test.

Figure 4.66 presents load-displacement traces of hybrid sandwich structures with 2/1 FML core and different thicknesses of FML skins under perforation test. An increase in the core layer reduces the buckling failure on the core, as shown in Figure 4.67. It seems a sliding of impact direction occurred clearly than in CO1 core type due to a thicker FML core. Near the edge of the impact area, the delamination on both the skin and the core can be observed as shown in CO2/SK3 sample in Figure 4.67.

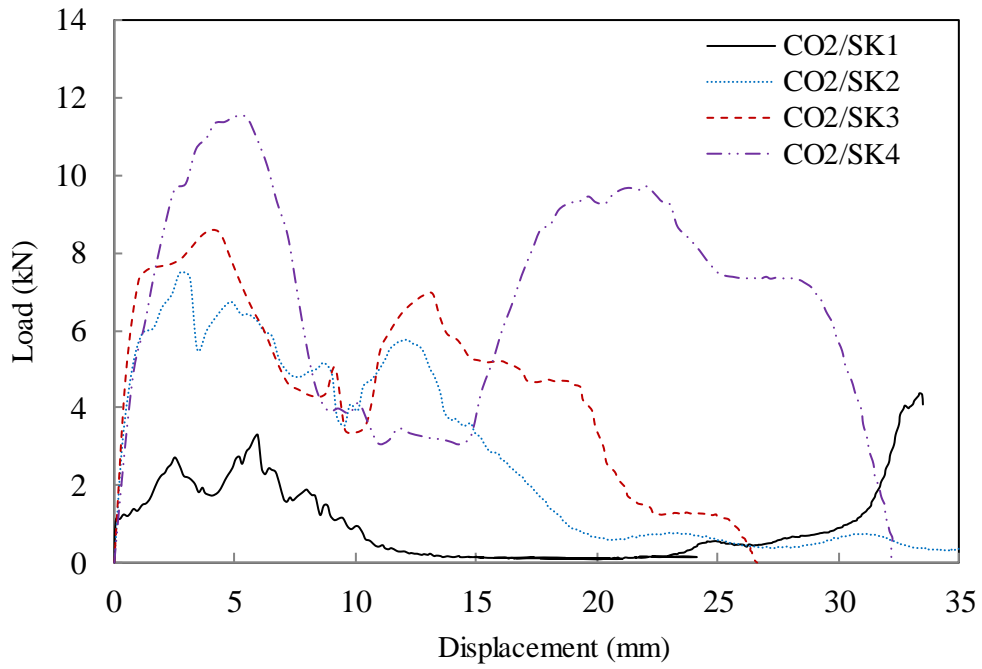


Figure 4.66: Load-displacement traces of hybrid sandwich structures with 2/1 FML core and different thicknesses of FMLs skins under perforation test.

Figure 4.68 gives the comparison of load-displacement traces of hybrid sandwich structures between 1 layer aluminium core and 2/1 FML core. The solid line represents the CO1-core, the dashed-line represents the CO2-core. FML 2/1 skin is shown in black and white colour and FML 4/3 skin is shown in red colour. It can be noticed that the energy dissipated for the samples with SK4 skins is certainly higher than the SK2 ones, due to the larger area under the load-displacement curves. However, CO2 based samples perform better than CO1 based ones, due to the thickness factor.

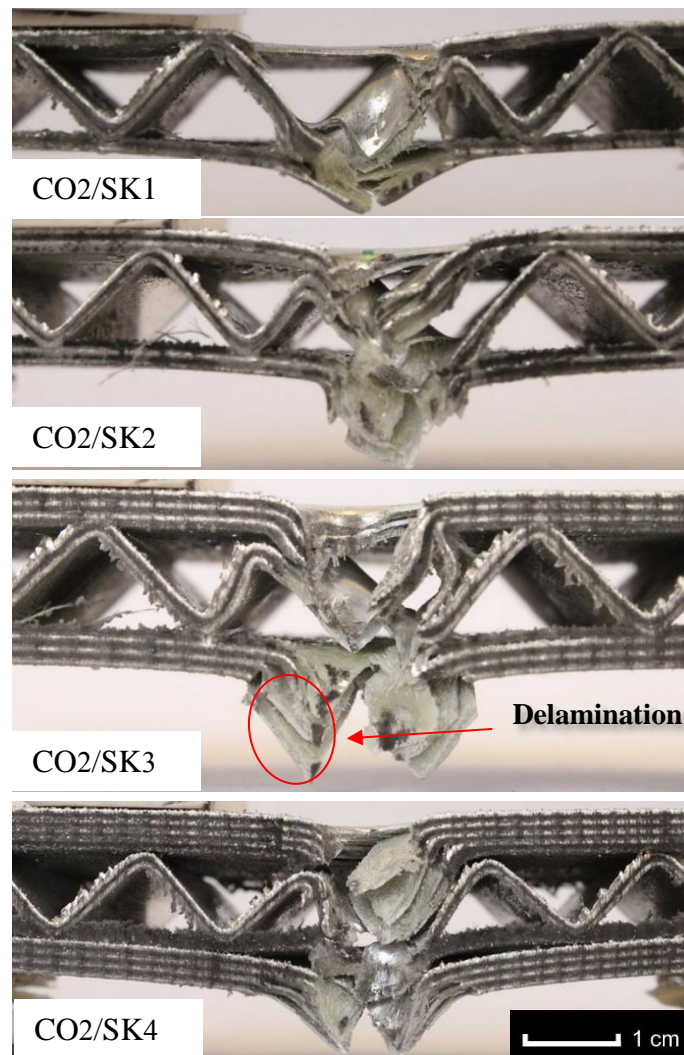


Figure 4.67: Low magnification optical micrographs of the cross-sections of hybrid sandwich structures with 2/1 FML corrugated-core and different thicknesses of FMLs skins after perforation test.

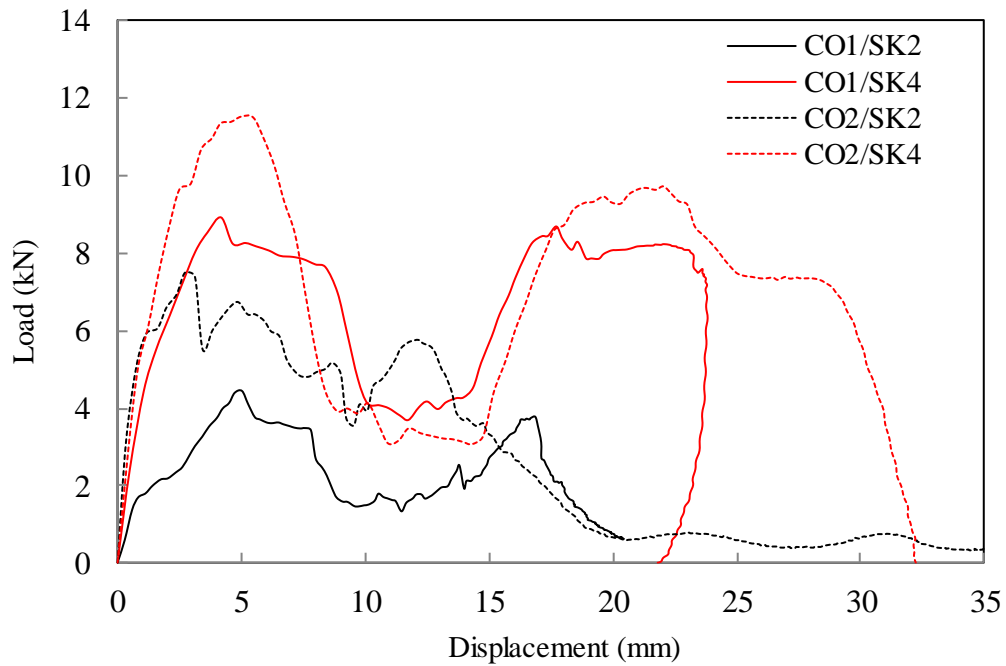


Figure 4.68: Comparison of load-displacement traces of hybrid sandwich structures between 1 layer aluminium core and 2/1 FML core. Continue-line : CO1- core, dash-line: CO2-core. FML 2/1 skin shown in Black and colour FML 4/3 skin shown in Red colour.

Table 4.8 shows a comparison of perforation energy and specific perforation energy of hybrid sandwich structures based on corrugated-core FMLs. Figure 4.69 suggests that the trend of specific perforation energy related to the panel thickness of CO2-core demonstrates a slightly high slope than CO1-core type. It can be seen that the peak load with panel density also increases in a linear fashion, as shown in Figure 4.70.

Table 4.8: Comparison of perforation energy and specific perforation energy of hybrid sandwich structures based on corrugated-core and FMLs.

Configuration	Area Density kg/m ²	Perforation Energy (J)	Specific perforation energy J/(kg/m ²)
CO1/SK1	2.77	20.63	7.5
CO1/SK2	4.47	49.12	11.0
CO1/SK3	4.77	97.63	20.5
CO1/SK4	5.37	165.38	30.8
CO2/SK1	5.03	115.23	22.9
CO2/SK2	5.56	140.51	14.5
CO2/SK3	6.14	167.32	27.3
CO2/SK4	8.93	221.64	24.8

Figure 4.71 presents a comparison of the perforation energy and the specific perforation energy of hybrid sandwich structures based on corrugated-core and FMLs in each condition. In general, the CO2-core type offers a higher specific energy absorption than the CO1-core type, except for the SK4 skin.

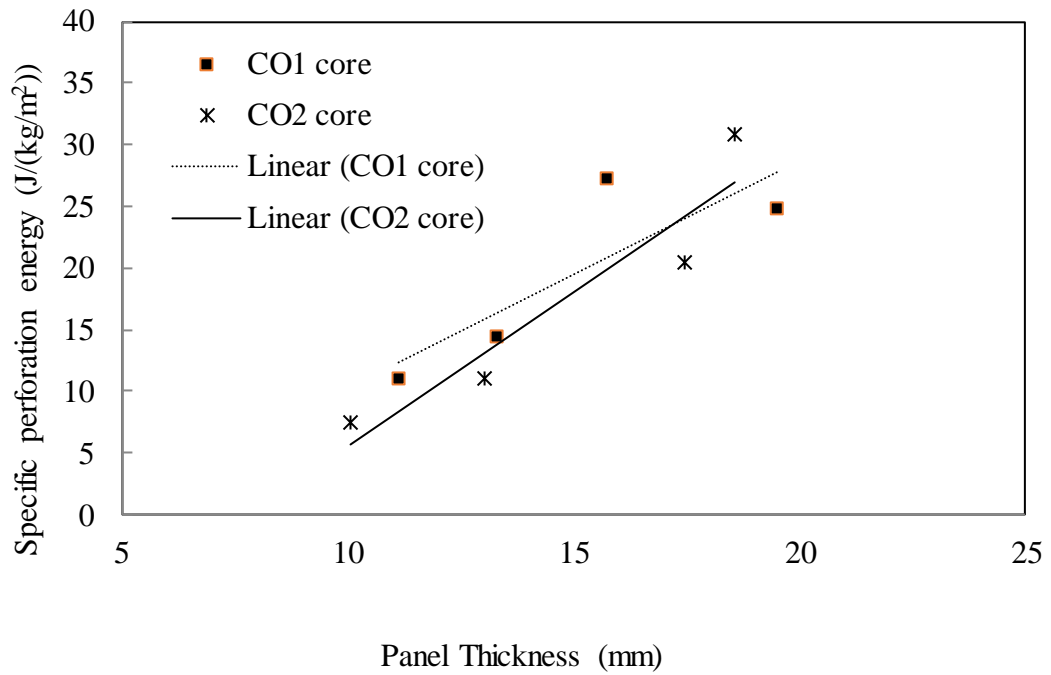


Figure 4.69: The relationship between panel thickness and specific perforation energy.

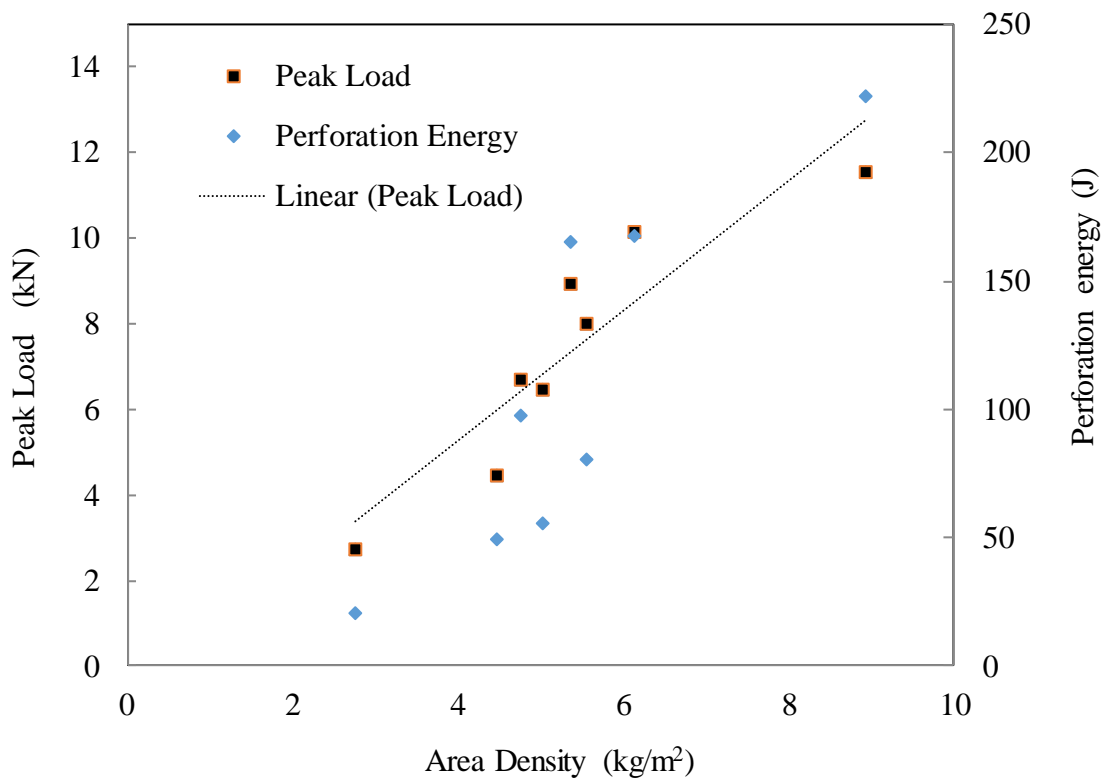


Figure 4.70: Peak load and area density relationship of hybrid sandwich structures based on corrugated-core and FMLs.

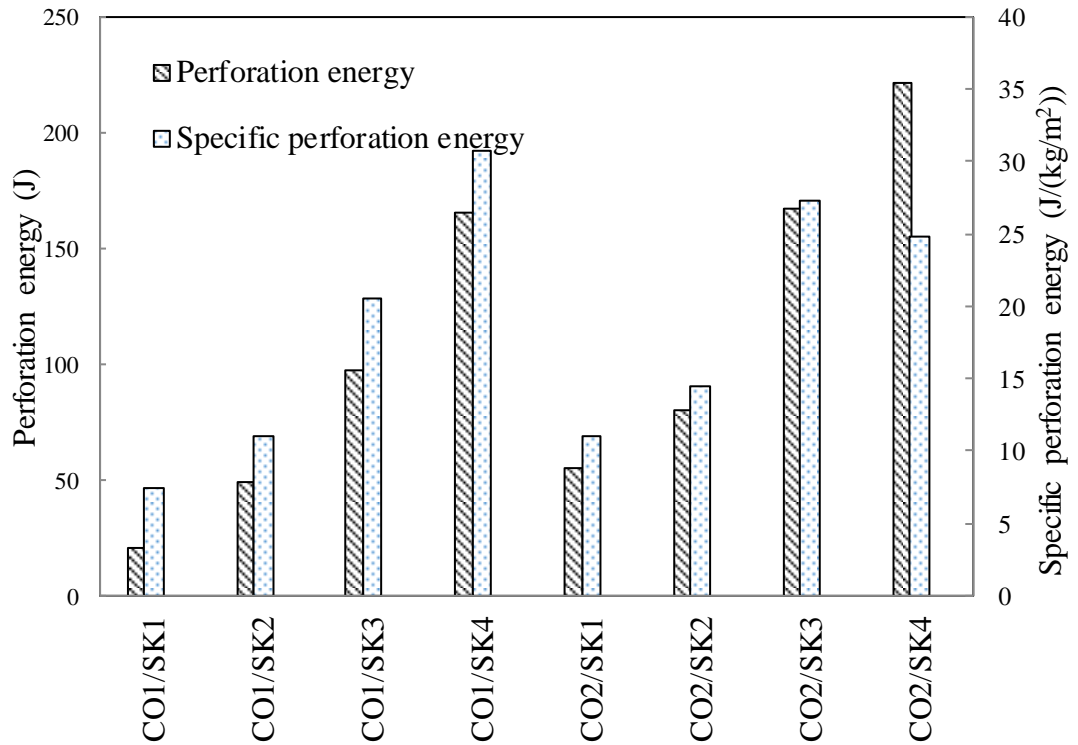


Figure 4.71: Perforation energy and specific perforation energy of hybrid sandwich structures based on corrugated-core and FMLs.

In summary, all evidences point out that increasing of core layer of FML led to different results as described above.

4.3.3 Blast tests

In this section, the author has a hypothesis that the newly developed hybrid sandwich structures can offer a good blast resistant performance. Their designs could limit the damage at the blast area that is very crucial when used in maritime applications such as ship compartments or bulkhead.

Table 4.9 summaries the samples ID, the explosive masses, impulses, and resulting front and back surface deflections. For the sample ALC4, both surfaces were perforated by the explosive impulse and therefore, the deflection could not be measured.

Table 4.9: Summary of the samples ID, the explosive masses, impulses, and resulting front and back surface deflections.

Sample ID	Mass (g)	Impulse (Ns)	Front plate deflection (mm)	Back plate deflection (mm)
ALC1	1	2.44	15.16	12.96
ALC2	3	5.43	22.67	21.56
ALC3	4	6.95	35.08	30.12
ALC4	5	8.44	-	-
ALC101	2	5.50	19.11	13.87
ALC102	3	6.63	23.84	17.73
ALC103	4	7.82	27.22	21.07
ALC104	5	9.36	28.64	25.96
GFRV101	4	8.15	7.01	5.54
GFRV102	5	9.10	10.00	10.86
GFRV103	7	10.4	10.67	22.82
GFRV104	8	11.72	13.62	32.88
GFRV201	7	10.61	9.37	4.76
GFRV202	9	12.22	10.26	7.42
GFRV203	11	16.43	13.03	15.52
GFRV204	12	17.56	16.70	20.33

Figure 4.72 gives a comparison of localized damage from the blast test between (a) monolithic curvilinear corrugated core panels made of aluminium (ALC and ALC1 samples) and (e) the hybrid sandwich panels based on corrugated cores and fibre metal laminates (GFRV1 and GFRV2 samples), (b) and (f): the side view, (c) and (g): the back surface view, (d) and (h): the front surface view. Regarding the monolithic curvilinear corrugated core sandwich structure, it is observed that for the 6 mm thick panels, when specimens are subjected to blast, crack is propagated along the

longitudinal corrugation direction of the sample. Also, large deformations occur, which generate a dome shape in the middle of the specimen. It is expected that as the amount of explosive increases, the dome shaped failure mode is extended. For instance the front and back face displacement of the specimen ALC2 is 15.16 and 12.96 mm respectively, in comparison to 22.67 and 21.56 mm front and back displacement of the specimen ALC3. This failure mode however is changed in ALC4, with 5 grams of explosives used, as the sandwich panel is perforated.

The ALC100 series of specimen, with a monolithic curvilinear corrugated core with a thickness of 10 mm, did also behave in the same way as the ALC1 series. Although the ALC100 series of specimen withstood a higher impulse rate, the damage behaviour was almost the same as ALC1 series.

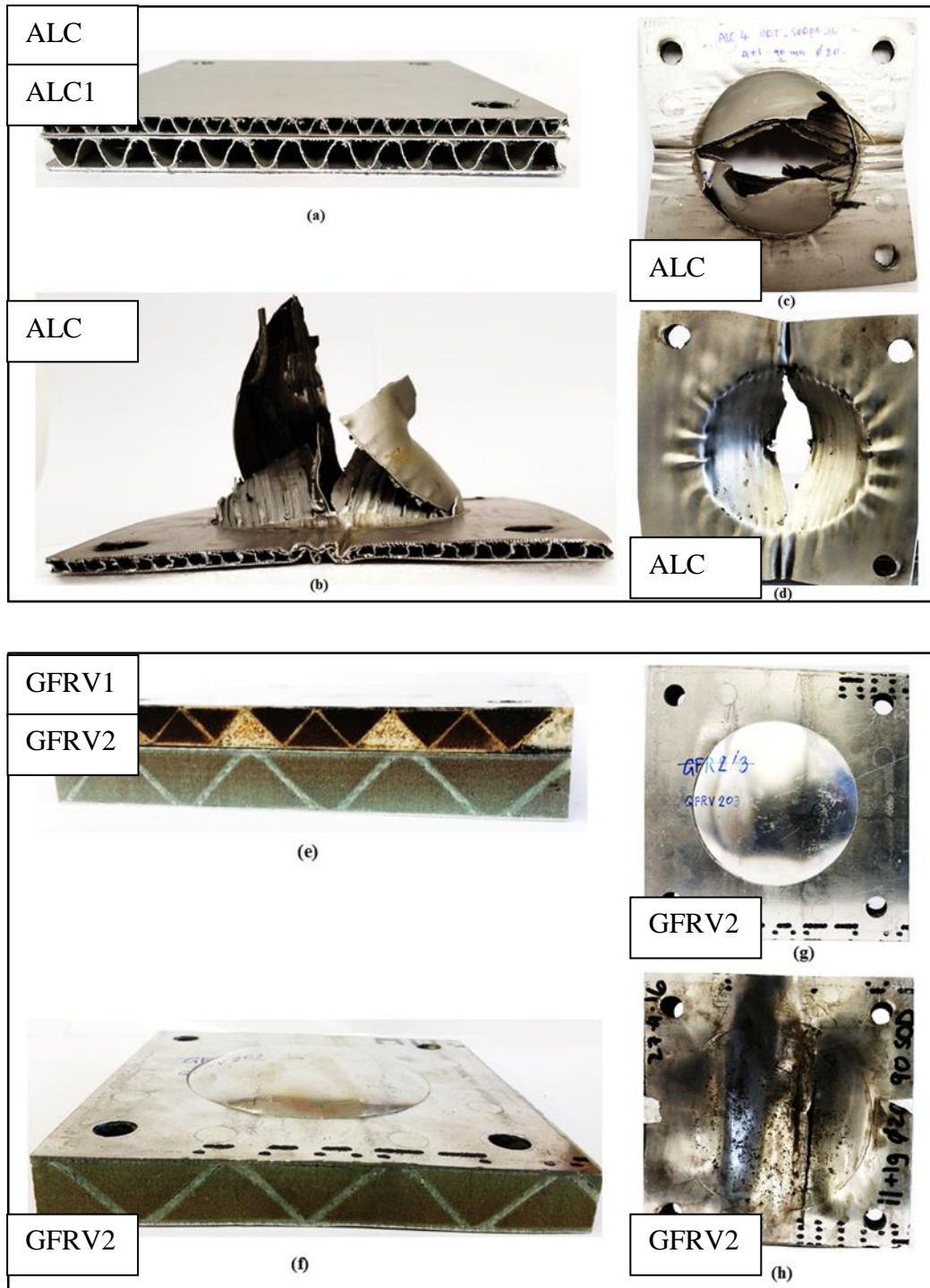


Figure 4.72: A comparison of localized damage from the blast test between (a) monolithic curvilinear corrugated core panels made of aluminium (ALC and ALC1 samples) and (e) the hybrid sandwich panels based on corrugated cores and fibre

metal laminates(GFRV1 and GFRV2 samples), (b) and (f):the side view, (c)and (g): the back surface view, (d)and (h): the front surface view.

The relation of impulses and explosive masses used for 4 different types of samples is shown in Figure 4.73. It indicates that the impulse is, in general, proportional to the explosive mass.

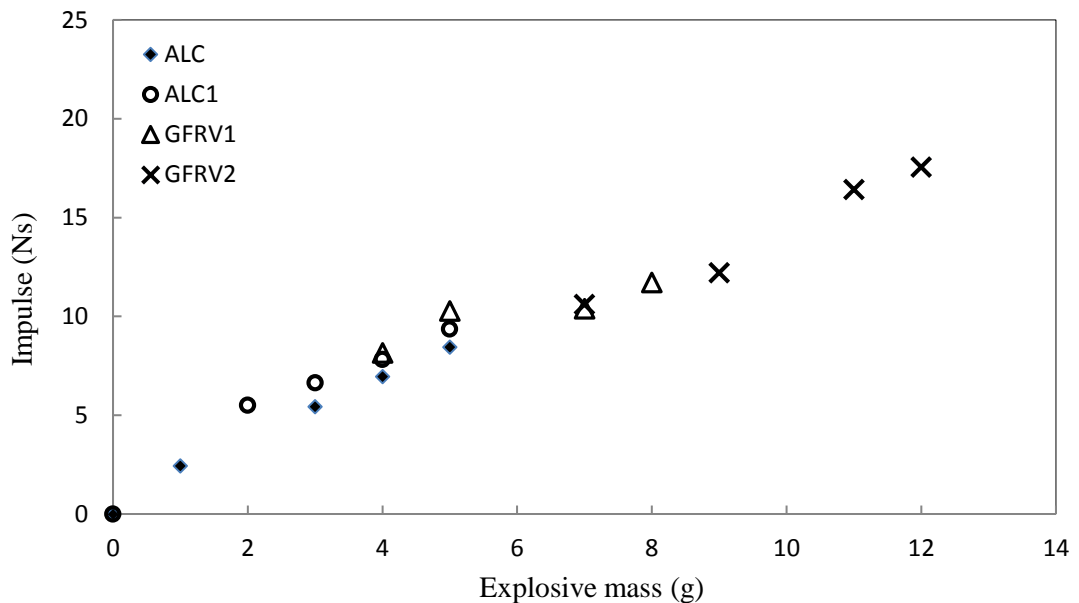


Figure 4.73: Relation of impulses and explosive masses used for 4 different types of samples

Figure 4.74 shows central deflections of the front and back faces of sample groups (a) ALC, (b) ALC1, (c) GFRV1 and (d) GFRV2. Apparently, the back face of the monolithic sandwiches has less deflection than the front. The deflection is quite different from the others on GFRV1 series. The deflection of the back face is less than the front face at a small impulse (about 8 Ns). Consequently, the back face deflection becomes significantly greater than the front face due to the severe crush on core. The impulse is much higher when a thicker panel was tested.

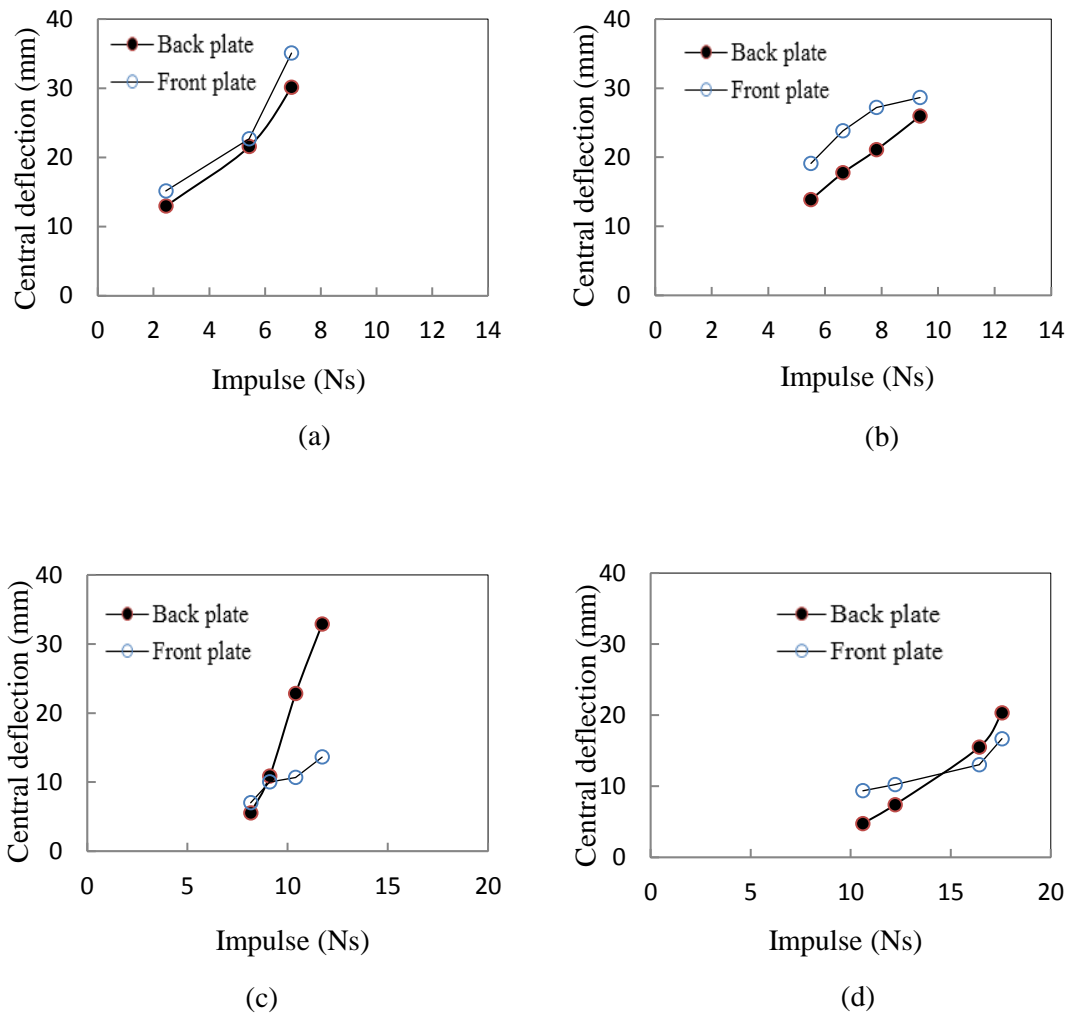


Figure 4.74: Central deflections of the front and back faces of sample groups (a): ALC, (b): ALC1, (c): GFRV1, (d): GFRV2

Figure 4.75-4.78 illustrates a damage development and failure modes of various corrugated sandwich structures investigated. For the monolithic sandwiches, as they consist of the ductile metal, the buckling failure was found, together with the wrinkle around the support region. Consequently, the crack grew from the middle of the blast area (Figs. 4.76-4.77). The failure of the hybrid sandwich panel exhibited in a less ductile manner, which initiated from the debonding between the aluminum back face and the core. Then the front and back face plates started to crack along the corrugation

direction. Finally, the aluminum face sheets and the foam core broken away from the support plate. It could be concluded that the hybrid sandwich plates seem offering a good blast resistance in terms of their superior stiffness.

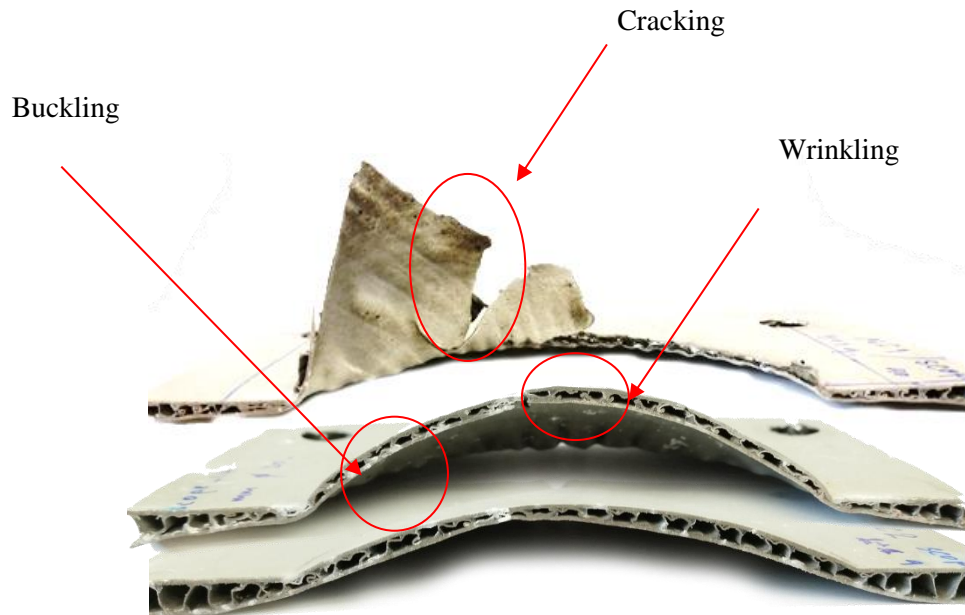


Figure 4.75: The Progressive damage development of ALC panel from the bottom to the top.

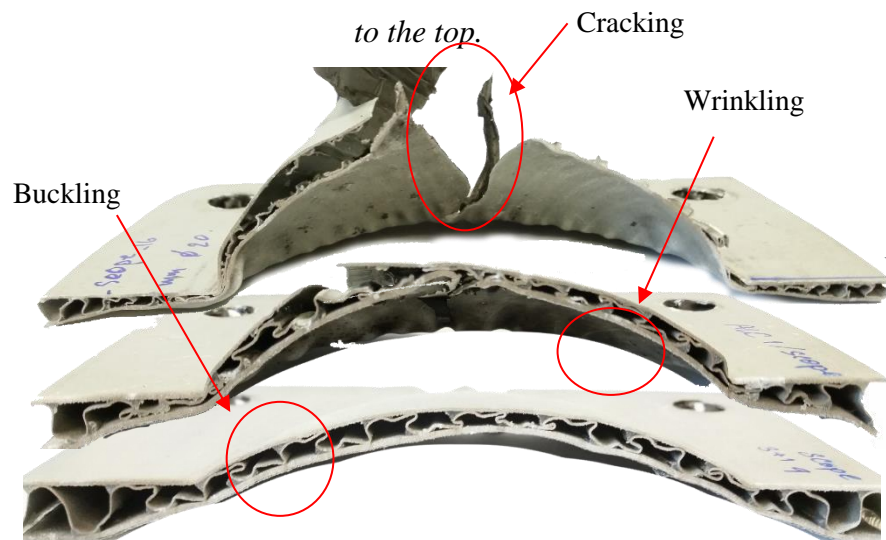


Figure 4.76: The progressive damage development of ALC1 panel from the bottom to the top.

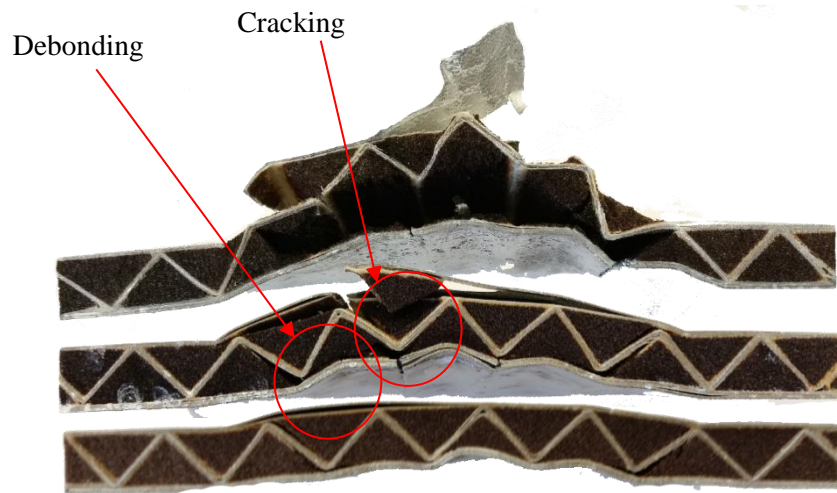


Figure 4.77: The progressive damage development of GFRV panel from the Breaking bottom to the top.

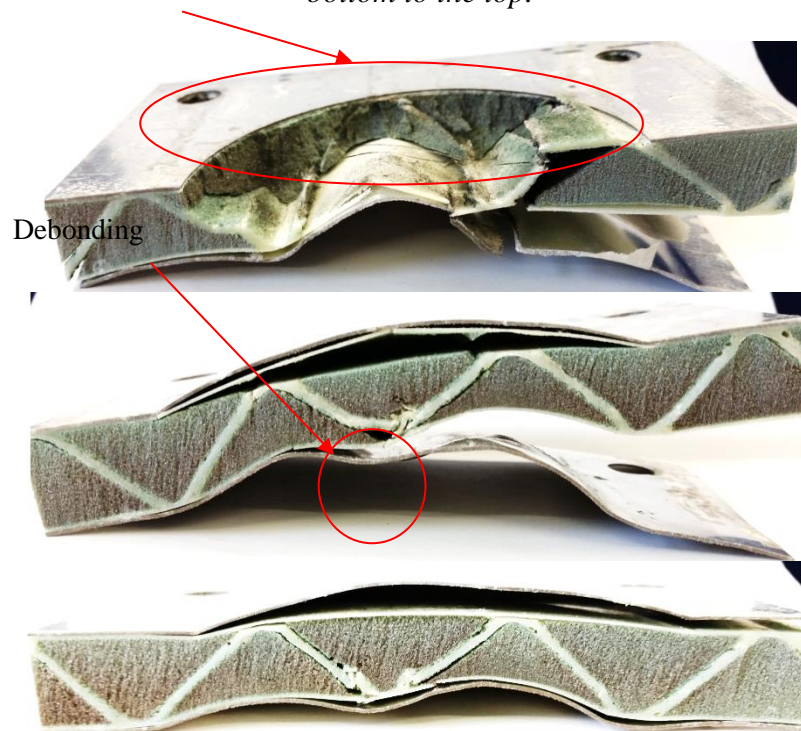


Figure 4.78: The progressive damage development of GFRV1 panel from the bottom to the top.

4.4 Discussion

As there are many parameters studied in Chapter 4, this section will discuss some aspects, in particular, the effect of filling foam, number of ply inside the core element on the specific absorption energy from compressive tests.

4.4.1 The effect of filling foam

Most corrugated core structures in this work consist of foam core filled inside the core cavity. Therefore, it is necessary to discuss how filling foam influence the response of structures under compressive loading in more details.

Figure 4.79 and Figure 4.80 show stress-strain curves of triangular corrugated core sandwich structures made with plain GFRP, filled without and with foam respectively. It can be clearly seen that filling foam into the core could significantly enhance the plateau stress and further to absorb more energy, as shown in the GFRP 2 plies (black colour). Without filling foam, the plateau compressive stress is only about 0.2 MPa,

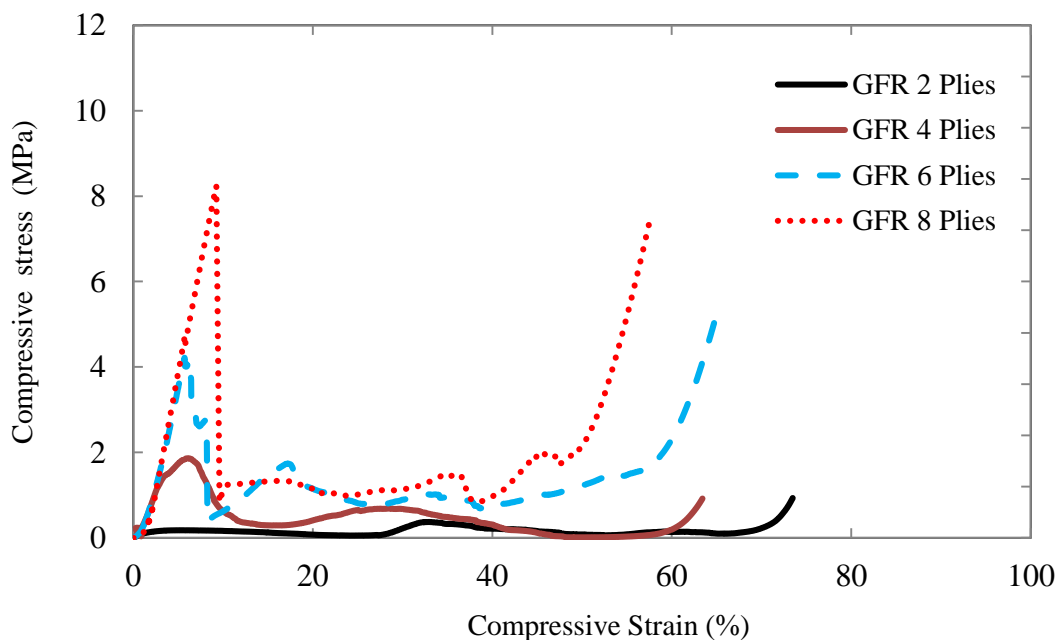


Figure 4.79: Stress-strain curve of triangular corrugated core sandwich structures with various plies.

however, such the stress is above 1 MPa after foam filling. It could be concluded that the expectation of filling foam is the key to absorb more energy exerting to the structure.

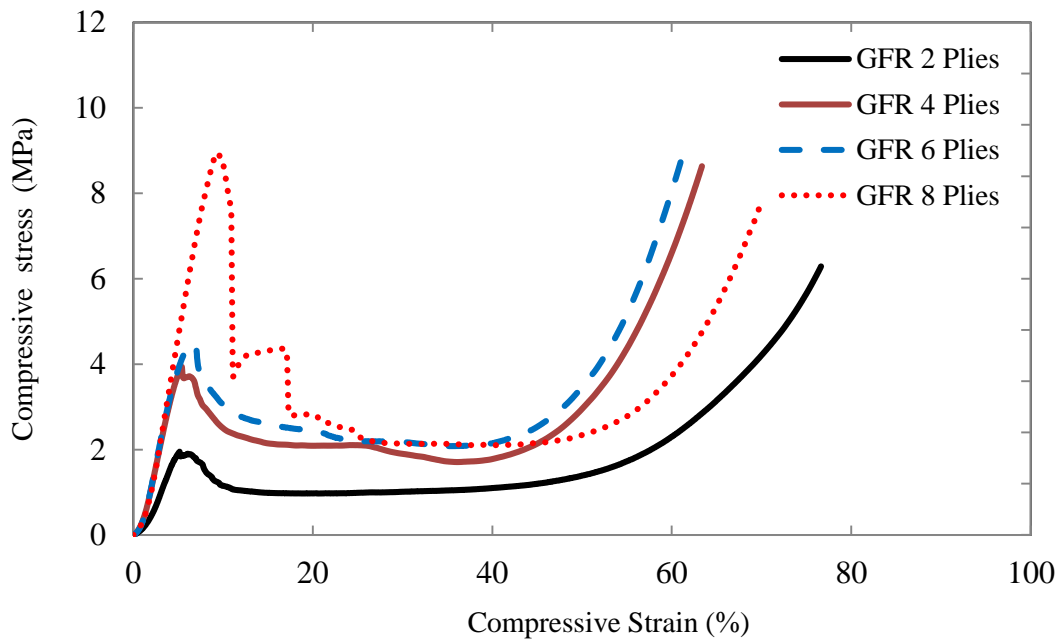


Figure 4.80: Stress-strain curve of triangular corrugated core sandwich structures with various plies and filled with foam core.

4.4.2 The number of ply and specific energy absorption

Table 4.10 and Figure 4.81 show the relation between number of GFRP ply inside the core element and specific energy absorption (SEA), i.e. energy absorption per unit mass. For the plain GFR core, the relation is almost in a linear fashion. However, the filled foam corrugated core sandwich structures seem have a steady SEA even with increasing number of ply, as show in Table 4.11 and Figure 4.82

Table 4.10: Relation between number of plies and specific energy absorption of plain GFR corrugated core sandwich structures.

Ply number	Mass	Energy	SEA
	kg	(J)	(Kj/kg)
2	0.0173	7.78	0.45
4	0.0210	18.50	0.88
6	0.0235	58.54	2.49
8	0.0401	102.71	2.56

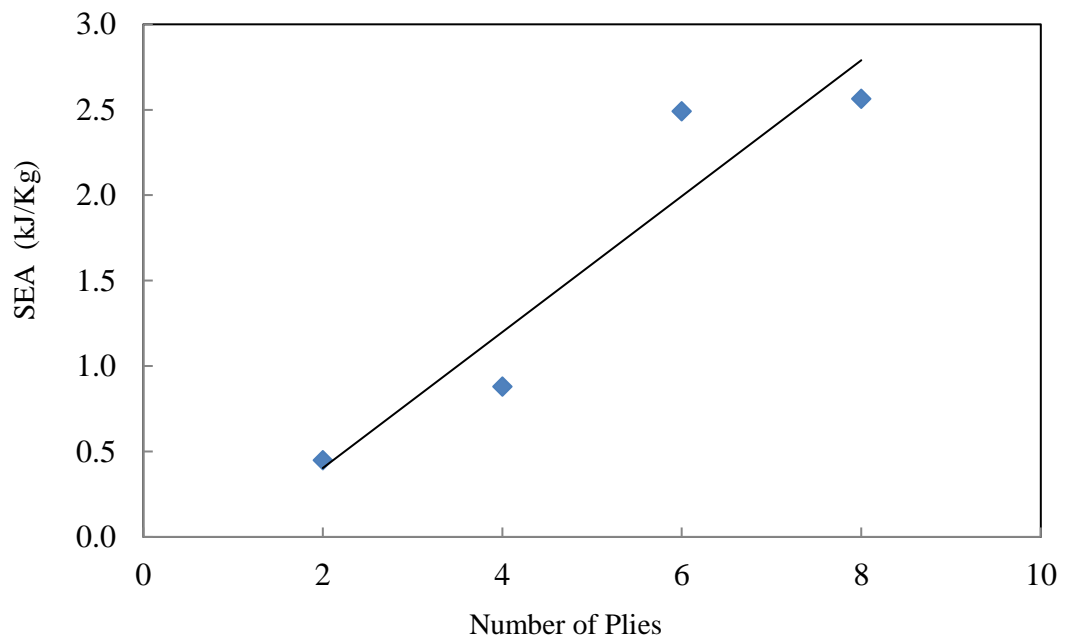


Figure 4.81: The trend of number of plies and specific energy absorption of plain GFR corrugated core sandwich structures.

Table 4.11: Relation between number of plies and specific energy absorption of GFRP corrugated core sandwich structures filled with foam.

Ply number	Mass	Energy	SEA
	kg	(J)	(Kj/kg)
2	0.0149	82.86	5.56
4	0.0234	106.38	4.55
6	0.0225	114.73	5.10
8	0.0297	142.80	4.82

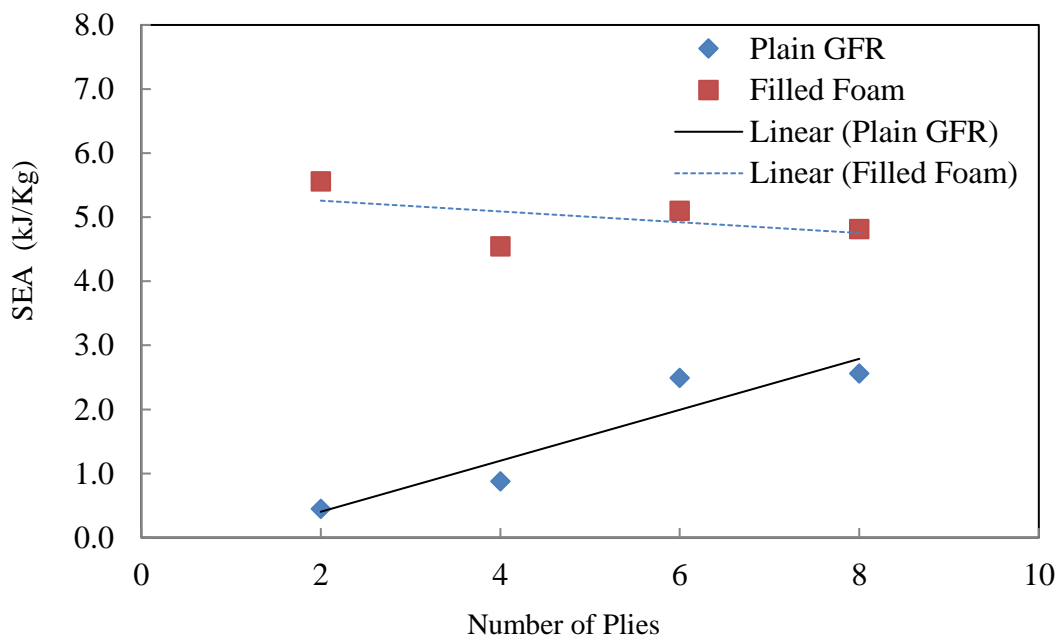


Figure 4.82: Comparison of corrugated core sandwich structures between plain GFRP and filled foam structures.

4.4.3 Specific energy absorption of corrugated core sandwich structures

In order to evaluate the structure performance, the specific energy absorption has been used as the main indicator of corrugated core structures in this study. Table 4.12 shows the list of various corrugated core sandwich structure types and their area density and the average specific energy absorption in terms of energy absorption per unit mass.

Table 4.12: Summary of Area density and specific energy absorption of various sandwich structures.

Structure types	Area Density (kg/m ²)	SEA (kJ/kg)
Plain GFRP corrugated	4.13	1.60
Filled Foam	4.96	5.01
Core configurations		
• Square	3.43	7.03
• Trapezoidal	3.35	4.84
Type of foam cores		
• C55+GFRP	3.05	6.11
• C55+PMI+GFRP	3.16	8.74
• C130+GFRP	3.25	9.56
• C200+GFRP	3.82	11.18
• C200+PMI+GFRP	3.97	13.20
Multi-core layer		
• 2 Layers	5.47	3.28
• 3 Layers	7.16	3.95
Unit cell size		
• 20 mm	4.18	4.07
• 40 mm	6.57	6.32
FMLs cores and skins	4.88	5.45
Cores with vertical reinforcements	2.20	26.26

The plain GFRP corrugated core sandwich structures have a less specific energy absorption at around 1.60 kJ/kg in average. However, this type of structure still has a benefit for some applications that require ventilation such as air or liquid flow pass through the structures. When the same plain GFRP corrugated core sandwich structures are filled with foam, the corresponding specific energy absorption is increased to 5.01 kJ/kg which is five times greater than its plain counterpart, but with losing the ventilation capability. On the other hand, of the foam filling corrugated core sandwich structures would benefit for maritime applications in particular gaining a buoyancy of a ship.

For core configurations with square and trapezoidal types, the former type has a greater specific energy absorption than the latter. By considering the GFRP core elements inside the structures, the square corrugated core sandwich structure type has more elements than the trapezoidal type. This gives the former structure the greater specific energy absorption than the latter structure even with gaining more overall structure mass.

The influence of using different types of foam core shows that the foam core with a higher density has a greater specific energy absorption. For example, using C200 and PMI as the mixed core could increase the specific energy absorption to 13.20 kJ/kg, while using C55 as a core would provide the specific energy absorption of only 6.11 kJ/kg.

Multi-layer core does not play an important role to increase specific energy absorption. As shown in Table 4.12, increasing the core layer from two to three only increase the specific energy absorption from 3.28 to 3.95 kJ/kg.

When increase the unit cell size, the results reveal a greater specific energy absorption due to increasing panel length and thickness. This leads to significantly increase energy absorption, without gaining much the mass of structure.

Using FML as a hybrid core does not make significant change on specific energy absorption. The best FML corrugated core sandwich structures could provide the specific energy absorption of 5.45 kJ/kg. This is likely due to ductility of aluminium. However, the FML corrugated structure offer a superior stiffness and additional protection from the skins.

In conclusion, the best corrugated core structure that has an outperformance in terms of specific energy absorption is the corrugated core sandwich structures with vertical reinforcements. This type of structures could offer a SEA 26.26 kJ/kg.

Furthermore, the specific energy absorption properties of the best structure in the current study are compared with other types of core materials from the literature, as shown in Table 4.13. The previous value of specific energy absorption in Table 4.12 is changed to be related to the others, as shown in the end of the table. Therefore, the performance of the corrugated core structure is similar to Aluminium foam of Altenaiji et al. [119], CFRP tubes embedded PVC foam of Alia et al. [124] and GFRP tubes supported by PS foam of Tarlochan et al. [126].

Table 4.13: Comparison of the SEA values of the best-performing corrugated core sandwich structure with those of other types of core material.

Core types	Density (kg/m³)	SEA (kJ/kg)	Author
PVC, PET, Linear Foam	40-200	8-15	Hassan et al. [116]
PMI foam, PVC foam	52–250	11–18	Heimbs [117]
PI/PU/PE foam	69.2- 104.2	2-9	Heimbs [118]
Aluminium foam	n/a	12.3-28.5	Altenaiji et al. [119]
Aluminium foam	270 -313	4.98- 5.5	Ochelski et al, [120]
Aluminium matrix syntactic foam	1640	50.6	Tao and Zhao [121]
Aluminium honeycomb	27–192	9–45	Heimbs [118]
Nature fibre honeycomb	0.1-0.4	0.6-6.5	Zuhri et al.[122]
Chiral CFRP honeycomb	n/a	96.5	Airoldi et al. [123]
Polypropylene honeycomb	40	3.1	Alia et al. [124]
Bamboo tube foam core	40-200	19-53	Umer et al, [125]
CFRP tubes embedded PVC foam	40-280	21-155	Alia et al. [124]
CFRP tubes embedded in PS foam	107.8	86	Heimbs [118]
GFRP tubes supported by PS foam	n/a	17.7–32.6	Tarlochan et al. [126]
Corrugated-cores	205-363	31.5-63.5	Ruzaimi and Cantwell [127]
Carbon foldcore	103–114	4.5–22.5	Heimbs [118]
Kevlar foldcore	48–113	2–7.5	Heimbs [118]
Nomex	29–48	8–18	Heimbs [118]
Lattice structure	3.5-13.9	0.6-6.4	Smith et al. [128]
Composite pyramidal truss cores	20-35	0.75-8	Xiong et al. [129]
Corrugated cores with vertical reinforcements	100-110	26.62	The current study

4.5 Summary

This chapter presents the experimental results on hybrid sandwich structures including reinforced foam and fibre metal laminates under various loading conditions. Here, the results from tensile tests, in plane shear tests and compression tests on rigid foams are firstly characterised to obtain the mechanical properties of bases materials such as aluminium alloy 2024-T3, GFRP composite laminates, and foams. Subsequently, the results on the various corrugated-core composite structures under quasi-static compression, three-point bending, and low velocity impact are analysed and discussed. Then, the experimental results obtained from the modified hybrid sandwich structures based on FML and corrugated-core under perforation and blast loading are evaluated. Finally, the failure mechanisms observed in the structures during and after the tests are presented and characterised. The results provide the first hand information on those novel sandwich structures, which will be useful for the further development and applications.

CHAPTER 5

FINITE ELEMENT MODELLING

There are three main parts of finite element modelling presented in this chapter. As the author started to study with the monolithic sandwich structures provided by a German company since in the beginning state in order to familiar with the materials and finite element modelling. First part is the finite element modelling of ‘low velocity impact response of curvilinear-core sandwich structures’. The relevant information including experimental procedure and results are listed here to avoid a confusion and easy to describe.

Then, the second and third parts come with more developments of the finite element modelling to study the flexural and compressive behaviour of hybrid corrugated core composite structures tested in the previous chapter.

The FE modelling results are verified and compared with the experimental results, following by parametric studies. A summary is presented at the end of this chapter to highlight the main findings.

5.1 The low velocity impact response of curvilinear-core sandwich structures

5.1.1 Introduction

Sandwich panels, consisting of thin skins bonded to a low density core material are finding widespread use in a wide range of applications, such as lightweight marine structures, impact-resistant land-transportation panels and high-performance load-bearing aerospace structures. Traditionally, most sandwich panels are based on either a lightweight polymer foam or metal foam or a honeycomb core. When skins are

bonded, the resulting structures offer exceptional specific strength-to-weight ratios and stiffness-to-weight ratios, buoyancy, dimensional stability, thermal and acoustical insulation characteristics. A number of research studies have focused on the properties of sandwich panels based on corrugated cores. Curvilinear corrugated-core sandwich structures offer superior mechanical properties and various types of such sandwich structure have been studied in detail [5, 9, 10, 20, 29, 148-152].

Curvilinear corrugated-core sandwich design has been used in the production of boxes and cardboard since the late 1800s [37]. They have been widely used in the packaging industry as a result of their low weight, recyclability and low cost. In the past, attempts have been made to predict the load-carrying capacity of corrugated box structures, most notably by McKee *et al.* [38]. Talbi *et al.* [37] analyzed the geometric and mechanical properties of corrugated board components. They also studied the behaviour of these corrugated structures when subjected to transverse shear and torsion. Allaoui *et al.* [39] noted that corrugated cardboard is very sensitive to atmospheric conditions. Shear buckling of the core of a corrugated paperboard structure was investigated by Isaksson and Gradin [40]. It was shown that the structural strength of the panel decreases rapidly below a critical thickness of fluting. Tian and Lu [41] studied the minimum weight of a corrugated panel based on fibre reinforced composites subjected to a uniform axial compressive load in order to design an optimal corrugated panel. Haj-Ali *et al.* [130] presented a refined nonlinear finite element approach for analyzing corrugated fiberboards. In their work, the anisotropic and nonlinear material stress-strain behaviour of the corrugated structured was modeled. It was found that the proposed refined modeling approach was able to accurately predict the overall mechanical behaviour and ultimate failure in a wide range of corrugated systems.

Metallic corrugated core sandwich structures offer potential for use in a wide range of applications, such as those involving impact/blast load mitigation. There is a limited amount of experimental and numerical data in the literature relating to the dynamic response of sandwich structures based on corrugated topologies. Rubino *et al.* [17] investigated the impact response of clamped stainless steel Y-framed and corrugated core sandwich plates loaded by aluminium foam projectiles. At low values of projectile momentum, the sandwich panels deflected less than their monolithic counterparts. However, at higher values of projectile momentum, the sandwich panels failed in a tearing mode, whereas the monolithic panels remained intact. Kılıçaslan *et al.* [18] conducted an experimental and numerical study on the impact response of layered trapezoidal corrugated aluminium core and aluminium sheet interlayer sandwich structures. Here, rate effects were attributed to micro-inertial effects that increased the critical buckling load of the fin at high rates of loading. Radford *et al.* [19] conducted impact tests on triangular corrugated, pyramidal and aluminium foam core sandwich plates. It was observed that the corrugated and metal foam core sandwich plates offered the best dynamic performance. Tilbrook *et al.* [20] investigated the dynamic crushing characteristics of sandwich panels based on prismatic lattice cores. Here, the quasi-static and dynamic compression deformation behavior of stainless steel corrugated and Y-frame sandwich cores were tested. At velocities below 30 m/s, micro-inertial stabilization against elastic buckling was observed to occur. At higher velocities the propagation of plastic waves within the core resulted in the front face stresses increasing with velocity, whilst the rear surface stresses remained roughly constant. Liang *et al.* [21] developed lightweight structural concepts for naval applications, with a view to replacing traditional designs with optimized metallic corrugated core sandwich panels. The optimum designs of metallic corrugated core sandwich panels

were modelled under blast loading. The authors showed that parameters, such as the corrugation angle and core thickness, are important when designing the core structure. Recently, Mohr and Marcadet [22] developed a phenomenological ductile fracture initiation model to predict ductile fracture in industrial practice. Here, an extended Mohr–Coulomb criterion is proposed, which makes use of the Hosford equivalent stress in combination with the normal stress acting on the plane of maximum shear. The validation with experimental results indicates that the proposed Hosford-Coulomb model can be used to accurately predict the onset of ductile fracture in advanced high strength steels. Also, Roth and Mohr [23] undertook extensive experimental and numerical work to investigate effect of strain rate on ductile fracture initiation in advanced high strength steel sheets. The extended stress-state dependent Hosford-Coulomb fracture initiation model is proposed to evaluate the strain rate effect on the onset of ductile fracture, which is also successfully validated against the experimental results. These state of the art theories could be used to simulate ductile fracture of metallic materials.

In the present work, a range of metallic curvilinear corrugated-core sandwich structures has been developed [144]. These panels are made in a continuous process by adhesively-bonding two face sheets to a core consisting of a wave-formed aluminium alloy. These panels are finding use in a range of applications in the construction sector, the transport industry and other load-bearing mechanical engineering applications.

The aim of this study is to investigate the dynamic response of such curvilinear corrugated-core sandwich structures, when subjected to low velocity impact loading. This scenario could be the impact response of these structures is subsequently modeled

and the resulting models are then used to investigate other loading conditions and material systems.

5.1.2 Experimental Procedure

The corrugated-core sandwich structures investigated in this study were based on an EN AW-5182 H48 aluminium alloys supplied by Metawell® in Germany [24]. The sandwich panels were manufactured by adhesively bonding two flat alloy skins to a curvilinear alloy core material. Figure 5.1 shows the basic design of the sandwich panels investigated here. Two panel configurations, with different face sheet thicknesses and core sizes, were tested, details of which are given in Table 5.1.

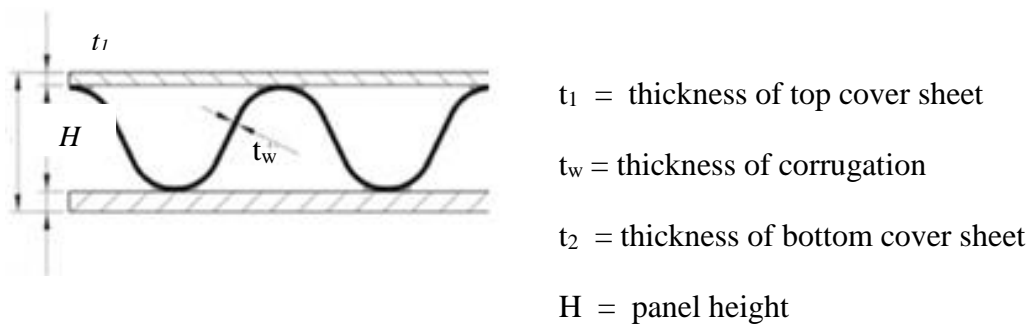


Figure 5.1: Schematic of the cross-section of the curvilinear sandwich panel.

Table 5.1: Panel dimensions and areal density for the aluminium alloy panels.

Type	t_1 (mm)	t_w (mm)	t_2 (mm)	H (mm)	Areal density (kg/m ²)
Alu hl/H6	0.5	0.2	0.5	6.0	3.8
Alu hl/H10	0.8	0.3	0.5	10.0	5.2

Low velocity impact tests were conducted using an Instron CEAST 9350 falling-weight impact tower. A piezoelectric load sensor was imbedded at the tip of an impactor holder, which makes impactor replaceable. An impact mass of 5.32 kg, with a 25.4 mm diameter spherical steel head, was used for all tests. Loading data were acquired as voltage output and then transferred into a module 64K DAS (Data Acquisition Station) at a frequency of 100 kHz. Impact velocity was acquired by a photoelectric sensor. During the impact test, the impactor holder was released and dropped vertically passing through the photoelectric sensor beam. At the tip of impactor right at the surface of specimen, the impact velocity was detected. The error of the measured velocity is within 0.01 m/s. Each impact velocity was acquired by a certain height, which calculated from the required impact energy. The tests were conducted by a varying impact velocity between 1.9 and 5.4 m/s. This range of velocities correlates the strain rate from 100 to 150 s⁻¹. Displacement was calculated by Pro Analyst software, basically considered from load-time relation.

Square test panels, with an edge length of 155 mm, were clamped by a cylindrical ring with inner and outer diameters of 76 and 100 mm, respectively. A clamping force of

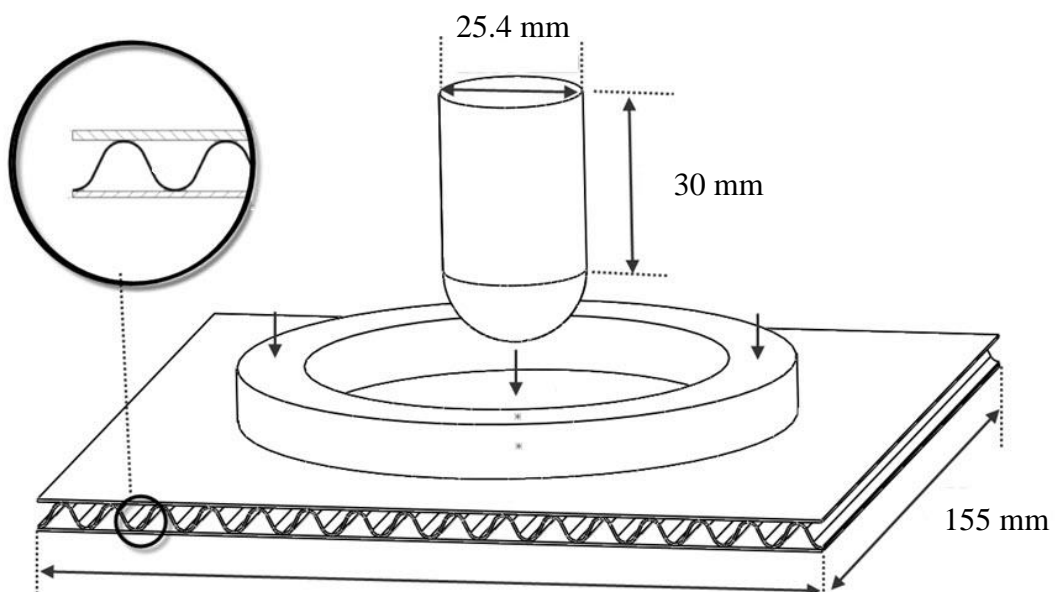


Figure 5.2: The experimental test set-up for low velocity impact testing.

200 Newtons was applied to hold the panels in place during testing. Further details of the panel configuration and test conditions are given in Figure 5.2. Following impact, the test panels were sectioned through the point of impact and examined under an optical microscope in order to highlight the failure mechanisms that occurred during the impact event.

The mechanical properties of the aluminium alloy were determined by conducting tensile tests on rectangular samples with length and width dimensions 200 x 25 mm, removed from the skin of an untested panel. The tests were undertaken on an Instron 4505 universal test machine at a crosshead displacement rate of 1 mm/minute, according to ASTM E8 / E8M [138]. The data obtained from the tensile tests on the aluminium alloy skins are given in Table 5.2.

Table 5.2: Isotropic hardening data for the EN AW-5182 H48 aluminium alloy.

Yield stress (MPa)	153	160	178	203	214	224	231	234	235
Plastic strain	0	0.0004	0.002	0.013	0.020	0.030	0.040	0.050	0.056

5.1.3 Finite element modelling

ABAQUS/Explicit [153] was used to develop numerical simulations of corrugated-core sandwich structures subjected to low velocity impact loading. The aluminium alloy was modelled as an elasto-plastic material that exhibits rate-dependent behaviour, according to a uniaxial flow rule, whereby:

$$\dot{\bar{\epsilon}}_{pl} = h(\bar{\sigma}, \bar{\epsilon}_{pl}) \quad (5.1)$$

In which h is a strain hardening function, $\bar{\sigma}$ is the von-Mises equivalent stress, and $\bar{\varepsilon}_{pl}$ is the equivalent plastic strain. The isotropic hardening data for the EN AW-5182 H48 aluminium alloy are given in Table 5.2. The density of the aluminium was taken as $\rho = 2690 \text{ kg/m}^3$. The material properties of this alloy are detailed in Table 5.3. A constant plastic strain-rate was used to cover the range of loading conditions considered when developing the finite element models.

Table 5.3: Materials properties and parameters for EN AW-5182 H48 aluminium alloy used in finite element modelling.

Property	Value
Young's modulus (GPa)	68
Density (kg/m ³)	2650
Strain rate (s ⁻¹)	100-150
Fracture strain for ductile damage	0.065
Stress triaxiality	0.33
Fracture energy (kJ/m ²)	67 [27]

The total strain-rate, $\dot{\varepsilon}$, can be decomposed into an elastic component, $\dot{\varepsilon}_{el}$, and a plastic component, $\dot{\varepsilon}_{pl}$, as:

$$\dot{\varepsilon} = \dot{\varepsilon}_{el} + \dot{\varepsilon}_{pl} \quad (5.2)$$

The uniaxial plastic strain, ε_{pl} , which is based on recoverable elastic strain, can be calculated using the following equation:

$$\varepsilon_{pl} = \varepsilon_{total} - \frac{\sigma_{total}}{E} \quad \sigma_{total} > \sigma_y^o \quad (5.3)$$

where σ_{total} is any stress level exceeding the initial yielding point, ε_{total} is the total strain corresponding to σ_{total} , E is modulus of elasticity and σ_y° is the initial yield stress. Furthermore, the constitutive equations with strain hardening employed in the numerical modelling can be expressed as

$$\bar{\sigma} = \begin{cases} \varepsilon_{el} E & , \sigma < \sigma_y^\circ \\ 15.649 \ln(\bar{\varepsilon}_{pl}) + 278.14 & , \sigma > \sigma_y^\circ \end{cases} \quad (5.4)$$

The rate-dependent hardening curves can be expressed using the following:

$$\bar{\sigma}(\bar{\varepsilon}_{pl}, \dot{\bar{\varepsilon}}_{pl}) = \sigma_y(\bar{\varepsilon}_{pl})R(\dot{\bar{\varepsilon}}_{pl}) \quad (5.5)$$

In which R is the stress ratio ($= \bar{\sigma} / \sigma_y$).

The ductile damage criterion is a phenomenological model for predicting the initiation of damage due to nucleation, growth as well as the coalescence of voids. The ductile damage model assumes that the equivalent plastic strain associated with the initiation of damage, $\bar{\varepsilon}_D^{pl}$, depends on the stress triaxiality and strain-rate:

$$\bar{\varepsilon}_D^{pl} = \bar{\varepsilon}_D^{pl}(\eta, \dot{\bar{\varepsilon}}_{pl}) \quad (5.6)$$

where η ($= -p/\bar{\sigma}$) is the stress triaxiality and p is the pressure stress. The condition for damage initiation is satisfied when:

$$\omega_D = \int \frac{d\bar{\varepsilon}_{pl}}{\bar{\varepsilon}_D^{pl}(\eta, \dot{\bar{\varepsilon}}_{pl})} = 1 \quad (5.7)$$

In which ω_D increases monotonically with increasing plastic deformation. Following each increment in the analysis, the ω_D is computed as:

$$\Delta\omega_D = \int \frac{\Delta\bar{\epsilon}_{pl}}{\bar{\epsilon}_D^{pl}(\eta, \dot{\epsilon}_{pl})} \geq 0 \quad (5.8)$$

When the ductile failure criterion is satisfied at a given point, all of the stress components are then reduced to zero and it is assumed that the material point is assumed to have failed. If all of the material points at any one section of an element fail, the element is removed.

In order to reduce CPU time, only a quarter of the model, with one element through the sheet thickness, was generated, as shown in Figure 5.3. The aluminium corrugated core and skin parts were discretized with a uniform mesh, consisting of 8-noded linear brick elements with reduced integration and hourglass control (C3D8R). The core and skins were fully bonded with a tie constraint at the interface areas, since debonding did not occur during the test. A 4-node 3-D bilinear rigid quadrilateral element (R3D4) was used to mesh the support rings and the spherical projectile. The finite element modelling has been carried out to investigate the influence of the number of elements through the thickness on the impact response. Figure 5.4 shows that there is no significant difference on the simulated load-displacement relationships obtained from the models with one, two or three elements through the thickness. Therefore, only one element through the sheet thickness is used in the current study.

The lower support ring was fully fixed, whilst the upper ring was clamped with a force of 200 Newtons to model the experimental clamping condition. The 5.32 kg projectile was constrained to move in the y-direction with a predefined initial velocity.

A surface-to-surface contact interaction was created to allow for sliding between the projectile surface and the individual nodes located in the central region of the target. Also, a general contact interaction was used for self-contact between the inner surfaces

of the skins and the individual cells in the core. A friction coefficient of 0.3 was used to represent tangential contact interactions and a hard contact was assumed in the normal direction.

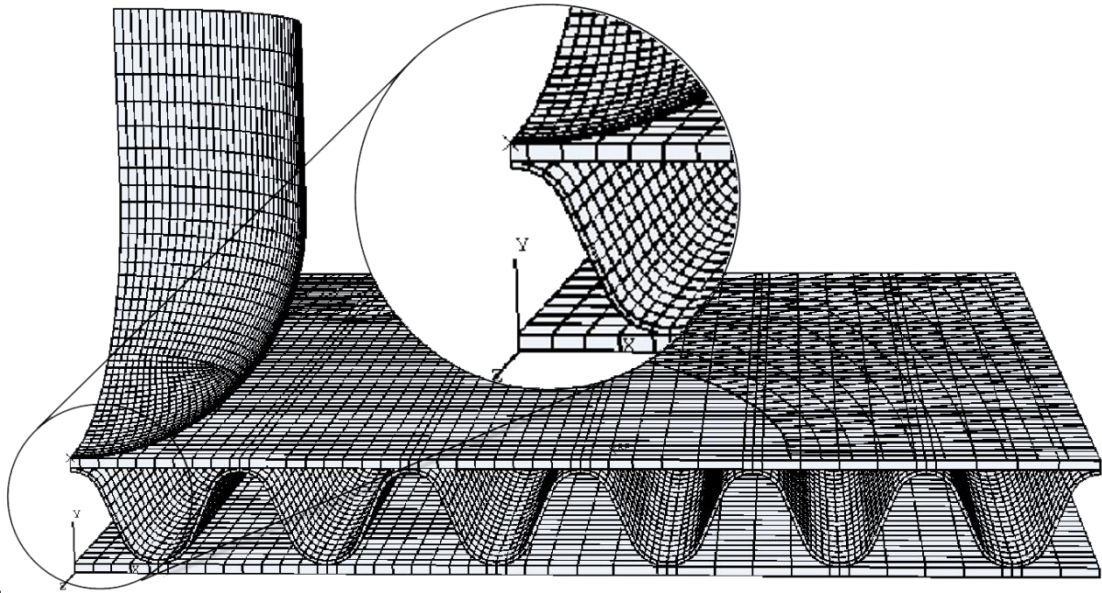


Figure 5.3: The finite element mesh of a quarter - sized model.

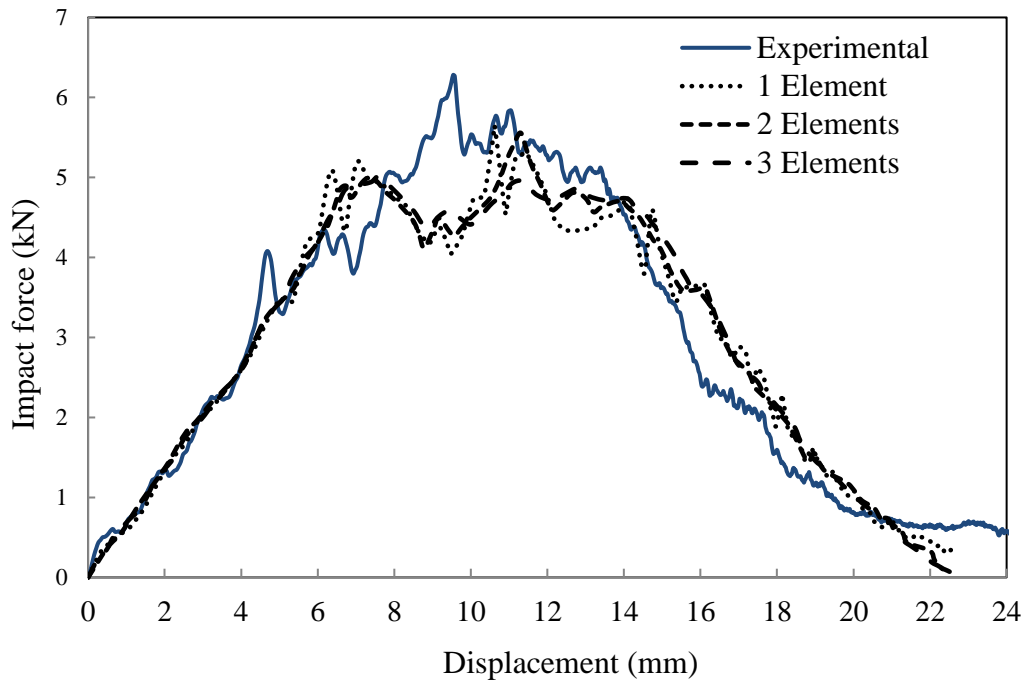


Figure 5.4: Comparison of the experimental load-displacement trace and the predicted ones using models with different number of elements through the sheet thickness for an Alu hl /H6 panel subjected to an impact energy of 80J.

5.1.4 Experimental results and validation of the numerical model

Figure 5.5 shows cross-sections of the 6 mm thick panels following impact at energies between 10 and 80 Joules. Damage at the lowest energy takes the form of buckling



Figure 5.5: The process of damage development in the 6 mm thick panel.

within the cells in the central region, as well as permanent plastic deformation in the uppermost skin. Increasing the energy to 20 Joules results in complete crushing of the cells under the impactor and slight deformation of the lower skin. Fracture of the top and bottom layer is in evidence following a 40 Joule impact, with this form of damage becoming more severe as the energy is increased to 50 and then 60 Joules. Finally, the target is fully perforated following an 80 Joule impact, with the projectile passing through the panel. In spite of the severe level of damage, it is interesting to note that this damage remains localised to the point of impact. Indeed, closer inspection of the cross - sections suggests that damage never extends beyond one cell width on either side of the impact zone. This evidence indicates that energy is absorbed over a region immediate to the point of impact.

Figure 5.6 shows cross-sections of the 10 mm panels following impact at energies between 15 and 120 Joules. Here, again, initial damage takes the form of buckling of the curvilinear cells under the indenter and plastic deformation of the uppermost skin. Following a 30 Joule impact, the central core region has been completely crushed and the top skin has fractured under the hemispherical impactor. The lower skin was

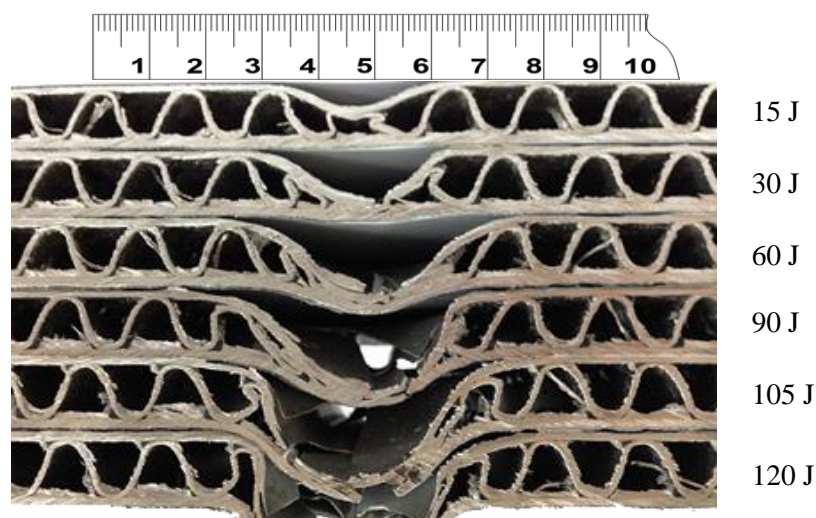


Figure 5.6: The process of damage development in the 10 mm thick panel.

fractured after a 90 Joule impact, where significant localised plastic deformation in outermost skin is evident. Finally, the projectile perforated the panel during a 120 Joule impact, leaving a failure zone in which damage is once again very localised to the point of impact.

Figure 5.7 shows typical load-displacement traces following low velocity impact tests on the 6 mm thick panels. Included in each trace is the prediction of the finite element model. At the lowest energy, 20 Joules, the experimental curve increases to an initial peak at 3000 Newtons, at which point the load drops slightly before increasing further via a number of small load drops to 4400 Newtons. Finally, the panel is unloaded as the projectile rebounds, leaving a residual displacement of approximately 6 mm. An examination of the figure indicates that the finite element model captures the principal features of the load-displacement traces. Closer inspection shows that the model does not predict the small oscillation prior to the maximum in the impact force. Figure 5.7(b) shows the corresponding load-displacement traces following a 30 Joule impact. Here, the experimental trace increases to an initial peak of 4200 Newtons, before reaching a maximum at approximately 5000 Newtons. The sudden spike in the load is

assumed to be associated with some form of ringing in the load-cell. Again the model predicts the impact response of these thinner panels with reasonable success.

Following the rebounding process, a residual dent of approximately 10 mm is observed in the experimental trace. Increasing the impact energy to 60 Joules results in an enlarged load-displacement trace with significant energy absorption occurring. Here, the experimental trace oscillates around a force of approximately 4500 Newtons, as the projectile penetrates through the panel. Finally, complete perforation of the corrugated sandwich panel occurs when the incident impact energy is increased to 80

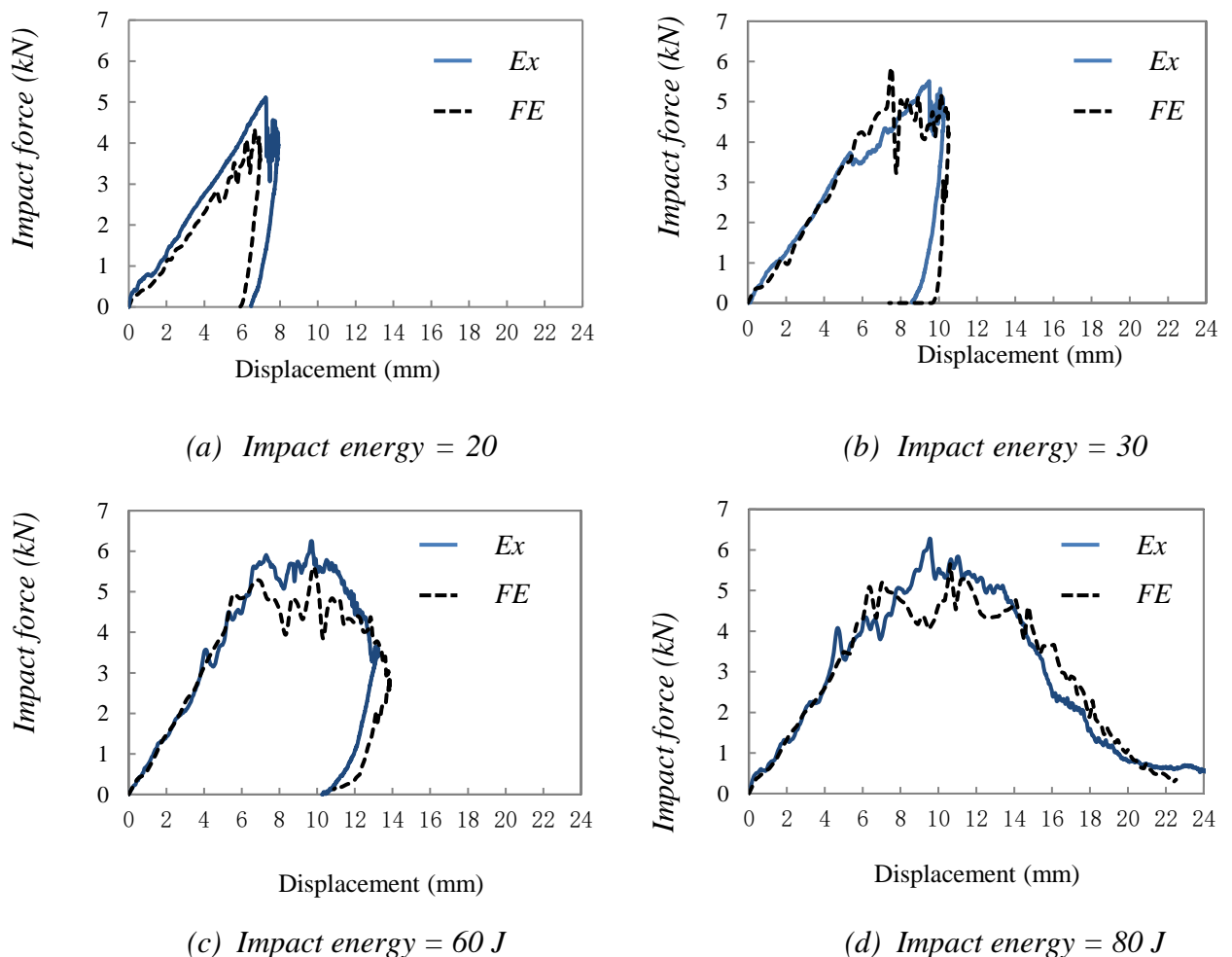
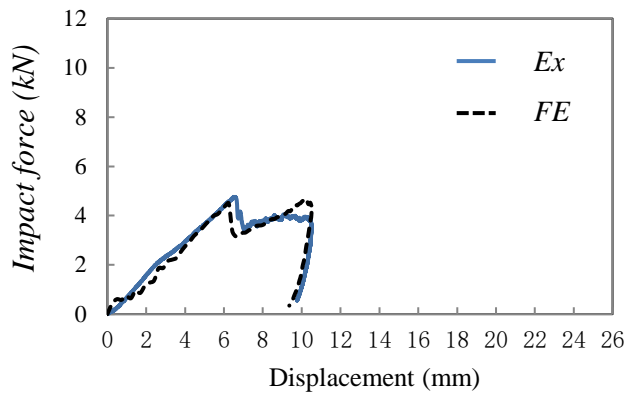


Figure 5.7: Load-displacement plots from Alu hl /H6 panels in ascending impact energy. (a) Impact energy = (a) 20 J, (b) 30 J, (c) 60 J, (g), (d) 80 J.

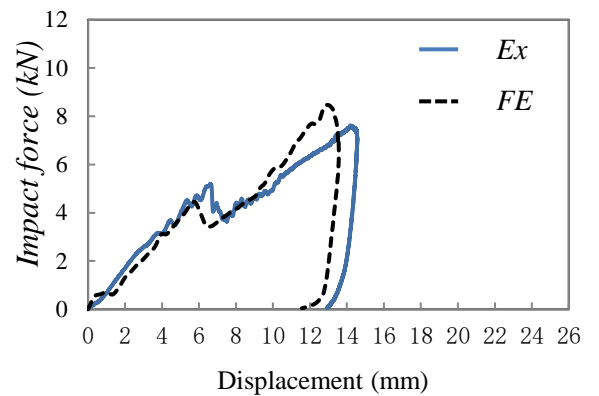
Joules. An examination of the two traces in Figure 5.7(d) indicates that there is very

good agreement between the predicted and measured response. The predicted value of perforation energy, as measured from the area under the load-displacement trace, is approximately 71 Joules, a value that is similar to the experimental value of 75 Joules.

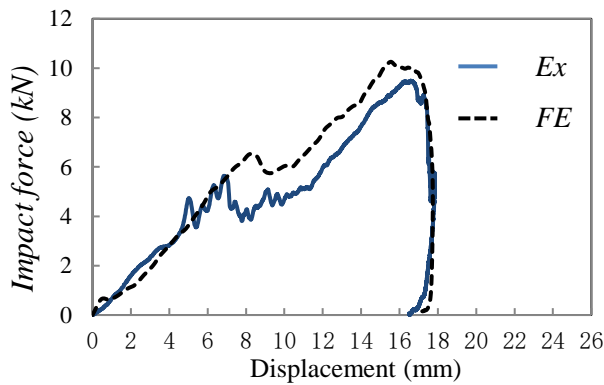
Figure 5.8 shows typical load-displacement traces following low velocity impact tests on the 10 mm thick sandwich panels. At the lowest energy of 30 Joules, Figure 5.8(a), the experimental load-displacement trace increases in a roughly linear fashion up to a peak at approximately 4400 Newtons before dropping rapidly, prior to increasing to a second peak and subsequent unloading. An examination of the figure indicates that the finite element model accurately predicts the overall response. An examination of the model indicates that the initial drop in load is associated with localised buckling in the curvilinear core. Increasing the incident energy to 60 and then to 90 Joules resulted in a similar trace, although the final peak load is clearly much higher than that at 30 Joules. Finally, the panel is completely perforated following impact at 120 Joules, with the panel absorbing an energy equivalent to approximately 116 Joules, a value that compares favourably with the predicted value of 121 Joules.



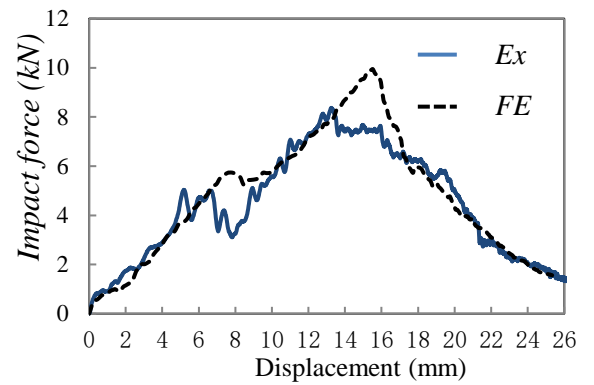
(a) Impact energy = 30 J



(b) Impact energy = 60 J



(c) Impact energy = 90 J



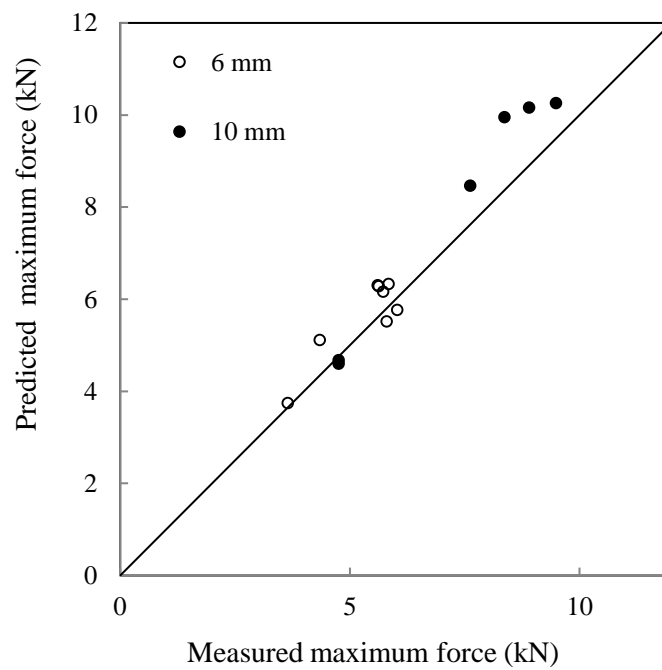
(d) Impact energy = 120 J

Figure 5.8: Load-displacement plots from Alu hl/H10 panels ascending impact energy (a) Impact energy = (a) 30 J, (b) 60 J, (c) 90 J, (d) 120 J.

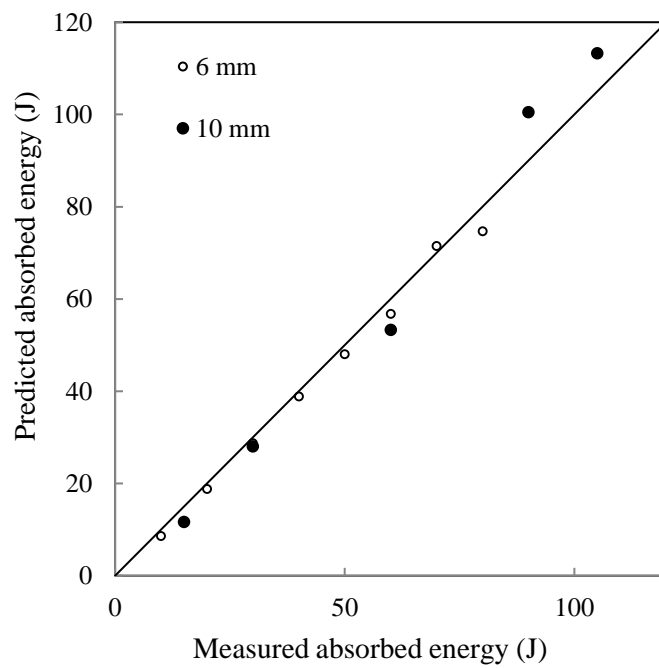
The accuracy of the finite element models was assessed by comparing the predicted maximum impact force against the corresponding experimental values and these data are presented in Figure 5.9(a). Here, it is clear that the predictions of the FE models are in close agreement with the experimentally-measured values for both the thin and thick sandwich panels. Indeed, the largest error between the two sets of data was approximately 10%. Similar levels of agreement are apparent when the predicted

levels of absorbed energy are plotted against the experimental values, Figure 5.9(b). Here, the average error between the predicted and measured values of absorbed energy is 7%. The evidences in Figure 5.9(a) and 5.9(b) support the conclusion that the finite element model is able to accurately predict the low velocity impact response of these corrugated core sandwich structures.

Figure 5.10 shows the numerical predictions of the cross-sections of the 6 mm thick sandwich panels. These cross-sections can be compared to the equivalent experimental cross-sections in Figure 5.5. A comparison of the experimental and numerical cross-sections indicates that the finite element model accurately captures the key failure mechanisms occurring within the panels. Here, the high levels of plastic deformation occurring within the upper and lower skins is clearly evident, as well as the localized region of fracture observed in the surface layers. Closer inspection indicates that the zones over which the upper and lower skins are seen to deform is slightly greater in the models than in the actual panels. Apart from this discrepancy, it appears that the model accurately predicts the failure processes in these sandwich panels.



(a)



(b)

Figure 5.9: (a) Comparison of predicted versus measured maximum force, (b) Comparison of predicted absorbed energy and measured absorbed energy.

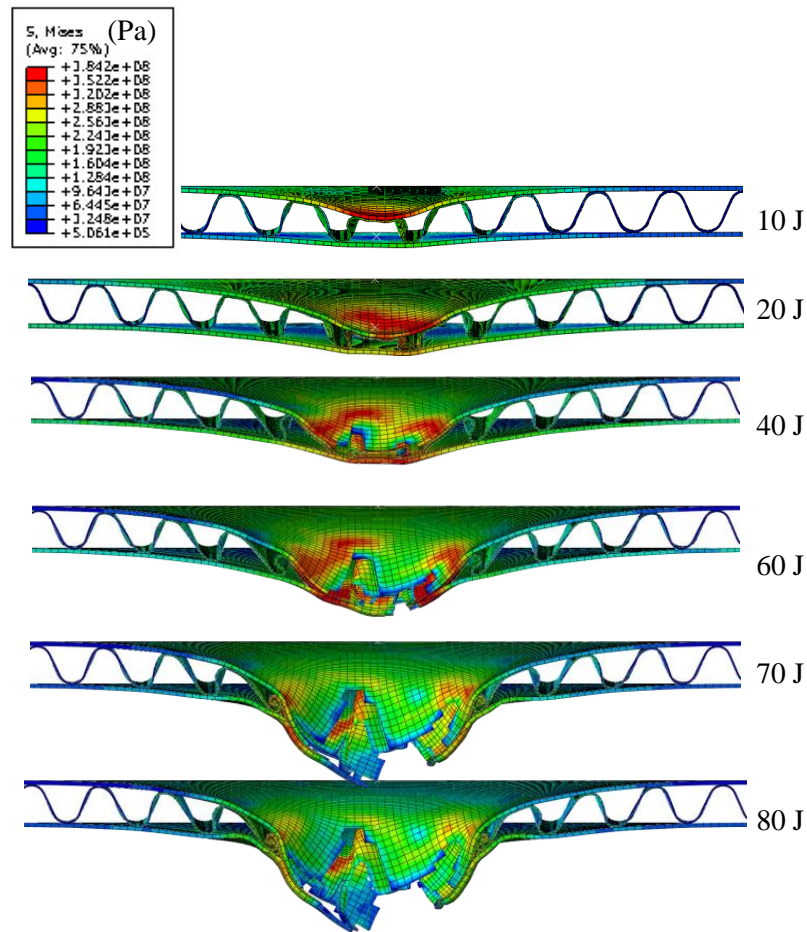


Figure 5.10: Finite element predictions of the damage characteristics in the 6 mm thick Al hl/H6 panels.

Figure 5.11 shows cross-sections of the impact-damaged 10 mm panels, as predicted by the finite element analysis. At the lowest energy, 15 Joules, the top skin is permanently deformed in the vicinity of the impactor, resulting in localized buckling of the curvilinear web. This is most evident in the central cell, where the walls of the web exhibit distinct bulges. Increasing the energy to 30 Joules forces the top skin in contact with the lower skins, effectively crushing the central cell in the process. At an impact energy of 60 Joules, the top face forces the lower skin downwards, a process that continues until the lower skin is clearly fractured following an impact energy of 90 Joules.

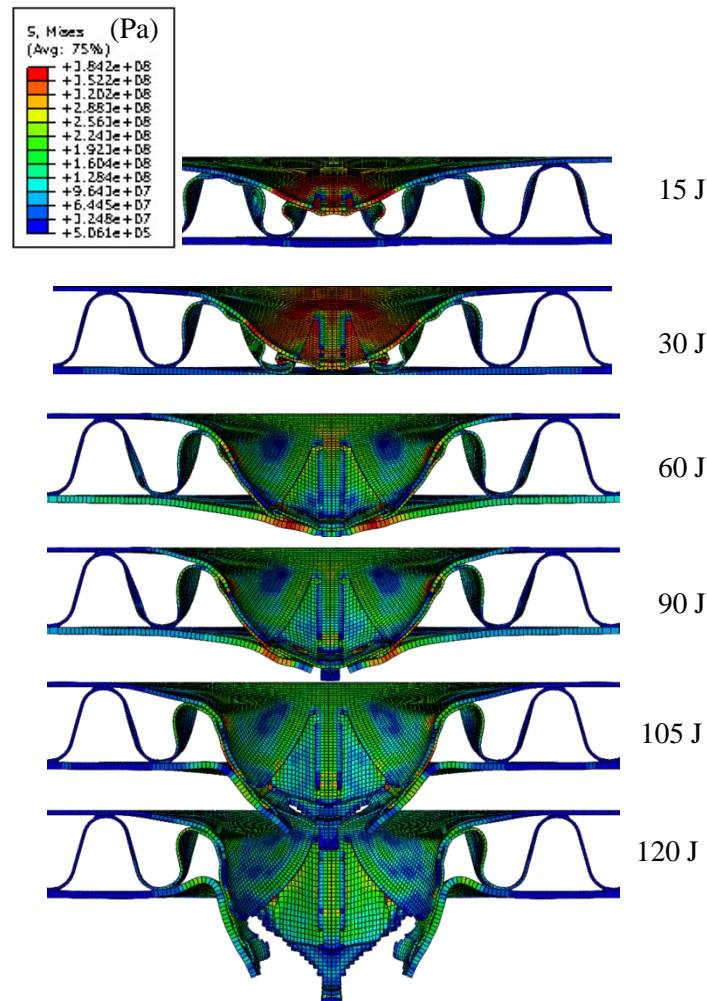


Figure 5.11: Finite element predictions of the damage characteristics in the 10 mm thick Al hl/H10 panels.

This process continues until the panel is fully perforated following a 120 Joule impact. Here, both skins have been highly deformed and the cell immediate to the perforation zone has been damaged. A comparison of these predicted damage patterns with those observed experimentally, Figure 5. 6, highlights a high level of agreement between the two. The model appears to identify the important failure processes and also predicts that damage remains concentrated over a small volume close to the point of impact.

In the final part of this research investigation, the finite element model was used to understand the influence of varying key parameters on the perforation resistance of these corrugated core sandwich structures. Here, attention focused primarily on

investigating the effect of varying the angle at which the projectile strikes the target, the projectile diameter as well as the material properties of the sandwich materials.

5.1.5 Parametric studies

5.1.5.1 Influence of impact angle on perforation resistance

Typically, it is very difficult to undertake oblique impact tests, particularly using a falling-weight impact rig. This is in part due to the fact that impacts of this nature generate a horizontal force component that drives the impactor against one of the vertical columns used to guide the impactor. One of the advantages of having validated the numerical model is that it can then be used to predict the response of these more complex impact events with reasonable confidence. Figure 5.12 shows load-displacement traces generated by the FE analysis for the 6 mm thick panel subjected to impact at angles between 90° (i.e. normal impact) and 50° . It should be noted that the force and displacement are measured along an axis corresponding to the trajectory of the projectile. The initial stiffness of all the panels is similar, with the force rising in a roughly linear fashion up to an initial peak load. The magnitude of this initial maximum in force is similar for all angles, having a value between 4 and 5 kN in all cases. Continued loading results in a second distinct peak, the magnitude of which appears to increase with increasing obliquity. For example, the maximum force predicted for a normal (90°) impact is approximately 5.7 kN, whereas that for a 50° impact is approximately 6.9 kN. The force then reduces to zero, as the projectile perforates the panel. Figure 5.13 presents the finite element predictions of the perforated panels following impact at angles between 90° and 50° . All figures again show that damage is localised to the region of impact. It is clear that the length of the distant petal (i.e. that produced as the projectile exits the structure) increases with

impact angle. An examination of the impact regions indicates that the formation of this exit petal triggers a localised buckle in the distal layer at higher angles of obliquity.

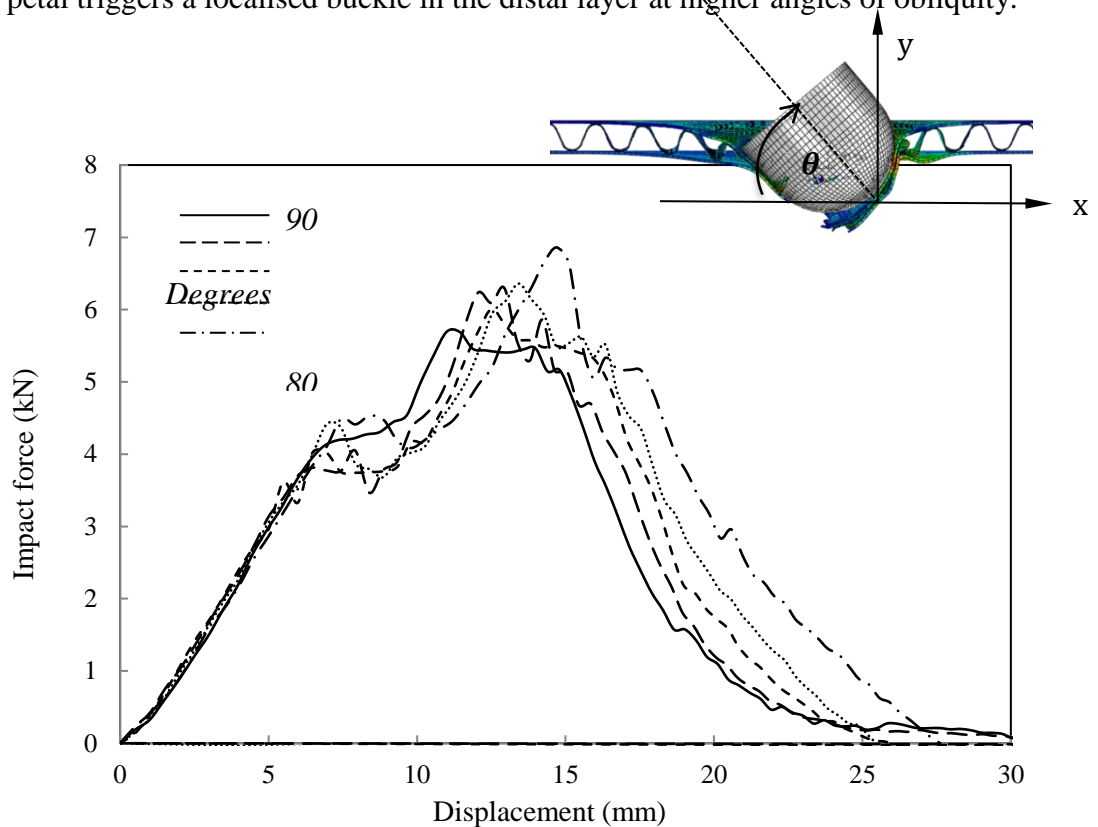


Figure 5.12: The influence of angle of obliquity on the perforation resistance of the 6 mm thick sandwich panels.

As before, the area under the load-displacement traces was used to determine the energy required to perforate the panels. Figure 5.14 shows the variation of perforation energy with impact angle for the five impact conditions considered for the three materials in this investigation. Here, it is evident that the energy required to perforate the panels increases from 95, 115 and 120 to approximately 148, 195 and 210 Joules for the 2024-T3, the stainless steel and the titanium alloy respectively, as the impact angle is varied from 90° to 50°. This increase in perforation energy is associated with the fact that the projectile has to fracture a larger volume of material as it passes through the target at an off-axis angle. It is also possible that changes in the buckling

and collapse response of the cores and the skins lead to a small increase in energy absorption.

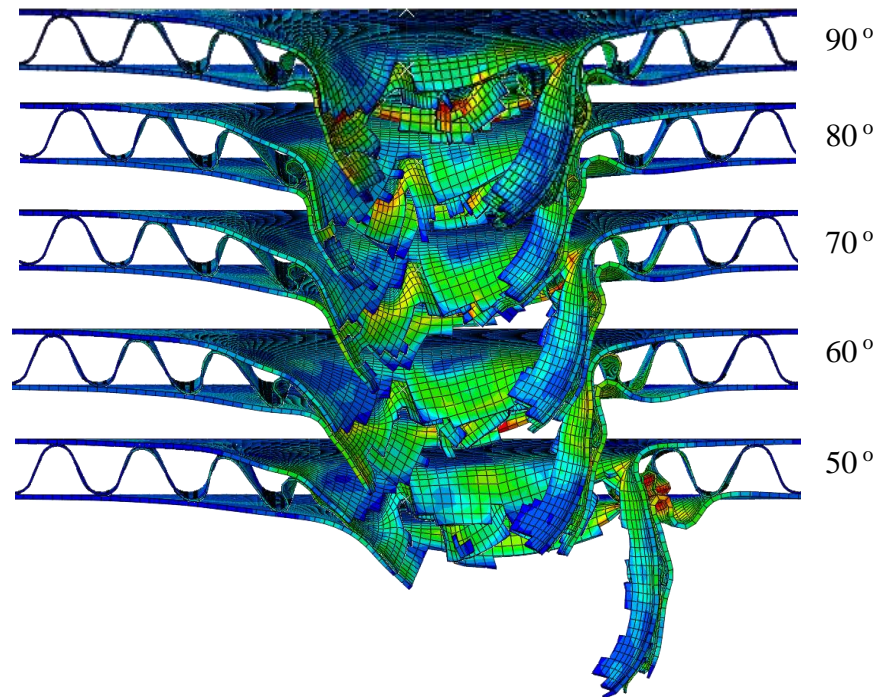


Figure 5.13: Finite element predictions of damage at the perforation threshold in 6 mm thick panels impacted at angles between 90 o (normal) and 50 o.

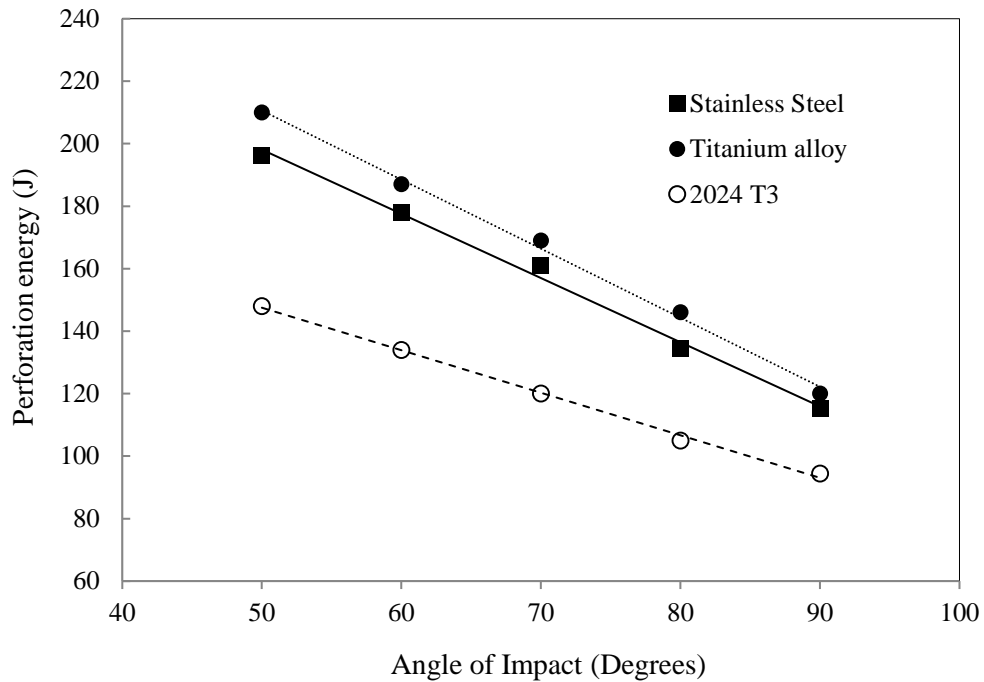


Figure 5.14: The validation of perforation energy with angle of obliquely for the 2024 - T3 aluminium alloy, the stainless steel and the titanium alloy.

5.1.5.2 The influence of material properties on perforation resistance

Clearly, the low velocity impact response of the corrugated sandwich structure studied here is likely to be strongly dependent on the type of material from which the cores and the skin are manufactured. In order to investigate this in more detail, finite element models were created based on five additional metallic substrates, these being a 2024-T3 aluminium alloy, an A5052 aluminium alloy, a 6061-T4 aluminium alloy, a stainless steel (X5CrNi18-10) [154] and a Ti6Al4V titanium alloy [155]. The mesh and boundary conditions were selected to be the same as those discussed previously and outlined in Figure 5.2 and 5.3. In each case, the response of the panels at the perforation threshold was examined and the energy required to perforate each structure determined from the load-displacement trace. Figure 5.15(a) shows the predicted perforation load-displacement traces for the four aluminium alloys.

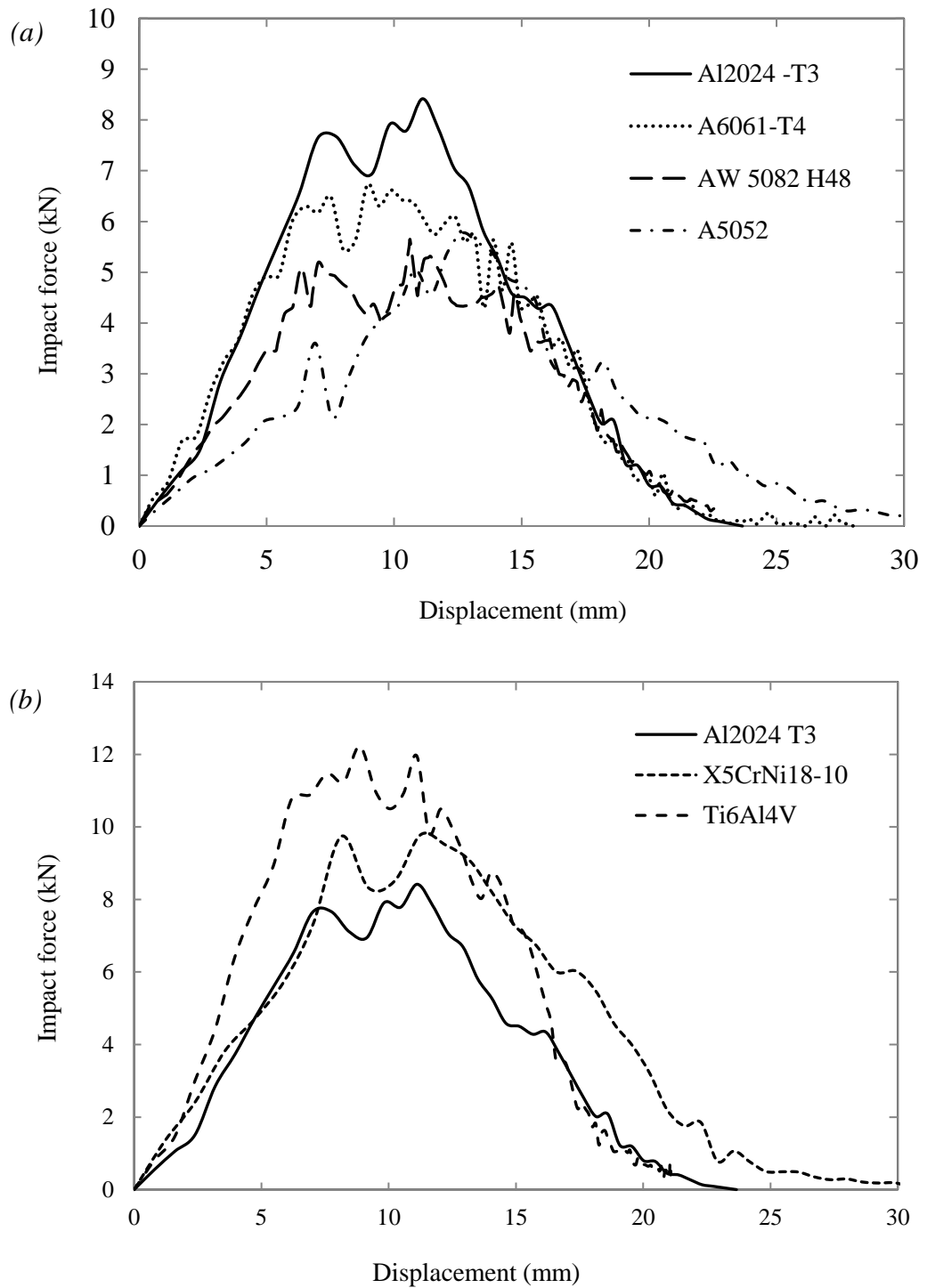


Figure 5.15: The predicted load-displacement traces of (a) the four aluminium alloys, (b) comparison of the stainless steel and titanium alloy with the 2024-T3 aluminium alloy.

An examination of the figure indicates that the 2024-T3 exhibits the highest maximum force, a value associated with the superior yield strength and tensile strength of this alloy. In contrast, the A5052 alloy offers a reduced response, linked to the poorer mechanical properties of this alloy. The model also predicts that this alloy undergoes a greater displacement during the impact event. Figure 5.15(b) compares the load-displacement responses of the titanium and stainless steel-based sandwich structures with the 2024-T3 alloy. Clearly, there is some similarity in all three traces, with the titanium alloy exhibiting the higher impact forces throughout the event.

Figure 5.16 summarises the predicted perforation resistances of the four aluminium alloy sandwich structures, as well as those of the stainless steel and the titanium alloy. An examination of the figure indicates that the 2024-T3 alloy offers the highest perforation energy of the four aluminium alloys. The predicted perforation energy for this alloy is approximately 45% above that of the A5052 system. Clearly, the stainless steel offers a superior perforation resistance to that of the aluminium alloys and the titanium alloy offers the highest values of perforation energy, with a value approaching 120 Joules. The perforation energies were divided by the areal density of the panels to yield specific values, and these data are included in Figure 5.16. Here, it is clear that the 2024-T3 alloy offers the highest specific perforation energy (SPE) of the six material systems considered here. Clearly, the higher densities of the stainless steel and titanium alloy greatly reduce the relative perforation resistances of these sandwich structures, with the SPE of the steel and titanium panels being only 33% and 58% that of the 2024-T3 alloy.

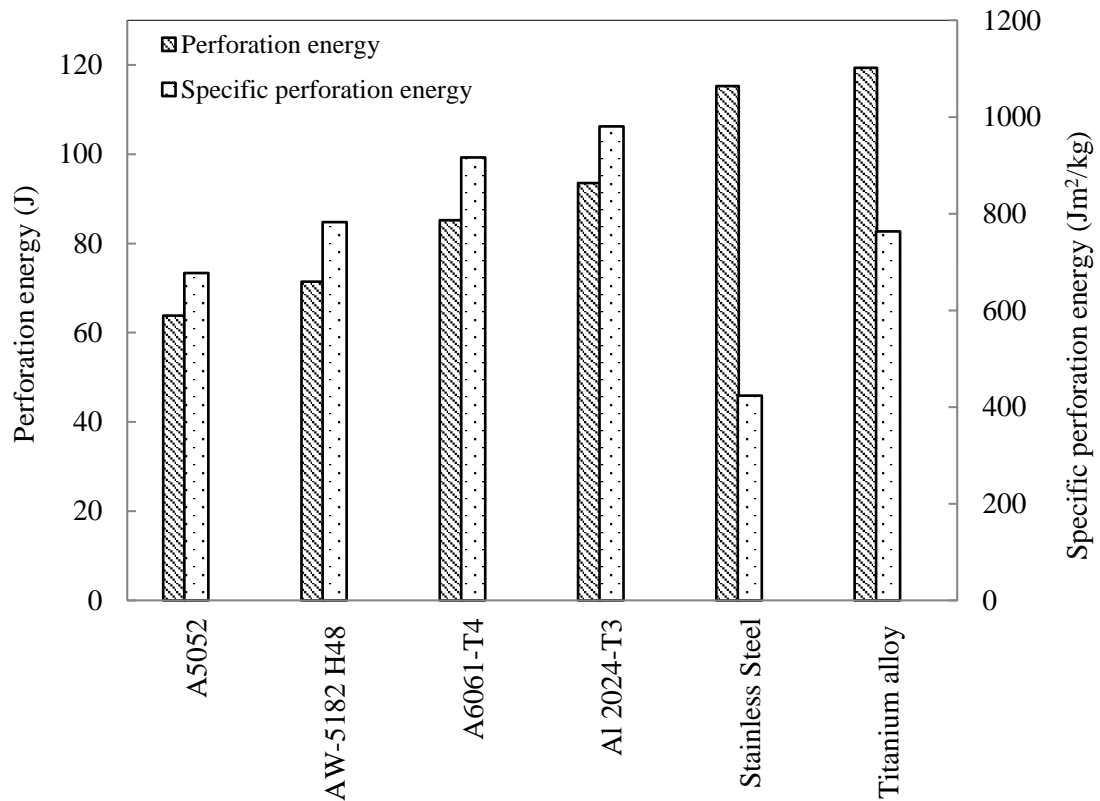


Figure 5.16: Summary of the predicted perforation energies and specific perforation energies for the six sandwich structures

5.1.5.3 The influence of projectile diameter

The final parameter to be investigated in this study was the projectile diameter. Here, the projectile diameter was varied between 5 to 30 mm. In each case, it was assumed that the projectile impinged the target directly above the apex of the curvilinear. Three material systems were investigated, these being stainless steel, titanium alloy and the 2024-T3 alloy. Figure 5.17 shows the variation of perforation energy with projectile diameter for the three material systems. As expected, the perforation energy is predicted to increase with projectile diameter. The predicted increase is non-linear. For example, the energy required to perforate the 2024-T3 panel with a 5 mm diameter impactor is predicted to be 10.3 Joules, whereas that for the 30 diameter impactor is

130 Joules. As before, the titanium alloy offers the most impressive performance, however this is at the expense of an increased panel weight.

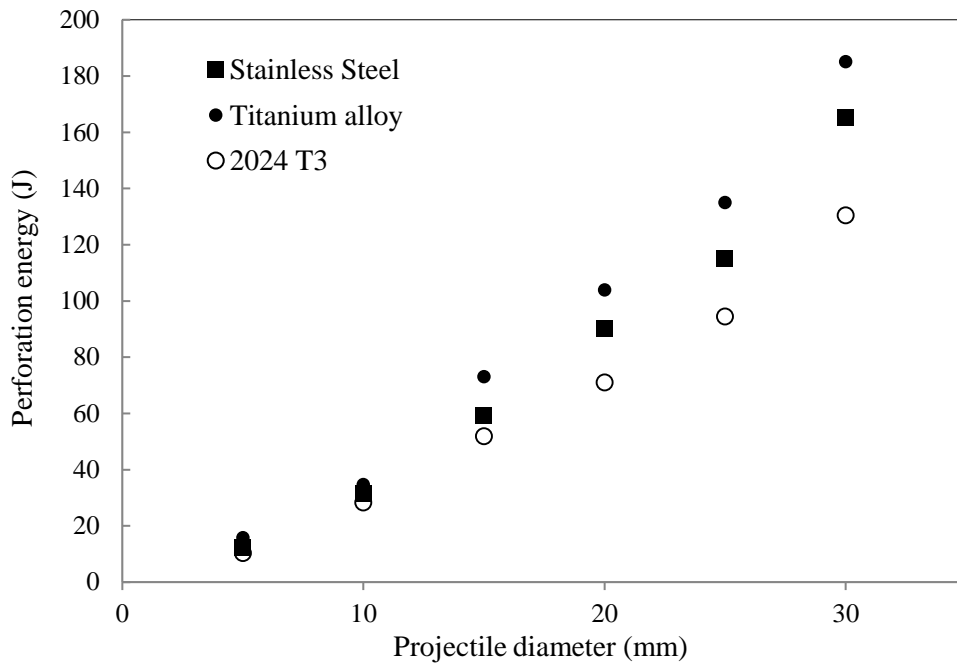


Figure 5.17: The variation of perforation energy with projectile diameter for three sandwich structures.

5.1.6 The main outcomes of the numerical modelling of aluminium curvilinear structures

The low velocity impact response of all-metal sandwich panels based on a curvilinear core has been investigated both experimentally and numerically. Initially, attention focused on understanding the experimental response of two thicknesses of an all-aluminium sandwich structure. Here, at low energies, failure took the form of a top surface dent, stretching of the upper skin and buckling of the core structure. Higher impact energies resulted in fracture of the skins and core, fracture mechanisms that were localized to the point of impact. The low velocity impact responses of the curvilinear panels were subsequently modelled using finite element analysis

techniques. Here, agreement between the measured and predicted load-displacement traces was good at all energy levels. An examination of the damage predicted by the FE analysis indicated that the models accurately captured all of the key failure mechanisms.

Following validation, the FE analysis was used to predict the effect of varying the projectile diameter and the angle of obliquity on the perforation resistance of sandwich panels based on a number of aluminium alloys, as well as a stainless steel and a titanium alloy. Here, it was shown that the perforation energy increases with impact angle, due to the increased volume of material fractured at higher impact angles. Similarly, it has been shown that increasing the projectile diameter serves to increase the perforation energy, with a 2024-T3 aluminium alloy offering the highest specific perforation energy of the six alloys considered here.

5.2 Modelling of the response of hybrid sandwich structure based on GFRP corrugated core subjected to flexural loading

Numerical models were developed to simulate the mechanical response of the hybrid sandwich structures based on GFRP corrugated core subjected to flexural loading. Modelling the failure behaviour of composite materials is a very complex process due to factors such as the variation of fibres and matrices materials.

The material models described below were implemented in Abaqus/Explicit and the predictions of the load-displacement responses and the associated failure modes were compared with the related experimental results.

5.2.1 Modelling of the Composite material (GFRP)

The composite GFRP corrugated sandwich samples were modelled as an orthotropic elastic material up to the onset of damage, followed by a damage initiation controlled by Hashin's failure criteria. Here, the theoretical part of Hashin's failure criteria was based on the work from Aziz [156].

The Hashin's damage model [157] consists of interaction of more than one stress components in evaluating failure modes. Hashin's damage initiation assumes that the response of the undamaged material is linearly elastic with the point stress calculations involving four failure modes. The failure modes are (i) fibre rupture in tension, (ii) fibre buckling and kinking in compression, (iii) matrix cracking under transverse tension and shearing and (iv) matrix crushing under transverse compression and shearing. By considering $\hat{\sigma}_{11}$, $\hat{\sigma}_{22}$ and $\hat{\tau}_{12}$ as the longitudinal, transverse and shear effective stresses, Hashin's damage initiation criteria take the general form as follows [157]:

(a) Fibre tension failure ($\hat{\sigma}_{11} \geq 0$):

$$F_f^t = \left(\frac{\hat{\sigma}_{11}}{X^T}\right)^2 + \alpha \left(\frac{\hat{\tau}_{12}}{S^L}\right)^2, d_f = 1 \quad (5.8)$$

(b) Fibre compressive failure ($\hat{\sigma}_{11} < 0$):

$$F_f^c = \left(\frac{\hat{\sigma}_{11}}{X^C}\right)^2, d_f = 1 \quad (5.9)$$

(c) Matrix tension failure ($\hat{\sigma}_{22} \geq 0$):

$$F_m^t = \left(\frac{\hat{\sigma}_{22}}{Y^T}\right)^2 + \left(\frac{\hat{\tau}_{12}}{S^L}\right)^2, d_m = 1 \quad (5.10)$$

(d) Matrix compression failure ($\hat{\sigma}_{22} < 0$):

$$F_m^c = \left(\frac{\hat{\sigma}_{22}}{2S^T}\right)^2 + \left[\left(\frac{Y^C}{2S^T}\right)^2 - 1\right] \frac{\hat{\sigma}_{22}}{Y^C} + \left(\frac{\hat{\tau}_{12}}{S^L}\right)^2, d_m = 1 \quad (5.11)$$

where X^T and X^C denote the tensile and compressive strength components in longitudinal direction by superscripts T and C , respectively. Similarly, Y^T and Y^C denote the tensile and compressive strengths in transverse direction, S^L and S^T are the longitudinal and transverse shear strengths. Table 5.4 gives a summary of the damage initiation data for glass fibre/epoxy. In Equation (5.), α is a coefficient that determines shear stress contribution to the fibre tensile initiation criterion. In this case, $\alpha = 1$ as the shear stress contribution was taken into account.

Table 5.4: Summary of the elasticity properties of the glass fibre/epoxy materials[72].

Parameters	Symbol	Glass fibre/epoxy
Density	ρ [kg/m ³]	2800
Young's modulus in longitudinal direction	E_1 [GPa]	23
Young's modulus in transverse direction	E_2 [GPa]	10.4
Young's modulus in thickness direction	E_3 [GPa]	5
In-plane shear modulus	G_{12} [GPa]	5
Out-of-plane shear modulus	G_{13} [GPa]	5
Out-of-plane shear modulus	G_{23} [GPa]	5
Major in-plane Poisson's ratio	ν_{12}	0.15
Out-of-plane Poisson's ratio	ν_{13}	0.15
Out-of-plane Poisson's ratio	ν_{23}	0.50
Tensile strength	X^T [MPa]	320
Compressive strength	X^c [MPa]	240
Tensile Yield strengths	Y^T [MPa]	320
Compressive Yield strengths	Y^c [MPa]	240
Longitudinal shear strengths	S^T [MPa]	320
Transverse shear strengths	S^c [MPa]	320

5.2.2 Geometrical model and contact conditions

The skins and core of GFRP were modelled using linear quadrilateral shell elements (S4R) with reduced integration and the supports were meshed with the linear quadrilateral rigid elements (R3D4). Figure 5.18 shows the FE modelling of three-

point bending test and Figure 5.19 shows loading and boundary conditions adopted in the finite element modelling.

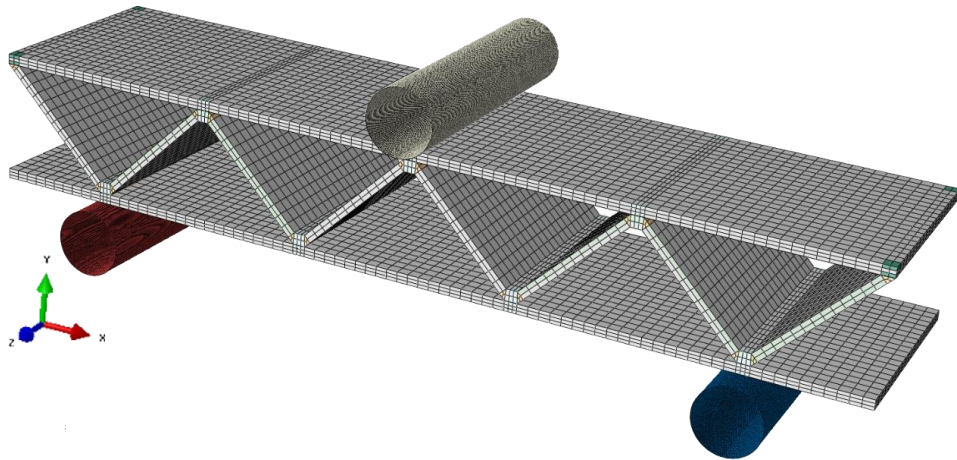


Figure 5.18: Schematic of three-point bending test using to model the FE modelling

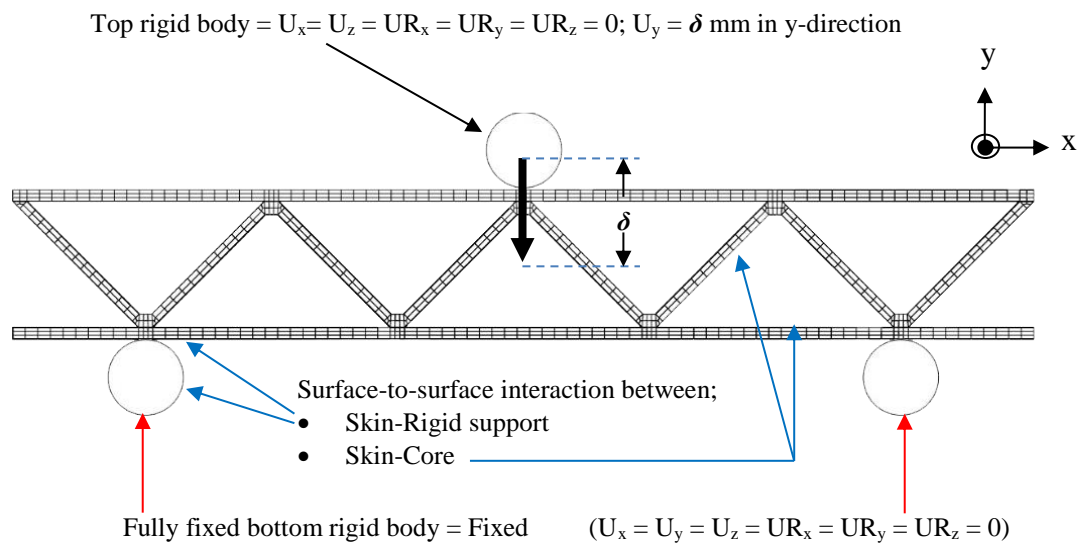


Figure 5.19: Loading and boundary conditions adopted in the finite element model

The cylindrical rigid supports were constrained as fully fixed as shown in the figure 5.19. A surface-to-surface interaction between the skin and the rigid supporters and also the skin and the core were applied with the different interaction properties. The top-middle supporter was defined to move in only y-direction with δ mm (depends on the thickness of the corrugated core of sandwich samples).

5.2.3 Mesh Sensitivity Analysis

A mesh sensitivity analysis was studied using a model of GFRP with 0.4 mm thickness with similar dimensions of the sample GFR4P used in Section 4.2.1.1.1. The fracture energy examined from the area under the load-displacement curve was used to indicate the reasonable number of elements. Here, four models were developed, with each containing elements 8440, 20898, 58840 and 322080 elements respectively. Details of mesh sensitivity analysis is shown in Table 5.5 and Figure 5.20. Figure 5.21 shows the mesh-sensitivity analysis indicating the number of elements required for the acceptable accurate output of the FE models of GFRP corrugated panels subjected to three-point loading. The meshes of the model were based on 8,440 elements (mesh size = 1 mm), 20,898 elements (mesh size = 0.75 mm), 58,840 elements (mesh size = 0.50 mm) and 322,080 elements (mesh size = 0.25mm).

Table 5.5: Details of mesh sensitivity analysis.

Number of Elements	Mesh size [mm]	CPU time [hour]	Fracture energy [J]	FE/exp difference [%]
Experiment	-	-	12.10	-
8,440	1.00	0.45	18.75	56.25
20,898	0.75	1.20	15.00	25.00
58,840	0.5	2.83	13.50	12.50
322,080	0.25	5.37	13.22	10.16

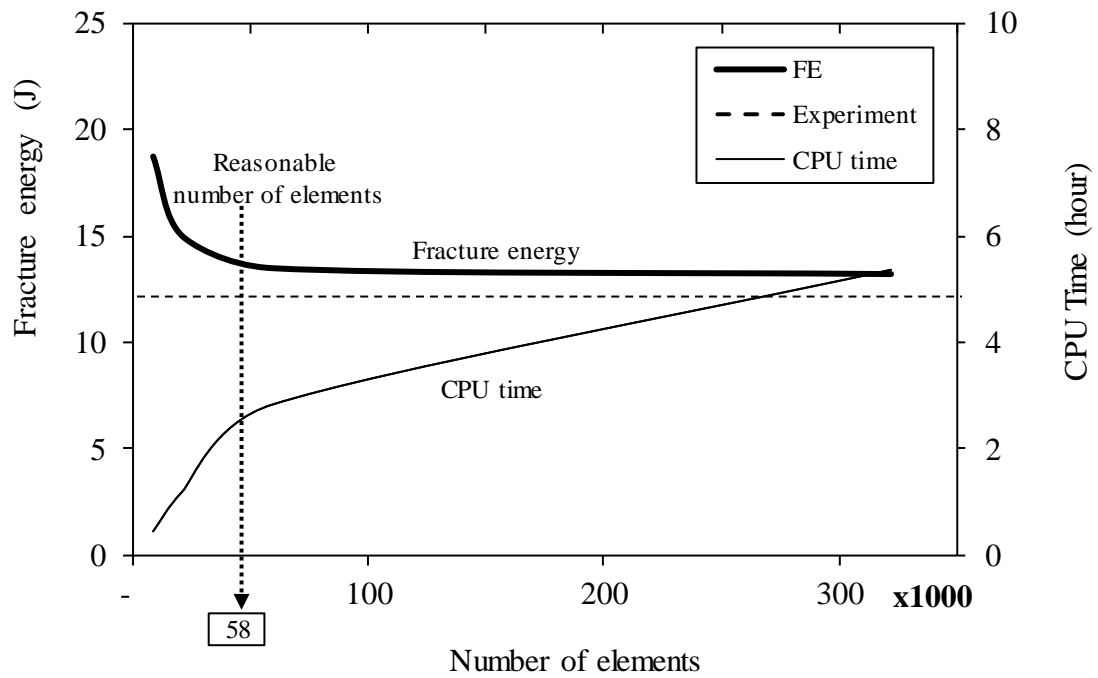


Figure 5.20: Mesh-sensitivity analysis showing the relationship of number of elements and fracture energy required for convergence of the FE model for GFRP corrugated panel subjected to three-point loading.

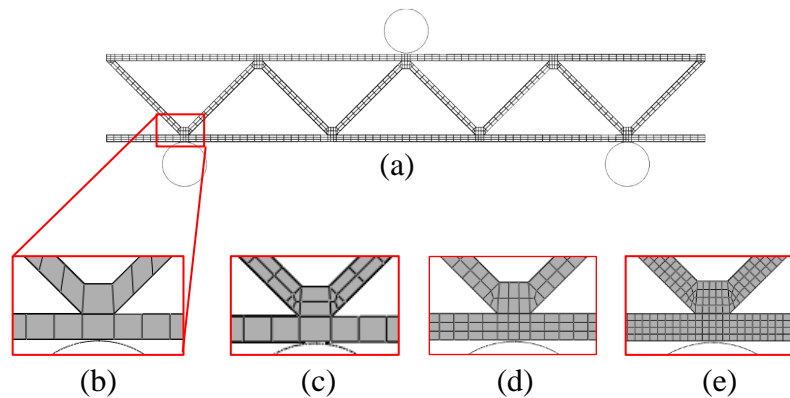


Figure 5.21: Mesh-sensitivity analysis showing the number of elements required for convergence of the FE model for GFRP corrugated panel subjected to three-point loading. The mesh of model based on (b) 8,440 elements (mesh = 1 mm), (c) 20,898 elements (me

5.2.4 Results and Discussion

Figure 5.22 shows the comparison of the simulated and experimentally failed sample, together the modelling of progressive failure. Clearly, the basic features of the failed sample are captured by the finite element model.

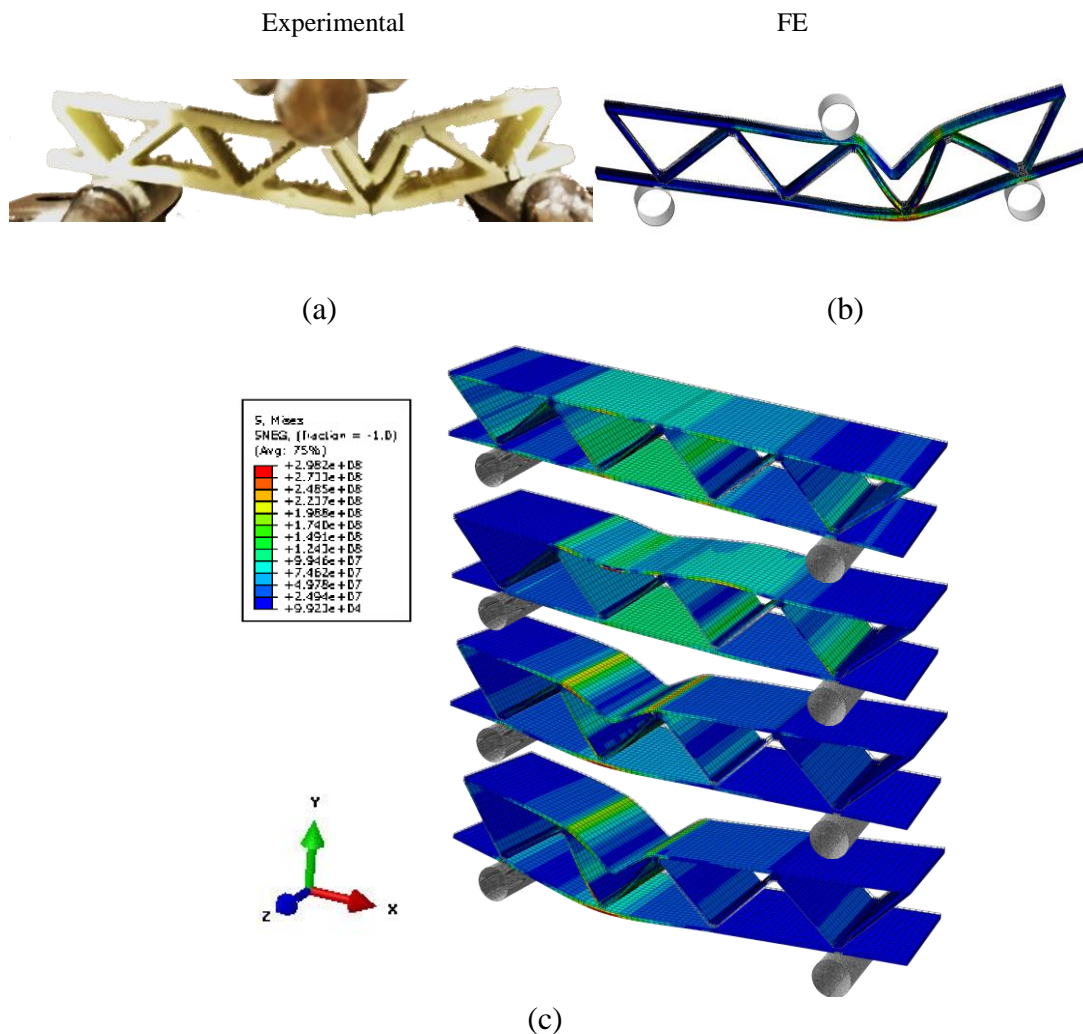


Figure 5.22: The progressive damage development of GFRP sandwich beam model (a) Image of the experiment, (b) FE modelling, (c) progressive damages

It can be seen that the progressive failure modes from the FE modelling reveals the similar style in the later stage of the failure, although the ultimate failure occurs at the left of the loading point. As shown in Figure 5.22(a) and (b), the weak point of the

sandwich beam was found near the mid-span of the upper skin. Apparently, as described before that GFRP composite performed in a brittle manner, which is also revealed in the modelling. However, this model cannot be used to predict the fracture mode as the damage evolution was not included in the model.

The predicted force-displacement curve from the finite element modelling is then compared to the experimental results (GFR4PBT1) taken from previous chapter in Section 4.2.1.1.1, as shown in Figure 5.23. The correlation is reasonably good, in terms of the initial stiffness, the peak force, the damage degradation and the plateau stage.

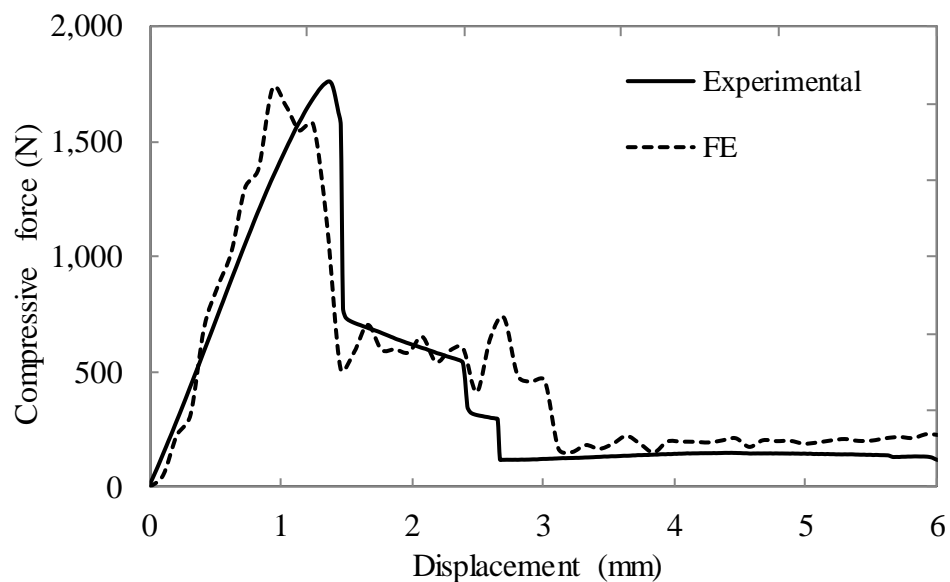


Figure 5.23: Experimental and numerical force-displacement traces for GFRP corrugated sandwich under three-point bending loading.

In general, both the traces demonstrate a linear fashion in the elastic region. It is clearly seen that the trace from FE modelling is not going up as smoothly as experimental data, which may be attributed to the slightly unstable interaction in the explicit modelling. Also, the simulated peak load is slightly ahead of the experimental

one due to the perfect boundary and loading engagement conditions, which contributed to a slightly higher stiffness.

5.3 Modelling of corrugated sandwich panel subjected to compressive loading

In this section, the finite modelling of plain GFRP corrugated composite sandwich panels with different corrugated core thickness were simulated under compressive loading, as described in Section 4.2.2.2. The composite material properties used are the same as that in the previous model in Section 5.2.1.

5.3.1 The modelling output

The GFRP skins and core were modelled using linear quadrilateral shell elements (S4R) with reduced integration. Again, the loading platen was meshed with the linear quadrilateral rigid elements (R3D4). Figure 5.24 shows the mesh generation of the GFRP corrugated sandwich panel, which was subjected to compression. Figure 5.25 shows the loading and boundary conditions adopted in the finite element model. The core was designed with a chamfer at the tips, so that it could easily make a partition with the same area of contact between core and skins as shown in a magnification view in Figure 5.24. In practical situation, the skins and the core of this panel was bonded with the resin from the prepreg which forms the skins and core. Therefore, for the simplification in the modelling, a tie constrain was used to fully bond the skins and the core together. For the boundary conditions, the bottom skin was fully fixed, and a rigid loading platen moved downward along the y-direction. Consequently, the panel was pressed by the rigid platen that has a interaction with the top surface of the panel through the surface-to-surface contact. The modelling was carried out using Abaqus/Explicit with a 5 second duration to eliminate any dynamic effect.

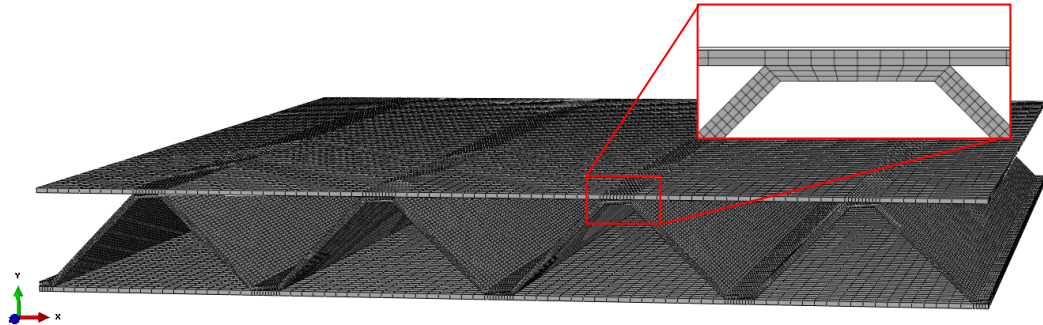


Figure 5.24: shows the FE modelling with meshes of GFRP corrugated sandwich panel under compression test.

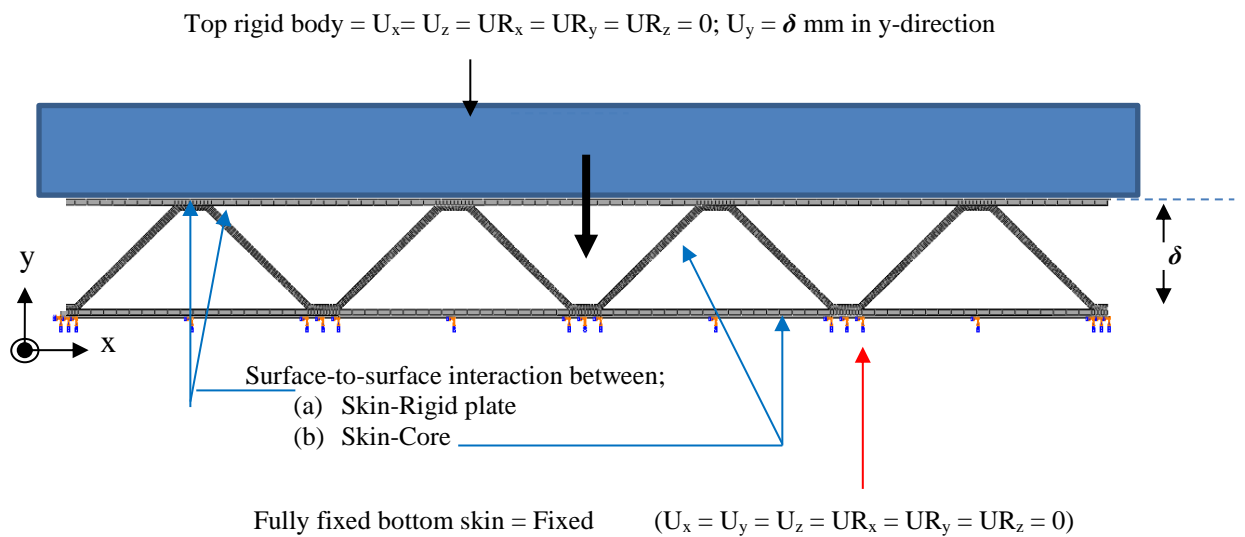


Figure 5.25: Loading and boundary conditions adopted in the finite element model

5.3.2 Results and Discussion

Figure 5.26 illustrates the simulated GFRP corrugated sandwich panel with the top skin removed for a better view. Here, the von-Mises stress distributions are shown,

with a legend at the top left. As it can be seen, the contour plot presents the different stress values on the panel core. Clearly, the high stresses are located near the mid-span of each inclined cell wall. This is understandable as all the connections between the skins and the core are tied. The high stress concentration regions on the core would be failure initiation locations.

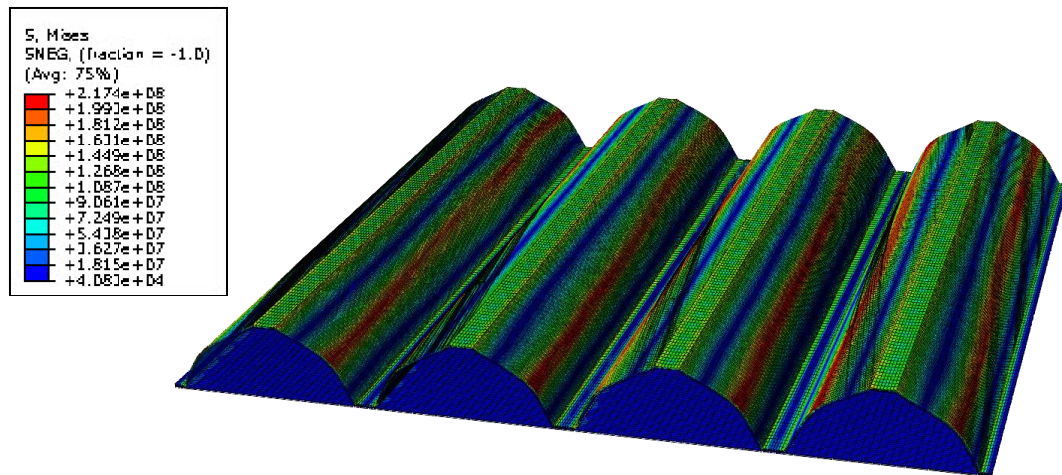


Figure 5.26: The predicted von-Mises distribution (in Pa) of the GFRP corrugated sandwich structure.

Figure 5.27 presents a comparison of the progressive damage development between the experimental (left) and FE modelling (right) results. It can be noticed that the progressive failure of the finite element modelling has a symmetrical bending of each unit cell wall. Unlike the failure mode occurring on the practical situation that the bending of individual cell walls are not symmetrical in most of the cells. In fact, only one unit cell on the right reveals the same pattern with the modelling prediction.

Figure 5.28 shows comparisons of load-displacement traces of GFRP corrugated sandwich structures obtained from experimental data and the FE results. In the all range of core thickness, the modelling output show a good agreement with the experimental data. However, the traces from the FE models demonstrate a less steep

drop of the force from the peak load, due to the damage evolution not being considered in the modelling.

Furthermore, the author tried to simulate a thicker core, showing in Figure 5.28 as GFR10P corresponding to 10 plies (1.25 mm), which shows a much higher plateau resistance after the force is dropped from the peak load. This may be caused by large plastic deformations for the thick cell wall, instead of pure buckling failure.

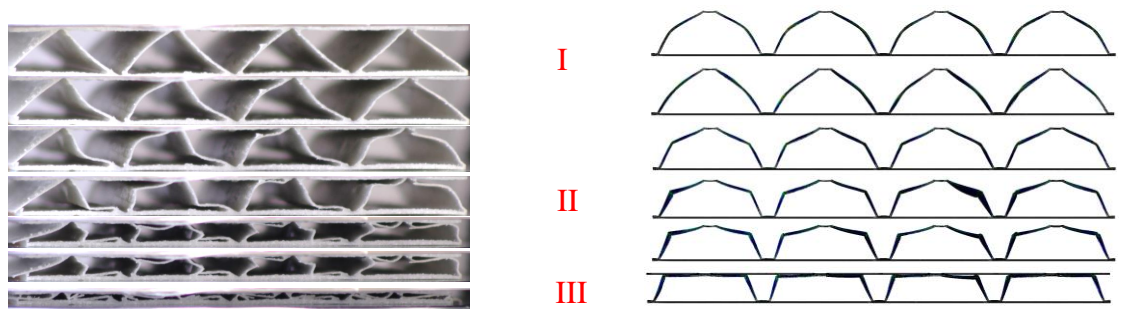


Figure 5.27: Comparison of progressive damage development between experimental (left) and FE modelling (right).

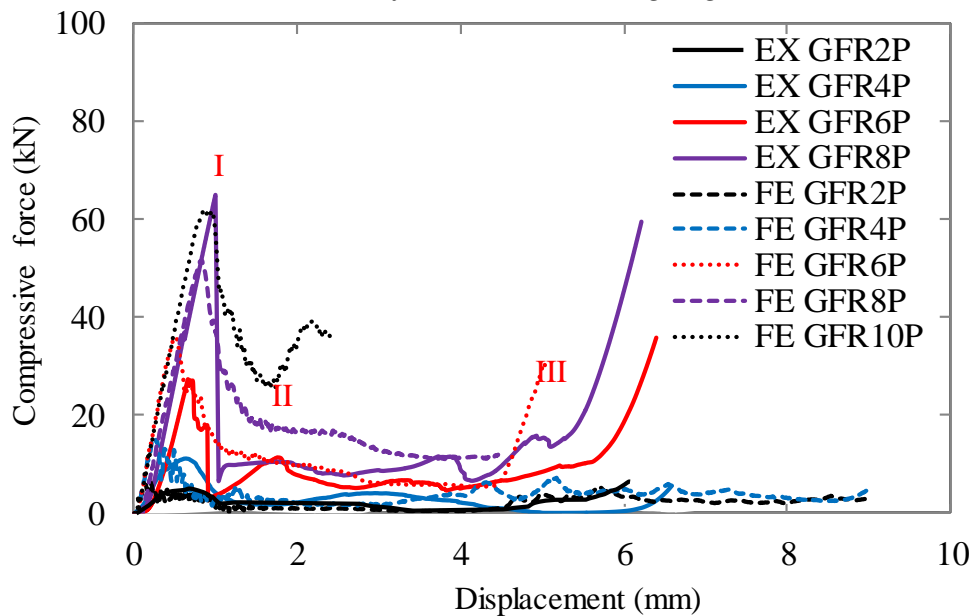


Figure 5.28: Comparison of load-displacement traces of GFRP corrugated sandwich structures between experimental FE data.

5.4 Summary

The finite element modelling results of various corrugated sandwich structures are compared and validated against the corresponding experimental data. The work demonstrate the capability of the modelling from the monolithic sandwich structure to the more complex GFRP corrugated sandwich structures subjected to quasi-static and impact loading. The agreements between the experimental results and the finite element modelling simulations are generally good in terms of the load-displacement trace, deformation and failure modes. The relevant failure mechanisms are also discussed. However, due to the limitation of the simplified finite element models, the fracture and delamination modes of the GFRP corrugated sandwich structures were not picked up.

CHAPTER 6

CONCLUSIONS AND RECOMMENDATIONS

In this final chapter, the major findings of this research are summarised. Following this, recommendations for future work will also be given.

6.1 Conclusions

The primary aim of this research is to propose the new technique developed for manufacturing the novel hybrid sandwich structures based on corrugated reinforced foam core. Based on the findings of this work, the following conclusions can be drawn.

- It could be concluded that the proposed manufacturing and fabrication techniques could reduce time consumption by fabricating all the assembly and then press them in a one-go process using a hot press.
- The newly introduced manufacturing and fabrication techniques can be used to produce the corrugated sandwich structures much easier than conventional techniques. There is no need of any adhesive agent to bond the core and the skin manually.
- The density of foam core is controllable rather than using liquid polyurethane injection technique for the corrugated sandwich reinforced foam core structures
- The finished panels have the same thickness, better bonding quality, core density and dimensions.
- The main outcome of this technique is the bonding quality that let the core and skins to be fully integrated as a whole body.
- However, the aluminium alloy sheet in FML core has to be pre-formed based on the corrugation moulds. Then FML core and skin corrugated sandwich structures can be produced. Therefore, there are two steps for fabricating this type of corrugated structure.

To investigate the mechanical properties of various hybrid sandwich structures, the corrugated reinforced foam cores made from composite materials and fibre metal laminates were subjected to both static and dynamic loading (tension, three-point bending, quasi-static compression and low-velocity impact and blast)

- The energy-absorbing characteristics of hybrid foam core sandwich structures were investigated from the area under curves of load-displacement traces obtained from the quasi-static and dynamic compression tests.
- The bending tests could also be used to investigate the flexural toughness, flexural modulus. The structures which has a higher flexural toughness per area density is a better structural designed and suitable to be selected for use.
- New hybrid structures offer superior mechanical properties in terms of compressive strength to weight ratio and energy absorption.
- The new hybrid triangular core sandwich structures based on FMLs and corrugated-core perform very well with a ductile failure mode.
- The key mechanical properties under static compression, such as strength, stiffness and energy absorption characteristics have been recorded for each corrugated-core sandwich specimen. The structures have shown excellent repeatability in terms of their mechanical response. The mechanical response in compression increases with specimen thickness.
- The strain rate has a small effect on the response of hybrid sandwich structures without the reinforced foam core under quasi-static and dynamic compressive loading. In contrast, the strain rate influences the peak load of the hybrid sandwich structures with the reinforced foam core by increasing it approximately by 33 % in comparison to the counterpart without reinforced foam core.

- The effect of core thickness of the plain GFRP sandwich structures under flexural loading has an exponential increase in the peak load with the ply number in the core and skins.
- Regarding to the effect of foam densities of hybrid composite sandwich structures, the sandwich structures have a linear relationship between core density and their peak load.
- The gradient foam core density could offer a potentially increase of the peak load. Therefore, it would be better to use this design on the structures for achieving the better energy absorption by having a low-high density order to face blast or impact loading.
- Under impact and blast loading, the designed structures can reduce or quarantine the damage area by the inter-bonding between core and skin and superior resistance offered by the vertical FML corrugation inside the foam core. Therefore this design may significantly absorb impact and blast energy so as to improve a watertight ability when used to be a ship bulkhead below the water line.

The impact response of curvilinear corrugated sandwich structures, in terms of progressive failure, deformation mode and load-displacement relationship, has been simulated successfully. Using the validated models, extensive parametric studies have been carried out to investigate structural responses under variation of materials, geometries and oblique impact. In addition, the structural behaviour the GFRP corrugated sandwich structures under bending and compression have been modelled appropriately, in a good agreement with the corresponding experimental results in terms of load-displacement trace, deformation and failure modes.

6.2 Recommendations for Future Work

From the above conclusions, it can be seen that this study has contributed the new fabrication techniques to produce the sandwich structures that provide a better bonding and integration. Also, the FML corrugated sandwich structures were studied comprehensively in the first time.

However, there is still much research that could be explored to build on the results achieved in this work. The following points address the areas which could be further investigated and highlights important aspects that should be considered in conducting future research work.

- It would be interesting for the further study to design a curvature corrugated core sandwich structures. It refers to the composite structures that is not just only flat panel as produced by the flat hot press. The drawback of flat panel is a limitation of use that is not versatile.
- The hybrid sandwich structures may offer a good performance when using as a superior pressure vessels or pipelines. If the cylindrical corrugated core could be designed, it could offer a good performance in terms of using in many pressure systems.
- It would be valuable to investigate the characteristics of the structures subjected to under-water impact or shock loading. This may be interested by the maritime industries.
- Modelling the complex fracture mechanisms of composite materials is a very challenging task. Therefore, in-depth understanding is needed before developing the numerical models.

- The skins and core were completely tied together in the current study. Therefore, the next step of study, the cohesive layer would be included in order to gain more reality of the bonding conditions.
- The optimisations of the composite corrugated structures need to be done. It would be very useful to extend this study to optimise the hybrid sandwich structure by using the data and knowledge of their structural responses to various loading conditions gained from this study.

REFERENCES

- [1] E. D. GmbH. (2004) The research requirements of the transport sectors to facilitate an increased usage of composite materials. Part I: The composite material research requirements of the aerospace industry.
- [2] J. Zhou, The Energy-Absorbing Behaviour of Novel Aerospace Composite Structures, PhD thesis, University of Liverpool, 2015.
- [3] M. Bakker and D. Eckroth, Wiley encyclopedia of packaging technology: J. Wiley, 1986.
- [4] M. Matsumoto, K. Masai, and T. Wajima, New technologies for railway trains, Hitachi Rev, vol. 48, 1999, pp. 134-138.
- [5] T. Yokozeki, S.-i. Takeda, T. Ogasawara, and T. Ishikawa, Mechanical properties of corrugated composites for candidate materials of flexible wing structures, Composites Part A: Applied Science and Manufacturing, vol. 37, 2006, pp. 1578-1586.
- [6] F. M., Building a better way of life for the future, Under sea Warfare Magazine: Submarine Force, vol. 87, 2004.
- [7] R. E. Melchers, Development of new applied models for steel corrosion in marine applications including shipping, Ships and Offshore Structures, vol. 3, 2008, pp. 135-144.
- [8] A. P. Mouritz, E. Gellert, P. Burchill, and K. Challis, Review of advanced composite structures for naval ships and submarines, Composite Structures, vol. 53, 2001/07/01/ 2001, pp. 21-42.
- [9] A. Herrmann, P. Zahlen, and I. Zuardy, Sandwich Structures Technology in Commercial Aviation, in Sandwich Structures 7: Advancing with Sandwich Structures and Materials, O. T. Thomsen, E. Bozhevolnaya, and A. Lyckegeard, Eds., ed: Springer Netherlands, 2005, pp. 13-26.
- [10] D. Zenkert, An introduction to sandwich construction: Engineering Materials Advisory Services Ltd, 1995.
- [11] W. J. Cantwell, P. Compston, and G. Reyes, The fracture properties of novel aluminum foam sandwich structures, Journal of Materials Science Letters, vol. 19, 2000, pp. 2205-2208.

- [12] L. Cui, S. Kiernan, and M. D. Gilchrist, Designing the energy absorption capacity of functionally graded foam materials, *Materials Science and Engineering: A*, vol. 507, 2009, pp. 215-225.
- [13] H. J. Rathbun, D. D. Radford, Z. Xue, M. Y. He, J. Yang, V. Deshpande, *et al.*, Performance of metallic honeycomb-core sandwich beams under shock loading, *International Journal of Solids and Structures*, vol. 43, 2006, pp. 1746-1763.
- [14] L. Aktay, A. F. Johnson, and B. H. Kröplin, Numerical modelling of honeycomb core crush behaviour, *Engineering Fracture Mechanics*, vol. 75, 2008, pp. 2616-2630.
- [15] B. Y. Ahn, D. Shoji, C. J. Hansen, E. Hong, D. C. Dunand, and J. A. Lewis, Printed origami structures, *Advanced Materials*, vol. 22, 2010, pp. 2251-2254.
- [16] S. Fischer, K. Drechsler, S. Kilchert, and A. Johnson, Mechanical tests for foldcore base material properties, *Composites Part A: Applied Science and Manufacturing*, vol. 40, 2009, pp. 1941-1952.
- [17] F. Côté, V. S. Deshpande, N. A. Fleck, and A. G. Evans, The compressive and shear responses of corrugated and diamond lattice materials, *International Journal of Solids and Structures*, vol. 43, 2006, pp. 6220-6242.
- [18] J.-H. Lim and K.-J. Kang, Mechanical behavior of sandwich panels with tetrahedral and Kagome truss cores fabricated from wires, *International Journal of Solids and Structures*, vol. 43, 2006, pp. 5228-5246.
- [19] M. Smith, W. Cantwell, Z. Guan, S. Tsopanos, M. Theobald, G. Nurick, *et al.*, The quasi-static and blast response of steel lattice structures, *Journal of Sandwich Structures and Materials*, vol. 13, 2011, pp. 479-501.
- [20] S. Kazemahvazi and D. Zenkert, Corrugated all-composite sandwich structures. Part 1: Modeling, *Composites Science and Technology*, vol. 69, 2009, pp. 913-919.
- [21] S. Kazemahvazi, D. Tanner, and D. Zenkert, Corrugated all-composite sandwich structures. Part 2: Failure mechanisms and experimental programme, *Composites Science and Technology*, vol. 69, 2009, pp. 920-925.

- [22] F. Zhu, G. Lu, D. Ruan, and Z. Wang, Plastic Deformation, Failure and Energy Absorption of Sandwich Structures with Metallic Cellular Cores, *International Journal of Protective Structures*, vol. 1, 2010, pp. 507-541.
- [23] L. J. Gibson and M. F. Ashby, *Cellular solids: structure and properties*: Cambridge university press, 1999.
- [24] H. N. Wadley, Multifunctional periodic cellular metals, *Philosophical Transactions of the Royal Society of London A: Mathematical, Physical and Engineering Sciences*, vol. 364, 2006, pp. 31-68.
- [25] L. L. Yan, B. Han, B. Yu, C. Q. Chen, Q. C. Zhang, and T. J. Lu, Three-point bending of sandwich beams with aluminum foam-filled corrugated cores, *Materials & Design*, vol. 60, 2014, pp. 510-519.
- [26] H. N. G. Wadley, K. P. Dharmasena, M. R. O'Masta, and J. J. Wetzel, Impact response of aluminum corrugated core sandwich panels, *International Journal of Impact Engineering*, vol. 62, 12// 2013, pp. 114-128.
- [27] J. J. Rimoli, B. Talamini, J. J. Wetzel, K. P. Dharmasena, R. Radovitzky, and H. N. G. Wadley, Wet-sand impulse loading of metallic plates and corrugated core sandwich panels, *International Journal of Impact Engineering*, vol. 38, 2011, pp. 837-848.
- [28] R. Rejab, *The Mechanical Properties Of Novel Lightweight Structures Based On Corrugated-Cores*, PhD Thesis, University of Liverpool 2013.
- [29] M. R. M. Rejab and W. J. Cantwell, The mechanical behaviour of corrugated-core sandwich panels, *Composites Part B: Engineering*, vol. 47, 2013, pp. 267-277.
- [30] B. Russell, A. Malcom, H. Wadley, and V. Deshpande, Dynamic compressive response of composite corrugated cores, *Journal of Mechanics of Materials and Structures*, vol. 5, 2010, pp. 477-493.
- [31] C. A. J. R. Vermeeren, An Historic Overview of the Development of Fibre Metal Laminates, *Applied Composite Materials*, vol. 10, 2003/07/01 2003, pp. 189-205.
- [32] J. Schijve, *Fatigue of structures and materials*: Springer, 2001.
- [33] G. H. J. J. Roebroeks, *The development of a fatigue insensitive and damage tolerant aircraft material*, 1991.

- [34] N. Buannic, P. Cartraud, and T. Quesnel, Homogenization of corrugated core sandwich panels, *Composite Structures*, vol. 59, 2003, pp. 299-312.
- [35] Y. Xia, M. I. Friswell, and E. I. S. Flores, Equivalent models of corrugated panels, *International Journal of Solids and Structures*, vol. 49, 2012, pp. 1453-1462.
- [36] A. Herrmann, P. Zahlen, and I. Zuardy, Sandwich structures technology in commercial aviation, *Sandwich structures 7: Advancing with sandwich structures and materials*, 2005, pp. 13-26.
- [37] N. Talbi, A. Batti, R. Ayad, and Y. Q. Guo, An analytical homogenization model for finite element modelling of corrugated cardboard, *Composite Structures*, vol. 88, 2009, pp. 280-289.
- [38] R. C. McKee, Gander, J.W., Wachuta, J.R., Compression strength formula for corrugated boxes, *Paperboard Packaging*, vol. 48, 1963, pp. 149-159.
- [39] S. Allaoui, Z. Aboura, and M. L. Benzeggagh, Effects of the environmental conditions on the mechanical behaviour of the corrugated cardboard, *Composites Science and Technology*, vol. 69, 2009, pp. 104-110.
- [40] P. Isaksson and P. Gradin, Shear buckling in the core of a corrugated board structure, *Composite Structures*, vol. 88, 2009, pp. 610-614.
- [41] Y. S. Tian and T. J. Lu, Optimal design of compression corrugated panels, *Thin-Walled Structures*, vol. 43, 2005, pp. 477-498.
- [42] D. Mohr and S. J. Marcadet, Micromechanically-motivated phenomenological Hosford–Coulomb model for predicting ductile fracture initiation at low stress triaxialities, *International Journal of Solids and Structures*, vol. 67–68, 2015, pp. 40-55.
- [43] C. C. Roth and D. Mohr, Effect of strain rate on ductile fracture initiation in advanced high strength steel sheets: Experiments and modeling, *International Journal of Plasticity*, vol. 56, 2014, pp. 19-44.
- [44] C. J. Wiernicki, F. Liem, G. D. Woods, and A. J. Furio, Structural analysis methods for lightweight metallic corrugated core sandwich panels subjected to blast loads, *Naval Engineers Journal*, vol. 103, 1991, pp. 192-202.

- [45] C.-C. Liang, M.-F. Yang, and P.-W. Wu, Optimum design of metallic corrugated core sandwich panels subjected to blast loads, *Ocean Engineering*, vol. 28, 2001, pp. 825-861.
- [46] W.-S. Chang, T. Krauthammer, and E. Ventsel, Elasto-Plastic Analysis of Corrugated-Core Sandwich Plates, *Mechanics of Advanced Materials and Structures*, vol. 13, 2006/03/01 2006, pp. 151-160.
- [47] I. Dayyani, S. Ziaei-Rad, and H. Salehi, Numerical and Experimental Investigations on Mechanical Behavior of Composite Corrugated Core, *Applied Composite Materials*, vol. 19, 2012, pp. 705-721.
- [48] A. J. Malcom, M. T. Aronson, V. S. Deshpande, and H. N. G. Wadley, Compressive response of glass fiber composite sandwich structures, *Composites Part A: Applied Science and Manufacturing*, vol. 54, 2013, pp. 88-97.
- [49] G. W. Kooistra, V. Deshpande, and H. N. G. Wadley, Hierarchical Corrugated Core Sandwich Panel Concepts, *Journal of Applied Mechanics*, vol. 74, 2005, pp. 259-268.
- [50] L. A. Carlsson, T. Nordstrand, and B. Westerlind, On the elastic stiffnesses of corrugated core sandwich, *Journal of Sandwich Structures and Materials*, vol. 3, 2001, pp. 253-267.
- [51] A. K. Noor, W. S. Burton, and C. W. Bert, Computational models for sandwich panels and shells, *Applied Mechanics Reviews*, vol. 49, 1996, pp. 155-155.
- [52] W.-S. Chang, E. Ventsel, T. Krauthammer, and J. John, Bending behavior of corrugated-core sandwich plates, *Composite Structures*, vol. 70, 8// 2005, pp. 81-89.
- [53] M. F. Ashby, The properties of foams and lattices, *Philosophical Transactions of the Royal Society A: Mathematical, Physical and Engineering Sciences*, vol. 364, 2006, pp. 15-30.
- [54] T. Lu, C. Chen, and G. Zhu, Compressive behaviour of corrugated board panels, *Journal of composite materials*, vol. 35, 2001, pp. 2098-2126.
- [55] F. R. Shanley, Inelastic column theory, *Journal of the aeronautical sciences*, 2012

- [56] M. T. Tilbrook, D. D. Radford, V. S. Deshpande, and N. A. Fleck, Dynamic crushing of sandwich panels with prismatic lattice cores, *International Journal of Solids and Structures*, vol. 44, 2007, pp. 6101-6123.
- [57] B. Han, K.-K. Qin, B. Yu, Q.-C. Zhang, C.-Q. Chen, and T. J. Lu, Design optimization of foam-reinforced corrugated sandwich beams, *Composite Structures*, vol. 130, 2015, pp. 51-62.
- [58] M. Richardson and M. Wisheart, Review of low-velocity impact properties of composite materials, *Composites Part A: Applied Science and Manufacturing*, vol. 27, 1996, pp. 1123-1131.
- [59] W. J. Cantwell and J. Morton, The impact resistance of composite materials - a review, *Composites*, vol. 22, 1991, pp. 347-362.
- [60] G. Bibo and P. Hogg, The role of reinforcement architecture on impact damage mechanisms and post-impact compression behaviour, *Journal of Materials Science*, vol. 31, 1996, pp. 1115-1137.
- [61] S. Abrate, Impact on laminated composites: recent advances, *Appl Mech Rev*, vol. 47, 1994, pp. 517-44.
- [62] S. Abrate, Impact on Laminated Composite Materials, *Applied Mechanics Reviews*, vol. 44, 1991, pp. 155-190.
- [63] N. Jones, *Structural impact: Cambridge university press*, 2011.
- [64] C. Calladine and R. English, Strain-rate and inertia effects in the collapse of two types of energy-absorbing structure, *International Journal of Mechanical Sciences*, vol. 26, 1984, pp. 689-701.
- [65] G. Taylor, The use of flat-ended projectiles for determining dynamic yield stress. I. Theoretical considerations, in *Proceedings of the Royal Society of London A: Mathematical, Physical and Engineering Sciences*, 1948, pp. 289-299.
- [66] A. Vlot, Impact loading on fibre metal laminates, *International Journal of Impact Engineering*, vol. 18, 1996, pp. 291-307.
- [67] S. Zhu and G. B. Chai, Low-velocity impact response of fibre–metal laminates – Experimental and finite element analysis, *Composites Science and Technology*, vol. 72, 2012, pp. 1793-1802.

- [68] M. Sadighi, R. C. Alderliesten, and R. Benedictus, Impact resistance of fiber-metal laminates: A review, *International Journal of Impact Engineering*, vol. 49, 2012, pp. 77-90.
- [69] G. Reyes Villanueva and W. J. Cantwell, The high velocity impact response of composite and FML-reinforced sandwich structures, *Composites Science and Technology*, vol. 64, 1// 2004, pp. 35-54.
- [70] G. H. Payeganeh, F. Ashenai Ghasemi, and K. Malekzadeh, Dynamic response of fiber-metal laminates (FMLs) subjected to low-velocity impact, *Thin-Walled Structures*, vol. 48, 2010, pp. 62-70.
- [71] F. D. Morinière, R. C. Alderliesten, and R. Benedictus, Energy distribution in GLARE and 2024-T3 aluminium during low-velocity impact, in *Proceeding of the 28th international congress of the aeronautical sciences*, Brisbane, Australia, 2012.
- [72] J. Fan, Z. W. Guan, and W. J. Cantwell, Numerical modelling of perforation failure in fibre metal laminates subjected to low velocity impact loading, *Composite Structures*, vol. 93, 2011, pp. 2430-2436.
- [73] G. Caprino, G. Spataro, and S. Del Luongo, Low-velocity impact behaviour of fibreglass-aluminium laminates, *Composites Part A: Applied Science and Manufacturing*, vol. 35, 2004, pp. 605-616.
- [74] W. J. Cantwell and J. Morton, Comparison of the low and high velocity impact response of cfrp, *Composites*, vol. 20, 1989, pp. 545-551.
- [75] W. J. Cantwell and J. Morton, The influence of varying projectile mass on the impact response of CFRP, *Composite Structures*, vol. 13, 1989, pp. 101-114.
- [76] M. R. Abdullah and W. J. Cantwell, The impact resistance of polypropylene-based fibre-metal laminates, *Composites Science and Technology*, vol. 66, 2006, pp. 1682-1693.
- [77] A. P. Christoforou and S. R. Swanson, Analysis of impact response in composite plates, *International Journal of Solids and Structures*, vol. 27, 1991/01/01 1991, pp. 161-170.
- [78] G. B. Chai and S. Zhu, A review of low-velocity impact on sandwich structures, *Proceedings of the Institution of Mechanical Engineers, Part L: Journal of Materials Design and Applications*, vol. 225, 2011, pp. 207-230.

- [79] W. J. Stronge, *Impact mechanics*: Cambridge university press, 2004.
- [80] S. Abrate, *Impact on composite structures*: Cambridge university press, 2005.
- [81] R. Olsson, Mass criterion for wave controlled impact response of composite plates, *Composites Part A: Applied Science and Manufacturing*, vol. 31, 2000, pp. 879-887.
- [82] W. Cantwell and J. Morton, The impact resistance of composite materials—a review, *composites*, vol. 22, 1991, pp. 347-362.
- [83] V. Rubino, V. S. Deshpande, and N. A. Fleck, The dynamic response of end-clamped sandwich beams with a Y-frame or corrugated core, *International Journal of Impact Engineering*, vol. 35, 2008, pp. 829-844.
- [84] C. Kılıçaslan, M. Güden, İ. K. Odacı, and A. Taşdemirci, The impact responses and the finite element modeling of layered trapezoidal corrugated aluminum core and aluminum sheet interlayer sandwich structures, *Materials & Design*, vol. 46, 2013, pp. 121-133.
- [85] D. D. Radford, N. A. Fleck, and V. S. Deshpande, The response of clamped sandwich beams subjected to shock loading, *International Journal of Impact Engineering*, vol. 32, 2006, pp. 968-987.
- [86] M. L. Wilkins, Mechanics of penetration and perforation, *International Journal of Engineering Science*, vol. 16, 1978, pp. 793-807.
- [87] M. Aktaş, C. Atas, B. M. İçten, and R. Karakuzu, An experimental investigation of the impact response of composite laminates, *Composite Structures*, vol. 87, 2// 2009, pp. 307-313.
- [88] R. Sriram, U. K. Vaidya, and J.-E. Kim, Blast impact response of aluminum foam sandwich composites, *Journal of Materials Science*, vol. 41, 2006, p. 4023.
- [89] S. C. K. Yuen, G. N. Nurick, M. D. Theobald, and G. S. Langdon, Sandwich Panels Subjected to Blast Loading, in *Dynamic Failure of Materials and Structures*, A. Shukla, G. Ravichandran, and Y. D. S. Rajapakse, Eds., ed Boston, MA: Springer US, 2010, pp. 297-325.
- [90] F. Zhu and G. Lu, A review of blast and impact of metallic and sandwich structures, *EJSE Special Issue: Loading and Structures*, 2007, pp. 92-101.

- [91] L. J. Gibson and M. F. Ashby, Cellular solids: structure and properties part 1: Cambridge university press, 1999.
- [92] A. Hanssen, L. Enstock, and M. Langseth, Close-range blast loading of aluminium foam panels, *International Journal of Impact Engineering*, vol. 27, 2002, pp. 593-618.
- [93] X. Cui, L. Zhao, Z. Wang, H. Zhao, and D. Fang, Dynamic response of metallic lattice sandwich structures to impulsive loading, *International Journal of Impact Engineering*, vol. 43, 2012, pp. 1-5.
- [94] G. S. Langdon and W. J. Cantwell, The blast response of composite and fibre-metal laminate materials used in aerospace applications. Cambridge: Woodhead Publ Ltd, 2015.
- [95] G. Nurick, G. Langdon, Y. Chi, and N. Jacob, Behaviour of sandwich panels subjected to intense air blast–Part 1: Experiments, *Composite Structures*, vol. 91, 2009, pp. 433-441.
- [96] A. G. Evans, J. Hutchinson, and M. Ashby, Multifunctionality of cellular metal systems, *Progress in Materials Science*, vol. 43, 1998, pp. 171-221.
- [97] Z. Xue and J. W. Hutchinson, Preliminary assessment of sandwich plates subject to blast loads, *International Journal of Mechanical Sciences*, vol. 45, 2003, pp. 687-705.
- [98] A. Vaziri, Z. Xue, and J. W. Hutchinson, Metal sandwich plates with polymer foam-filled cores, *Journal of Mechanics of Materials and Structures*, vol. 1, 2006, pp. 97-127.
- [99] M. Tilbrook, V. Deshpande, and N. Fleck, Underwater blast loading of sandwich beams: regimes of behaviour, *International Journal of Solids and Structures*, vol. 46, 2009, pp. 3209-3221.
- [100] M. Tilbrook, V. Deshpande, and N. Fleck, The impulsive response of sandwich beams: analytical and numerical investigation of regimes of behaviour, *Journal of the Mechanics and Physics of Solids*, vol. 54, 2006, pp. 2242-2280.
- [101] D. Karagiozova, G. Nurick, and G. Langdon, Behaviour of sandwich panels subject to intense air blasts–Part 2: Numerical simulation, *Composite Structures*, vol. 91, 2009, pp. 442-450.

- [102] S. Gupta and A. Shukla, Blast performance of marine foam core sandwich composites at extreme temperatures, *Experimental mechanics*, vol. 52, 2012, pp. 1521-1534.
- [103] M. Yazici, J. Wright, D. Bertin, and A. Shukla, Experimental and numerical study of foam filled corrugated core steel sandwich structures subjected to blast loading, *Composite Structures*, vol. 110, 4// 2014, pp. 98-109.
- [104] G. S. Langdon, S. L. Lemanski, G. N. Nurick, M. C. Simmons, W. J. Cantwell, and G. K. Schleyer, Behaviour of fibre-metal laminates subjected to localised blast loading: Part I-Experimental observations, *International Journal of Impact Engineering*, vol. 34, 2007, pp. 1202-1222.
- [105] S. L. Lemanski, G. N. Nurick, G. S. Langdon, M. C. Simmons, W. J. Cantwell, and G. K. Schleyer, Behaviour of fibre metal laminates subjected to localised blast loading-Part II: Quantitative analysis, *International Journal of Impact Engineering*, vol. 34, 2007, pp. 1223-1245.
- [106] S. L. Lemanski, G. N. Nurick, G. S. Langdon, M. S. Simmons, W. J. Cantwell, and G. K. Schleyer, Understanding the behaviour of fibre metal laminates subjected to localised blast loading, *Composite Structures*, vol. 76, 10// 2006, pp. 82-87.
- [107] A. R. Aziz, The Energy-absorbing Characteristics of Novel Tube-reinforced Sandwich Structures, PhD thesis, University of Liverpool, 2015.
- [108] M. F. Ashby and D. Cebon, Materials selection in mechanical design, *Le Journal de Physique IV*, vol. 3, 1993, pp. C7-1-C7-9.
- [109] M. F. Ashby, *Materials selection in mechanical design*, Butterworth-Heinemann, ISBN 0, vol. 7506, 2005, p. 2.
- [110] K. Fujikake, B. Li, and S. Soeun, Impact Response of Reinforced Concrete Beam and Its Analytical Evaluation, *Journal of Structural Engineering*, vol. 135, 2009, pp. 938-950.
- [111] S. Lee, *An Introduction to mathematics for engineers*: Hodder Education, 2008.
- [112] P. Thornton, J. Harwood, and P. Beardmore, Fiber-reinforced plastic composites for energy absorption purposes, *Composites Science and Technology*, vol. 24, 1985, pp. 275-298.

- [113] Q. Li, I. Magkiriadis, and J. Harrigan, Compressive strain at the onset of densification of cellular solids, *Journal of cellular plastics*, vol. 42, 2006, pp. 371-392.
- [114] F. Laurin and A. J. Vizzini, Energy absorption of sandwich panels with composite-reinforced foam core, *Journal of Sandwich Structures & Materials*, vol. 7, 2005, pp. 113-132.
- [115] G. L. Farley, Energy absorption of composite materials, *Journal of composite Materials*, vol. 17, 1983, pp. 267-279.
- [116] M. Hassan and W. Cantwell, The influence of core properties on the perforation resistance of sandwich structures—An experimental study, *Composites Part B: Engineering*, vol. 43, 2012, pp. 3231-3238.
- [117] S. Heimbs, Computational methods for bird strike simulations: A review, *Computers & Structures*, vol. 89, 2011, pp. 2093-2112.
- [118] S. Heimbs, B. Van Den Broucke, Y. D. Kergomard, F. Dau, and B. Malherbe, Rubber impact on 3D textile composites, *Applied composite materials*, vol. 19, 2012, pp. 275-295.
- [119] M. Altenaiji, Z. Guan, W. Cantwell, Y. Zhao, and G. Schleyer, Characterisation of aluminium matrix syntactic foams under drop weight impact, *Materials & Design*, vol. 59, 2014, pp. 296-302.
- [120] S. Ochelski, P. Bogusz, and A. Kiczko, Static axial crush performance of unfilled and foamed-filled composite tubes, *Bulletin of the Polish Academy of Sciences: Technical Sciences*, vol. 60, 2012, pp. 31-35.
- [121] X. Tao and Y. Zhao, Compressive behavior of Al matrix syntactic foams toughened with Al particles, *Scripta Materialia*, vol. 61, 2009, pp. 461-464.
- [122] M. Zuhri, Z. Guan, and W. Cantwell, The mechanical properties of natural fibre based honeycomb core materials, *Composites Part B: Engineering*, vol. 58, 2014, pp. 1-9.
- [123] A. Airoidi, P. Bettini, M. Zazzarini, and F. Scarpa, Failure and energy absorption of plastic and composite chiral honeycombs, *Structures under Shock and Impact XII*, 2012, pp. 101-114.

- [124] R. Alia, W. Cantwell, G. Langdon, S. Yuen, and G. Nurick, The energy-absorbing characteristics of composite tube-reinforced foam structures, *Composites Part B: Engineering*, vol. 61, 2014, pp. 127-135.
- [125] R. Umer, S. Balawi, P. Raja, and W. Cantwell, The energy-absorbing characteristics of polymer foams reinforced with bamboo tubes, *Journal of Sandwich Structures & Materials*, vol. 16, 2014, pp. 108-122.
- [126] F. Tarlochan, S. Ramesh, and S. Harpreet, Advanced composite sandwich structure design for energy absorption applications: blast protection and crashworthiness, *Composites Part B: Engineering*, vol. 43, 2012, pp. 2198-2208.
- [127] M. Rejab, K. Ushijima, and W. Cantwell, The shear response of lightweight corrugated core structures, *Journal of Composite Materials*, vol. 48, 2014, pp. 3785-3798.
- [128] M. Smith, Z. Guan, and W. Cantwell, Finite element modelling of the compressive response of lattice structures manufactured using the selective laser melting technique, *International Journal of Mechanical Sciences*, vol. 67, 2013, pp. 28-41.
- [129] J. Xiong, A. Vaziri, L. Ma, J. Papadopoulos, and L. Wu, Compression and impact testing of two-layer composite pyramidal-core sandwich panels, *Composite Structures*, vol. 94, 2012, pp. 793-801.
- [130] R. Haj-Ali, J. Choi, B.-S. Wei, R. Popil, and M. Schaepe, Refined nonlinear finite element models for corrugated fiberboards, *Composite Structures*, vol. 87, 2009, pp. 321-333.
- [131] J. Zhou, Z. Guan, and W. Cantwell, Numerical modelling of perforation impact damage of fibre metal laminates,
- [132] W. He, J. Liu, B. Tao, D. Xie, J. Liu, and M. Zhang, Experimental and numerical research on the low velocity impact behavior of hybrid corrugated core sandwich structures, *Composite Structures*, vol. 158, 12/15/ 2016, pp. 30-43.
- [133] M. P. Nemeth, Buckling and postbuckling behaviour of laminated composite plates with a cut-out, in *Buckling and Postbuckling of Composite Plates*, G. J. Turvey and I. H. Marshall, Eds., ed: Springer Netherlands, 1995, pp. 260-298.

- [134] Data sheet for AIREX C70-200 universal structural foam, Airex AG,2016, [Accessed: 31 Jan 2017], <http://www.airexbaltekbanova.com/downloads.html>
- [135] Data sheet for ROHACELL®71 WF Technical Information, Evonik Resource Efficiency GmbH,2016, [Accessed: 9 November 2016]
<http://www.rohacell.com/sites/lists/RE/DocumentsHP/ROHACELL%20WF%20Product%20Information.pdf>
- [136] A. Asundi and A. Y. N. Choi, Fiber metal laminates: An advanced material for future aircraft, Journal of Materials Processing Technology, vol. 63, 1997, pp. 384-394.
- [137] Data sheet for PTFE Coated Glass Cloth - Slit Coils (Self Adhesive Backed), PAR-group Ltd,2016, [Accessed: 11 Feb 2017], <http://www.par-group.co.uk/site-content/1/Docs/updates/4-high-temperature-insulation/4.15-ptfe-coated-glass-cloth-a5108-10thou-tds.pdf>
- [138] ASTM E8/E8M – 16a, Standard test methods for tensile testing of metallic materials, Section Standard test methods for tensile testing of metallic materials, ASTM International, West Conshohocken, PA, 1997.
- [139] BS-527-4, Plastics, Section Plastics, BS, Brussels: European Committee for Standardization, 1997
- [140] ASTM D1621-16, Standard Test Method for Compressive Properties of Rigid Cellular Plastics, Section Standard Test Method for Compressive Properties of Rigid Cellular Plastics, ASTM International, West Conshohocken,PA, 2016.
- [141] ASTM D790, Standard Test Methods for Flexural Properties of Unreinforced and Reinforced Plastics and Electrical Insulating Materials, Section Standard Test Methods for Flexural Properties of Unreinforced and Reinforced Plastics and Electrical Insulating Materials, ASTM International, 2015.
- [142] Data Sheet, Type 9323AA Kistler Group,2010, [Accessed: 15 Feb 2017], <http://web.sensor-ic.com:8000/ZLXIAZAI/KISTLER/000-704e-09.10.pdf>
- [143] M. Tenaiji, Characterisation of aluminium matrix syntactic foams under static and dynamic loading, PhD thesis, University of Liverpool, 2014.

- [144] Data sheet, The light weight panel, Metawell,2016, [Accessed: 12 Feb 2017], https://www.metawell.com/wp-content/uploads/2016/02/Metawell_data_sheets.pdf
- [145] S. Davids, The influence of charge geometry on the response of cylinders to internal air blasting, PhD thesis, University of Cape Town, 2016.
- [146] M. R. Sonne, C. C. Tutum, J. H. Hattel, A. Simar, and B. de Meester, The effect of hardening laws and thermal softening on modeling residual stresses in FSW of aluminum alloy 2024-T3, *Journal of Materials Processing Technology*, vol. 213, 2013, pp. 477-486.
- [147] M. Z. Hassan, Z. W. Guan, W. J. Cantwell, G. S. Langdon, and G. N. Nurick, The influence of core density on the blast resistance of foam-based sandwich structures, *International Journal of Impact Engineering*, vol. 50, 2012, pp. 9-16.
- [148] M. E. Biancolini, Evaluation of equivalent stiffness properties of corrugated board, *Composite Structures*, vol. 69, 2005, pp. 322-328.
- [149] U. Nyman and P. J. Gustafsson, Material and structural failure criterion of corrugated board facings, *Composite Structures*, vol. 50, 2000, pp. 79-83.
- [150] J. Xiong, L. Ma, L. Wu, J. Liu, and A. Vaziri, Mechanical behavior and failure of composite pyramidal truss core sandwich columns, *Composites Part B: Engineering*, vol. 42, 2011, pp. 938-945.
- [151] Y.-K. Lin, H.-K. Liu, W.-S. Kuo, and Y.-D. Chen, Fracture evolution in thick composites under compression, *Polymer Composites*, vol. 28, 2007, pp. 425-436.
- [152] Z. S. Zhang Y, Wang Z., Crush behavior of corrugated cores sandwich panels, *Advanced Materials Research*, vol. 217-218, 2011, pp. 1584-1589.
- [153] Abaqus6.12-3, Analysis User's Manual, Dassault Systemes Simulia Corp. , 2012
- [154] W. Ozgowicz, E. Kalinowska-Ozgowicz, and A. Kurc, Influence of plastic deformation on structure and mechanical properties of stainless steel type X5CrNi18-10, *Journal of Achievements in Materials and Manufacturing Engineering*, vol. 32, 2008, pp. 37-40.

- [155] D. R. Lesuer, Experimental investigation of material models for Ti-6Al-4V Titanium and 2024-T3, Lawrence Livermore National Laboratory FAA Report DOT/FAA/AR-00/25, 2000.
- [156] A. R. Aziz, The Energy-absorbing Characteristics of Novel Tube-reinforced Sandwich Structures, University of Liverpool, 2015.
- [157] Z. Hashin, Fatigue failure criteria for unidirectional fiber composites, ASME, Transactions, Journal of Applied Mechanics, vol. 48, 1981, pp. 846-852.

